JUNO's Sensitivity to the Neutrino Mass Ordering in Presence of a Fine Structure in the Reactor Antineutrino Spectrum

Dissertation

der Mathematisch-Naturwissenschaftlichen Fakultät
der Eberhard Karls Universität Tübingen
zur Erlangung des Grades eines
Doktors der Naturwissenschaften
(Dr. rer. nat.)

vorgelegt von
Tobias Daniel Heinz
aus Reutlingen

Tübingen
2024

Gedruckt mit Genehmigung der Mathematisch-Naturwissenschaftlichen Fakultät der Eberhard Karls Universität Tübingen.

Tag der mündlichen Qualifikation:	16.09.2024
Dekan:	Prof. Dr. Thilo Stehle
1. Berichterstatter:	Prof. Dr. Tobias Lachenmaier
2. Berichterstatter:	Prof. Dr. Josef Jochum

Abstract

To answer one of the most important open questions in neutrino physics, the neutrino mass ordering (NMO), the Jiangmen Underground Neutrino Observatory (JUNO) is constructed in the Guangdong province in the southeast of China. To reach the goal of determining the NMO with a significance of 3σ in about six years of data taking, it features a 20 kt liquid scintillator detector with an unprecedented energy resolution of better than 3% at 1 MeV which will measure the oscillated electron antineutrino spectrum from nuclear reactors at a distance of 53 km. In addition, its satellite detector, the Taishan Antineutrino Observatory (TAO), filled with 2.8 tons of Gadolinium-loaded liquid scintillator, will measure the unoscillated reactor antineutrino spectrum to provide a reference spectrum with a resolution of better than 2% at 1 MeV. Detailed calculations of the reactor antineutrino spectrum based on nuclear data show the existence of a fine structure that has not yet been observed but could have implications on the determination of the neutrino mass ordering in a high resolution detector like JUNO.

In this work, a variety of spectra with such a possible fine structure have been generated to test possible implications on JUNO's sensitivity to the neutrino mass ordering. It was demonstrated that the lack of knowledge on the fine structure can significantly impact the sensitivity of JUNO if the reference spectrum only relies on the known reactor models. Therefore, the reference spectrum measured with the satellite detector TAO is included in a combined fit to take into account the unknown fine structure in the unoscillated spectrum. It was shown that the fine structure does not introduce a negative impact on the sensitivity if the JUNO spectrum is constrained by the TAO measurement. In addition, it was demonstrated that the requirement of the energy resolution of TAO to be better than the resolution of JUNO is crucial to achieve the desired sensitivity. It was found that with an exposure of 6.5 years $\times$ 26.6 $\mathrm{GW_{th}}$ and the unprecedented energy resolutions of better than 3% at 1 MeV of JUNO and better than 2% at 1 MeV of TAO, a median sensitivity of 3σ (3.1σ) for a true normal (inverted) mass ordering can be achieved with JUNO regardless of the presence of a fine structure in the reactor antineutrino spectrum showing that the Asimov sensitivity of the case without fine structure gives a valid estimate of JUNO's median sensitivity to the NMO.

Zusammenfassung

Um eine der wichtigsten offenen Fragen der Neutrinophysik zu beantworten, der Frage nach der Neutrinomassenhierarchie, wird zurzeit das Jiangmen Underground Neutrino Observatory (JUNO) in der Provinz Guangdong im Südosten Chinas gebaut. Um das Ziel zu erreichen, die Massenhierarchie mit einer Signifikanz von 3σ in etwa sechs Jahren Messdauer zu bestimmen, verwendet das Experiment einen Flüssigszintillatordetektor mit einer Masse von 20 kt und einer bisher unerreichten Energieauflösung von mehr als 3% bei einer Energie von 1 MeV zur Messung des oszillierten Elektron-Antineutrino-Spektrums zweier Kernkraftwerke im Abstand von 53 km. Zusätzlich wird im Rahmen des Experiments ein zweiter Detektor, das Taishan Antineutrino Observatory (TAO), gebaut, der mit 2.8 Tonnen Gadolinium-versetztem Flüssigszintillator gefüllt ist, um ein unoszilliertes Referenzspektrum mit einer Auflösung von mehr als 2% bei einer Energie von 1 MeV zu messen. Detaillierte Berechnungen des Reaktor-Antineutrino-Spektrums, welche auf nuklearen Messdaten basieren, zeigen die Existenz einer Feinstruktur, die bisher noch nicht nachgewiesen wurde, jedoch Auswirkungen auf die Bestimmung der Neutrinomassenhierarchie in einem hochauflösenden Detektor wie JUNO haben könnte.
In dieser Arbeit wurde eine Vielzahl potentieller Spektren mit solch einer Feinstruktur generiert, um die möglichen Auswirkungen auf die Sensitivität von JUNO zur Bestimmung der Massenhierarchie zu untersuchen. Es wurde gezeigt, dass eine fehlende Kenntnis über die genaue Form der Feinstruktur einen signifikanten Einfluss auf die Sensitivität haben kann, sofern nur bekannte Modelle des Reaktorspektrums als Referenz herangezogen werden. Deshalb wird das Spektrum, welches mit dem Detektor TAO gemessen wird, in einer kombinierten Analyse als Referenzspektrum verwendet, um die unbekannte Feinstruktur mit Hilfe des unoszillierten Spektrums zu berücksichtigen. Es konnte gezeigt werden, dass die Feinstruktur keinen negativen Effekt auf die Sensitivität des Experiments hat, wenn das JUNO-Spektrum durch die Referenzmessung des TAO-Detektors korrigiert wird. Des Weiteren wurde demonstriert, dass es ausschlaggebend für das Erreichen der geplanten Sensitivität ist, dass die Energieauflösung des TAO-Detektors höher ist als die des JUNO-Detektors. Es konnte gezeigt werden, dass mit einer Messdauer von 6.5 Jahren bei $26.6\,\mathrm{GW_{th}}$ Reaktorleistung sowie der bislang unerreichten Energieauflösung von weniger als 3% bei 1 MeV des JUNO-Detektors und weniger als 2% bei 1 MeV des TAO-Detektors, eine Sensitivität von 3σ (3.1σ) für eine normale (invertierte) Massenhierarchie trotz der Präsenz einer Feinstruktur im Reaktorneutrinospektrum mit JUNO erreicht werden kann. Dies zeigt, dass die Asimov-Sensitivität im Fall ohne Feinstruktur eine gültige Abschätzung der durchschnittlichen Sensitivität des JUNO-Experiments auf die Neutrino-Massenhierarchie darstellt.

Contents

1 | Introduction

There's always something that you can learn and something you can teach.

– Roman Reigns - *WWE Superstar*

From the postulation of the existence of neutrinos by Wolfgang Pauli in 1930 [1] over the first detection of neutrinos from a nuclear reactor by Cowan and Reines in 1960 [2] to the final proof of the existence of neutrino oscillations by the KamLAND experiment in 2003 [3], neutrino physics has evolved into a large research field in particle physics which still offers a lot of potential to answer fundamental questions of modern physics.
One of the remaining open questions in the field is the ordering of the neutrino masses which has a small influence on the oscillatory behavior of the neutrinos. The Jiangmen Underground Neutrino Observatory (JUNO) aims to measure the oscillated neutrino spectrum from nuclear reactors to determine the neutrino mass ordering (NMO) to a significance level of 3σ in about 6 years of data taking. The JUNO experiment will feature a 20 kt liquid scintillator (LS) detector located at 53 km from two nuclear power plants as well as a second 2.8 ton LS detector, the Taishan Antineutrino Observatory (TAO), at a few meters distance from one of the reactor cores.
To resolve the difference in the oscillated neutrino spectrum between the neutrino mass orderings, the unoscillated spectrum emitted from the nuclear reactor has to be known precisely. However, current models for the reactor antineutrino spectrum have shortcomings and show differences in rate and shape compared to the measurements by recent experiments [4]. Additionally, the prediction of the reactor antineutrino spectrum shows the possibility of a fine structure in the spectrum that has not yet been visible in previous measurements as the energy resolution has been too low to resolve such small scale fluctuations [5].
With the unprecedented energy resolution of the JUNO detector better than 3% at 1 MeV that is necessary for the NMO determination, however, also this unknown fine structure could be visible and potentially impact the sensitivity of the experiment. Therefore, the satellite detector TAO will measure a reference spectrum from one of the reactor cores with an energy resolution of better than 2% at 1 MeV.

In this work, the implications by the previously undetected fine structure in the reactor antineutrino spectrum on the sensitivity to the NMO determination of the JUNO experiment is studied extensively.
The basic theoretical concepts on neutrinos, oscillations and mass ordering are discussed in chapter 2 while chapter 3 introduces the JUNO experiment, its detector concept, and its physics potential. The calculation of the reactor antineutrino spectrum and the origin

of the fine structure is presented in chapter 4. Chapter 5 focuses on the analysis software Global Neutrino Analysis (GNA) and the prediction of the measured spectrum in the detectors using the GNA software. In the following chapters, the actual analysis of the impact of the fine structure on the NMO sensitivity is presented. The calculation and modeling of the fine structure performed in this work to be used for the analysis is discussed in chapter 6. Chapter 7 presents the NMO sensitivity analysis for the JUNO detector while chapter 8 focuses on the combined analysis with the satellite detector TAO, which provides an unoscillated reference spectrum. An analysis of a variety of systematic effects on the NMO sensitivity in presence of the fine structure in the reactor neutrino spectrum is discussed in chapter 9. The thesis concludes with a summary of the results and an outlook on further possibilities in the scope of reactor antineutrino fine structure analysis.

2 Neutrinos, Oscillations and Mass Ordering

In the spirit of science, there really is no such thing as a 'failed experiment'. Any test that yields valid data is a valid test.

– Adam Savage, *American special effects designer*

In the Standard Model of Particle Physics, neutrinos are electrically neutral fermions that only interact via weak interaction. For each charged lepton (electron, muon, and tau) there is a corresponding neutrino (electron neutrino ν_e, muon neutrino ν_μ, and tau neutrino ν_τ) resulting in a total of three neutrino flavors. Neutrinos are naturally produced in various sources like the sun, the earth and its atmosphere as well as supernovae. Besides the natural sources, neutrinos can be produced in man-made sources like accelerators and nuclear reactors, the latter playing the central role for this thesis. Figure 1 illustrates the fluxes of neutrinos and antineutrinos that are measured or expected for the different sources depending on their energy spanning a broad range from $10^{-6}\,\mathrm{eV}$ to more than $10^{18}\,\mathrm{eV}$.

2.1 Neutrino Sources

In the following an overview of the sources of neutrinos is given as neutrinos from different sources play a key role in the exploration of the neutrino properties either as directly observed particles or as background.

Atmospheric Neutrinos

In the upper atmosphere, cosmic rays are interacting with the nuclei of the earth's atmosphere producing secondary mesons like pions and kaons. These mesons decay weakly into muons and the respective neutrino via

$$\begin{aligned} \pi^- &\rightarrow \mu^- + \overline{\nu_\mu} \\ \pi^+ &\rightarrow \mu^+ + \nu_\mu \\ K^- &\rightarrow \mu^- + \overline{\nu_\mu} \quad . \end{aligned}$$

In a second step the muons also decay via

$$\begin{aligned} \mu^- &\rightarrow \mathrm{e}^- + \overline{\nu_e} + \nu_\mu \\ \mu^+ &\rightarrow \mathrm{e}^+ + \nu_e + \overline{\nu_\mu} \end{aligned}$$

which in combination builds up the atmospheric neutrinos.

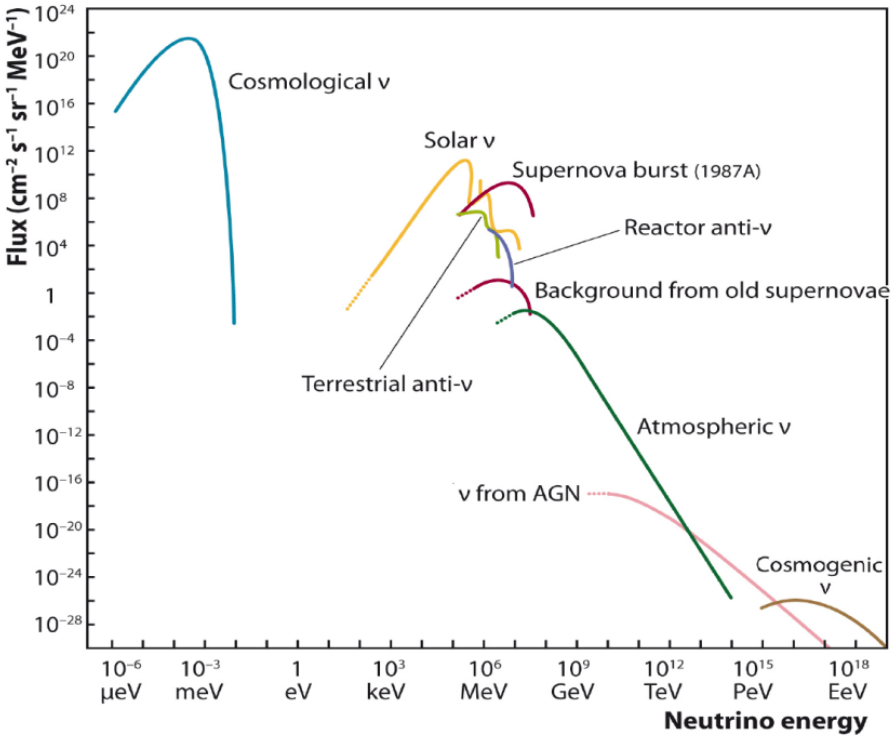

Figure 1: Measured and expected flux of (anti-)neutrinos emitted from natural sources and nuclear reactors as a function of neutrino energy. Their energies span a broad range from less than 10^{-6} eV to more that 10^{18} eV. Figure adapted from [6].

Cosmogenic Sources

These neutrinos are expected to have the largest energy as they are produced in the reaction of ultra-high-energy protons with the photons of the cosmic microwave background [7]. These ultra-high energetic neutrinos are then produced via the resonance of the Δ^+-baryon which decays via

$$\Delta^+ \rightarrow n + \pi^+ \rightarrow n + \mathrm{e}^+ + \nu_e + \nu_\mu + \overline{\nu_\mu} \quad .$$

Additionally, neutrinos from active galactic nuclei (AGN), the highly active supermassive black holes in the center of distant galaxies, have very high energies. However, due to the large distances of these neutrino sources, the flux is small.

Cosmic Neutrino Background

These cosmological neutrinos of lowest energy are the relic of the neutrino freeze-out in the early universe. Like the cosmic microwave background (CMB) there is the assumption of a uniform cosmological background of neutrinos with a temperature of 1.95 K [8] which is however still undetected.

Geoneutrinos

Also the earth itself is a natural source of electron-antineutrinos. These are produced in radioactive decays of potassium (^{40}K) as well as from the uranium and thorium chains inside the earth as first proposed in [9].

Nuclear Reactors

In nuclear reactors, the fission of the reactor fuel isotopes uranium and plutonium produces neutron rich daughter isotopes that decay via beta decay. This produces a large flux of electron antineutrinos in an energy range of around $1-14\,\mathrm{MeV}$. As the focus of this thesis is mainly on reactor antineutrinos, this will be discussed in more detail in chapter 4.

Solar Neutrinos

In the fusion process in the sun, which is producing helium from protons by

$$4\mathrm{p} \rightarrow {}^{2}_{4}\mathrm{He} + 2\mathrm{e}^{+} + 2\nu_e \quad ,$$

two electron neutrinos are produced. This makes the sun a powerful neutrino source with a continuous spectrum up to 18.77 MeV [10]. Since the upper fusion reaction does not work directly but has intermediate steps, the neutrinos are usually separated in *pp*, *pep*, ^{7}Be, and ^{8}B neutrinos depending on the involved reaction producing the neutrino (c.f. chapter 3.5.5).

Neutrinos from Supernovae

At the end of the life of a massive star, it may collapse in a core-collapse supernova (CCSN). Around 99% of its gravitational binding energy is released in form of a burst of neutrinos and antineutrinos of all flavors [11]. Additionally, it is assumed but up to now undetected that the neutrinos emitted from all supernovas that have occurred in the past add up to an integral background, the diffuse supernova neutrino background (DSNB) [12].

2.2 Neutrino Oscillations

The first measurement of the solar neutrino flux in the Homestake experiment [13] showed that the flux of electron neutrinos was too low compared to the prediction which was also confirmed by GALLEX [14] and Kamiokande-II [15]. The Super-Kamiokande experiment detected a zenith angle dependent difference in the flux of atmospheric neutrinos which gave a hint on flavor oscillations depending on the propagation distance resulting in the deficit [16]. A non-electron flavor component in the solar neutrino flux was later detected by the Sudbury Neutrino Observatory (SNO) [17] explaining the observed discrepancy for solar neutrinos increasing the evidence for the flavor oscillations. Finally, these flavor oscillations in the neutrino sector were experimentally shown by KamLAND [3]. In the following, the theoretical concept of these flavor oscillations will be discussed.
In case of neutrinos the flavor eigenstates are not identical to the mass eigenstates, but every flavor eigenstate $|\nu_\alpha\rangle$ is a superposition of the three mass eigenstates $|\nu_i\rangle$

$$|\nu_\alpha\rangle = \sum_{i=1}^{3} U_{\alpha i} \, |\nu_i\rangle \quad . \tag{1}$$

The $U_{\alpha i}$ are the elements of the unitary Pontecorvo-Maki-Nakagawa-Sakata (PMNS)-matrix

$$U = \begin{pmatrix} c_{12}c_{13} & s_{12}c_{13} & s_{13}e^{-i\delta} \\ -s_{12}c_{23} - c_{12}s_{13}s_{23}e^{i\delta} & c_{12}c_{23} - s_{12}s_{13}s_{23}e^{i\delta} & c_{13}s_{23} \\ s_{12}s_{23} - c_{12}s_{13}c_{23}e^{i\delta} & -c_{12}s_{23} - s_{12}s_{13}c_{23}e^{i\delta} & c_{13}c_{23} \end{pmatrix} \quad , \tag{2}$$

where $s_{ij} = \sin\theta_{ij}$ and $c_{ij} = \cos\theta_{ij}$ with the mixing angles θ_{ij} [18]. The δ describes a potential CP-violating phase.
To calculate the time evolution of these states we have to consider how the mass eigenstates propagate. As a solution to the time-dependent Schrödinger equation their propagation in vacuum can be described by a plane wave of the form

$$|\nu_i(t)\rangle \;=\; |\nu_i\rangle \; \mathrm{e}^{i(\vec{p_i}\cdot\vec{x} - E_i\cdot t)} \tag{3}$$

with 3-momentum $\vec{p_i}$ and energy E_i [19].
Therefore, the probability to find a neutrino of energy E in a state β that was produced in a state α after a time t is given by

$$P(\nu_\alpha \to \nu_\beta) \;=\; |\langle \nu_\beta | \Psi_\nu(\vec{x},t)\rangle|^2 \quad , \tag{4}$$

where $|\Psi_\nu(\vec{x},t)\rangle$ is the wave function of the neutrino. Using equations 1 and 3 it is given by

$$|\Psi_\nu(\vec{x},t)\rangle \;=\; \sum_i U_{\alpha i}\, |\nu_i\rangle \; \mathrm{e}^{i(\vec{p_i}\cdot\vec{x} - E_i\cdot t)} \quad . \tag{5}$$

To calculate the probability given in equation 4 we have to replace the mass eigenstate $|\nu_i\rangle$ in equation 5 with the flavor eigenstate which is given by the inverse transformation using the unitarity of U which gives

$$|\nu_i\rangle \;=\; \sum_\alpha U^*_{\alpha i}\, |\nu_\alpha\rangle \tag{6}$$

with U^* denoting the complex conjugate of U. The probability finding a neutrino produced in state $|\nu_\alpha\rangle$ in a state $|\nu_\beta\rangle$ is then given by

$$P_{\nu_\alpha \to \nu_\beta}(E,t) \;=\; \sum_{k,j} U_{\alpha k} U^*_{\beta k} U^*_{\alpha j} U_{\beta j}\, \mathrm{e}^{i(E_j - E_k)t} \quad . \tag{7}$$

Due to the low rest masses of the neutrinos they can be considered ultra-relativistic and with $p_i \gg m_i$ we can therefore make the approximation

$$E_i \;=\; \sqrt{p_i^2 + m_i^2} \;\approx\; p_i \;+\; \frac{m_i^2}{2p_i} \;\approx\; E \;+\; \frac{m_i^2}{2E} \quad , \tag{8}$$

which gives a final expression for the oscillation probability of

$$\begin{aligned} P_{\nu_\alpha \to \nu_\beta}(E,L) \;=\; \delta_{\alpha\beta} \;-\; 4 \sum_{j<k} \mathfrak{Re}\left(U_{\alpha k} U^*_{\beta k} U^*_{\alpha j} U_{\beta j}\right) \sin^2\left(\frac{\Delta m^2_{jk} L}{4E}\right) \\ +\; 2 \sum_{j<k} \mathfrak{Im}\left(U_{\alpha k} U^*_{\beta k} U^*_{\alpha j} U_{\beta j}\right) \sin\left(\frac{\Delta m^2_{jk} L}{2E}\right) \quad . \end{aligned} \tag{9}$$

Here, we replaced the time t with the propagated distance L via $t = cL$ and the differences of the squared masses are defined by $\Delta m^2_{jk} = m^2_j - m^2_k$. This shows directly that at least one of the neutrino masses m_i has to be non-zero to allow neutrino oscillations at all.
In case of antineutrinos, the transformation of mass eigenstates to flavor eigenstates is done via the complex conjugate of the PMNS-matrix, which simply yields to a replacement of each $U \to U^*$ as well as $U^* \to U$ in the expression for the oscillation probability.
From experimental observations of the oscillation probability, the values for the mixing angles and mass differences can be determined. The current best fit values are listed in table 1.

Table 1: Current best fit values of 3-neutrino oscillation parameters from a global fit of neutrino oscillation data [18]. Given are the best-fit values with the 68% C.L. uncertainties. Here, NO and IO refer to normal resp. inverted mass ordering (see chapter 2.3.5).

Parameter	Best fit
$\Delta m^2_{21}/10^{-5}\,\mathrm{eV}^2$	7.53 ± 0.18
$\Delta m^2_{32}/10^{-3}\,\mathrm{eV}^2$ (NO)	2.453 ± 0.033
$\Delta m^2_{32}/10^{-3}\,\mathrm{eV}^2$ (IO)	-2.536 ± 0.034
$\sin^2\theta_{12}$	$0.307\,^{+0.013}_{-0.012}$
$\sin^2\theta_{13}/10^{-2}$	2.20 ± 0.07
$\sin^2\theta_{23}$ (NO)	0.546 ± 0.021
$\sin^2\theta_{23}$ (IO)	0.539 ± 0.022
δ/π	$1.36\,^{+0.20}_{-0.16}$

2.3 Open questions in neutrino physics

Neutrino physics still offers a broad spectrum of unanswered questions on the properties of these particles.

2.3.1 Absolute neutrino mass

The observation of neutrino flavor oscillations leads to the requirement that at least two of the three neutrino masses have to be non-zero. While the absolute values for the differences of the squared masses is also known within some uncertainty, the absolute values of the individual masses are still unknown. There are several approaches to determine the absolute neutrinos mass. From cosmological observations of large scale structures in addition with data of the CMB from the Planck observatory, an upper limit on the sum of the neutrino masses can be given to $\sum m_\nu < 0.14\,\mathrm{eV}$ [20]. However, this result is highly dependent on model estimations. The best limit on the neutrino mass from direct measurements is from the KATRIN experiment using beta decay endpoint spectroscopy measuring the effective neutrino mass given as

$$m_\nu = \sqrt{|U_{e1}|^2\, m_1^2 + |U_{e2}|^2\, m_2^2 + |U_{e3}|^2\, m_3^2} \quad . \tag{10}$$

They report an upper limit for the effective neutrino mass of $m_\nu < 0.8\,\mathrm{eV}$ with 90% C.L. [21].

2.3.2 CP-violation

The violation of CP-symmetry in weak interaction, describing a different behavior of physical processes when charge is conjugated and parity is changed, was first experimentally observed in the decay of the neutral kaon [22] leading to a non-zero CP-violation phase in the Cabibbo-Kobayashi-Maskawa (CKM)-matrix which describes the quark mixing in weak interaction [23]. The effect of CP-violation in the quark sector in weak interaction, however, is too small to describe the observed matter-antimatter-imbalance in the universe. Therefore, it is assumed that the PMNS-matrix, in analogy to the CKM-matrix, also contains a CP-violating phase as described in chapter 2.2. At the current experimental

precision, there is still no significant proof for CP-violation as the CP-conserving values of $\delta_{\mathrm{CP}} = 0$ and $\delta_{\mathrm{CP}} = \pi$ are ruled out on 90% C.L., however, are still allowed at a level of 2σ as reported by T2K and NOνA [24].

2.3.3 Majorana particle

Another open question which is linked to the CP-violation described above, is the question whether the neutrino is a Majorana or a Dirac particle, i.e. whether it is its own anti-particle or not. In case of the Majorana nature of neutrinos, the PMNS-matrix additionally contains two CP-violating Majorana phase factors $\mathrm{e}^{i\sigma/2}$ and $\mathrm{e}^{i\rho/2}$ [25]. In contrast to the CP-violating Dirac phase δ, these two phases do not change the oscillation probability and the Majorana nature of neutrinos can therefore only be observed directly via neutrino-less double beta decay. For specific isotopes, normal beta decay is energetically forbidden but double beta decay is allowed. Regarding the example of $\beta\beta^-$-decay, two neutrons are transformed into two protons, two electrons, and two antineutrinos. In case of the neutrino being a Majorana particle, the decay could also happen without emitting any neutrinos giving a discrete value for the total energy of the electrons instead of a typical continuous spectrum. There are various experiments like LEGEND [26], CUORE [27], and KamLAND-Zen [28] searching for the neutrino-less double beta decay.

2.3.4 Sterile neutrinos

The standard model only contains three different neutrino flavors as described in chapter 2.2. In past experiments, anomalies in neutrino appearance and disappearance experiments raised the question if there are additional neutrino states that do not interact via the weak interaction, however participate in the neutrino mixing [29]. Therefore, the PMNS-matrix would have to be extended from a 3×3 to a $(3+N)\times(3+N)$ matrix with N so called sterile neutrino states. This would affect the oscillation properties which gives a possibility to search for sterile neutrinos. However, there are no significant evidences on sterile neutrinos and various experiments show contradictions to the results of other experiments [30].

2.3.5 Neutrino Mass Ordering

An additional open question in neutrino physics, which is also the main motivation for this work, is the question for the specific ordering of the neutrino masses m_1, m_2, and m_3, where m_i is the mass corresponding to the mass eigenstate ν_i. As shown in table 1, the value and sign for Δm^2_{21} could already be determined showing that $m_2 > m_1$. In case of the difference to m_3, the absolute value was determined within some uncertainty, however, the sign of the difference is still remaining unknown which gives the two possible options of $m_1 < m_2 < m_3$ (normal ordering) and $m_3 < m_1 < m_2$ (inverted ordering). Figure 2 shows a graphical illustration of the two NMO possibilities.
The nature of this NMO also impacts the oscillation probabilities. As equation 9 shows, it depends on the difference of the squared neutrino masses $\Delta m^2_{ij} = m^2_i - m^2_j$. Since it will play a major role in this work, the specific case that electron antineutrinos are again detected as electron antineutrinos after some distance L will be discussed now. The probability for this case is denoted as survival probability P_{surv}[a].

[a] This refers to the fact that the initial flavor state survived in the oscillation process.

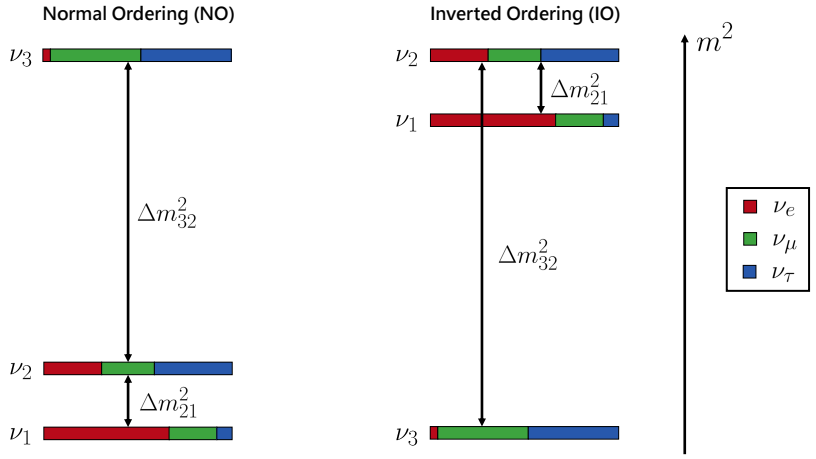

Figure 2: Illustration of the two possible mass orderings. The colors depict the superposition of the flavor eigenstates ν_e (red), ν_μ (green), and ν_τ (blue) that gives the respective mass eigenstate ν_i.

For its calculation, equation 9 is used with replacing $U \leftrightarrow U^*$ to account for the antineutrino case and setting $\alpha = \beta = e$. This then gives

$$P_{\text{surv}} = 1 - 4 \sum_{j<k} \mathfrak{Re}\left(|U_{ek}|^2 |U_{ej}|^2\right) \sin^2\left(\frac{\Delta m^2_{jk} L}{4E}\right) + 2 \sum_{j<k} \underbrace{\mathfrak{Im}\left(|U_{ek}|^2 |U_{ej}|^2\right)}_{=0} \sin\left(\frac{\Delta m^2_{jk} L}{2E}\right) \quad . \tag{11}$$

Executing the sum and inserting the corresponding matrix elements yields

$$\begin{aligned} P_{\text{surv}} &= 1 - 4\left[s^2_{12} c^2_{12} c^4_{13} \sin^2\Delta_{12} + s^2_{12} s^2_{13} c^2_{13} \sin^2\Delta_{23} + c^2_{12} s^2_{13} c^2_{13} \sin^2\Delta_{13}\right] \\ &= 1 - c^4_{13} \sin^2 2\theta_{12} \sin^2\Delta_{12} + \sin^2 2\theta_{13}\left(s^2_{12} \sin^2\Delta_{23} + c^2_{12} \sin^2\Delta_{13}\right) \quad , \end{aligned} \tag{12}$$

where $\Delta_{jk} = \frac{\Delta m^2_{jk} L}{4E}$.
This survival probability is dependent on the fraction of propagation distance L over neutrino energy E as well as on the differences of the squared neutrino masses Δm^2_{jk}. Therefore, it will differ for the two possible NMOs. The survival probability of electron antineutrinos for normal and inverted mass ordering as a function of the fraction L/E as well as of the neutrino energy in case of a distance of $L = 53\,\text{km}$ as it will be the case for the JUNO experiment (see chapter 3) are displayed in figures 3 and 4 respectively.

The fact that the NMO has a measurable effect on this survival probability can be used to determine the NMO that is realized in nature which will be the main goal of the JUNO experiment that will be described in chapter 3.

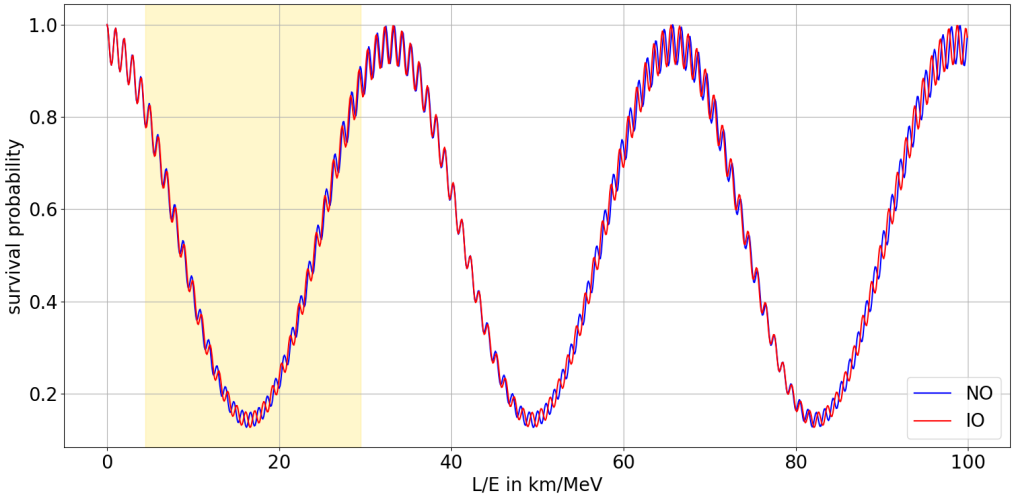

Figure 3: Survival probability of electron antineutrinos for normal (blue) and inverted (red) mass ordering as a function of the fraction L/E. The yellow shaded area corresponds to the L/E region where the JUNO detector is located. The curves were calculated according to equation 12 using the best fit values of the parameters given in table 1.

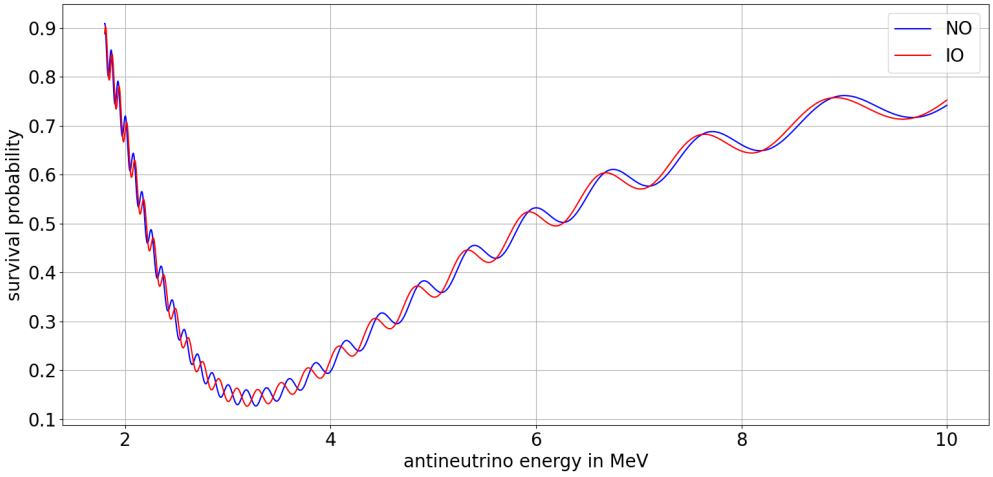

Figure 4: Survival probability of electron antineutrinos for normal (blue) and inverted (red) mass ordering as a function of the antineutrino energy E for a distance of $L = 53\,\text{km}$. The energy interval was chosen according to the typical energy range of reactor neutrinos detected via inverse beta decay as in JUNO (see chapter 3). The curves were calculated according to equation 12 using the best fit values of the parameters given in table 1.

3 The Jiangmen Underground Neutrino Observatory

Success isn't always about greatness. It's about consistency. Consistent hard work leads to success. Greatness will come.

– Dwayne Johnson - *American actor*

The JUNO experiment is a multi-purpose experiment currently under construction near Kaiping in the Guangdong Province in the southeast of China. Its central detector consists of an acrylic sphere with a diameter of 35.4 m filled with 20 kt of LS [31]. It is designed to have an unprecedented energy resolution of better than 3% @ 1 MeV [31] to achieve its main goal to determine the NMO with 3σ in about 6 years of data taking measuring the oscillated spectrum of electron antineutrinos emitted from two nuclear power plants (NPPs) in Taishan and Yangjiang. It also features a satellite detector, the Taishan Antineutrino Observatory (TAO), with a target mass of 2.6 t and a design goal for the energy resolution of better than 2% @ 1 MeV located in a distance of a few tens of meters from one of the Taishan reactor cores to provide a precise unoscillated reference spectrum [32].
Besides its main goal, JUNO features a broad physics program including solar, atmospheric, supernova and geoneutrinos as well as the search for dark matter or proton decay [33]. This will be addressed in detail in chapter 3.5.

3.1 The Experimental Site

The JUNO site is located at a distance of around 53 km from the two NPPs in Yangjiang and Taishan with a total of 8 reactor cores and a thermal power of 26.6 GW [34]. The location near two NPPs was chosen to provide a large neutrino flux while maximizing the observed difference in the antineutrino spectrum distorted by neutrino oscillations between the assumption of normal and inverted ordering to ensure a high sensitivity to the NMO determination. To prevent a decrease in sensitivity due to an averaging effect of the oscillations, the distances to the reactor cores have to be as equal as possible. A detailed list of the reactor powers and baselines is shown in table 2 and an illustration of the geographical location is displayed in figure 5.
The detector itself is located in an underground laboratory under Dashi Hill with 693.35 m rock overburden at the detector center which corresponds to 1800 m water equivalent to reduce atmospheric backgrounds [35].

Table 2: Baseline and thermal power of the 8 reactor cores from the Yangjiang and Taishan power plants and the more distant Daya Bay nuclear reactors [34].

Reactor	Baseline in km	Thermal Power in GW
Yangjiang Core 1	52.74	2.9
Yangjiang Core 2	52.82	2.9
Yangjiang Core 3	52.41	2.9
Yangjiang Core 4	52.49	2.9
Yangjiang Core 5	52.11	2.9
Yangjiang Core 6	52.19	2.9
Taishan Core 1	52.77	4.6
Taishan Core 2	52.64	4.6
Daya Bay	215	17.4

3.2 Detection of reactor antineutrinos in JUNO and TAO

The detection of the electron antineutrinos from the reactors is done via the IBD reaction [33]. An electron antineutrino interacts with a proton of the LS and produces a positron and a neutron

$$\overline{\nu}_e + \mathrm{p} \rightarrow \mathrm{e}^+ + \mathrm{n} \quad . \tag{13}$$

The produced positron will deposit its kinetic energy in the LS and finally annihilate with an electron creating two 511 keV photons which gives a prompt signal in the detector. The neutron thermalizes in the detector and is captured by a proton on average approximately 200 μs later resulting in a delayed signal of a 2.2 MeV photon. The coincidence of these prompt and delayed signals then gives a unique characteristic signal to identify the IBD. Figure 6 illustrates the signal creation via IBD in the detector.
Due to the mass difference of the in- and outgoing particles, the threshold for the energy of the electron antineutrino for reaction to take place is $E_{\mathrm{th}} = 1.806\,\mathrm{MeV}$ which can be calculated from the relativistic 4-momentum conservation. The energy of the prompt signal visible in the detector is given by the sum of the energy of the incident neutrino and the energy released by the annihilation minus the IBD threshold which gives

$$E_{\mathrm{vis}} = E_\nu + 2 \cdot 511\,\mathrm{keV} - 1.806\,\mathrm{MeV} = E_\nu - 0.784\,\mathrm{MeV} \quad . \tag{14}$$

Therefore, a direct translation of the energy observed in the detector to the energy of the incident antineutrino is possible.

Figure 5: Illustration of the location of the JUNO site near the large cities Guangzhou, Shenzhen, and Hong Kong. The equal distances of 53 km to the NPPs of Yangjiang and Taishan (where the satellite detector TAO will be located) as well as the more distant NPP in Daya Bay are shown. The picture is adapted from [35].

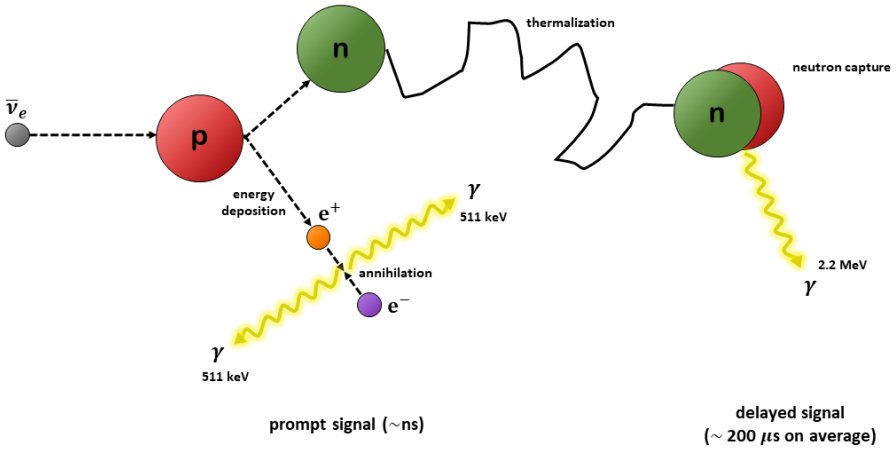

Figure 6: Exemplary illustration of the IBD signal creation for the detection of electron antineutrinos. The electron antineutrino interacts with a proton and creates a positron and a neutron. The positron deposits its energy in the detector and annihilates with an electron creating two 511 keV photons which gives a prompt signal. The neutron is thermalized and captured by a proton around 200 μs later releasing a 2.2 MeV photon creating a delayed signal.

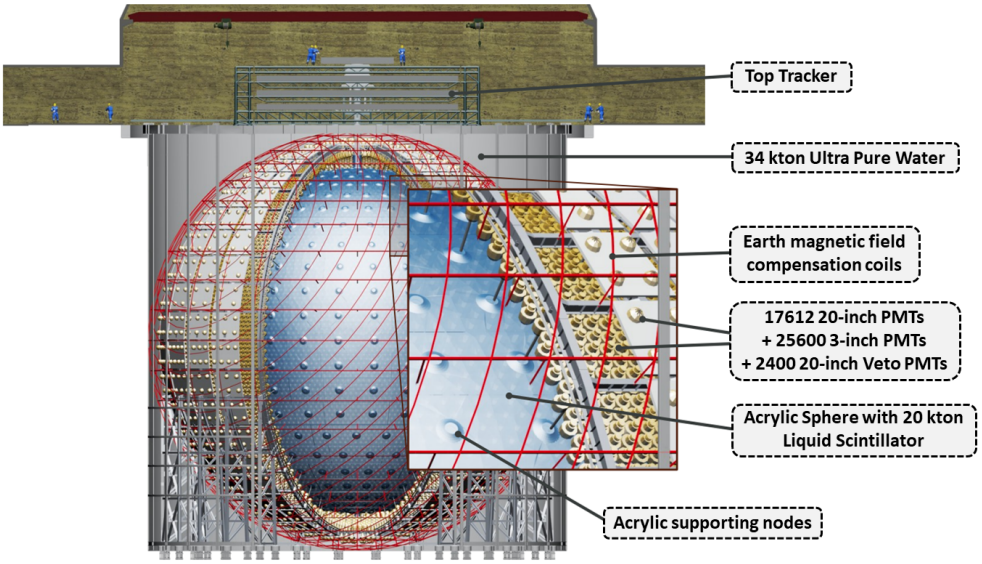

Figure 7: Sketch of the JUNO detector with its main components. Figure adapted from [36].

3.3 The JUNO Detector Design

Its central detector consists of an acrylic sphere with a diameter of 35.4 m filled with 20 kt of LAB-based liquid scintillator. The acrylic sphere is surrounded by 17,612 20-inch photomultiplier tubes (PMTs) and 25,600 3-inch PMTs. With this number, an optical coverage of 77.9% is achieved [35]. The acrylic sphere and the PMTs are mounted on a stainless steel supporting structure. The central detector is surrounded by a cylindrical pool with 34 kt of ultrapure water serving as additional shielding that is also equipped with 2,400 20-inch PMTs to be used as an active water Cherenkov muon veto [35]. On top of the detector a muon top tracker will be installed. Additionally, coils will be installed around the detector to compensate the earth's magnetic field by a current [35]. Figure 7 shows a sketch of the detector design with its main components. The individual detector parts will be discussed in detail in the following.

3.3.1 Liquid Scintillator

The main solvent in the LS is linear alkyl benzene (LAB), which has the chemical formula $C_6H_5C_nH_{2n+1}$ where the n will be in the range of 10-13. Additionally, 2,5-diphenyloxazole (PPO) is solved at a concentration of 2.5 g/L [37] and serves a a fluor. The energy of the positrons created via IBD is deposited in the LAB which yields an excitation of the LAB molecules. This energy is then non-radiatively transferred to the PPO molecules which are emitting photons during deexcitation. The wavelength of these photons will be different from the absorption wavelength of the LAB molecules preventing self-absorption and therefore large attenuation of the scintillation light. To increase the detector performance, bis-MSB is added as a wavelength-shifter with a concentration of 5 mg/L[37] to further reduce attenuation and match the range for the best sensitivity of the PMTs. The wavelength of the finally produced scintillation light will have its emission peak at 430 nm. Figure 8 shows the chemical structure formulas of these molecules. Before being filled in the detector, the LS will undergo several purification steps like aluminum column chro-

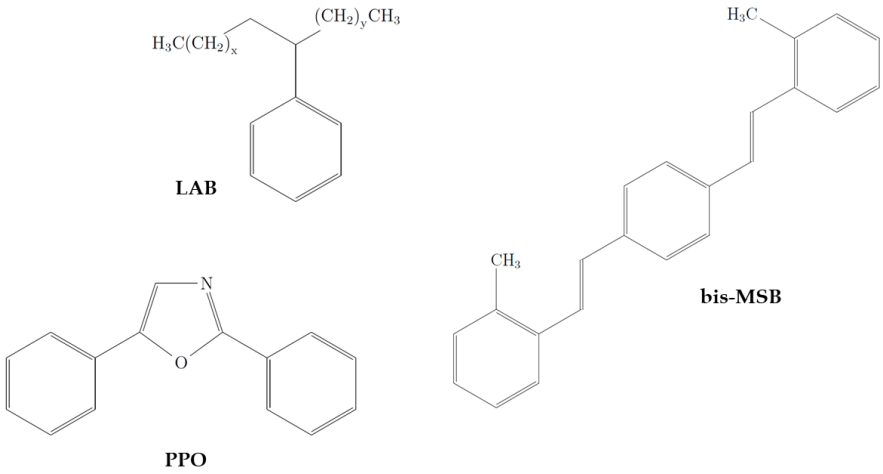

Figure 8: Structure formula of the three components of the JUNO LS: LAB (top left), PPO (bottom left), and 1,4-Bis(2-methylstyryl)benzene (bis-MSB) (right).

matography, distillation, water extraction, and steam stripping to ensure an attenuation length of more than 20 m at 430 nm and a high radiopurity [31]. Additionally, the LS will be investigated by a pre-detector, the Online Scintillator Internal Radioactivity Investigation System (OSIRIS), for its quality to ensure a concentration of less than 10^{-15}g/g of ^{238}U and ^{232}Th in the LS [38].
With the final mixture of the scintillator, JUNO is expected to have a light yield of ~ 1665 photoelectrons per MeV for events at the center of the detector [39]. However, due to quenching effects in the LS, there is a non-linearity in the light yield as a function of deposited energy. In general, this effect can be described by Birk's law [40]

$$\frac{\mathrm{d}S}{\mathrm{d}x} = \frac{A \cdot \frac{\mathrm{d}E}{\mathrm{d}x}}{1 + kB \cdot \frac{\mathrm{d}E}{\mathrm{d}x}} \quad , \tag{15}$$

where $\frac{\mathrm{d}S}{\mathrm{d}x}$ is the specific fluorescence, $\frac{\mathrm{d}E}{\mathrm{d}x}$ the energy per unit path length of the ionizing particle (e.g. positron). A and kB are material- and particle-specific constants describing the number of emitted photons and the quenching effect. Since the energy of the incident antineutrino and therefore of the positron is crucial for the NMO determination, this effect of liquid scintillator non-linearity (LSNL) has to be taken into account. This will be further addressed in chapter 5.2.

3.3.2 Photomultiplier Tubes

The scintillation light produced inside the LS is detected by 17,612 20-inch PMTs and 25,600 3-inch PMTs. These PMTs are manufactured by three different companies [41]: 20-inch dynode PMTs of type R12860 HQE from Hamamatsu, 20-inch micro-channel plate PMTs from NNVT, and 3-inch dynode PMTs from HZC Photonics. The performance of the PMTs is crucial for the energy resolution of JUNO. Since they make up $\sim 75\%$ of 77.9% of the optical coverage, there are various requirements for the large PMTs like a detection efficiency of better than 24% with an average of at least 27% over all PMTs and a dark count rate of less than 50 kHz [42].

The energy resolution of the detector can be estimated via the parametrization [33]

$$\frac{\sigma_E}{E} = \sqrt{\left(\frac{a}{\sqrt{E}}\right)^2 + b^2 + \left(\frac{c}{E}\right)^2} \tag{16}$$

for the visible energy E in MeV, where a is mainly dominated by the statistical fluctuation of the detected photoelectrons, b by the detector non-uniformity, and c by the dark noise of the PMTs.
The large PMTs have been carefully tested for the requirements in a specially designed mass testing facility described in [41] and [43] as well as in a scanning station for a more detailed test of individual PMTs [44]. Taking into account the final measured properties of the PMTs, the total number of photoelectrons per MeV is estimated to be ~ 1665 [39] which gives an expected energy resolution of $\sigma = 2.95\%$ at $E = 1\,\text{MeV}$ [45].

3.3.3 Detector Calibration

To reach this energy resolution, also the energy non-linearity and spatial non-uniformity of the detector response have to be corrected. Therefore, the JUNO detector will be calibrated with multiple sources and scanning systems as discussed in detail in [46]. Via an automatic calibration unit (ACU) [47] multiple radioactive sources as well as a UV laser diffuser ball can be deployed through the chimney on the central axis of the detector. Via two cable loop systems (CLS), additional radioactive sources can be moved to off-axis positions for non-uniformity measurements [48]. To investigate the detector response at the boundary of the detector, a source is mounted in a longitudinal guide tube on the outside of the acrylic sphere that can be moved around the detector. A remotely operated vehicle can also be deployed to reach other positions in the detector to enable a scan of the entire volume.

3.3.4 Muon Veto

The veto system of JUNO consists of three parts, a water Cherenkov detector surrounding the central detector, a muon top tracker placed above the detector and the central detector itself which can serve as muon tracker. The muon flux at the detector location 700 m underground is estimated to be $4\,\text{mHz/m}^2$ with an average energy of 207 GeV [35]. These muons can create ^{9}Li and ^{8}He isotopes in the detector that can mimic the IBD event signature via their beta decays. Additionally, the cosmic muons can create fast neutrons in the detector materials and surrounding rock which can scatter off protons in the LS and are then captured also creating an IBD-like event.
The water pool surrounding the central detector is cylindrical with a diameter of 43.5 m and a height of 44 m which already provides few meters of shielding from the fast neutrons and additional radioactivity from the surrounding rocks due to the ultrapure water. The water pool is additionally equipped with 2,400 20-inch PMTs to detect the Cherenkov radiation from the muons passing through the water pool [49].
The top tracker is mounted on top of the water pool and will consist of 3 layers of plastic scintillator strips refurbished from the OPERA top tracker [50]. It is rebuilt in a grid of 3 x 7 and covers around 60% of the detector surface which allows a detection of around 30% of atmospheric muons [51]. Although it does only detect a fraction of muons coming from above the detector, it plays an important role in the development of the muon track reconstruction methods.

In the central detector itself, muons also create Cherenkov as well as scintillation light which is used to reconstruct the tracks of the muons together with the other parts of the veto. Due to the size of the detector, the muon flux inside is too large to be able to veto the entire detector. Therefore, a special muon veto strategy is applied as described in [34]. If a muon is passing the water pool and/or the central detector, a veto of 1 ms is applied over the entire fiducial volume to suppress spallation neutrons and short-lived radio-isotopes. In case of well-reconstructed muon tracks inside the central detector from a single or two far-apart muons, a veto of 0.6 s, 0.4 s, and 0.1 s is applied to events with reconstructed vertices closer than 1 m, 2 m, and 4 m to the track(s), respectively. For parallel muons with a distance of less than 3 m which occurs in around 0.6% of all muon-related events, the veto is only applied to a single cylinder with the radius extended by the separation of the muon tracks. In roughly 2% of all muon-related events, more than two muons are passing the detector simultaneously which causes a non-sufficient track reconstruction. Therefore, a veto has to be applied for 0.5 s on the whole fiducial volume. Additionally, events inside a sphere with a radius of 3 m around spallation neutron capture events are rejected for 1.2 s. With this strategy, the IBD selection efficiency of the veto system will be 91.6% [34].

3.4 The TAO Detector Design

The Taishan Antineutrino Observatory is JUNO's satellite detector and was originally proposed to be located in a distance of about 30 m from one of the 4.6 GW nuclear reactor cores at the Taishan NPP [32]. However, the final location had recently to be changed to a new distance to the reactor cores of 44 m and 217 m resp. [52] (c.f. chapter 9.2). It will be located outside the concrete containment of the reactor 9.6 m underground reducing the cosmic muon flux to a fraction of around one third compared to ground level [32].
The location near the reactor core provides a high flux of electron antineutrinos while the effect of the NMO on the spectrum is negligible compared to JUNO making it a suitable reference spectrum. The detection reaction for the reactor antineutrinos in TAO will also be the IBD.
Figure 9 shows a sketch of the TAO detector with its components that will be discussed in the following. This description is mainly based on [32].
The central detector consists of an acrylic sphere with a diameter of 1.8 m filled with 2.8 tons of gadolinium-doped LS. The LS-mixture is similar to the JUNO-LS with LAB as solvent with 2 g/L PPO as fluor and 1 mg/L of the wavelength-shifter bis-MSB. Gadolinium is added with a mass fraction of 0.1 % which provides an additional characteristic signal when the neutron produced via IBD is captured by the gadolinium releasing several gammas with a total energy of around 8 MeV which is above the energy of gammas from natural radioactivity. The acrylic sphere is surrounded by a copper shell with an array of 4100 silicon photomultipliers (SiPMs) with a total area of about 10 m^2 yielding an optical coverage of $> 95\%$. To reduce the dark count rate of the SiPMs the central detector is cooled to a temperature of $-50\,^{\circ}C$ using a cryostat with cooling pipes mounted on the outer surface of the copper shell. The copper shell is located in a cylindrical stainless steel tank with 3.45 tons of LAB buffer which is insulated with a polyurethane layer to prevent large heat transport from the outside. On top of the detector a HDPE shield is placed to reduce spallation neutrons from cosmic muons and a lead shield at the bottom will reduce gammas from natural radioactivity. The entire detector is additionally surrounded by a water-Cherenkov muon veto equipped with 3-inch PMTs and an expected efficiency of $> 90\%$. A layer of plastic scintillator on top will serve as a muon tagger. For the cali-

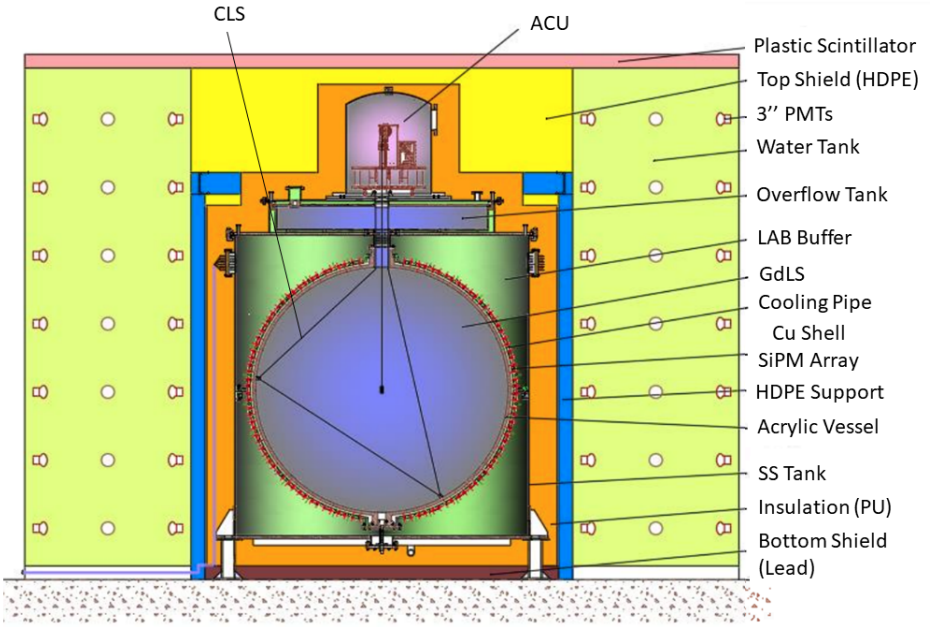

Figure 9: Illustration of the TAO detector design with its components. The figure was taken from [53].

bration of the detector, an ACU is installed to deploy sources inside of the central detector which can also be positioned off-axis via a CLS [54].
With this detector design, a light yield of around 4500 photoelectrons per MeV is expected which gives an estimated energy resolution of better than 2% at 1 MeV.

3.5 Physics Potential

As described in chapter 2.3, there are still many open questions in neutrino physics. The JUNO detector is designed to investigate several topics in neutrino physics and particle physics in general. This broad physics potential is described in the following according to [38].

3.5.1 Neutrino mass ordering

The main purpose of the JUNO experiment is the determination of the NMO to 3σ within around 6 years of data taking. As already described in chapter 2.3.5, the oscillation probability is depending on the actual NMO which can be measured with the high energy resolution of better than 3% at 1 MeV of JUNO. In contrast to experiments with accelerator or atmospheric neutrinos, JUNO fully relies on vacuum oscillations while the other experiments include matter effects. Additionally, the JUNO spectrum is not depending on the unknown CP-violating phase (c.f. chapter 2.3.2) providing a unique measurement in the field of experiments investigating the NMO. The topic of sensitivity analysis for the NMO determination will also be discussed in more detail in the remainder of this thesis.

3.5.2 Precision measurement of the oscillation parameters

As JUNO is measuring the oscillated reactor antineutrino spectrum, it will also be capable of providing updated values on the neutrino oscillation parameters. Due to the medium baseline, the slow oscillations, driven by Δm^2_{21} and modulated by $\sin^2 2\theta_{12}$, as well as the fast oscillations, driven by Δm^2_{31} and modulated by $\sin^2 2\theta_{13}$, can be measured at the same time. Figure 10 shows this oscillatory behavior in the JUNO spectrum. It is estimated that JUNO can provide the world-leading precision for Δm^2_{31}, Δm^2_{21}, and $\sin^2 2\theta_{12}$ with 0.5%, 0.3%, and 0.2% respectively [34].

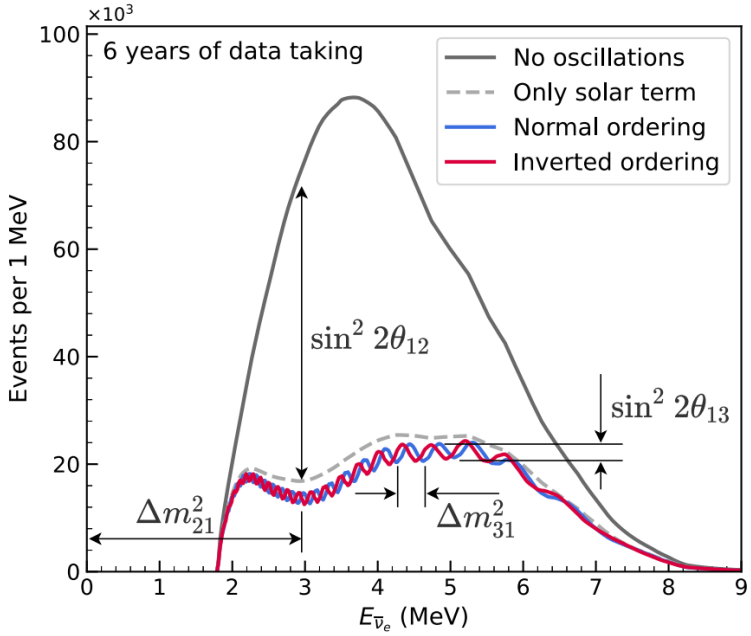

Figure 10: Exemplary illustration of the spectrum measured by JUNO in case of no oscillations (black), with the solar oscillation term only (gray dashed), as well as with all oscillation terms in case of normal (blue) and inverted (red) mass ordering. The influence of the four oscillation parameters Δm^2_{21}, Δm^2_{31}, $\sin^2 2\theta_{12}$, and $\sin^2 2\theta_{13}$ on the oscillations observed in the spectrum are additionally shown. The picture is taken from [34].

3.5.3 Supernova Neutrinos

Due to its large fiducial volume, JUNO will be able to detect a large number of events from a galactic CCSN playing an important part in the understanding of the processes during a CCSN. However, previously, there have only been detected 11 events from Supernova 1987a by Kamiokande-II [55], eight in the Irvine-Michigan-Brookhaven water-Cherenkov detector [56], as well as five events in Baksan [57] which does not allow significant analyses of the neutrino properties from CCSN.
For a typical galactic supernova distance of 10 kpc, JUNO will be able to measure around $\sim$ 5000 IBD events, $\sim$ 2000 events from neutrino scattering on protons, $\sim$ 300 events from neutrino-electron scattering, as well as $\sim$ 300 events and $\sim$ 200 events from neutral current (NC) and charged current (CC) interactions of neutrinos on ^{12}C nuclei.
Additionally, JUNO can serve as a real-time supernova neutrino monitor as part of a multi-messenger trigger for CCSN [58].

3.5.4 Diffuse Supernova Neutrino Background

Besides the neutrinos coming directly from a CCSN, JUNO also aims to measure neutrinos from the DSNB. Such a detection could provide information on the star forming rate as well as the rate of their deaths in the observable universe. In case of a detection, JUNO could reach a significance of 3σ within 5 years and 5σ within 10 years [59].

3.5.5 Solar Neutrinos

Despite being the target of many experiments in the past, the detection of solar neutrinos still provides important information on the neutrino oscillation behavior like the transition region from the vacuum to oscillations in matter described by the Mikheyev-Smirnov-Wolfenstein (MSW) effect. JUNO is expected to improve the flux measurements of Borexino [60] for ^{7}Be and *pep*-neutrinos [61], as well as ^{8}B neutrinos [62] significantly.

3.5.6 Atmospheric Neutrinos

Neutrinos created in the earth's atmosphere following the interaction with a cosmic ray are a natural source of neutrinos that contain important information on the NMO. Data from atmospheric neutrinos measured in JUNO could complement the main analysis of reactor antineutrinos to improve the sensitivity for the NMO determination. Additionally, the wrong θ_{23} octant could be ruled out with a significance of 1.8σ (NO)/0.9σ (IO) for $\theta_{23} = 35°$ [33]. It was also shown in [63] that the atmospheric neutrino spectrum in JUNO could be reconstructed in an energy range from 100 MeV to 10 GeV for electron and muon neutrinos separately.

3.5.7 Geoneutrinos

Additionally, JUNO will also take part in the measurement of geoneutrinos. A precise measurement of these neutrinos provides a better understanding of the composition of the earth, its radiogenic power, as well as its formation process. Geoneutrinos have been previously measured by KamLAND [64] and Borexino [65], however, JUNO is expected to measure geoneutrinos with much larger statistics due to its size [66] leading to a better modeling of the uranium and thorium distribution in the earth.

3.5.8 Other Physics

JUNO also aims to search for physics beyond standard neutrino physics. To answer the question of matter-antimatter asymmetry in the universe, it is capable of searching for rare baryonic decays that violate the baryon number conservation which is one of the key parts to solve this question [67]. After 10 years of data taking, JUNO is expected to increase the current sensitivity to the lifetime of the proton in the decay via the reaction $p \to \bar{\nu}K^+$ from Super-Kamiokande [68] to $\tau/\mathrm{Br}(p \to \bar{\nu}K^+) > 9.6 \cdot 10^{33}$ years at 90% C.L. [69].
Additionally, JUNO can contribute in the search for dark matter. It will be able to indirectly detect dark matter via an excess of mono-energetic neutrinos produced by dark matter self-annihilation $\chi\chi \to \nu\bar{\nu}$. For dark matter particles in a mass range of 15 MeV to 100 MeV accumulated in the center of the Milky Way, JUNO could increase the sensitivity by a factor of 2 to 10 compared to previous results [70].

3.5.9 Fine structure measurement

Besides providing a reference spectrum for JUNO, TAO will also have its own physics goal. It is assumed that the reactor antineutrino spectrum is not as smooth as predicted by previous models, but will show some fine structure [5]. With the energy resolution of TAO of better than 2% at 1 MeV, this could be measured for the first time [32]. This fine structure will also play a crucial part in this thesis and is discussed in more detail in chapter 4.

4 The Reactor Neutrino Spectrum and its possible fine structure

Well, sometimes things are hidden under the surface... You just gotta know how to bring 'em out.

– Angus MacGyver - *MacGyver*

The prediction of the spectrum of electron-antineutrinos emitted by nuclear reactors is a crucial part for a variety of neutrino experiments. However, the precise prediction of this spectrum is a still on-going research field and previous measurements of the spectrum are lacking of a limited energy resolution of the antineutrino detectors. This chapter will discuss the possibilities to predict this spectrum and short-comings of current spectrum models are presented.

4.1 General prediction of the reactor spectrum

The total antineutrino spectrum emitted by nuclear reactors is built up as the sum of the individual antineutrino spectra $\frac{\mathrm{d}N_i}{\mathrm{d}E_\nu}$ per fission of the four reactor fuel isotopes ^{235}U, ^{238}U, ^{239}Pu, and ^{241}Pu

$$S(E_\nu) = \sum_i f_i \left(\frac{\mathrm{d}N_i}{\mathrm{d}E_\nu}\right) \quad , \tag{17}$$

where f_i is the total number of fissions of isotope i. The number of fissions is connected to the thermal energy W_{th} of the reactor which can be used to calculate the total spectrum by [71]

$$S(E_\nu) = \frac{W_{\mathrm{th}}}{\sum_i (f_i/F) e_i} \sum_i \frac{f_i}{F} \left(\frac{\mathrm{d}N_i}{\mathrm{d}E_\nu}\right) \quad , \tag{18}$$

where f_i/F denotes the fission fractions which describe the fraction of contribution of each isotope i to the total amount of fissions and e_i is the effective energy that is released after a single fission of the isotope i which is given in table 3.

With those known values and the thermal power and fission fractions provided by the reactor operator via simulations of the reactor core evolution, the only unknown part is the individual antineutrino spectrum per fission for each isotope $\frac{\mathrm{d}N_i}{\mathrm{d}E_\nu}$.
To calculate these spectra, two different approaches are commonly used, the *ab-initio summation* and the *conversion method*. Both approaches are described in the following.

Table 3: Effective energy e_i released per neutron induced fission [72]. It is defined as the sum of the energy released by the fission and the energy produced by neutron capture on reactor materials minus the total energy carried away by antineutrinos.

Isotope i	e_i
^{235}U	$202.36 \pm 0.26\,\mathrm{MeV}$
^{238}U	$205.99 \pm 0.52\,\mathrm{MeV}$
^{239}Pu	$211.12 \pm 0.34\,\mathrm{MeV}$
^{241}Pu	$214.26 \pm 0.33\,\mathrm{MeV}$

4.1.1 The ab-initio summation

With this method, the spectra are calculated by summing up all beta decay spectra contributing to the total cumulative spectrum [71]

$$\frac{\mathrm{d}N_i}{\mathrm{d}E_\nu} = \sum_{A,Z,n} Y_n(Z,A,t) \sum_k b_{n,k}(E_0^k)\, P_{\bar{\nu}}(E_{\bar{\nu}}, E_0^k, Z) \quad . \tag{19}$$

Here $Y_n(Z,A,t)$ denotes the cumulative fission yield which describes the probability that a certain fission fragment with atomic number Z and mass number A at a time t after fission is produced in the reactor. This fragment can either be produced directly by fission or via beta decay of isotopes with a larger number of neutrons. The index n denotes whether the isotope is in its ground state or in an isomeric state. The fission yield will become independent of time after a sufficient burn time and will reach an equilibrium. The $b_{n,k}(E_0^k)$ are the branching ratios for the beta decay of the isotopes as a single isotope can undergo beta decay with several possible endpoints E_0^k with a certain probability. The final part is the normalized beta spectrum shape [71]

$$P_{\bar{\nu}}(E_{\bar{\nu}}, E_0^k, Z) = K p_\mathrm{e} E_\mathrm{e} (E_0^k - E_\mathrm{e})^2 F(Z,E_\mathrm{e}) C(Z,E_\mathrm{e})(1 + \delta(Z,A,E_\mathrm{e})) \quad , \tag{20}$$

where K is the normalization constant, $p_\mathrm{e} E_\mathrm{e} (E_0^k - E_\mathrm{e})^2$ is the phase space factor of the beta decay with electron momentum p_e and energy $E_\mathrm{e} = E_0^k - E_{\bar{\nu}}$. $F(Z,E_\mathrm{e})$ denotes the Fermi correction which accounts for the interaction of the negatively charged electron with the positively charged nucleus and $C(Z,E_\mathrm{e})$ is the shape factor which is $C(Z,E_\mathrm{e}) \neq 1$ if the decay is not allowed due to parity violation. Further small corrections like finite size, weak magnetism, and radiative correction are summarized in $\delta(Z,A,E_\mathrm{e})$ (c.f. chapter 6.2). To compute the cumulative antineutrino spectra, all these necessary data have to be known, however, current nuclear databases are still incomplete or provide the data with large uncertainties [73]. A more detailed description of the components that are taken into account in this summation is discussed in chapter 6.2.

4.1.2 The conversion method

This method avoids the insufficient nuclear data by using actually measured electron spectra of the reactor fuel isotopes ^{235}U, ^{238}U, ^{239}Pu, and ^{241}Pu from research reactors at the Institut Laue–Langevin (ILL) in Grenoble [74], [75], at the Kurchatov Institute [76], and in Garching [77] that are already the cumulative sum of all contributing beta decay branches. Figure 11 shows the electron spectrum for ^{235}U measured at the ILL. To retrieve the antineutrino spectrum from the measured electron spectrum, a sum of a few virtual

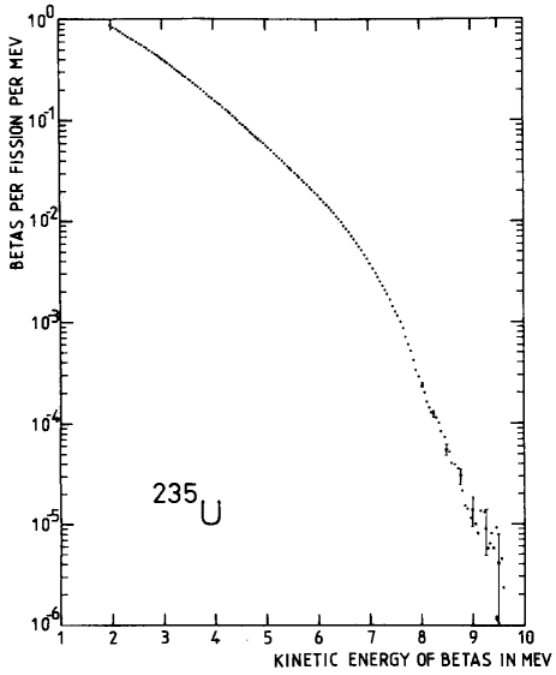

Figure 11: Experimentally measured electron spectrum for the fission of ^{235}U. The measurement was taken with the BILL spectrometer at the ILL [75].

beta decay branches $\frac{\mathrm{d}N_i}{\mathrm{d}E_\nu} = \sum_k a_k P(E,E_0^k,Z)$ with assumed spectrum shapes $P(E,E_0^k,Z)$ is fitted to the electron spectrum with variable amplitudes a_k and endpoints E_0^k to reproduce the measured spectrum and then the energy of the electron E_e is simply replaced by $E_0^k - E_{\bar{\nu}}$ in every virtual branch [71].
However, although this method relies on actual measurements, it also has its shortcomings. Since the spectrum shapes are assumed in order to fit to the electron spectrum, differences in the corrections to the spectrum shape between electrons and antineutrinos are not properly converted yielding small spectral differences between converted and summation spectra. This topic is addressed in detail in chapter 4.3.

4.2 The Huber-Mueller spectrum model

The most commonly used reactor neutrino spectrum model is the Huber-Mueller model derived in [78] and [79]. It is a hybrid model using both methods described in chapters 4.1.1 and 4.1.2. For the isotopes with well-known nuclear data, the electron spectrum is summed up. Then, this sum is subtracted from the measured aggregate electron spectrum and the remaining spectrum is then calculated using the conversion method. After its publication it became widely used as the new standard model for the reactor antineutrino spectrum. Compared to the experimentally measured spectra by Daya Bay [80], Double Chooz [81], and RENO [82], it predicted a by 6% larger antineutrino flux. This observation commonly known as *Reactor Antineutrino Anomaly* was first described in [83]. Further, all three experiments report an excess of events in the $4-6\,\mathrm{MeV}$ region, which is referred to as *5-MeV-Bump*. Figure 12 shows the measured IBD spectra from the three experiments and compares them to the predicted IBD spectrum. The ratio of measured to predicted spectrum clearly shows this observation in a similar way in all the three experiments. This discrepancy between measurement and prediction raised doubts on the validity of the

Huber-Mueller spectrum. Additionally, the Huber-Mueller spectrum model only provides the antineutrino yield in 250 keV steps in antineutrino energy which is too coarse for future high resolution detectors like JUNO and TAO as there might be variations in the spectrum on a smaller energy scale. This is now discussed in chapter 4.3.

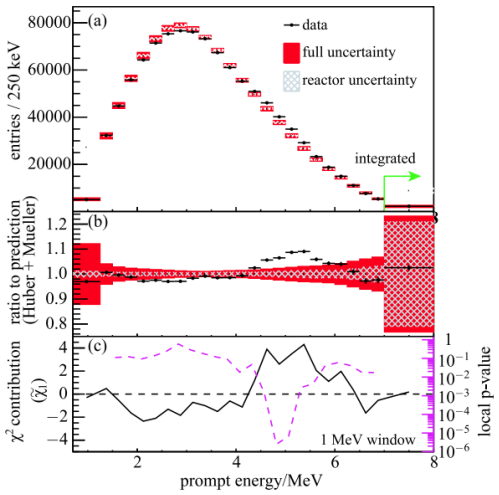

(a) Daya Bay near detector (adapted from [80])

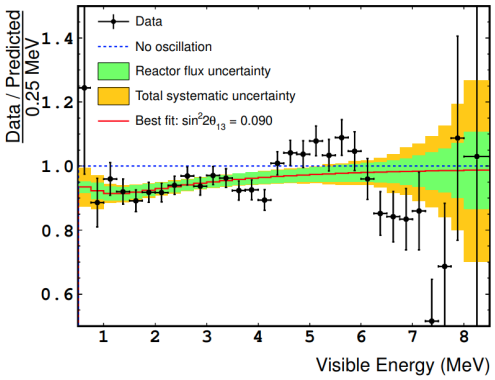

(b) Double Chooz far detector (adapted from [81])

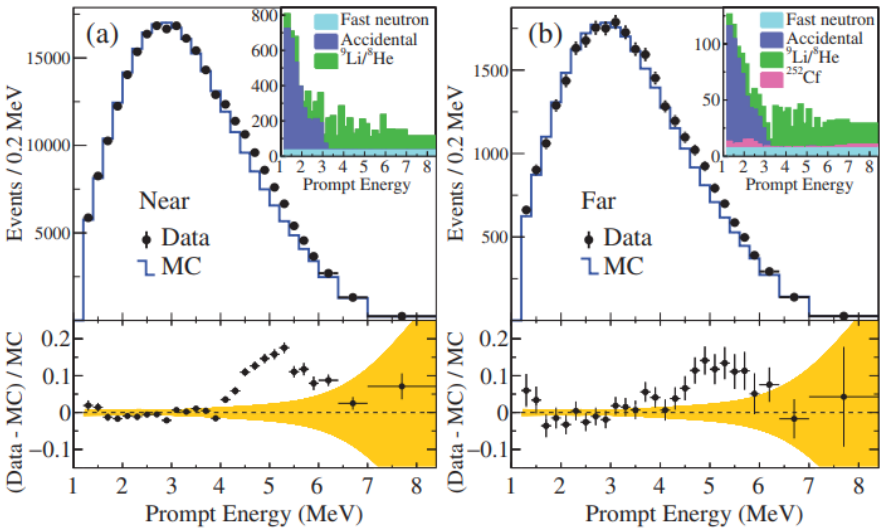

(c) RENO near (left) and far (right) detector (adapted from [82])

Figure 12: Results from the Daya Bay (a), Double Chooz (b), and RENO (c) experiments showing the excess of events in the $4 - 6$ MeV range compared to the spectrum prediction from the Huber-Mueller model.

4.3 Origin of the fine structure in the antineutrino spectrum

One of the major corrections to the spectrum shape as shown in equation 20 is the Fermi correction. It describes the Coulomb interaction of the outgoing electron with energy E_e and momentum p_e with the remaining nucleus of charge Z and is given by

$$F(Z,E_e) \;=\; 2(\gamma+1)(2p_eR)^{2(\gamma-1)}e^{\pi\alpha ZW/p_e}\frac{|\Gamma(\gamma+i\alpha ZW/p_e)|^2}{\Gamma(2\gamma+1)^2} \quad , \tag{21}$$

where $W = 1 + E_e/(m_ec^2)$, $\gamma = \sqrt{1-(\alpha Z)^2}$, R describes the nuclear radius, and α is the Sommerfeld constant [78].
Due to the Coulomb interaction of the outgoing electron with the daughter nucleus, the electron is slowed down which results in a shift of the electron spectrum to lower energies. Figure 13a shows how the spectra for the four example isotopes ^{92}Rb, ^{96}Y, ^{100}Nb, ^{102}Tc would look like if only the phase space factor would contribute to the spectrum and figure 13b shows how the electron spectra are shifted to lower energies if the Fermi correction is applied. Due to energy conservation, the corresponding antineutrino spectra are shifted to higher energies which is displayed in figure 13c. This has the direct consequence that at the endpoint of the antineutrino spectra sharp cut-offs are observed instead of a smooth decrease.
Since the conversion method (see 4.1.2) is based on the measured electron spectra fitted with a few virtual beta decay branches, these cut-offs are not correctly represented in the conversion models yielding a smooth cumulative spectrum.
However, if the cumulative antineutrino spectrum emitted by a nuclear reactor is now calculated by ab-initio summation (see 4.1.1) as a sum of hundreds of these individual spectra, a rugged substructure can be observed as it was first reported in [5]. This substructure in the antineutrino spectrum is further referred to as *fine structure*. Figure 14 shows an exemplary summation spectrum compared to the Huber-Mueller spectrum model described in chapter 4.2. It also illustrates how the energy resolution affects the appearance of the fine structure. For a binwidth of less than 100 keV, first small distortions appear and a fine structure becomes even more visible for smaller energy bins. This raises the question on the implications by such a fine structure that is potentially visible in the high resolution spectra of JUNO and TAO on the experimental results, in particular on the NMO determination, where small differences between the fast oscillations in the neutrino spectrum have to be resolved, and proves that the Huber-Mueller model is not a suitable candidate for a precise reactor antineutrino model.
The prediction of reactor antineutrino spectrum models with fine structure in the context of this work is further discussed in chapter 6.

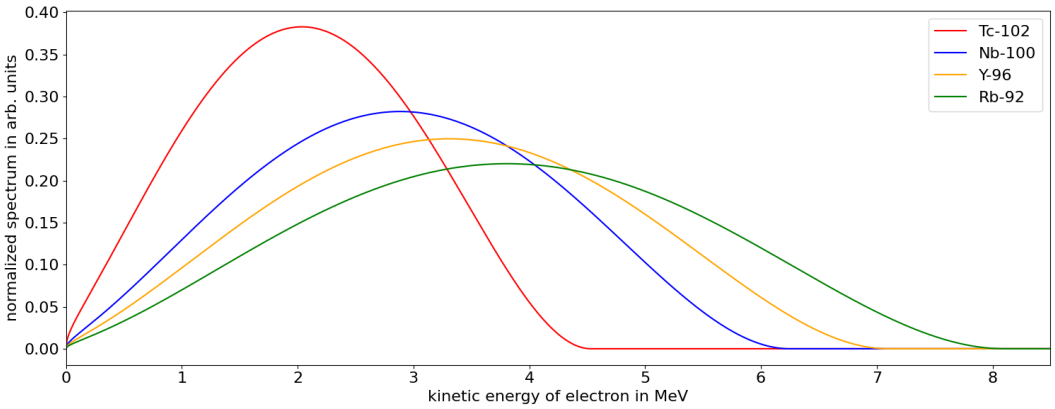

(a) Only phase space contribution

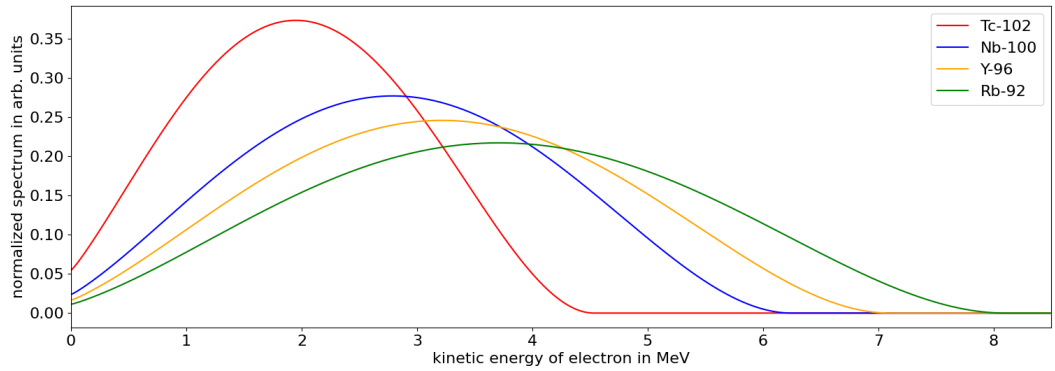

(b) Electron spectrum with Fermi correction

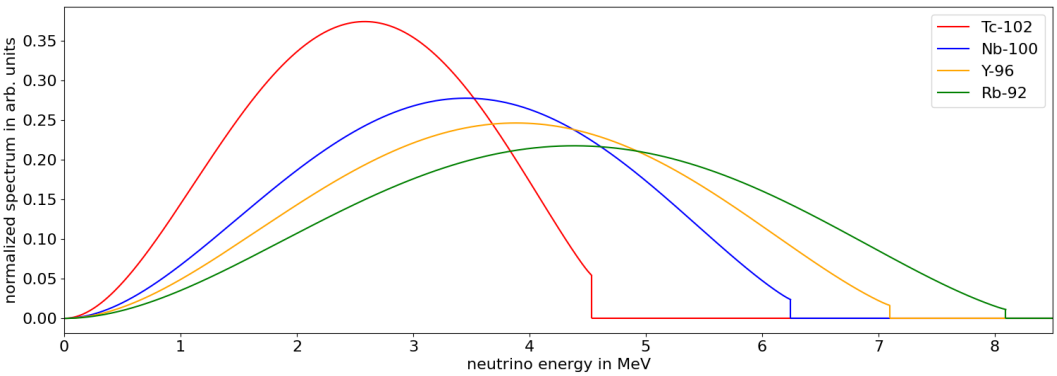

(c) Antineutrino spectrum with Fermi correction

Figure 13: Exemplary illustration how the Fermi correction affects the electron and antineutrino spectra shown with the spectra of the isotopes ^{92}Rb, ^{96}Y, ^{100}Nb, ^{102}Tc.

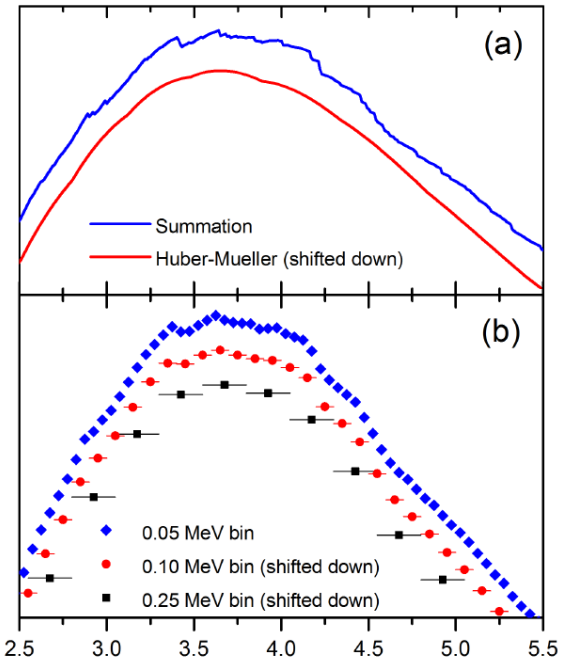

Figure 14: The upper panel shows the Daya Bay IBD spectrum calculated with a summation spectrum (blue) compared to the Huber-Mueller spectrum (red) which is shifted down for better visibility of the fine structure in the summation model. The lower panel displays the same summation spectrum binned in 50 (blue), 100 (red), and 250 keV (black) intervals where the red and black spectra are again shifted down. For smaller binning, the fine structure becomes more visible. The plot is adapted from [5].

5 Prediction of the IBD Spectrum in JUNO and TAO

Hello, IT, have you tried turning it off and on again?

– Roy Trenneman - *The IT Crowd*

In the first part of this chapter, the software used to perform the analyses in this work will be discussed. It is designed to compute the expected spectra in JUNO and TAO and minimize the statistics function to estimate the NMO sensitivity. While this is discussed in detail in chapter 7, the second part of this chapter presents how the IBD spectrum that is expected in the JUNO and TAO detectors is calculated which builds the central part of the sensitivity analysis.

5.1 The Global Neutrino Analysis Software

In the following, the software framework GNA [84, 85] that was used to perform the NMO sensitivity analyses presented in this work will be introduced. The description is mainly based on the software documentation available in [86]. It was originally developed at Joint Institute for Nuclear Research (JINR) in Dubna since 2014 and then was adapted to fit the analysis needs in this work.
The GNA is based on the dataflow programming principle which means that input data follows a directed graph from operation to operation which are defined in individual computation blocks called transformations. This provides the possibility to access the data at every step in the calculation chain providing large flexibility in the analysis of the data. Additionally, the outputs of these individual transformations are associated with taintflags that provide information whether the output has been changed. With this lazy evaluation, complex computation models can be created by scaling up the computational graph repeating individual calculations with different configurations without large increase in computation time as only the parts that are affected by a change are recalculated. To additionally increase computing efficiency, these transformations are written in C++ while the computational graph itself is build and configured using Python which is more convenient from the user's perspective. Figure 15 shows an illustration of the software design with its four levels that build up the GNA. The individual layers of the software will be discussed in more detail in the following.

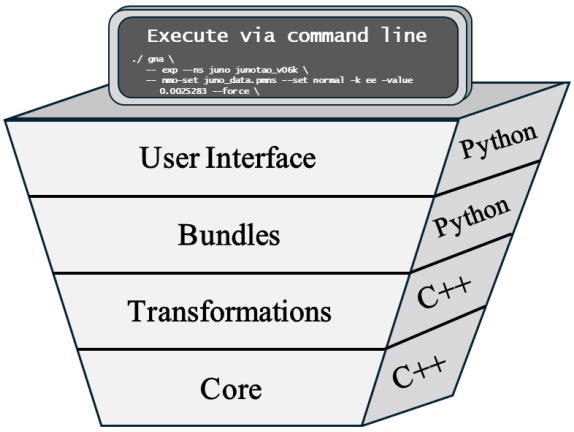

Figure 15: Graphic illustration of the software structure. GNA has four layers that build up the entire software. The core and transformations are written in C++ and contain basic calculations, memory allocation and datatypes. The bundles and user interface are written in Python and define configurations and build the computational chain. The execution of the GNA is done via command line.

Core

The core defines how objects like variables, parameters and transformations are handled in GNA. It defines datatypes and manages memory allocation. The previously mentioned taintflags are defined here which show if an output of a transformation has been reevaluated or not.

Transformations

Transformations define actual calculations of different types, from a simple sum or multiplication to more complex calculations like interpolations, integration or building statistic functions. Transformations have none or more inputs and at least one output which can be bound together to build a computational chain. The input(s) and output(s) are generally data arrays and the output type is automatically derived from the input type to fit the actual calculation performed within the transformation. Additionally, a transformation can depend on variables that also manipulate the output of the transformation.

Bundles

A bundle is a small computational chain of transformations that defines a certain manipulation of the data. This usually represents certain physical processes that affect the data in the same way which is defined by the computational chain and the configuration of additional variables. Since the same calculations may be executed several times for different parts of the computational chain, the bundles provide the option for indexing. This means that the same bundle is executed for different inputs/outputs depending on the index. With this method, the whole computational model can easily be scaled up. Figure 16 shows a flowchart of the *reactor_ anu_ spectra* bundle which loads the reactor antineutrino spectra from input files, multiplies the flux with variables that allow a variation of the spectrum and interpolates the neutrino flux to the energy definition passed as input to the bundle. As the antineutrino spectrum has to be loaded and interpolated for

all four reactor isotopes, this bundle is scaled by an index iterating over the four isotopes. With this indexing, the bundle can conveniently be integrated in building a more complex physical model which will be discussed in the following.

User interface

To build a complex computational chain that represents the calculation of an actual physical model like the expected JUNO and TAO spectrum (see chapter 5.2), the bundles that define small calculations have to be connected in the correct order. In addition, each bundle has to be configured to define inputs, indexes and options. The benefit of building the computational chain in this way is that the whole calculation is modular and allows to add or remove specific parts of the calculation or change configurations of the bundles without having to reimplement most of the code. Therefore, a detailed analysis of various parts (e.g. reactor spectrum model, energy resolution, energy binning, ...) affecting the expected spectrum can be performed conveniently. Additionally, GNA features a statistics module to perform statistical analyses with the computed physics model. For the minimization it provides the *iminuit* interface for the *Minuit2* library from the ROOT framework.

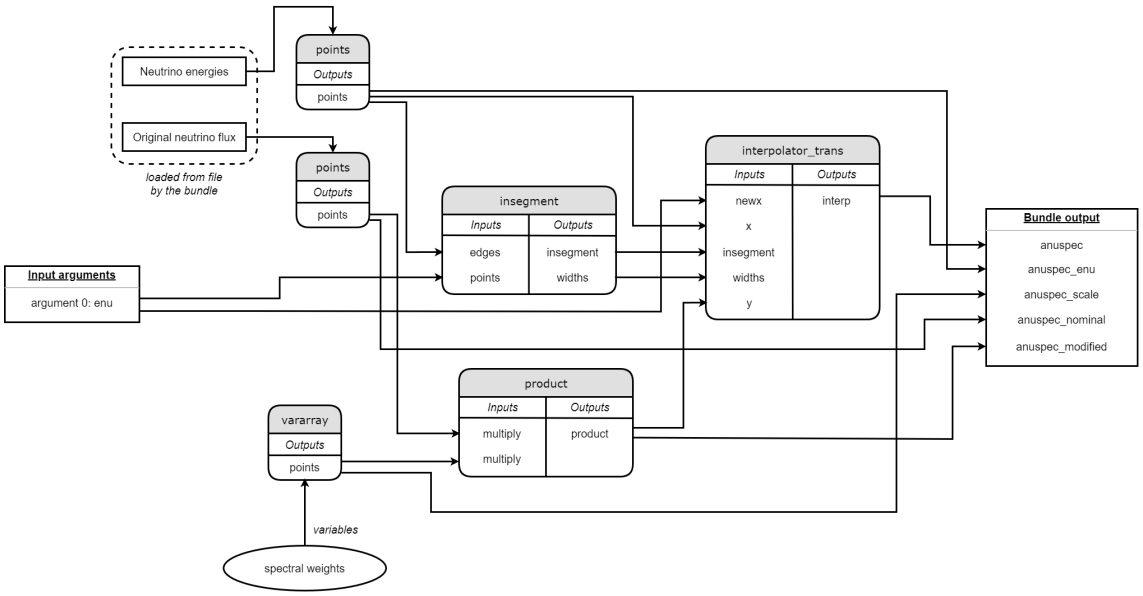

Figure 16: Flowchart representation of the computational chain of the *reactor_ anu_ spectra* bundle. It has one input given by *enu* which is connected to the '*points*'-input of the *insegment*-transformation and the '*newx*'-input of the *interpolator_ trans*-transformation. The bundle loads the antineutrino spectrum flux and energies from input files and creates arrays via the *points*-transformation which are connected to the inputs of the respective subsequent transformations. Spectral weights are defined as variables in the bundle and also created as an array with the *vararray*-transformation whose output is connected to the input of the *product*-transformation and to the bundle output. The output of this transformation which contains the product of spectral weights and original neutrino flux is connected to the bundle output and the '*y*'-input of the *interpolator_ trans*-transformation. The *insegment*-transformation determines to which segment of the '*edges*' -input each value of the '*points*'-input belongs to ('*insegment*'-output) and the widths of the segments ('*widths*'-output). These outputs are connected to the corresponding inputs of the *interpolator_ trans*-transformation which calculates the actual interpolation of the '*y*'-input sampled at input '*x*' at the values given by '*newx*'-input. The '*interp*'-output of the *interpolator_ trans*-transformation is then connected to the bundle output and contains the neutrino flux multiplied with the spectral weights and interpolated to the neutrino energies given by the bundle input *enu*.

5.2 Description of the calculation procedure for the IBD spectra

In the following it will be discussed how the expected IBD spectra in JUNO and TAO are calculated with the previously described GNA software to be used for the analysis of the sensitivity to the NMO. This is mainly based on the description in [45] and [87].
A schematic overview of the individual steps included in the spectrum prediction for both detectors is shown in figure 17.

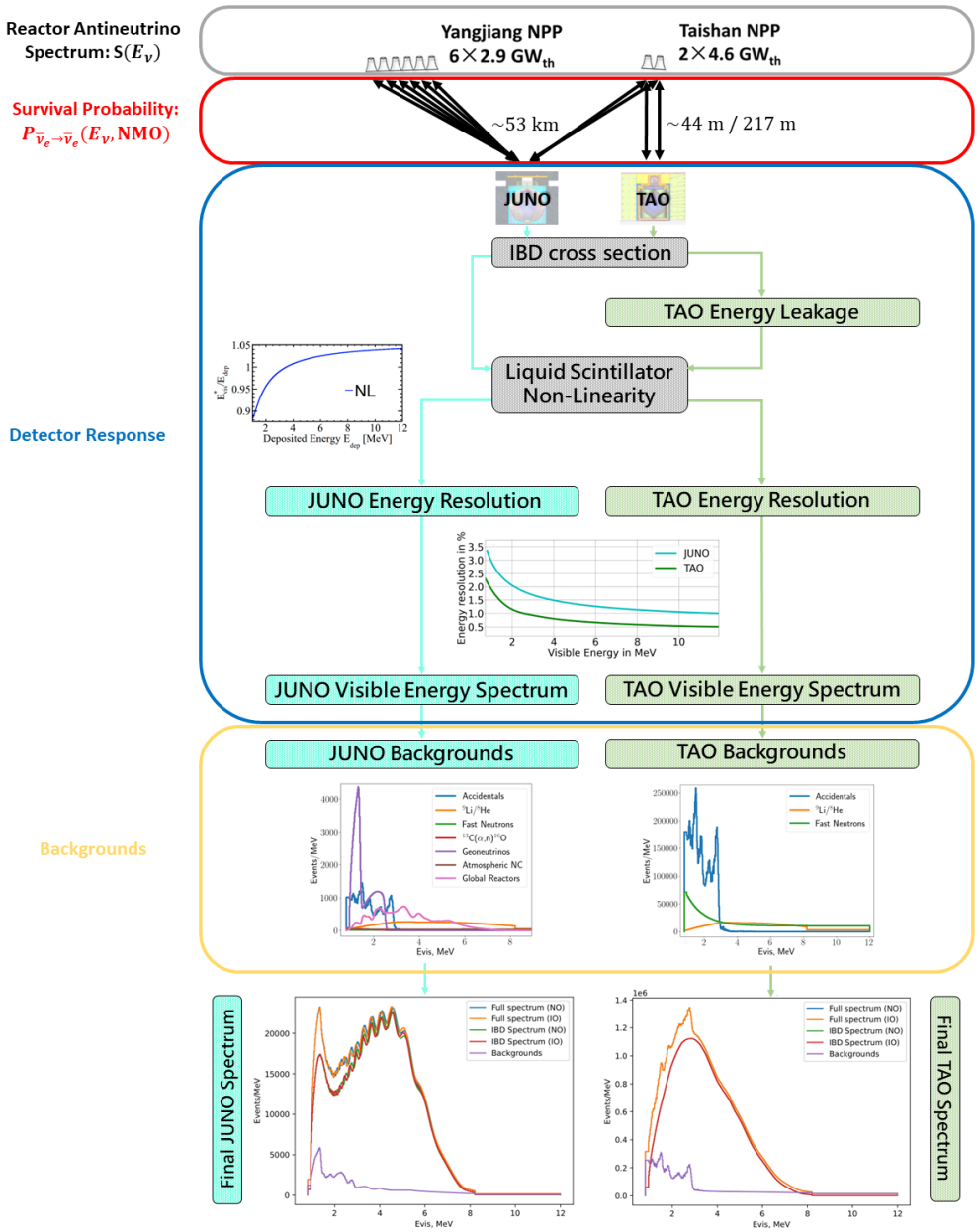

Figure 17: Schematic overview of the steps included in the IBD spectrum prediction.

5.2.1 Emitted reactor antineutrino spectrum

As starting point, the electron antineutrino fluxes as a function of the neutrino energy $S_i(E_\nu)$ for the four reactor isotopes ^{235}U, ^{238}U, ^{239}Pu, and ^{241}Pu (see chapter 4) are used as input to the calculation. The individual spectra are weighted with the fission fractions f_{ir} for each isotope i and scaled with the thermal power W^r_{th} in the reactor r (c.f. eq. 18) resulting in

$$\left(\frac{\mathrm{d}N(E_\nu)}{\mathrm{d}E_\nu}\right)_r = \sum_i \frac{W^r_{\text{th}} f_{ir}}{\sum_{i'} f_{i'r} e_{i'}} S_i(E_\nu) = \sum_i \left(R_{\text{fission}}\right)_{ir} S_i(E_\nu) \quad , \tag{22}$$

where e_i is the thermal energy released in a single fission of isotope i listed in table 3. The thermal power for the reactors contributing to the spectrum are given in table 2. All values are assigned with an uncertainty of 0.5%. Table 4 gives the average values for the fission fractions f_{ir} which are used and approximated to be similar in each reactor core.

Table 4: Fission fractions f_{ir} for all reactors and the four reactor isotopes as used in the spectrum prediction according to [33]. All four values are assigned with an uncertainty of 5%.

Isotope i	^{235}U	^{238}U	^{239}Pu	^{241}Pu
f_{ir}	0.58	0.07	0.30	0.05

Since there are also long-lived isotopes in the reactor, their decay rates are not in equilibrium with their production rates. Additionally, the nuclear fuel, which is removed after being burnt in the reactor, is stored near the reactor core for cooling while still emitting electron antineutrinos which also contribute to the spectrum. Both effects are taken into account by adding a correction to the spectrum according to [80].
The final spectrum emitted by reactor core r is then given by

$$\begin{aligned}\left(\frac{\mathrm{d}N(E_\nu)}{\mathrm{d}E_\nu}\right)_r &= \sum_i \left(R_{\text{fission}}\right)_{ir} S_i(E_\nu) \\ &+ \left[\sum_i \left(R_{\text{fission}}\right)_{ir} S_i(E_\nu)\right]_{\text{nominal}} \left[n_{\text{offeq}} C_i^{\text{offeq}}(E_\nu) - 1\right] \\ &+ \left[\sum_i \left(R_{\text{fission}}\right)_{ir} S_i(E_\nu)\right]_{\text{nominal}} \left[n_{\text{SNF}} C_{\text{SNF}}(E_\nu) - 1\right]\end{aligned} \tag{23}$$

with the energy dependent corrections of the spectrum shape for off-equilibrium $C_i^{\text{offeq}}(E_\nu)$ and spent nuclear fuel (SNF) $C_{\text{SNF}}(E_\nu)$. Both corrections are given as relative deviation to the nominal spectrum, so in case of $C_{\text{SNF}}(E_\nu) = C_i^{\text{offeq}}(E_\nu) = 1$ no correction is applied and only the first term is left. To propagate uncertainties in the analysis, the additional scale factors n_{offeq} and n_{SNF} are introduced which are set to a value of $n = 1$ with an uncertainty of 30%. The same off-equilibrium correction is used for all isotopes and reactors as it is assumed that the reactors have a burn-up history close to average during the data acquisition (DAQ) time. Although, the nominal spectrum input is changed in the analysis to introduce spectra with fine structure, we can still use the same corrections as all input spectra are corrected for rate and bump according to the Daya Bay measurement (see chapter 6.3) and $C_{\text{SNF}}(E_\nu)$ as well as $C_i^{\text{offeq}}(E_\nu)$ are both provided as ratios to the Daya Bay spectrum. The corrections are shown in figure 80 in appendix A.

5.2.2 Reactor antineutrino spectrum at the detector location

The electron antineutrinos are isotropically emitted by the reactor which leads to a geometrical reduction of the flux proportional to the squared distance. Additionally, the survival probability of the electron antineutrinos $P(L_{rd}, E_\nu)$ as a function of distance L_{rd} from reactor r to detector d and neutrino energy E_ν has to be taken into account. The total spectrum at the detector location is then given by the sum of all spectra emitted by the contributing reactors weighted by the survival probability and geometrical flux reduction as

$$\left(\frac{\mathrm{d}N(E_\nu)}{\mathrm{d}E_\nu}\right)_d = \sum_r \frac{P(L_{rd}, E_\nu)}{4\pi L_{rd}^2} \left(\frac{\mathrm{d}N(E_\nu)}{\mathrm{d}E_\nu}\right)_r \quad . \tag{24}$$

For the JUNO detector, the reactors contributing to the spectrum with their corresponding baselines are listed in table 2. In case of the TAO detector, only the two reactors from the Taishan NPP are significantly contributing to the spectrum. Due to a change in the actual TAO detector location, there are two baselines for the TAO detector used in this analysis, referred to as *original* and *updated* baselines as listed in table 5.

Table 5: Original baselines of the TAO reactors TS1 and TS2 as in [32] and the updated baselines due to a change in detector location according to [52].

reactor	original baseline	updated baseline
TS1	30 m	44 m
TS2	225 m	217 m

For the survival probability, the expression including matter effects as described in equations (15) to (20) in [88] is used. The values for the oscillation parameters to calculate the survival probability are given in table 6. The two mass splittings $|\Delta m^2_{12}|$ and $|\Delta m^2_{13}|$ as well as the solar mixing amplitude $\sin^2 2\theta_{12}$ are included as free parameters in the analysis.

Table 6: The oscillation parameters used in the analysis to compute the survival probability of the electron antineutrinos. The label „free“ in uncertainty indicates that the parameter is treated as a free parameter in the analysis. The values of the oscillation parameters and the uncertainty of $\sin^2 2\theta_{13}$ are taken from Particle Data Group (PDG)2020 [89]. The earth crust density was estimated by a local geological survey.

parameter	value	uncertainty
mass splitting $\lvert\Delta m^2_{12}\rvert$	$7.53 \cdot 10^{-5}\,\mathrm{eV}^2$	free
mass splitting $\lvert\Delta m^2_{13}\rvert$ (NO)	$0.0025283\,\mathrm{eV}^2$	free
mass splitting $\lvert\Delta m^2_{13}\rvert$ (IO)	$0.0024707\,\mathrm{eV}^2$	free
solar mixing amplitude $\sin^2 2\theta_{12}$	0.851004	free
reactor mixing amplitude $\sin^2 2\theta_{13}$	0.085299	0.00267792
earth crust density ρ	$2.45\,\mathrm{g/cm^3}$	$0.15\,\mathrm{g/cm^3}$

5.2.3 Detected IBD spectra in both detectors

In both detectors the electron antineutrinos are detected via the IBD reaction as described in 3.2. The cross section for this reaction is used from [90] and is shown in figure 18.

As the energy is deposited in the detector by the positron, also the kinematics of the IBD have to be considered to calculate the spectrum as a function of the positron energy. Therefore, the neutrino energy can be given in terms of positron energy as

$$E_\nu = \frac{E_e + \delta}{1 - \frac{E_e}{m_p}\left(1 - \frac{p_e}{E_e}\cos\theta\right)} \quad , \tag{25}$$

where $\delta = (m_n^2 - m_p^2 - m_e^2)/(2m_p) \ll 1$ with the masses of neutron, proton, and positron and θ being the angle between the directions of antineutrino and positron. This substitution of $E_\nu(E_e, \cos\theta)$ is included in the integration of the neutrino event rate in each energy segment and over the angle θ. Since at this point the application of the detector effects differs between the JUNO and TAO detectors as it is also illustrated in figure 17, it will be distinguished between the interaction rates R_ν^{JUNO} and R_ν^{TAO} in the following.

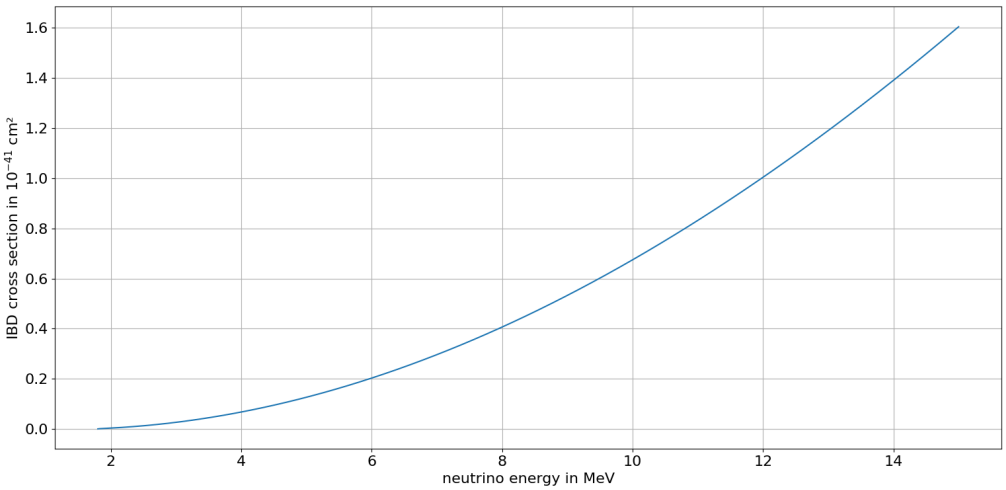

Figure 18: Cross section for the IBD reaction as a function of neutrino energy according to [90] as used in the prediction of the measured spectrum.

Energy leakage

In case of the TAO spectrum, energy leakage has to be taken into account as a fraction of the visible signal is lost when the positron does not deposit its total energy inside the fiducial volume due to its small size in comparison to the JUNO detector where this effect is negligible. Energy leakage is applied as smearing via multiplication with matrix C_{leak} (see figure 79 in appendix A). To perform this multiplication, the kinematic integration for each energy segment j has to be performed using the substitution from equation 25 and the differential cross section via

$$(R_\nu^{\text{TAO}})_j = \int_{-1}^{1} \mathrm{d}\cos\theta \int_{E_{\text{dep}}^j}^{E_{\text{dep}}^{j+1}} \mathrm{d}E_{\text{dep}} \left(\frac{\mathrm{d}N(E_\nu)}{\mathrm{d}E_\nu}\right)^{\text{TAO}} \frac{\mathrm{d}\sigma(E_\nu, \cos\theta)}{\mathrm{d}\cos\theta} \frac{\mathrm{d}E_\nu(E_{\text{dep}}, \cos\theta)}{\mathrm{d}E_{\text{dep}}} \quad , \tag{26}$$

where $E_{\text{dep}} = T_e + 2m_e$ is the deposited energy in the detector given by the kinetic energy of the positron and two electron masses from the annihilation of the positron.

Liquid Scintillator Non-Linearity

In the next step, the LSNL is applied to the spectrum which causes another distortion of the energy scale. The LSNL describes how the deposited energy E_{dep} translates to the energy visible in the detector E_{vis} which is not proportional due to the energy transfer mechanism in the scintillator causing quenching effects. It is assumed to be the same for JUNO and TAO as the scintillator composition is approximately similar.
However, due to the previously introduced energy leakage, the LSNL has to be introduced differently for the JUNO and TAO spectrum prediction. In case of the TAO spectrum, the LSNL curve is converted into a matrix C_{lsnl} and applied via matrix multiplication after the energy leakage. For the JUNO spectrum, it is applied in the kinematic integration via a second substitution of the variables by

$$(R_\nu^{\text{JUNO}})_j = \int_{-1}^{1} \mathrm{d}\cos\theta \int_{E_{\text{vis}}^j}^{E_{\text{vis}}^{j+1}} \mathrm{d}E_{\text{vis}} \left(\frac{\mathrm{d}N(E_\nu)}{\mathrm{d}E_\nu}\right)^{\text{JUNO}} \frac{\mathrm{d}\sigma(E_\nu,\cos\theta)}{\mathrm{d}\cos\theta} \frac{\mathrm{d}E_\nu(E_{\text{dep}},\cos\theta)}{\mathrm{d}E_{\text{dep}}} \frac{\mathrm{d}E_{\text{dep}}(E_{\text{vis}})}{\mathrm{d}E_{\text{vis}}} \quad . \tag{27}$$

To take into account the uncertainty of the LSNL, four characteristic pull curves $f_i(E_{\text{dep}})$ were selected from a Monte Carlo simulation with calibration data and their uncertainties estimated to be similar to those of Daya Bay [91]. These curves are added as differences to the nominal curve $f_0^{\text{DYB}}(E_{\text{dep}})$ from Daya Bay weighted with four different nuisance parameters $a_i = (0 \pm 1)$ and rescaled to match the curve from the JUNO detector simulation $f_0^{\text{Simulation}}(E_{\text{dep}})$ via

$$\frac{E_{\text{vis}}}{E_{\text{dep}}} = \left[f_0^{\text{DYB}}(E_{\text{dep}}) + \sum_i a_i \left(f_i(E_{\text{dep}}) - f_0^{\text{DYB}}(E_{\text{dep}}) \right) \right] \frac{f_0^{\text{Simulation}}(E_{\text{dep}})}{f_0^{\text{DYB}}(E_{\text{dep}})} \quad . \tag{28}$$

The LSNL response curve obtained from the JUNO detector simulation as well as the nominal and pull curves from Daya Bay [91] are shown in figure 19.

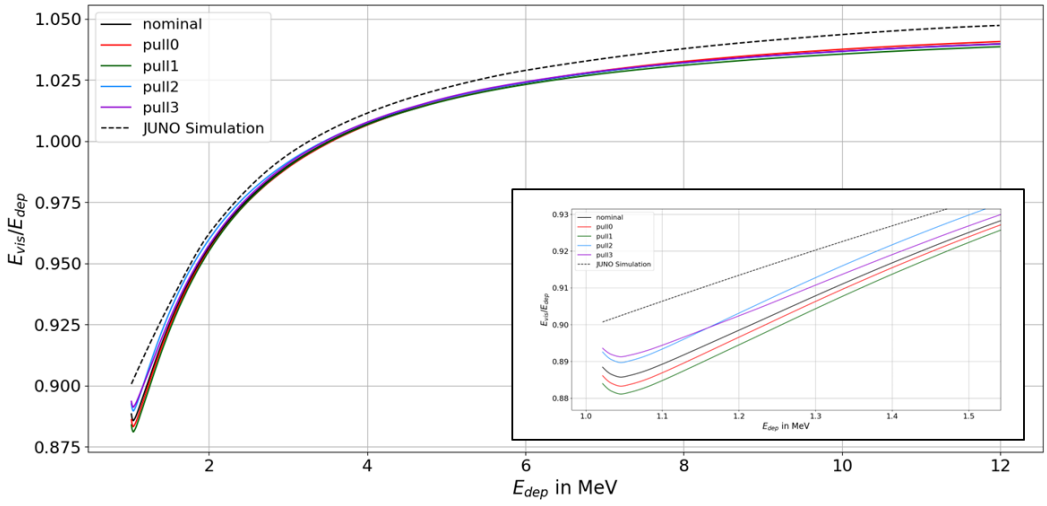

Figure 19: Nominal LSNL curve (black) showing the ratio of energy visible in the detector E_{vis} to the deposited energy E_{dep} as a function of E_{dep} as well as four characteristic pull curves for the application of systematic uncertainties (*pull0*, *pull1*, *pull2*, *pull3*) obtained from Daya Bay [91]. The dashed line represents the LSNL curve from the JUNO detector simulation used to rescale the nominal and pull curves. The inlet shows a zoom into the low energy region.

Energy resolution

The next step is to apply the energy resolution of the detectors which is done by multiplication with another matrix C_{eres} to perform the energy smearing due to the limited resolution. The energy resolution is in general parametrized via the parametrization

$$\frac{\sigma}{E} = \sqrt{\frac{a^2}{E} + b^2 + \frac{c^2}{E^2}} \quad , \tag{29}$$

where a describes the contribution due to photon statistics, b accounts for residual effects after the spatial non-uniformity correction due to limited time resolution, and c is introduced by dark noise. The energy resolution curve for the JUNO and TAO detectors are shown in figure 20. These curves are then converted into the matrix C_{eres}.

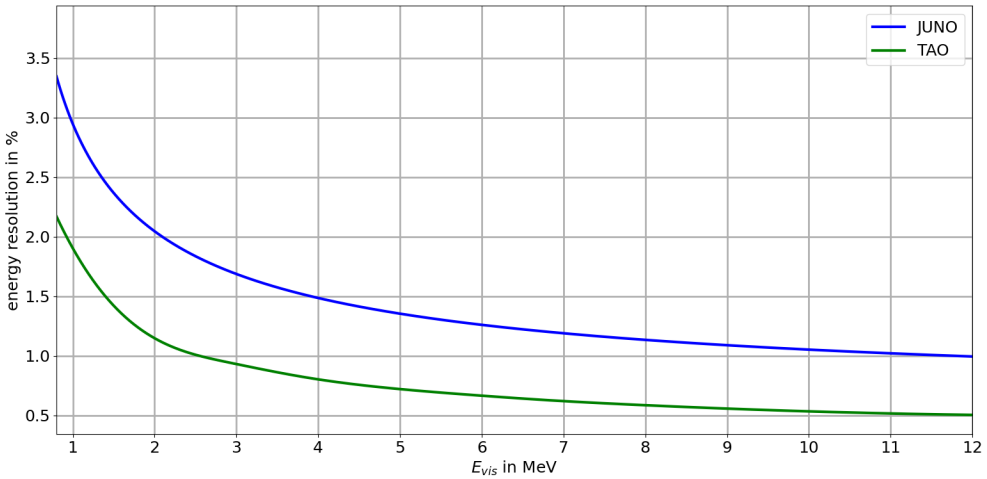

Figure 20: Energy resolution of the JUNO (blue) and TAO (green) detectors as a function of the visible energy used for the calculation of the estimated spectrum.

IBD event number

To get the final expected IBD spectrum from the reactor antineutrinos, detection efficiency, number of target protons for the IBD reaction, and the DAQ time T, which is given in years with a year assuming 365.25 days, and a duty cycle of the reactors that is assumed to be 11/12, have to be taken into account. The number of target protons N_p can be calculated from the mass fraction of ^{1}H in the 20 kt of JUNO LS and 2.8 t of TAO LS and the mass of a single ^{1}H to $N_p^{\text{JUNO}} = 1.43512 \cdot 10^{33}$ and $N_p^{\text{TAO}} = 2.00917 \cdot 10^{29}$ respectively. The detection efficiency of the JUNO detector is calculated from simulations taking into account a fiducial volume cut, an energy cut on the IBD signal, a time difference and vertex distance cut on the difference between prompt and delayed signal as well as the dead time of the detector due to the muon veto. Table 7 gives an overview on the IBD selection criteria used to estimate the detection efficiency in the JUNO detector which is calculated to be $\epsilon^{\text{JUNO}} = 0.822$ [34]. For the TAO detector, only IBD events with neutron capture on gadolinium inside a fiducial volume are taken into account while those on hydrogen are not considered. Additionally, cuts on the energies and time difference of prompt and delayed signal are applied giving an IBD detection efficiency of $\epsilon^{\text{TAO}} = 0.17$ [92]. The detailed selection criteria are listed in table 8. The dead time due to the muon veto also further reduces the number of IBD events in TAO by a factor of $\epsilon^{\text{TAO}}_{\text{VETO}} = 0.909$ [87].

Table 7: IBD selection criteria in JUNO and their impact on the detection efficiency according to [34]. The fiducial volume describes the volume in which IBD events in the detector are accepted. The IBD events themselves are selected by the energy of the prompt and delayed signal as well as the time difference and spatial distance between prompt and delayed signal. Additionally, the number of detected IBDs is reduced by the veto time.

Type	Criteria	Efficiency (%)
No cuts	-	100
Fiducial volume	$R < 17.2\,\mathrm{m}$	91.5
IBD signal cuts		98.1
Energy range	$E_{\mathrm{prompt}} \in [0.7,12.0]$ MeV $E_{\mathrm{delayed}} \in [1.9,2.5]$ MeV $\cup$ [4.4,5.5] MeV	99.8
Time correlation	$\Delta T_{p-d} < 1\,\mathrm{ms}$	99.0
Spatial correlation	$\Delta R_{p-d} < 1.5\,\mathrm{m}$	99.2
Muon veto	-	91.6
Combined		82.2

Table 8: IBD selection criteria in TAO and their impact on the detection efficiency according to [92]. The fiducial volume describes the volume in which IBD events in the detector are accepted. Additionally, only delayed signals from neutron capture on gadolinium are accepted and those on hydrogen are ignored to reduce background. The IBD events themselves are selected by the energy of the prompt and delayed signal as well as the time difference between prompt and delayed signal.

Type	Criteria	Efficiency (%)
No cuts	-	100
Fiducial volume	$R < 0.65\,\mathrm{m}$	38
Gd:H capture fraction	89 : 11	89
IBD signal cuts		49
Energy range	$E_{\mathrm{prompt}} \in [0.9,9.0]$ MeV $E_{\mathrm{delayed}} \in [7,9]$ MeV	51
Time correlation	$1\,\mu\mathrm{s} < \Delta T_{p-d} < 100\,\mu\mathrm{s}$	96
Combined		17

The final number of detected reactor antineutrinos is then given by

$$N_\nu^{\mathrm{JUNO}} = \epsilon^{\mathrm{JUNO}} \cdot T \cdot N_p^{\mathrm{JUNO}} \cdot C_{\mathrm{eres}}^{\mathrm{JUNO}} \cdot R_\nu^{\mathrm{JUNO}} \tag{30}$$

and

$$N_\nu^{\mathrm{TAO}} = \epsilon^{\mathrm{TAO}} \cdot \epsilon_{\mathrm{VETO}}^{\mathrm{TAO}} \cdot T \cdot N_p^{\mathrm{TAO}} \cdot C_{\mathrm{eres}}^{\mathrm{TAO}} \cdot C_{\mathrm{lsnl}}^{\mathrm{TAO}} \cdot C_{\mathrm{leak}}^{\mathrm{TAO}} \cdot R_\nu^{\mathrm{TAO}} \quad , \tag{31}$$

where R_ν^{TAO} and R_ν^{JUNO} are the arrays containing the interaction rates for every energy segment j calculated in equations 26 and 27.

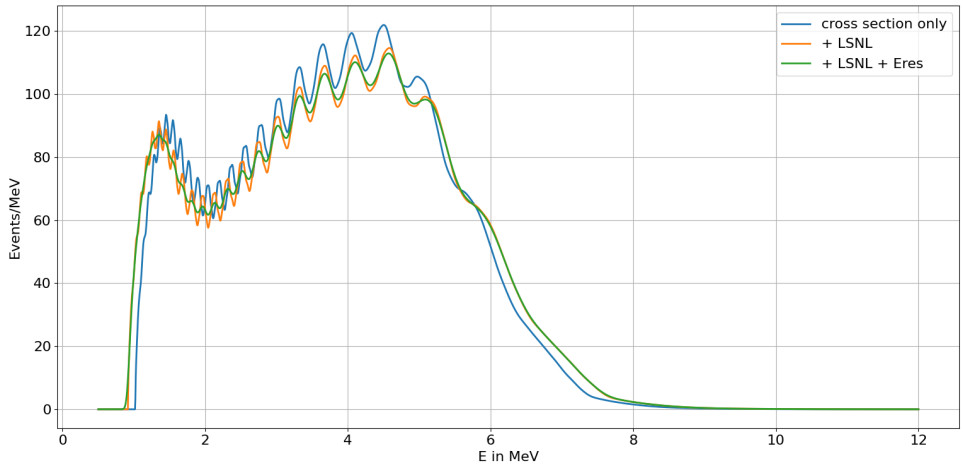

Figure 21: Expected IBD spectrum measured with JUNO for a true normal ordering (NO) after 6 years assuming the Huber-Mueller model with Daya Bay rate and shape correction for the reactor spectrum. The spectrum is shown after applying the different detector effects of LSNL (orange), LSNL and energy resolution (green) compared to the spectrum at the detector location multiplied with the IBD cross section only (blue). The spectrum is binned to energy segments with a width of 5 keV.

To account for uncertainties in the calculation of the number of IBD events, a relative uncertainty of 2% is applied on the reactor flux as well as 1% and 10% on the detection efficiencies of JUNO and TAO respectively. Additionally, an overall uncertainty on the energy scale of 0.5% is applied on the application of the LSNL for TAO, as the matrix approach is less accurate than the substitution method used for JUNO.
This final model for the number of IBD events from reactor antineutrinos in both the JUNO and TAO detectors as well as the intermediate steps in the application of the detector effects are shown in figures 21 and 22 using the Huber-Mueller model (see chapter 4.2) with Daya Bay rate and shape correction (see chapter 6.3.1) for the reactor spectrum assuming a normal NMO. It is observed that the detector effects significantly affect the energy scale and therefore the spectrum shape in both detectors which shows why the previously described precise prediction of the measured spectrum is crucial for the NMO sensitivity analysis. Taking into account all detector effects and event selection cuts, a total reactor antineutrino event rate of $47\,\mathrm{day}^{-1}$ and around $1000\,\mathrm{day}^{-1}$ is expected in JUNO and TAO respectively [45].

5.2.4 Backgrounds

Despite applying all the IBD selection criteria, there are still background events left that have to be added to the predicted spectra. This is discussed in the following.
There are two types of backgrounds that are added to the expected number of IBD events: those that mimic an IBD signal and actual neutrinos from other sources than the two NPPs.
For the first type of backgrounds there are four different sources that have to be taken into account for JUNO. The accidental background is formed by random coincidence of two uncorrelated events where the prompt signal is produced by natural radioactivity in the detector material and surrounding environment while the delayed signal can consist of either such radiogenic events or spallation neutrons produced by cosmic muons in the

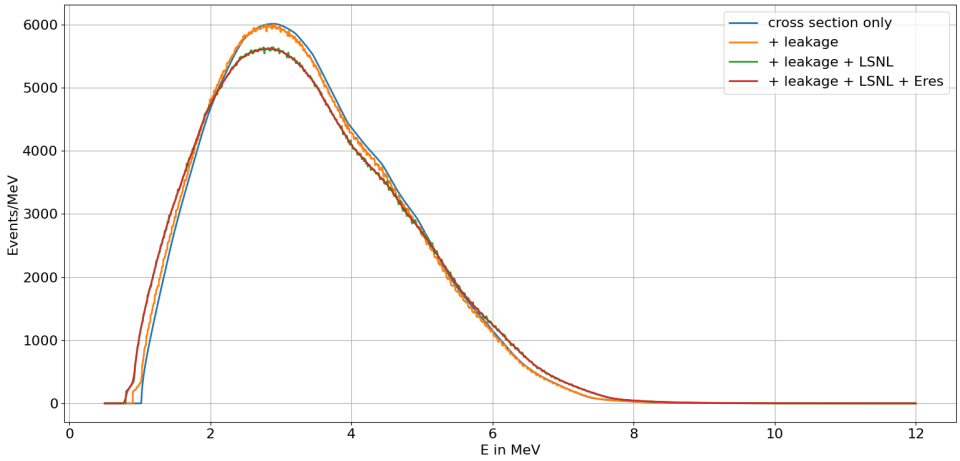

Figure 22: Expected IBD spectrum measured with TAO for a true NO after 6 years assuming the Huber-Mueller model with Daya Bay rate and shape correction for the reactor spectrum. The spectrum is shown after applying the different detector effects of energy leakage (orange), energy leakage and LSNL (green) as well as energy leakage, LSNL, and energy resolution (red) compared to the spectrum at the detector location multiplied with the IBD cross section only (blue). The spectrum is binned to energy segments with a width of 5 keV.

detector material. It was estimated to 0.80 per day with a 1% rate and negligible shape uncertainty using information on the JUNO detector design and material in [93].
High energetic neutrons produced by cosmic muons can also scatter off protons and afterwards be captured which imitates the prompt-delayed signature of the IBD signal which is referred to as fast neutron background. This is estimated using simulation and actual measured data from Daya Bay showing a flat spectrum up to energies of $\sim 100\,\text{MeV}$ [94] to 0.1 per day with a 100% rate and 20% shape uncertainty.
A third source of background is the beta decay of the long-lived isotopes ^{9}Li and ^{8}He which can be produced by cosmic muons in the detector which also mimics the IBD signature. Additional to the JUNO detector simulation, the measurements from Borexino and KamLAND [95, 96, 97] were used to estimate this background resulting in 0.8 per day with a 20% rate and 10% shape uncertainty.
The last background source that can imitate the IBD signal is the reaction $^{13}\text{C}(\alpha,\text{n})^{16}\text{O}$ where α-particles produced by natural radioactivity interact with the ^{13}C from the LS. De-excitation photons from the ^{16}O that could be produced in an excited state or the neutron scattering off protons can produce a prompt signal while the delayed signal is caused by the neutron being captured. This background is also obtained from simulations together with the Daya Bay measurements in [94] and is given by 0.05 per day with a 50% rate and 50% shape uncertainty.
For the second type of background that are actual neutrinos interacting in the detector, three different sources are taken into account.
The main source of electron antineutrinos in JUNO are produced by the two NPPs in Yangjiang and Taishan. The more distant NPP in Daya Bay is also added in the estimation of the flux, but there are also electron antineutrinos from even more distant reactors that could interact in the JUNO detector. These neutrinos from reactors with baselines of $L > 300\,\text{km}$ are considered as background with a rate of 1.00 per day and a rate and shape uncertainty of 2% and 5% respectively.

Table 9: Expected rates of the backgrounds in the JUNO detector with corresponding rate and shape uncertainties according to [45].

Background source	Rate (day^{-1})	Rate unc. (%)	Shape unc. (%)
Accidentals	0.80	1	0
Fast neutrons	0.1	100	20
^{9}Li/^{8}He	0.8	20	10
^{13}C(α,n)^{16}O	0.05	50	50
Reactors ($L > 300\,\mathrm{km}$)	1.00	2	5
Geoneutrinos	1.2	30	5
Atmospheric neutrinos	0.16	50	50

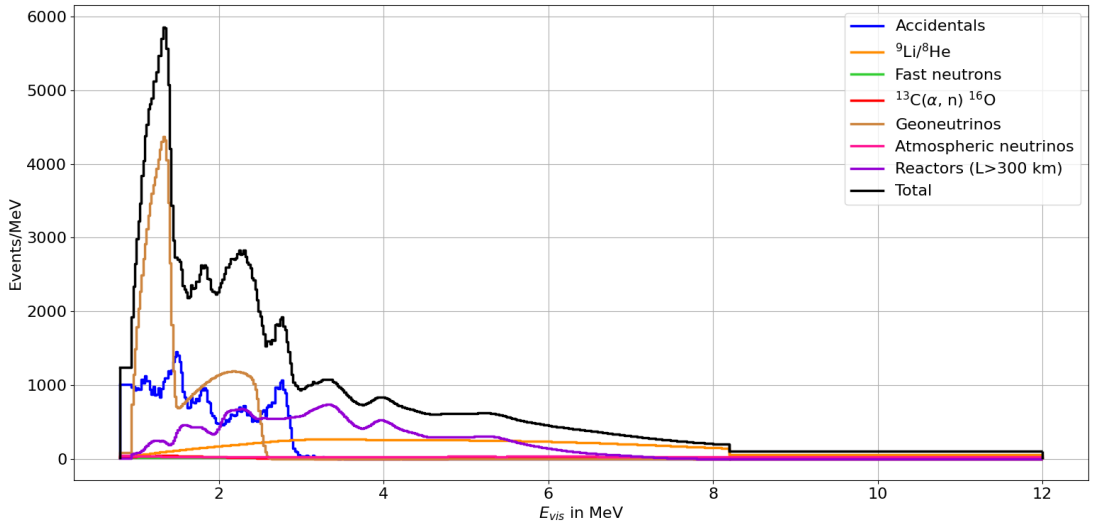

Figure 23: Expected backgrounds in JUNO for the nominal DAQ time of 6 years using the background rates listed in table 9 as well as the total background (black). The displayed spectra are binned as described in table 11 in chapter 5.2.5.

As described in chapter 1, there are also natural sources of neutrinos that need to be considered as background for the NMO measurement, mainly geoneutrinos and atmospheric neutrinos. For geoneutrinos, according to the potential of JUNO for their detection as described in [35] and [66], their background rate is estimated for this analysis to $1.2(1 \pm 30\%)$ per day with a shape uncertainty of 5%.
Atmospheric neutrinos can interact in the detector via NC or CC interaction. It was shown in [98] that the NC interaction on the ^{12}C in the LS can produce final-state particles like gammas and neutrons that can create a background signal. For JUNO, it is estimated to 0.16 per day with a 50% rate and 50% shape uncertainty.
A summary of all background rates along with their corresponding rate and shape uncertainty is listed in table 9. The expected background spectra in JUNO for the nominal DAQ time of 6 years is shown in figure 23.

Table 10: Estimated rates of the backgrounds in the TAO detector with corresponding rate and shape uncertainties according to [87].

Background source	Rate (day^{-1})	Rate unc. (%)	Shape unc. (%)
Accidentals	155	1	-
Fast neutrons	92	-	10
^{9}Li/^{8}He	54	20	10

For the TAO detector, accidentals form the largest background which is estimated according to the JUNO simulation to a rate of 155 per day with a 1% rate and negligible shape uncertainty. The second largest background in TAO is caused by fast neutrons which are simulated by the TAO detector simulation to have a rate of 92 per day with a 10% shape and negligible rate uncertainty. Since there will be a reactor-off time of one month every year, accidentals and fast neutrons will be precisely measured during the DAQ time of TAO. The third background source are the ^{9}Li/^{8}He-decays which are assumed to have a similar shape as in JUNO with a rate of 54 per day. It is assigned with a rate uncertainty of 20% and a shape uncertainty of 10%.
Further backgrounds considered in the JUNO spectrum are negligible due to the smaller detector size reducing their rates and the lower overburden increasing the rates of the three dominant background types. Additionally, the short distance to the nuclear reactor increases the antineutrino signal rate which also makes them negligible.
Table 10 gives an overview on the estimated backgrounds in the TAO detector. The estimated background spectra in the TAO detector for the nominal DAQ time of 6 years with a duty cycle of 11/12 are shown in figure 24.

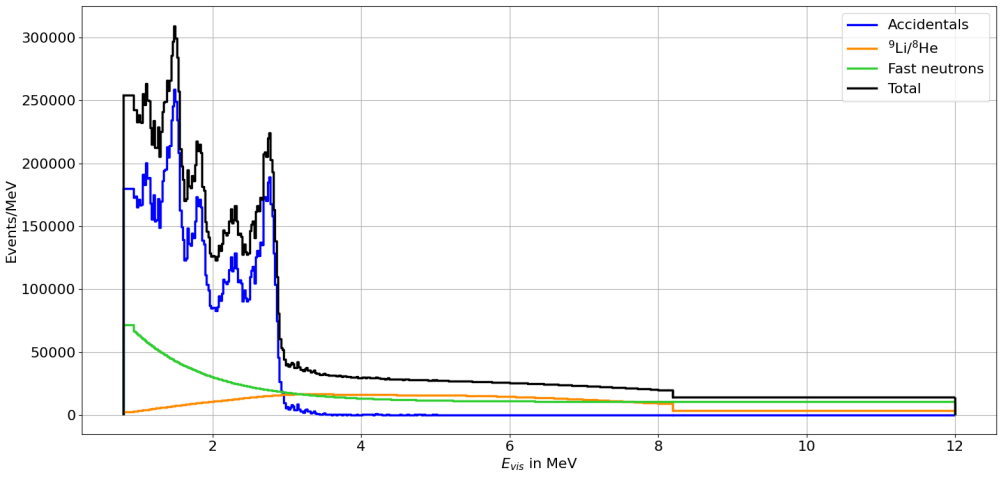

Figure 24: Expected backgrounds in the TAO detector for the nominal DAQ time of 6 years with a duty cycle of 11/12 using the background rates listed in table 10 as well as the total background (black). The displayed spectra are binned as described in table 11 in chapter 5.2.5.

Table 11: The final binning of the observed spectra for JUNO and TAO used for the NMO sensitivity analysis which provides a sufficient number of events in every bin. *Left Edge* refers to the left edge of the first bin with the given width and *Right Edge* to the right edge of the last bin with the given width.

Left Edge	Right Edge	Width	Number of Bins
0.8 MeV	0.94 MeV	140 keV	1
0.94 MeV	7.44 MeV	20 keV	325
7.44 MeV	7.8 MeV	40 keV	9
7.8 MeV	8.2 MeV	100 keV	4
8.2 MeV	12 MeV	3.8 MeV	1

5.2.5 Final spectrum

The final spectra of the JUNO and TAO detectors used for the analysis of the sensitivity to identify the NMO is then given by the sum of the final IBD spectra calculated in chapters 5.2.1 to 5.2.3 and the individual background spectra estimated in chapter 5.2.4.
To compute the final spectrum to be used for the NMO sensitivity analysis, it is rebinned taking into account the energy resolution and a sufficient number of events per bin. While the IBD spectra where the detector effects are applied are binned to constant energy segments with a width of 5 keV the final observed spectra are binned according to the definition given in table 11.
For the assumption of the Huber-Mueller model for the reactor antineutrino spectrum (see chapter 4.2) corrected for the rate and shape anomaly according to the Daya Bay measurement (see chapter 6.3.1), the estimated final spectrum for JUNO and TAO for a DAQ time of 6 years are shown in figures 25 and 26. The spectra are shown for a normal and inverted NMO to display the small variation in the spectrum depending on the actual NMO realized in nature which can be observed with JUNO. Due to the short distance of the TAO detector to the reactor, the difference between the measured spectra for both NMOs in the TAO detector are negligible. In both detectors the residual backgrounds significantly affect the measured spectra. Figure 27 shows the ratio of the expected JUNO spectra for the assumption of a true inverted ordering (IO) to a true NO in case of the IBD spectrum only and including the residual background contribution according the spectra displayed in figure 25. It is clearly visible that the residual backgrounds are well under control and their contribution reduces the difference in the spectra between the two NMO possibilities only to a small amount. Therefore, a large decrease of the NMO sensitivity can be avoided.

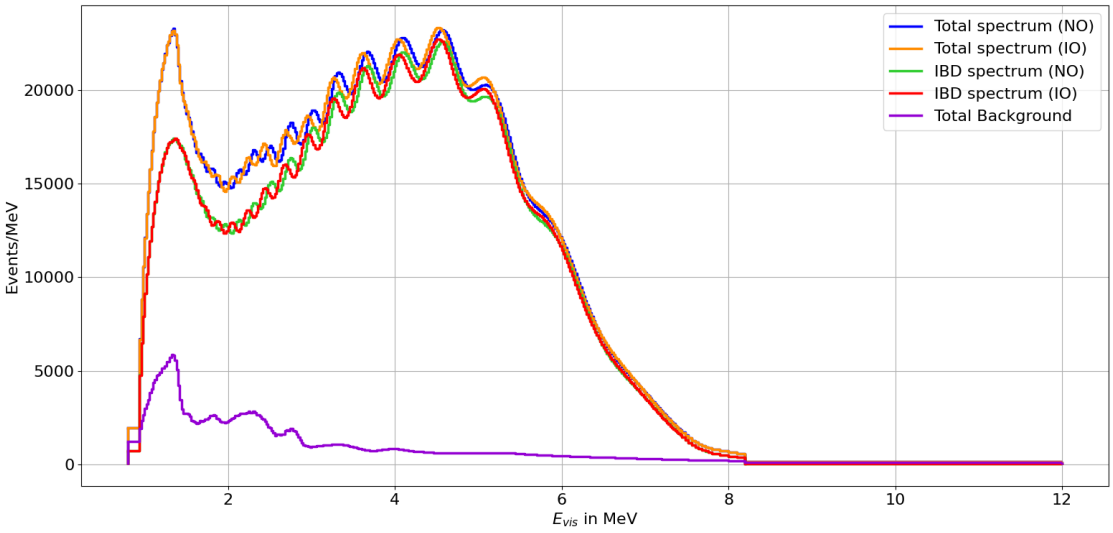

Figure 25: Total spectra with backgrounds expected in JUNO for 6 years of data taking using the Huber-Mueller model with Daya Bay rate and shape correction as reactor spectrum model for the assumption of normal (blue) and inverted (orange) mass ordering. As comparison the reactor IBD spectra without backgrounds for NO (green) and IO (red) are displayed. The contribution by the remaining backgrounds after applying the IBD selection cuts for the DAQ time of 6 years is also shown (violet).

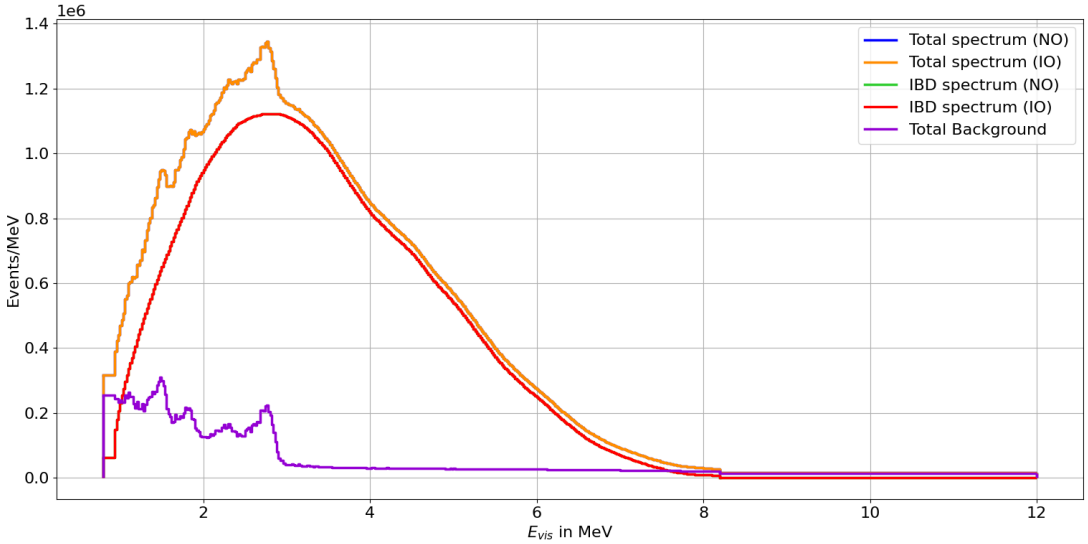

Figure 26: Total spectra with backgrounds expected in TAO for 6 years of data taking using the Huber-Mueller model with Daya Bay rate and shape correction as reactor spectrum model for the assumption of NO and IO (orange). As comparison the reactor IBD spectra without backgrounds for NO and IO are displayed (red). Due to the proximity to the reactor, the difference between the spectra for the two mass orderings is negligible. The contribution by the remaining backgrounds after applying the IBD selection cuts for the DAQ time of 6 years is also shown (violet).

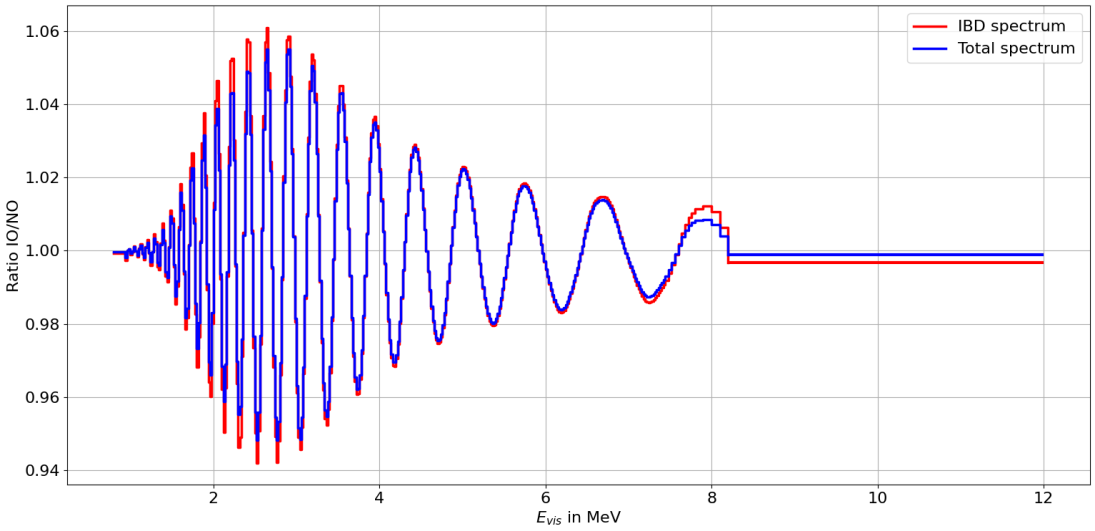

Figure 27: Ratio of the expected JUNO spectra for the assumption of a true IO to a true NO in case of the IBD spectrum only (red) and including the residual background contribution (blue) according the spectra displayed in figure 25 for a DAQ time of 6 years using the Huber-Mueller model with Daya Bay rate and shape correction.

6 Modeling the Fine Structure in the Reactor Spectrum for the NMO Sensitivity Estimation with GNA

Aye, and I saw Sisyphus in violent torment, seeking to raise a monstrous stone with both his hands.

– Homer - *The Odyssey*

To investigate the impact of the fine structure in the reactor neutrino spectrum on the NMO sensitivity with JUNO, two different approaches were used in this work concerning the introduction of the fine structure to the spectrum models. In this chapter both methods, the fluctuation model and the summation model, will be discussed.

6.1 Fluctuation Model

A simple approach to introduce a fine structure to the smooth Huber-Mueller spectrum model is adding random fluctuations to produce a rugged structure. Therefore, a new bundle was introduced to the GNA to add random fluctuations to the smooth Huber-Mueller input spectrum by

$$\left(\frac{\mathrm{d}N_i}{\mathrm{d}E_\nu}\right)_{\text{fine}} = \left(\frac{\mathrm{d}N_i}{\mathrm{d}E_\nu}\right)_{\text{HM}} \cdot SF(E_\nu) \quad , \tag{32}$$

where $\left(\frac{\mathrm{d}N_i}{\mathrm{d}E_\nu}\right)_{\text{fine}}$ is the antineutrino spectrum model for isotope i with fluctuations, $\left(\frac{\mathrm{d}N_i}{\mathrm{d}E_\nu}\right)_{\text{HM}}$ the Huber-Mueller spectrum model [78, 79], and $SF(E_\nu)$ is the scale factor which determines the amplitude of the fluctuation at energy E_ν which is defined in steps of 10 keV in order to be smaller than the final binwidth of the JUNO and TAO spectra for a proper application of the detector resolution.
In the following, it will be described in detail how the fluctuations are introduced to the spectrum.

6.1.1 Generation of random fluctuations

The scale factor $SF(E_\nu)$ in equation 32 is defined in two steps. First, the energies E_{fluc} where the fluctuations occur, are defined by an array with equidistant values from 1.8 MeV to 13 MeV. The size of the equidistant steps define the energy width of the fluctuations.

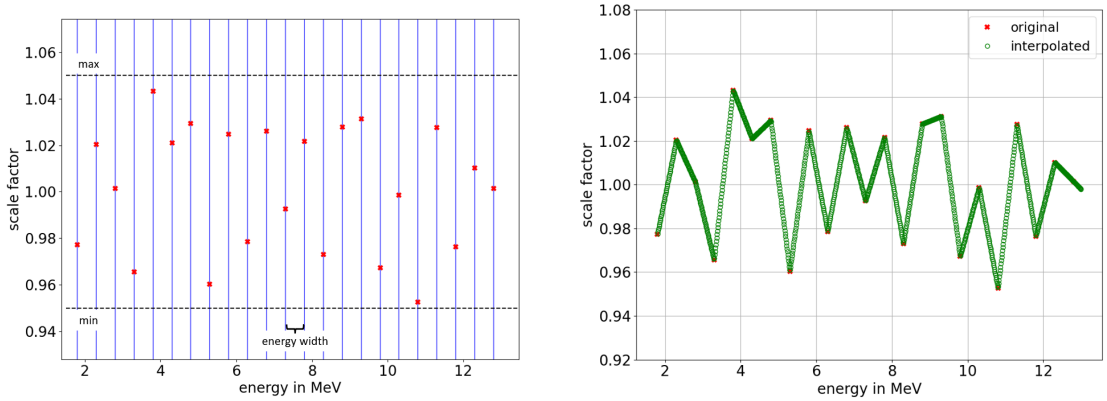

(a) Random generation of scale factor

(b) Interpolation of the scale factor

Figure 28: Exemplary representation of the application of fine structure-like fluctuations to the smooth spectrum based on the Huber-Mueller model. Figure 28a shows how a scale factor is sampled at defined energy values with a step size of 500 keV as uniform random value in an interval of $[1-5\%, 1+5\%]$ as described in chapter 6.1.1. Figure 28b illustrates the interpolation of the random scale factor to the input binwidth of the Huber-Mueller spectrum with the *reactor_finestructure_spectra* bundle described in chapter 6.1.2.

In principle, the generation is not limited to fixed energy widths but any definition of the energy array in the given energy range is possible. For a systematic analysis of the energy widths, however, this was not used in this work.
In a second step, for each defined energy value E_{fluc}, a scale factor is randomly chosen from a uniform distribution in the interval $[1-a, 1+a]$ with the fluctuation amplitude a which defines the maximum possible relative variation of the spectrum which can also be arbitrarily chosen. Figure 28a illustrates the definition of the random fluctuations.
Since the input data for the Huber-Mueller model are given with a binning of 10 keV, the arbitrarily defined fluctuations with energy width defined by E_{fluc} have to be interpolated to the input binning. Therefore, a new bundle was implemented in GNA which will be discussed in the following.

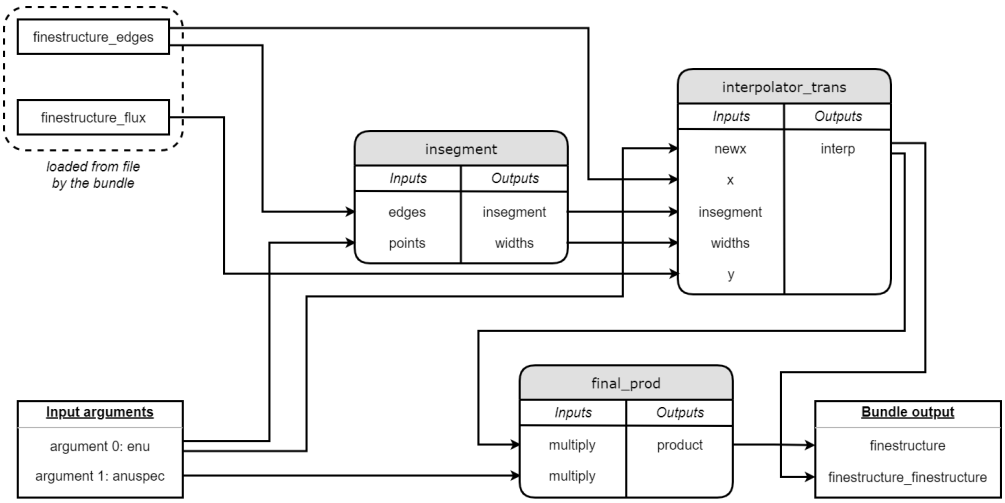

Figure 29: Flowchart representation of the fine structure bundle.

6.1.2 The 'reactor_finestructure_spectra' bundle

The randomly generated scale factors for the defined energies that are saved to files, can be loaded by the bundle for each of the four reactor isotopes. An overview of the bundle is shown in figure 29. Scale factor and energy are loaded to the inputs *finestructure_flux* and *finestructure_edges* respectively and afterwards interpolated to meet the internal binning *enu* of the smooth input spectrum. The interpolation is done by the *InterpLinear* transformation of GNA. It consists of a combination of the two transformations *insegment* and *interpolation_trans*. The *insegment* transformation determines the indices j of the edges e_j, so that $e_j \leq x_i < e_{j+1}$ where x_i are the points of the new binning. The outputs of this transformation are internally connected to the corresponding inputs of the *interpolation_trans* transformation. Additionally, the *finestructure_flux*, *finestructure_edges* and the input argument of the bundle which is connected to the edges of the neutrino energy binning are connected to the remaining inputs. The transformation then calculates the interpolated values of the scale factor as shown in figure 28b via a linear interpolation of the form

$$y_i = k \cdot (x_i - e_j) + y(e_j) \quad , \tag{33}$$

where k are weights defined by

$$k = \frac{y(e_{j+1}) - y(e_j)}{e_{j+1} - e_j} \quad . \tag{34}$$

The bundle allows for interpolation of both wider and narrower energy segments to the Huber-Mueller energy binning.
Finally, the value of the input spectrum *anuspec* is multiplied with the scale factor in every bin which gives the spectrum with fine structure. An exemplary spectrum of ^{235}U with fluctuations using an amplitude of 5% and an energy width of 50 keV compared to the smooth Huber-Mueller spectrum is shown in figure 30.

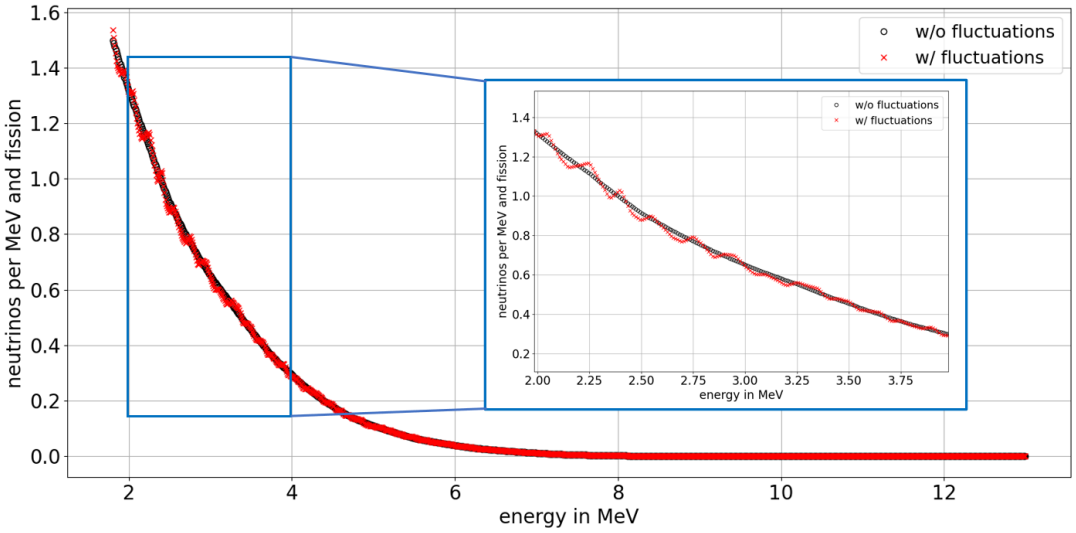

Figure 30: Exemplary spectrum of ^{235}U with fluctuations using an amplitude of 5% and an energy width of 50 keV compared to the smooth Huber-Mueller spectrum. The inlet displays a zoom into the interval from 2 to 4 MeV for better visibility of the applied fluctuations.

6.2 Summation Model

The calculation of the spectra is based on the oklo spectrum generator by Daniel Dwyer which is publicly available via GPL-3.0 license [99]. It performs the calculation of the antineutrino spectra of the individual reactor isotopes according to the ab-initio summation described in chapter 4.1.1 by

$$\frac{\mathrm{d}N_i}{\mathrm{d}E_\nu} = \sum_{A,Z,n} Y_n(Z,A) \sum_k b_{n,k}(E_0^k)\, P_{\bar{\nu}}(E_{\bar{\nu}}, E_0^k, Z) \quad . \tag{35}$$

The neutron induced fission product yields $Y_n(Z,A)$ are taken from the ENDF/B-VII.1 library [100] (which are the same as in the recent ENDF/B-VIII.0 library [101]) and branching ratios $b_{n,k}(E_0^k)$ as well as endpoint energies E_0^k are initially taken from the ENSDF-6 database, but updated for the spectrum generator as given in [99]. It has to be added that one major shortcoming of the nuclear databases is the fact that for some isotopes the fission yields and branching ratios are only given with large uncertainties or are not known at all.
As given in equation 20 in chapter 4.1.1, the spectrum shape is calculated by

$$P_{\bar{\nu}}(E_{\bar{\nu}}, E_0, Z) = K\, E_{\bar{\nu}}^2\, (E_0 - E_{\bar{\nu}}) \sqrt{(E_0 - E_{\bar{\nu}})^2 - m_\mathrm{e}^2} \\ F(E_\mathrm{e},Z)\, C(E_\mathrm{e},Z)\, [1 + \delta_\mathrm{rad} + \delta_\mathrm{FS} + \delta_\mathrm{WM}] \quad , \tag{36}$$

where the $E_\mathrm{e} = E_0 - E_{\bar{\nu}}$ and $p_\mathrm{e} = \sqrt{E_\mathrm{e}^2 - m_\mathrm{e}^2}$ was used. Additionally, the Fermi correction $F(E_\mathrm{e},Z)$, the shape factor $C(E_\mathrm{e},Z)$, radiative correction δ_rad, finite size correction δ_FS, and weak magnetism correction δ_WM to the spectrum shape are taken into account.

6.2.1 Corrections to the spectral shape

In the following, the corrections to the phase space term in the spectral shape according to various effects in beta decay are discussed in detail.

Fermi correction

The Fermi correction accounts for the Coulomb interaction of the outgoing electron with energy E_e and momentum p_e with the remaining nucleus of charge Z and is given by [78, 102]

$$F(E_\mathrm{e},Z) = 2(\gamma+1)(2p_\mathrm{e}R)^{2(\gamma-1)} \mathrm{e}^{\pi\alpha Z E_\mathrm{e}/p_\mathrm{e}} \frac{|\Gamma(\gamma + \mathrm{i}\alpha Z E_\mathrm{e}/p_\mathrm{e})|^2}{\Gamma(2\gamma+1)^2} \quad , \tag{37}$$

where $\gamma = \sqrt{1-(\alpha Z)^2}$, R describes the nuclear radius, and α is the Sommerfeld constant.

Shape factor

The shape factor is a correction of the spectral shape due to the type of beta decay transition. If the spin vectors of the emitted electron and antineutrino are anti-parallel ($S = 0$), the beta decay is called *Fermi transition* while it is called *Gamow-Teller transition* if these are aligned parallel ($S = 1$). If the angular momentum of the electron-antineutrino system in the center-of-mass frame is $L = 0$, the decay is called "allowed" (Gamow-Teller) or "super-allowed" (Fermi) and the spectral shape remains unchanged resulting in a shape factor of $C(E_e,Z) = 1$. However, around 30% of all beta decays in nuclear reactors are

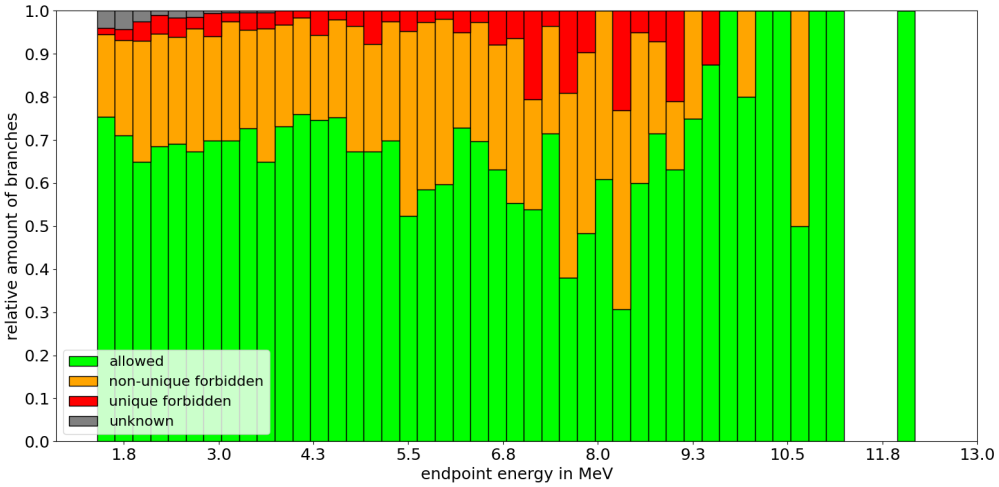

Figure 31: Relative amount of allowed (green), non-unique forbidden (orange), unique forbidden (red) decays and those where the type is unknown (gray) contributing to the reactor antineutrino spectrum as a function of the endpoint energies of the respective decays. The data are taken from the ENSDF-6 database as given in [99].

transitions with $L > 0$ which are suppressed and therefore called "forbidden" where the value of L defines the degree of forbiddenness [71]. In these decays, the initial and final state of the nucleus can also be of opposite parity ($\Delta\pi = \pi_i\pi_f = -1$) leading to parity violation in beta decay. The total angular momentum is given by $\vec{I} = \vec{L}+\vec{S}$ which leads to a third discrimination of beta decay types. If the change in total nuclear angular momentum $\Delta I = I_f - I_i$ between the initial and final state of the nucleus is $\Delta I = L+1$ the transition is called unique while in the cases $\Delta I = L-1$ and $\Delta I = L$ they are called non-unique. The relative amount of the different types of transitions contributing to the reactor antineutrino spectrum is shown in figure 31 as a function of the endpoint energies.
Depending on the type of forbidden transition, the spectral shape differs from the shape of allowed decays which can be theoretically calculated. The change of the spectral shape compared to the shape of the allowed decays is considered by a shape factor $C(E_e,Z) \neq 1$. The expressions for the shape factor that were used in the oklo generator are shown in table 12 and were taken from [103].

Table 12: Expressions for shape factors $C(E_e,Z)$ used for the calculation of antineutrino spectra for different beta decay transition types according to [103]. Here, $T_{\bar{\nu}}$ is the kinetic energy of the antineutrino, $E_e = T_e + m_e$ is the total energy of the electron where T_e is the kinetic energy of the electron. p_e describes the momentum of the electron given by $p_e = \sqrt{E_e^2 - m_e^2}$ and $\beta = p_e/E_e$.

Type	ΔI^π	$C(E_e,Z)$
Non-unique 1st-order forbidden Gamow-Teller	0^-	$p_e^2 + T_{\bar{\nu}}^2 + 2\beta^2 T_{\bar{\nu}} E_e$
Non-unique 1st-order forbidden Gamow-Teller	1^-	$p_e^2 + T_{\bar{\nu}}^2 - \frac{4}{3}\beta^2 T_{\bar{\nu}} E_e$
Unique 1st-order forbidden Gamow-Teller	2^-	$p_e^2 + T_{\bar{\nu}}^2$
Non-unique 1st-order forbidden Fermi	1^-	$p_e^2 + T_{\bar{\nu}}^2 + \frac{2}{3}\beta^2 T_{\bar{\nu}} E_e$

Radiative correction

This correction accounts for the QED effects of first order in α which impact the spectral shape. Independent of the type of transition it is given by [104]

$$\delta_{\text{rad}} = \frac{\alpha}{2\pi}\left[3\ln\left(\frac{m_p}{2(T_{\text{max}}+m_e)}\right)+\frac{23}{4}-\frac{4\pi^2}{3}-3\ln\left(1-\frac{T_{\bar{\nu}}}{T_{\text{max}}+m_e}\right)\right] \quad , \tag{38}$$

where m_p is the mass of the proton.

Finite size correction

The Fermi correction (see 6.2.1) holds for point-like nuclei, however, in reality, the nuclei have a finite size. This correction accounts for the change in spectral shape due to the finite size of the nucleus. It is given by [103]

$$\delta_{\text{FS}} = -\frac{54}{35}\frac{\alpha Z}{\hbar c}R\left[E_e-\frac{T_{\bar{\nu}}}{27}+\frac{m_e^2c^4}{3E_e}\right] \quad , \tag{39}$$

where the radius of the nucleus is approximated with $R = 1.2\cdot A^{\frac{1}{3}}$ fm.

Weak magnetism correction

This correction accounts for the interaction of the emitted electron with the magnetic moment of the nucleus. It is calculated from the interference of the spin distribution of the axial current with the distribution of the magnetic moment of the vector current $\vec{\nabla}\times\vec{\mu}$ [71]. Table 13 shows the expressions used in the calculation of the spectra depending on the type of transition. In case of allowed and non-unique 1st-order forbidden Fermi transitions, the weak magnetism correction is vanishing [103].

Table 13: Expressions for the weak magnetism correction δ_{WM} used for the calculation of the antineutrino spectra for the different beta decay transition types according to [103]. Again, $T_{\bar{\nu}}$ is the kinetic energy of the antineutrino, $E_e = T_e + m_e$ is the total energy of the electron where $T_e = T_{\text{max}} - T_{\bar{\nu}}$ with the endpoint energy of the neutrino T_{max}. p_e describes the momentum of the electron given by $p_e = \sqrt{E_e^2 - m_e^2}$ and $\beta = p_e/E_e$. Furthermore, m_N is the nucleon mass, $\mu_v = 4.7$ is the nucleon isovector magnetic moment, and $g_A = 1.2759$ is the axial vector coupling constant.

Type	ΔJ^π	δ_{WM}
Allowed Gamow-Teller	1^+	$\frac{2}{3}\frac{\mu_v-1/2}{m_N g_A}\left(E_e\beta^2 - T_{\bar{\nu}}\right)$
Non-unique 1st-order forbidden Gamow-Teller	0^-	0
Non-unique 1st-order forbidden Gamow-Teller	1^-	$\frac{\mu_v-1/2}{m_N g_A}\left[\frac{\left(p_e^2+T_{\bar{\nu}}^2\right)\left(E_e\beta^2-T_{\bar{\nu}}\right)+\frac{2}{3}\beta^2E_eT_{\bar{\nu}}(T_{\bar{\nu}}-E_e)}{p_e^2+T_{\bar{\nu}}^2-\frac{4}{3}\beta^2T_{\bar{\nu}}E_e}\right]$
Unique 1st-order forbidden Gamow-Teller	2^-	$\frac{3}{5}\frac{\mu_v-1/2}{m_N g_A}\left[\frac{\left(p_e^2+T_{\bar{\nu}}^2\right)\left(E_e\beta^2-T_{\bar{\nu}}\right)+\frac{2}{3}\beta^2E_eT_{\bar{\nu}}(T_{\bar{\nu}}-E_e)}{p_e^2+T_{\bar{\nu}}^2}\right]$

6.2.2 Uncertainties in the spectrum

The total uncertainty of the cumulative reactor antineutrino spectrum is build up by the contribution of the individual uncertainties of fission yields, branching ratios, and endpoint energies from the nuclear databases as well as of the corrections applied to the spectrum shape which are rough estimates listed in table 14.
In this work, the oklo spectrum generator [99] was modified to take these uncertainties into account in the process of spectrum generation. Therefore, each nuclear parameter (fission yields, branching ratios, endpoint energies) in the calculation was randomly sampled from a Gaussian distribution with mean and standard deviation according to the nuclear databases. Additionally, the energy dependent corrections were randomly sampled in the same way using the constant relative uncertainty from table 14. With this modification, a variety of random sets of nuclear parameters and corrections according to the nuclear databases can be generated.

Table 14: Uncertainties assigned to the corrections to the spectral shape for the different transition types as proposed in [71]. The relative uncertainty is treated as constant over the whole energy range.

Correction	Transition Type	ΔJ^π	uncertainty
$C(E_e,Z)$	Allowed	1^+	0
$C(E_e,Z)$	Forbidden	2^-	0
$C(E_e,Z)$	Forbidden	$0^-, 1^-$	30 %
δ_{FS}	Allowed	1^+	50 %
δ_{FS}	Forbidden	$0^-, 1^-, 2^-$	100 %
δ_{WM}	Allowed	1^+	20 %
δ_{WM}	Forbidden	0^-	0
δ_{WM}	Forbidden	1^-	25 %
δ_{WM}	Forbidden	2^-	20 %

6.2.3 The cumulative summation spectrum

The previously described modification to randomly sample the nuclear parameters and corrections allows to generate a set of spectra $\frac{\mathrm{d}N_i}{\mathrm{d}E_\nu}$ for all four reactor isotopes i (^{235}U, ^{238}U, ^{239}Pu, ^{241}Pu) for Monte Carlo analysis of the fine structure in the spectrum which differs for each dataset.
For the analyses in this work, a set of 1000 summation spectra was generated which are shown in figure 32. Figure 33 displays the average spectra with their corresponding standard deviation calculated from the set of 1000 randomly generated spectra.
For a better visualization of the variation of each individually generated spectrum, figure 34 displays the relative difference of each of the 1000 generated spectra to the corresponding average spectrum. For all four reactor isotopes, the relative difference at the IBD threshold energy of 1.8 MeV is below 10 % and starts to increase for energies larger than $5-6$ MeV. It also shows that the fine structure differs for each spectrum providing a set of possible realizations of this not yet experimentally observed effect. However, it also shows a variation in rate as displayed in figure 35 which has to be corrected to be in agreement with actual measurements as a significant part of the spectra has smaller or larger rate as measured in the Daya Bay experiment. This will be discussed in the following.

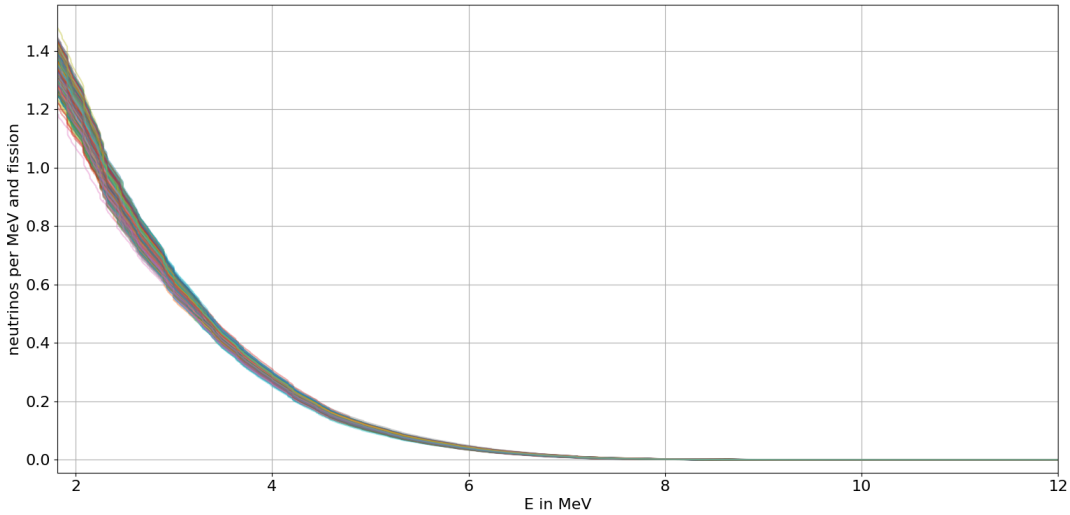

(a) 1000 summation spectra for U-235

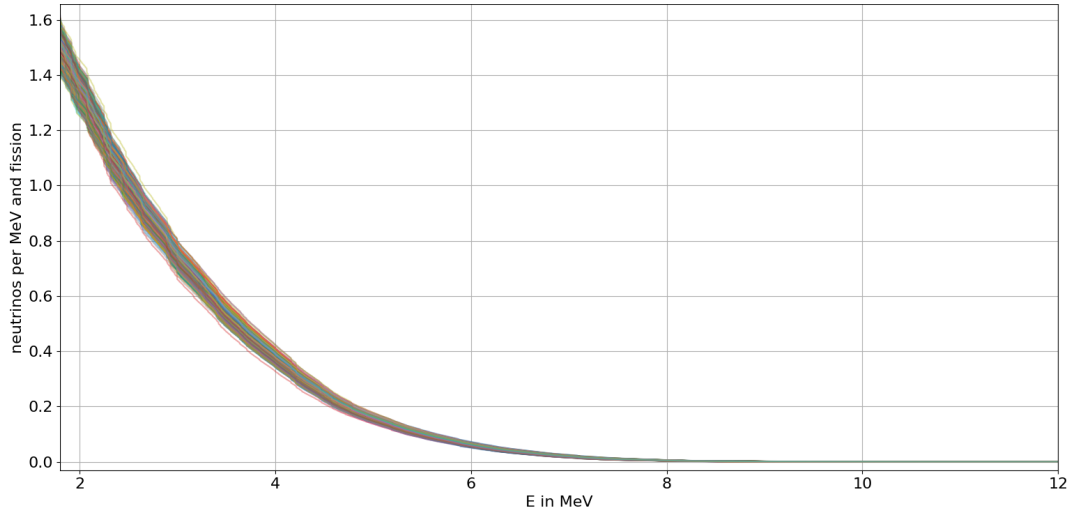

(b) 1000 summation spectra for U-238

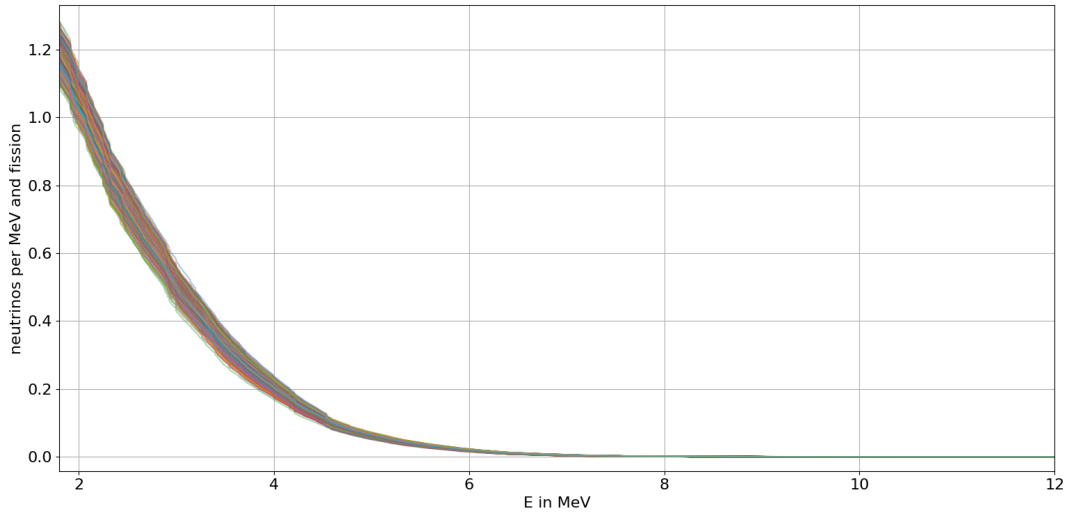

(c) 1000 summation spectra for Pu-239

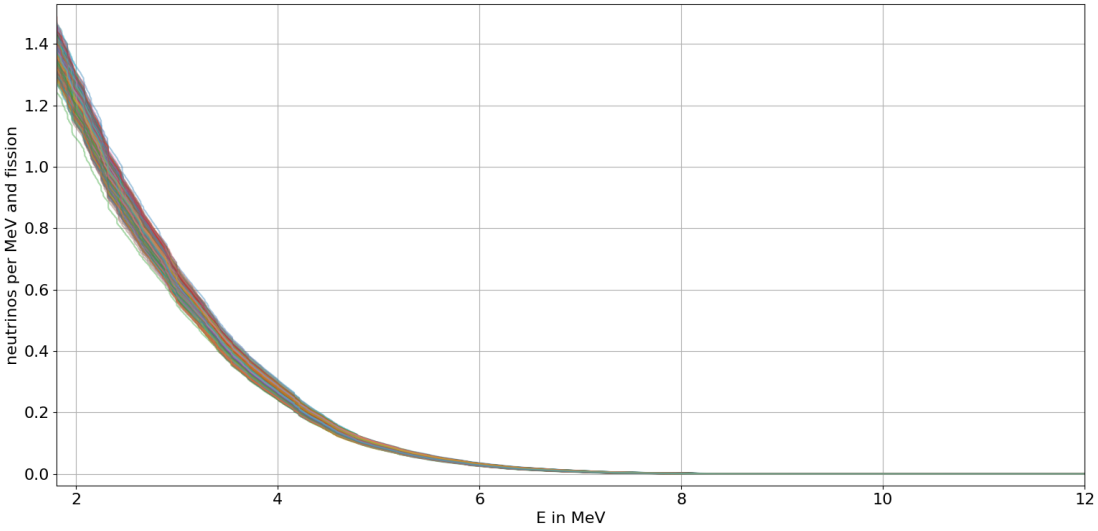

(d) 1000 summation spectra for Pu-241

Figure 32: A set of 1000 generated summation spectra for each isotope with the modified oklo spectrum generator generated by randomly fluctuate the spectra according to the uncertainties of the nuclear parameters and correction uncertainties.

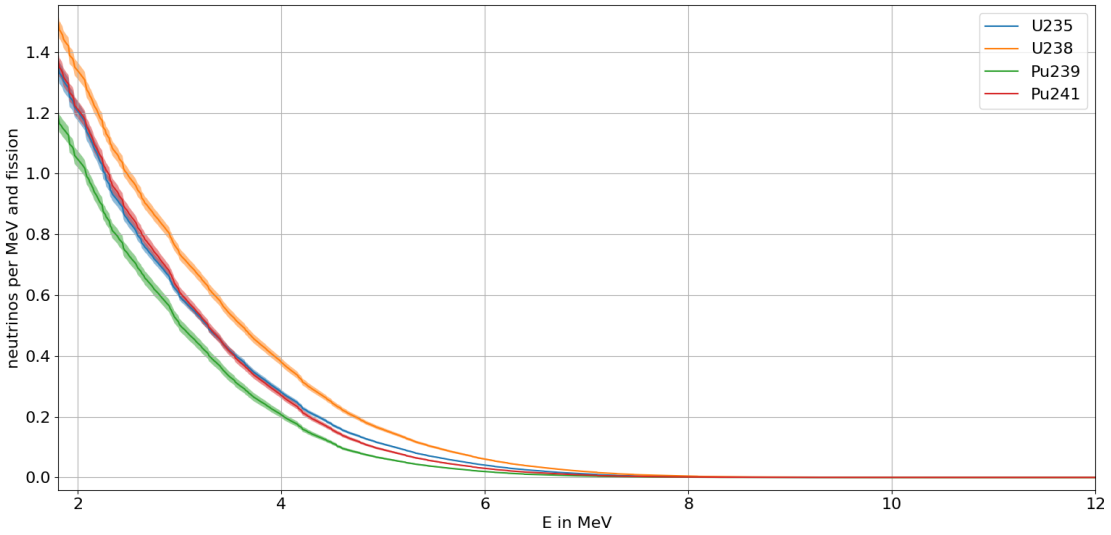

Figure 33: Average spectra for the four reactor isotopes calculated from the 1000 randomly generated spectra. The shaded band represents the interval of one standard deviation.

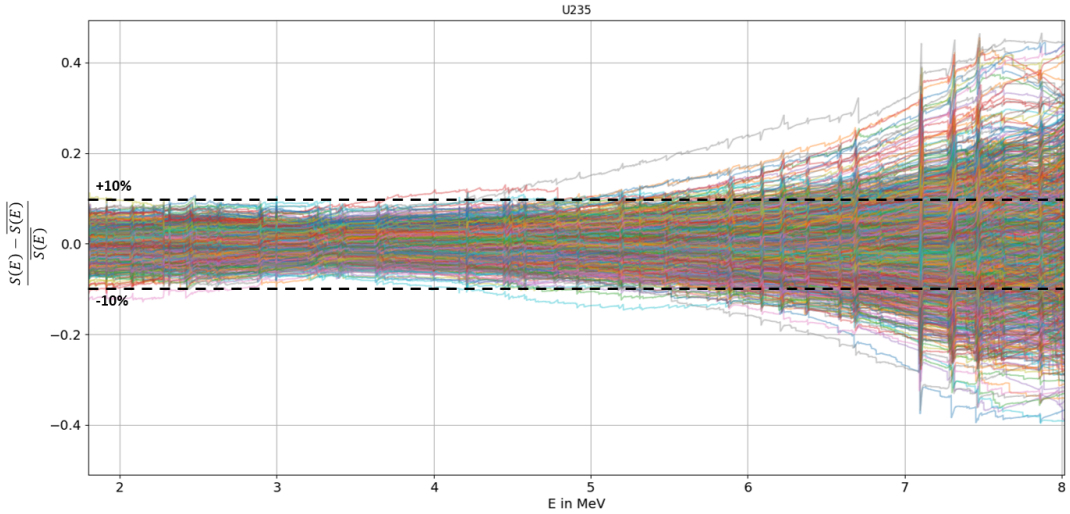

(a) U-235

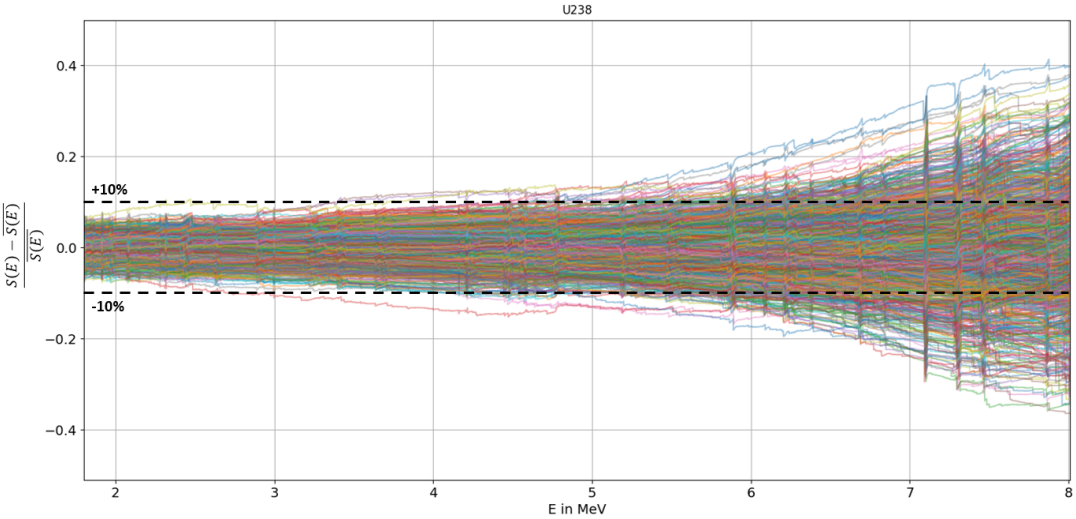

(b) U-238

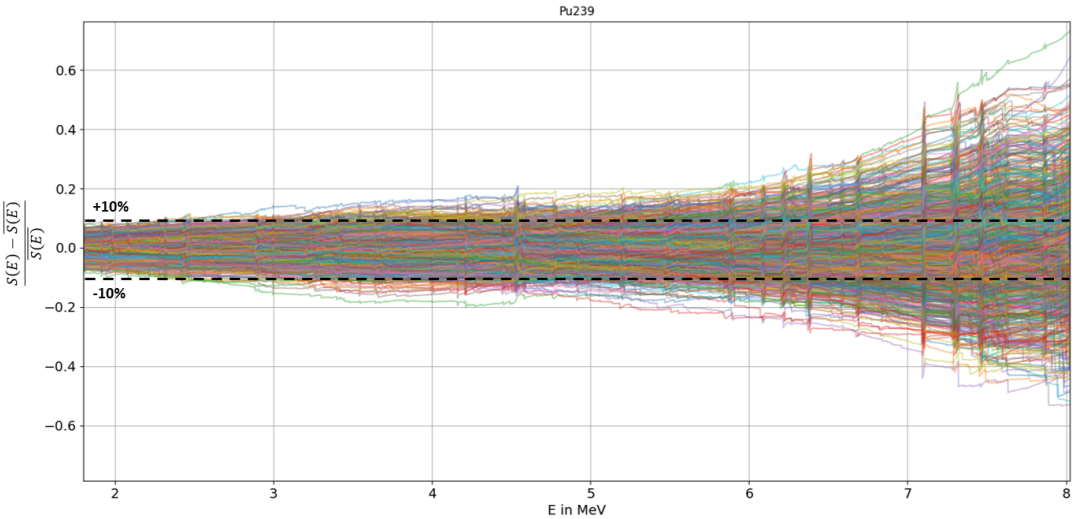

(c) Pu-239

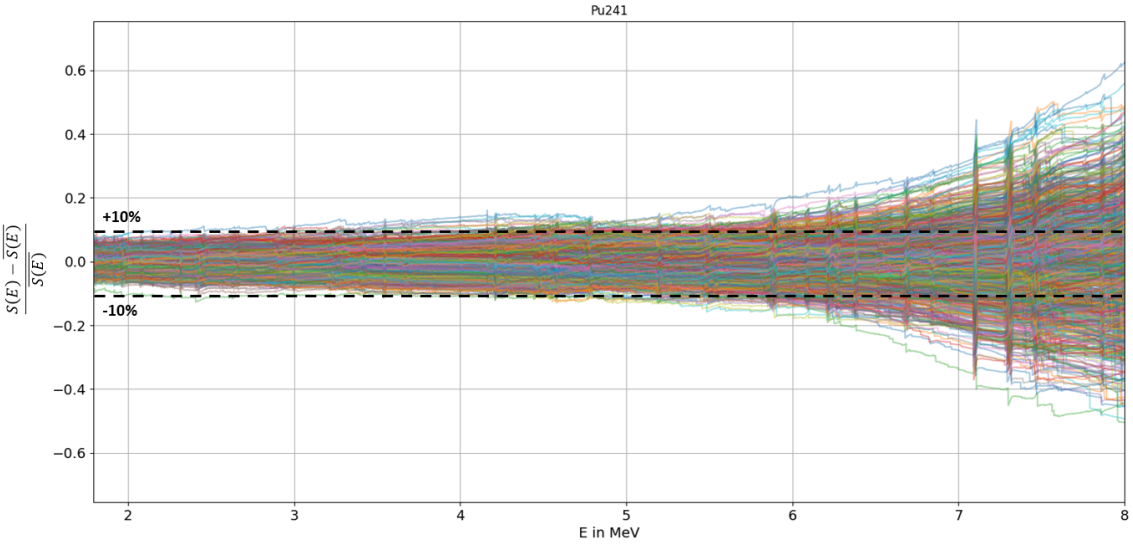

(d) Pu-241

Figure 34: Relative difference of the 1000 individually generated spectra $S(E)$ to the average spectrum $\overline{S(E)}$ for each of the four reactor isotopes. The $S(E)$ refers to the cumulative spectrum $\frac{\mathrm{d}N_i}{\mathrm{d}E}$ for the isotope i. The dashed lines represent the $\pm 10\%$ relative difference.

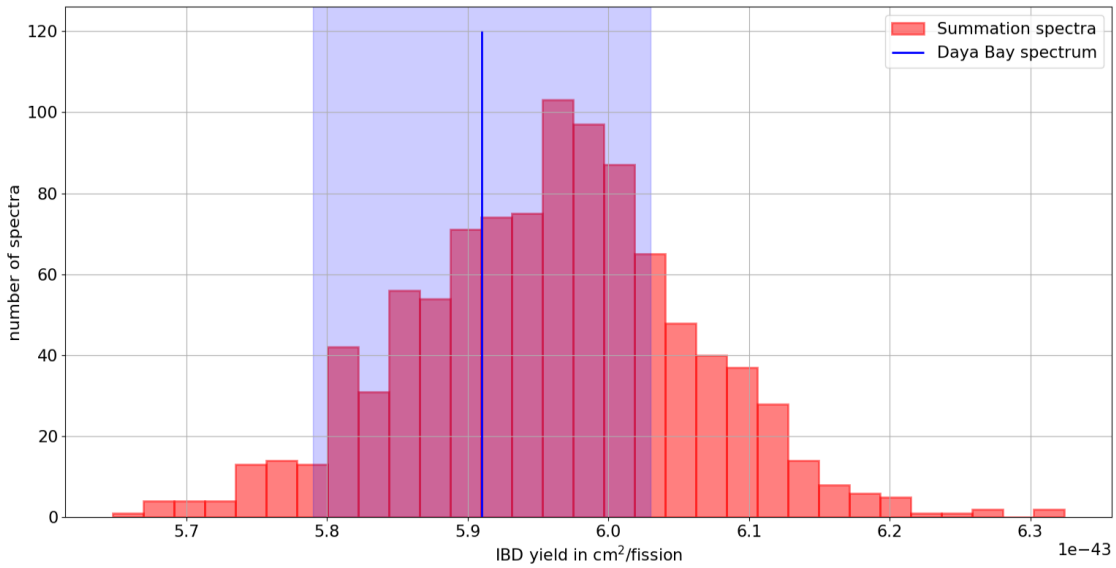

Figure 35: IBD yield for the different summation spectra with fine structure (red) compared to the Daya Bay result [80] (blue). The blue shaded area displays the uncertainty interval from the Daya Bay measurement. The IBD yield is calculated as product of the total spectrum using Daya Bay fission fractions from [80] and IBD cross section which is integrated for energies larger than 1.8 MeV.

6.3 Correction of the spectrum models

As discussed in chapter 4.2, the model predictions of the reactor neutrino spectrum show an excess in the rate of emitted antineutrinos compared to the measurements by DayaBay [80], Double Chooz [81], and RENO [82]. As this discrepancy between model prediction and real measurement is well known, however still not fully explained, the differences of the models to the actual data can be taken into account to avoid any impact on the NMO sensitivity by those known effects. Therefore, the spectrum models generated in chapter 6.1 and 6.2 are corrected for the differences in rate and bump compared to the measurement by the Daya Bay experiment. Since the Daya Bay spectrum [80] is given in energy bins of 250 keV which are too coarse to analyze any fine structure effects, the finer binned models have to be used with the rate and bump constraint to the Daya Bay data.
Figure 36 displays the Huber-Mueller model that is used as base to apply the fluctuations as described in chapter 6.1 as well as the average spectrum of the summation approach (see chapter 6.2) compared to the actual Daya Bay data [80] which also shows the anomaly and bump discussed in chapter 4.2.

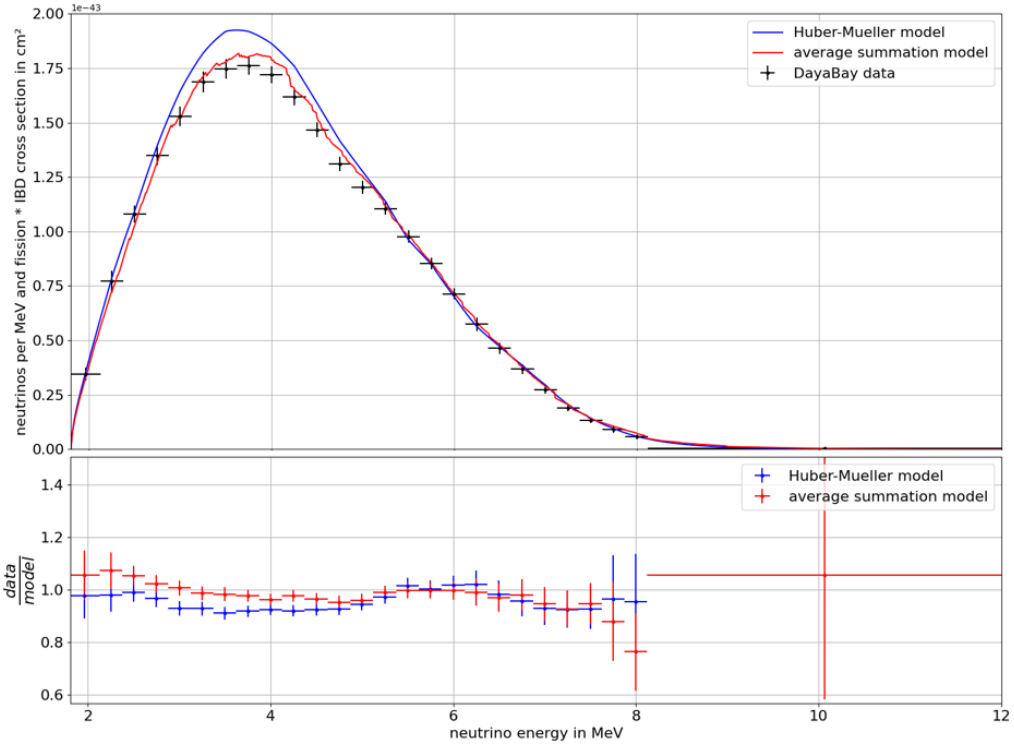

Figure 36: Predicted spectrum of the Huber-Mueller model used as base for the fluctuation method and average of the summation model compared to the Daya Bay measurement (data from [80]). The upper panel shows the total spectrum multiplied with the IBD cross section where the y-axis is given in multiples of 10^{-43}. The lower panel shows the ratio of the Daya Bay data to the model. For the calculation of the total spectra of both models the average fission fractions from Daya Bay (U-235: 0.586; U-238: 0.076; Pu-239: 0.288; Pu-241: 0.050 [80]) were used. The overall deficit in rate and the excess of events in the 6 MeV region is visible.

6.3.1 Correction of the Huber-Mueller spectrum

To correct the Huber-Mueller spectrum model for the differences in rate and shape to be consistent with the spectrum measured by the Daya Bay experiment, a simple correction function can be calculated and applied to the spectrum. Therefore, the cumulative Huber-Mueller model spectra $\frac{\mathrm{d}N_i}{\mathrm{d}E}$ are weighted by the Daya Bay fission fractions f_i and multiplied with the IBD cross section $\sigma(E)$ [90]

$$S_{\text{weighted}}(E) = \left(\sum_i f_i \cdot \frac{\mathrm{d}N_i}{\mathrm{d}E}\right) \cdot \sigma(E) \quad . \tag{40}$$

This weighted spectrum is then rebinned to the coarse binning of the Daya Bay spectrum. For each coarse bin k a correction factor is calculated as

$$n^k_{\text{corr}} = \frac{S^k_{\text{DYB}}}{S^k_{\text{weighted, rebinned}}} \quad . \tag{41}$$

Each individual cumulative spectrum $\frac{\mathrm{d}N_i}{\mathrm{d}E}$ is then multiplied with the correction factor in each small bin m via

$$\left(\frac{\mathrm{d}N_i}{\mathrm{d}E}\right)^m_{\text{corr}} = n^k_{\text{corr}} \cdot \left(\frac{\mathrm{d}N_i}{\mathrm{d}E}\right)^m \tag{42}$$

for each small bin m that is located within the coarse bin k. This method does not provide an individual correction for the spectra of each isotope, but the total weighted spectrum is in agreement with the Daya Bay data.
In the lower panel of figure 37, the correction function is displayed and the upper plot shows the comparison of uncorrected and corrected spectrum compared to the Daya Bay data. It is demonstrates that the corrected Huber-Mueller model is fully in agreement with the mean of the measured spectrum.

6.3.2 Correction of the summation spectra

As the summation spectra are generated with random variations of the nuclear parameters, each generated spectrum has individual differences from the Daya Bay data and has therefore to be corrected individually as described in chapter 6.3.1. However, as the correction for rate and shape is calculated for the coarser binning of the Daya Bay data, the individual fine structure is still present after correction. Figure 38 shows the 1000 generated summation spectra before and after correction compared to the Daya Bay data. The inlet in figure 38b shows a zoom into the $3-4\,\mathrm{MeV}$ range to display the variations of the corrected spectra in more detail.

As a result from this chapter, two methods were implemented to generate reactor antineutrino spectra that are compatible in rate and shape with the Daya Bay data but have a finer binning and include a non-smooth fine structure that is either randomly generated or based on nuclear database information on beta decays. With these features, the generated spectra are useful for the analysis of the implications of the not yet experimentally observed fine structure on JUNO's NMO sensitivity which will be the main topic of the remainder of this thesis.

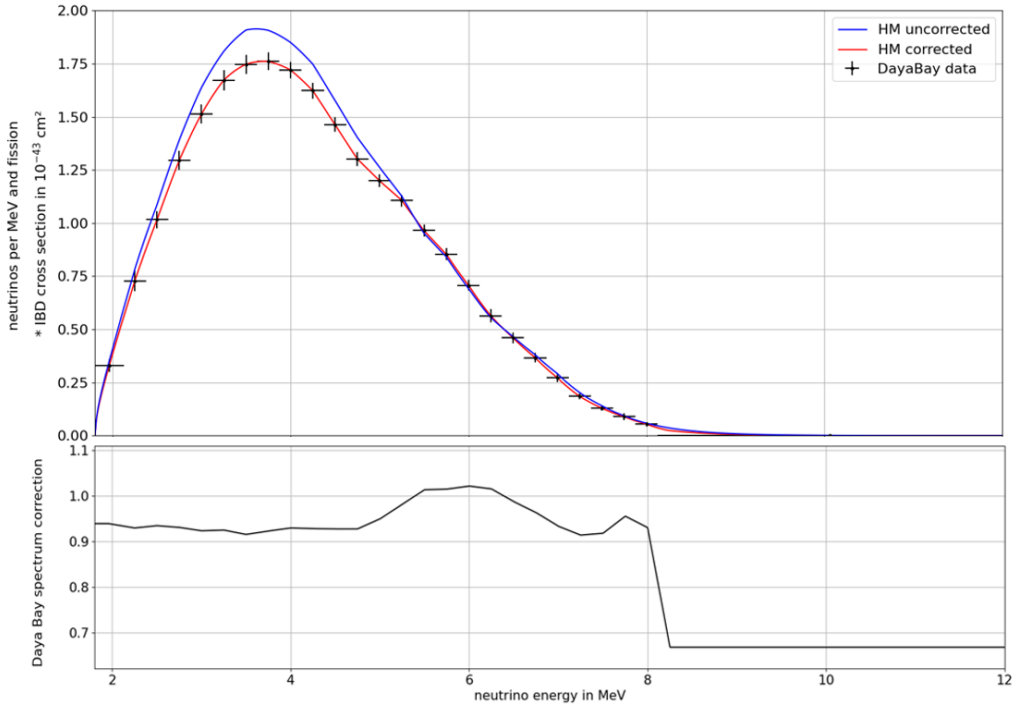

Figure 37: Weighted cumulative spectrum calculated with the original Huber-Mueller spectrum model (blue), with the modified model with the rate and shape correction according to the Daya Bay data applied (red) and the Daya Bay data (black) multiplied with the IBD cross section. The lower panel shows the correction function which represents the ratio of corrected to uncorrected spectrum model.

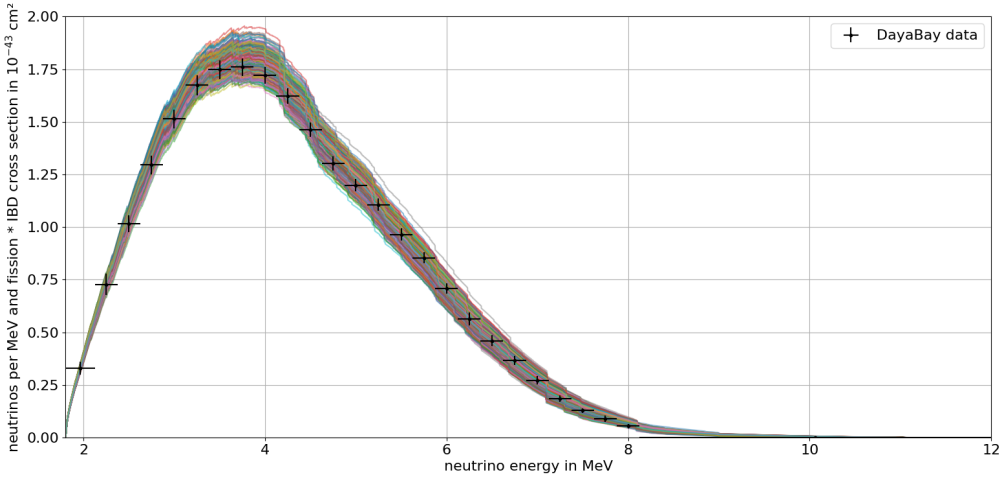

(a) Uncorrected summation spectra

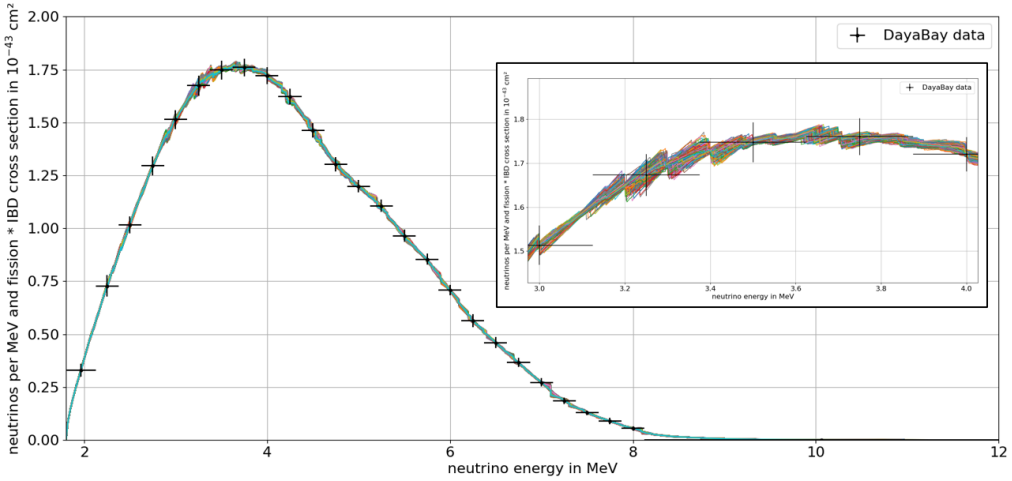

(b) Corrected summation spectra

Figure 38: Total reactor antineutrino spectra measured with Daya Bay [80] compared to 1000 generated summation spectra. Figure 38a displays the originally generated spectra, while figure 38b shows the generated spectra after the rate and shape correction according to the Daya Bay data was applied. The inlet displays the energy interval from 3 to 4 MeV for a more detailed visualization of the variation of fine structure which is still present after the correction.

7 JUNO's Sensitivity to the Neutrino Mass Ordering

Is it easy? No. Do I like it? No, I don't. But do I do it? Yeah, I do!

– Michael Scott - *The Office*

With the prediction of the spectra measured in JUNO, the sensitivity to distinguish between both NMOs can be determined. This sensitivity is based on a fit of the estimated spectrum model to an Asimov dataset [105]. The test statistic is defined by [106]

$$\Delta\chi^2 \;=\; \min \chi^2_{\text{False NMO}} - \min \chi^2_{\text{True NMO}} \quad . \tag{43}$$

The test statistic itself is based on the Pearson's χ^2 function with

$$\chi^2 \;=\; [\boldsymbol{x} - \boldsymbol{\mu}(\boldsymbol{\theta},\boldsymbol{\eta})]^T \; V^{-1} \; [\boldsymbol{x} - \boldsymbol{\mu}(\boldsymbol{\theta},\boldsymbol{\eta})] \quad , \tag{44}$$

where $\mu_i(\boldsymbol{\theta},\boldsymbol{\eta})$ is the expected number of events in each bin i which depends on free parameters $\boldsymbol{\theta}$ and nuisance parameters $\boldsymbol{\eta}$ (see table 15). x_i is the observed number of events in bin i from the Asimov dataset, and V is the covariance matrix.
Systematic uncertainties of the nuisance parameters η are included via Gaussian penalty terms

$$\chi^2_{\text{penalty}} \;=\; \frac{(\eta - \eta^0)^2}{\sigma_\eta^2} \tag{45}$$

with mean η^0 and uncertainty σ_η for all uncorrelated parameters. In case of the correlated fission fractions, the penalty term has the matrix form

$$\chi^2_{\text{penalty}} \;=\; \left(\boldsymbol{\eta} - \boldsymbol{\eta^0}\right)^T \; V_\eta^{-1} \; \left(\boldsymbol{\eta} - \boldsymbol{\eta^0}\right) \quad , \tag{46}$$

where $\boldsymbol{\eta}$ is a vector of the four fission fractions and V_η is the covariance matrix computed from the systematic uncertainty of the fission fractions and the correlation matrix for the fission fractions [33]

$$C_{\text{ff}} \;=\; \begin{pmatrix} 1.0 & -0.22 & -0.53 & -0.18 \\ -0.22 & 1.0 & 0.18 & 0.26 \\ -0.53 & 0.18 & 1.0 & 0.49 \\ -0.18 & 0.26 & 0.49 & 1.0 \end{pmatrix} \quad . \tag{47}$$

Table 15: Overview of all parameters of the JUNO model used in the fit to estimate the NMO sensitivity. All parameters were introduced in detail in chapter 5.2. Except the three free oscillation parameters Δm^2_{21}, Δm^2_{31}, and $\sin^2 2\theta_{12}$, all parameters are constrained.

Parameter Group		Number	Comment
Oscillation	Free oscillation parameters	3	Δm^2_{21}, Δm^2_{31}, $\sin^2 2\theta_{12}$
	$\sin^2 2\theta_{13}$	1	constrained
	ρ	1	matter effect
Reactor	Total power normalization	1	Rate at detector location
	Individual reactor power	9	6× Yangjiang, 2× Taishan, Daya Bay
	Fission fractions	36	4 isotopes per reactor
	Corrections	2	SNF and off-equilibrium
	Energy per fission	4	^{235}U, ^{238}U, ^{239}Pu, ^{241}Pu
Detector	Normalization	1	Detection efficiency, target protons, etc.
	LSNL	4	for each pull curve
	Energy resolution	3	a, b, c
Backgrounds	Background rates	7	accidentals, fast neutrons, ^{9}Li/^{8}He, ^{13}C(α,n)^{16}O, reactors ($L > 300\,$km), geoneutrinos, atmospheric neutrinos
Total		72	

Additionally, the bin-to-bin uncertainties from the residual backgrounds described in chapter 5.2.4 are included into the covariance matrix V in equation 44 by

$$V = V_{\text{stat}} + V_{\text{bkg b2b}} \quad , \tag{48}$$

where V_{stat} contains the statistical uncertainties and $V_{\text{bkg b2b}}$ contains the bin-to-bin uncertainties of the background spectra. A complete overview on the parameters used in the fit (which are defined in the spectrum model described in chapter 5.2) is given in table 15. In addition, the bin-to-bin uncertainties from the TAO spectrum relative to the expected IBD spectrum in JUNO are added to the covariance matrix to provide a comparable result to the approach of a combined JUNO+TAO analysis as presented in chapter 8. Therefore, the final covariance matrix is given as

$$V = V_{\text{stat}} + V_{\text{bkg b2b}} + V_{\text{TAO b2b}} \quad . \tag{49}$$

The total bin-to-bin uncertainty as well as its individual contributions included in this covariance matrix are shown in figure 39.
The total statistics function

$$\chi^2 = \chi^2_{\text{stat}} + \sum_{\eta} \chi^2_{\text{penalty}}(\eta) \tag{50}$$

is then minimized for the assumption of both NMOs to determine the median NMO sensitivity.

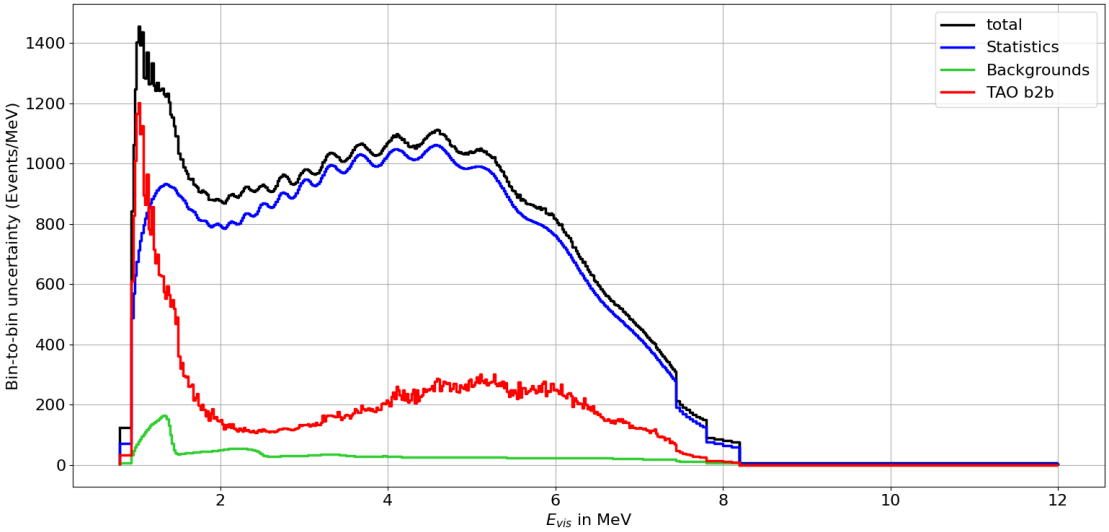

Figure 39: Total bin-to-bin uncertainty (diagonal of the covariance matrix) for the JUNO spectrum model (black) as well as its individual contributions from statistics (blue), residual backgrounds (green) and the additional bin-to-bin uncertainty of TAO (red) which is added relative to the JUNO spectrum to make the JUNO sensitivity comparable to the sensitivity of a combined analysis which is discussed in chapter 8.

In this work, the median sensitivities will be given in terms of the $\Delta\chi^2$ values which, however, can be translated to $n\sigma$ with the approximated relation in equation 69 derived in appendix B.

7.1 NMO sensitivity in case of no fine structure

To be able to quantify how the presence of a fine structure in the reactor spectrum affects JUNO's sensitivity to the NMO, first, an ideal case for a smooth reactor antineutrino spectrum without any fine structure will be discussed.
For this reference analysis, the Huber-Mueller model corrected for rate and shape according to the Daya Bay measurement (see chapter 6.3.1) is used as reactor neutrino spectrum input. With the GNA, the JUNO spectrum is calculated and the χ^2 function is defined using an Asimov dataset assuming one of the NMOs as true. Figure 40 exemplarily shows the estimation of the Asimov sensitivity for the assumption of a true normal and inverted ordering. The value for the χ^2 highly depends on the value of the mass splitting Δm^2_{31}. The minimum for the χ^2-function differs for both NMO assumptions for the fit model. Since the Asimov dataset is created from the same JUNO spectrum model assuming a true ordering, the minimum for this model is exactly at $\chi^2 = 0$ while the model does not exactly fit to the Asimov dataset for the assumption of the wrong ordering giving a minimum of $\chi^2 = 8.17$, resulting in a value of $\Delta\chi^2 = 8.17$, in case of an Asimov dataset with a true NO and $\Delta\chi^2 = 8.65$ for a true IO. The larger value for a true inverted mass ordering can be explained by the oscillation pattern being slightly shifted in energy allowing a better NMO discrimination.

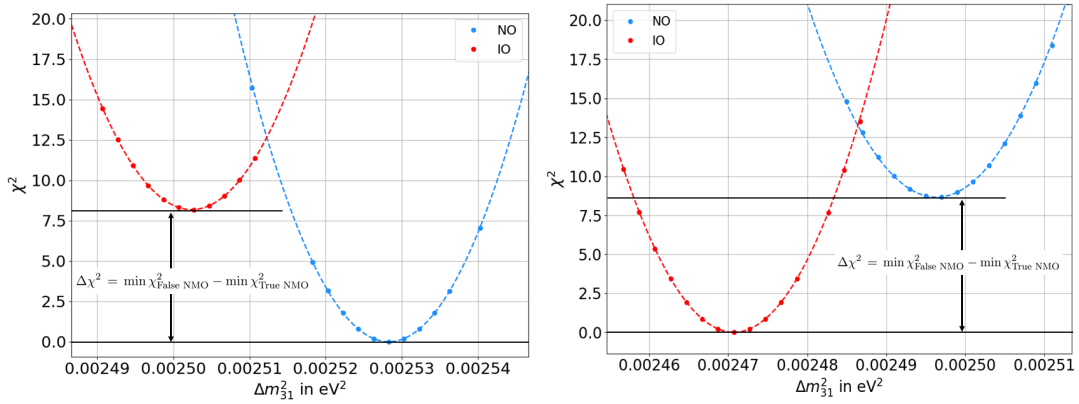

(a) True NO **(b)** True IO

Figure 40: χ^2 curves for the fit of the JUNO model under the assumption of IO (red) and NO (blue) to Asimov data with fixed true NO (a) and IO (b) as a function of the mass splitting Δm^2_{31}. The median sensitivity to the NMO is given by the difference of the minima of the χ^2 curves for both assumptions as given in equation 43.

7.2 NMO sensitivity in presence of fine structure-like fluctuations

In this section, it will be discussed how random fine structure-like fluctuations in the reactor antineutrino spectrum affect the sensitivity of JUNO to the NMO. For a systematic analysis of these effects, sets of fluctuations with different amplitudes and energy widths are randomly generated and applied to the Daya Bay corrected Huber-Mueller spectrum as described in chapter 6.1. For each combination of fluctuation amplitude of 1%, 2%, 3%, 4%, 5%, 6%, 7%, 8%, 9%, 10%, 15%, 20% and energy width of 1 keV, 5 keV, 10 keV, 20 keV, 30 keV, 40 keV, 50 keV, 75 keV, 100 keV, 100 Asimov datasets for the expected JUNO spectrum are generated. For the fitmodel, the smooth Daya Bay corrected Huber-Mueller model without fine structure (as in chapter 7.1) is used because the exact information on the fine structure is unknown in reality. The χ^2-function is constructed in the same way as previously described and the fit is performed assuming both NMOs to calculate the $\Delta\chi^2$. For the sets of Asimov data with true NO with an energy width of 10 keV the resulting distribution of the $\Delta\chi^2$ values are shown in figure 41 as histograms for all amplitudes. It can directly be seen that the width of the distributions increases for larger fluctuation amplitudes which is also expected as larger bin-to-bin differences between data and model due to the variation in the input spectrum reduce the impact of the bin-to-bin difference caused by the difference in the survival probability due to different NMO. In addition, the mean of the distribution is comparable to the case without fluctuations discussed in chapter 7.1 as the average of the fluctuations gives the smooth Huber-Mueller model. For the other energy widths the histograms are shown in figures 82 to 89 in appendix C.
To get a more detailed look on these implications and to quantify how these fluctuation affect the NMO sensitivity, each of these histograms is fitted with a standard Gaussian

$$f(\Delta\chi^2) = a \cdot \exp\left(-\frac{(\Delta\chi^2 - \overline{\Delta\chi^2})^2}{2\sigma^2}\right) \quad , \tag{51}$$

where a is the amplitude of the Gaussian, $\overline{\Delta\chi^2}$ the mean of the distribution and σ its standard deviation.

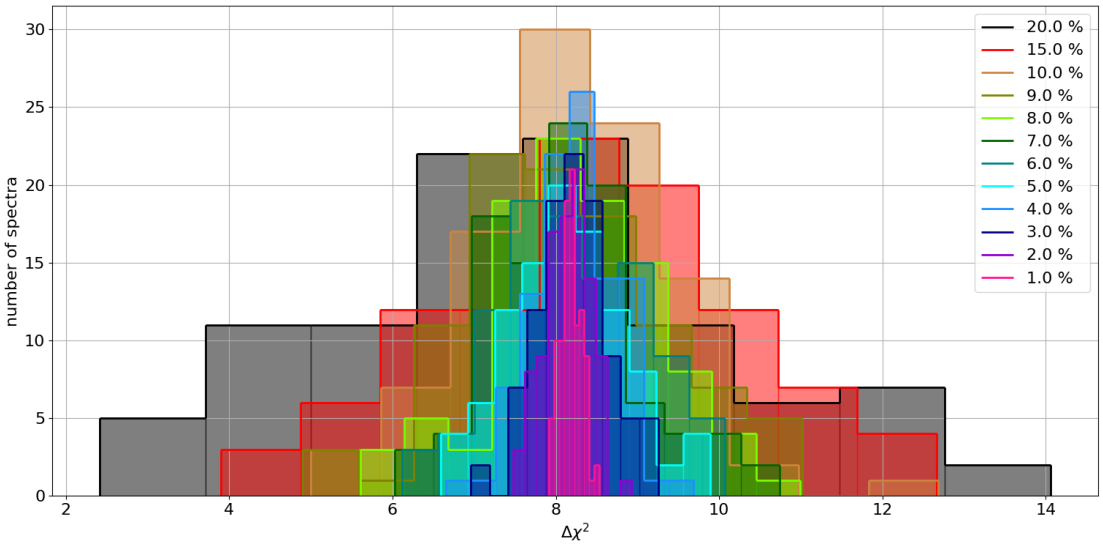

Figure 41: Distribution of the $\Delta\chi^2$ values for the Asimov datasets with true NO and a fluctuation energy width of 10 keV for all fluctuation amplitudes. The histograms are binned to 10 bins.

Figure 42 shows an example of the Gaussian fit to the histogram of the $\Delta\chi^2$ distribution for the fluctuation with an amplitude of 5% and an energy width of 10 keV. For this example, we can see that the average is $\overline{\Delta\chi^2} = 8.11 \pm 0.09\,(95\%\,\text{C.L.})$ which is indeed in agreement with the Asimov value for the case without fine structure as expected. The result for the standard deviation of the distribution is $\sigma = 0.71 \pm 0.09\,(95\%\,\text{C.L.})$ which means that for this set of properties of the fine structure fluctuations the Asimov $\Delta\chi^2$ is varying in an interval of around 1.4 in 68% of cases. This is the result of the fluctuations being present in the data but not in the model as these are unknown. Therefore, it has to be emphasized that the increase and decrease in sensitivity compared to the Asimov sensitivity in the case without fine structure is not physical, but a result of an insufficient model. The adaption of the model and the implications on the NMO sensitivity will be discussed in chapter 7.3.3.

For all fluctuation models that were analyzed with respect to these implications due to insufficient reactor model prediction, the results for the average of the $\Delta\chi^2$ and the standard deviation of its distribution depending on fluctuation amplitude and energy width of the fluctuations is shown in figure 43 for an assumed true NO and IO. It can be seen that the amplitudes of the fluctuations as well as the width in energy of the individual fluctuations significantly affect the width of the distribution of the $\Delta\chi^2$ independent of the assumed true NMO. An increasing fluctuation amplitude as well as a larger width in energy leads to a wider distribution. This is also the expected behavior as larger bin-to-bin differences between the model and the data directly add up to the χ^2. As the final binning of the JUNO spectrum is 20 keV the fluctuations with smaller energy widths cancel out when being rebinned which reflects in a narrow distribution for the 1 keV fluctuations which increases for larger energy widths. The standard deviations for the $\Delta\chi^2$ are separately plotted as a function of the energy widths of the fluctuations for all fluctuation amplitudes and also as a function of the fluctuations amplitude for all analyzed energy widths are shown in figure 45 for a true NO and in figure 90 in appendix C for a true IO.

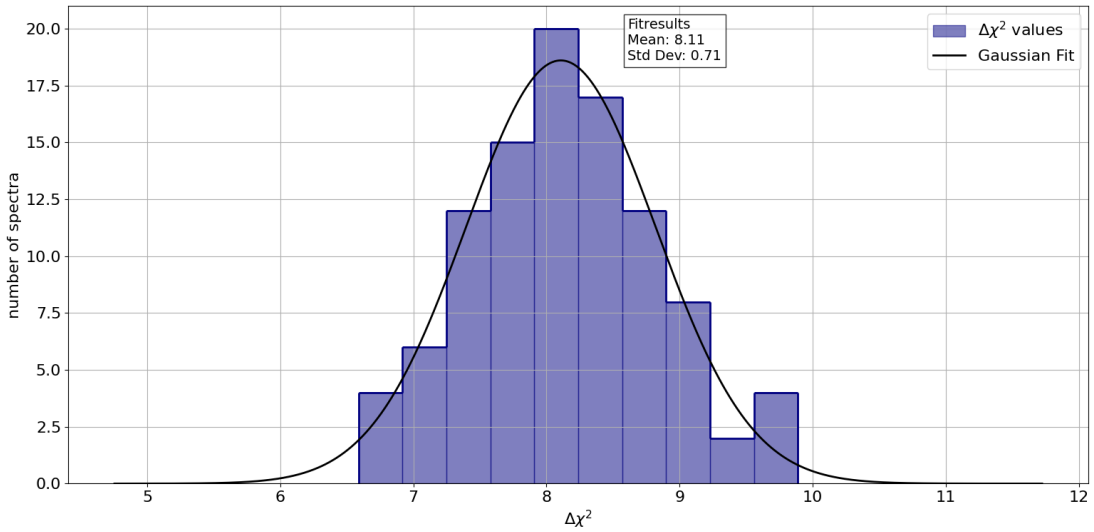

Figure 42: Example of the Gaussian fit to the histogram of the $\Delta\chi^2$ distribution for the spectral fluctuation with an amplitude of 5% and an energy width of 10 keV. The Gaussian fit results in a mean of $\overline{\Delta\chi^2} = 8.11 \pm 0.09$ (95% C.L.) for the distribution with a standard deviation of $\sigma = 0.71 \pm 0.09$ (95% C.L.).

Concerning the mean of the $\Delta\chi^2$ distribution we observe in figure 43 a variation for large energy widths and fluctuation amplitudes while it was expected that the fluctuations do not significantly influence the average $\Delta\chi^2$. However, this can be explained by a statistical effect as the number of samples is the same for all tested datasets which results in a larger uncertainty for the mean in the Gaussian fit if the width of the distribution increases. This behavior can be seen in detail in figure 44 for a true NO and in figure 91 in appendix C for a true IO, where the mean of the $\Delta\chi^2$ distributions are separately plotted as a function of the energy widths of the fluctuations for all fluctuation amplitudes and also as a function of the fluctuation amplitudes for all analyzed energy widths with their respective 95% C.L. uncertainties. Taking into account the fit uncertainties there is no systematic change in the observed average depending on any property of the fluctuations. We also observe the same increase in average sensitivity for a true IO as in the case without fine structure.
This analysis shows the importance of a proper knowledge of the input spectra as fine structure-like fluctuations in the spectrum that are not considered in the fitmodel can significantly impact the sensitivity estimation. While large scale fluctuations of up to 100 keV with large fluctuation amplitudes of up to 20% lead to $\Delta\chi^2$ distributions with standard deviations of nearly 100% of their mean, they do not represent a realistic version of the actual fine structure in the reactor antineutrino spectrum and just show the behavior of the estimated sensitivity in extreme cases. However, the more realistic small scale fluctuations with less than 20 keV and a maximum of $3-4$% fluctuation amplitude still introduce a variation in the possible $\Delta\chi^2$ of up to 1.0, which is still a significant impact for a high-precision experiment like JUNO.

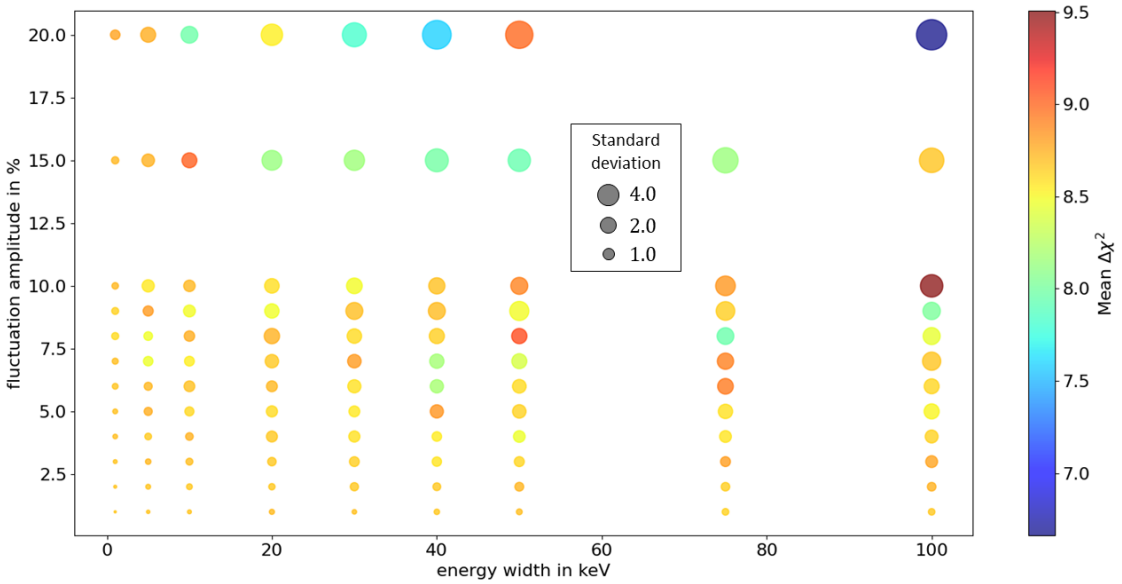

(a) True NO

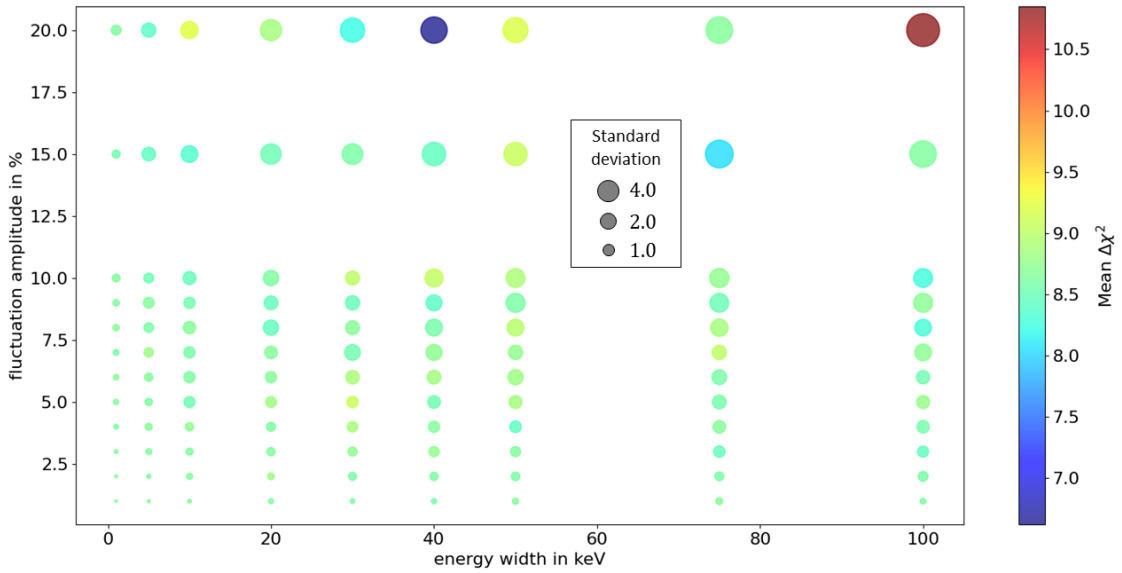

(b) True IO

Figure 43: Mean and standard deviation of the $\Delta\chi^2$ distribution depending on fluctuation amplitude and energy width of the fluctuations for an assumed true normal (a) and inverted (b) mass ordering. The color represents the mean of the distribution according to the colorscale on the right and the size of the dots represent the standard deviation. For reference, the dots for a standard deviation of 1.0, 2.0 and 4.0 are also shown. In figure (a) the fit for the fluctuations with 75 keV width and 20% amplitude failed and is therefore not shown.

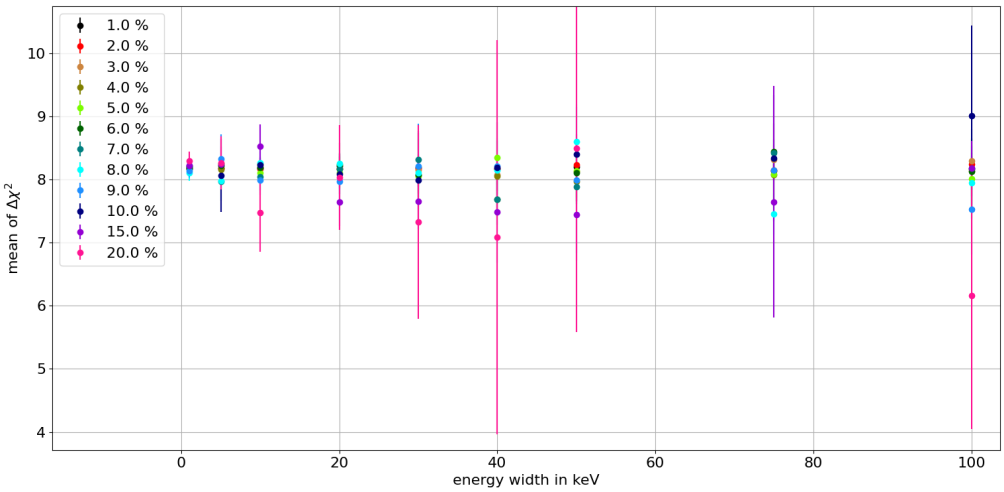

(a)

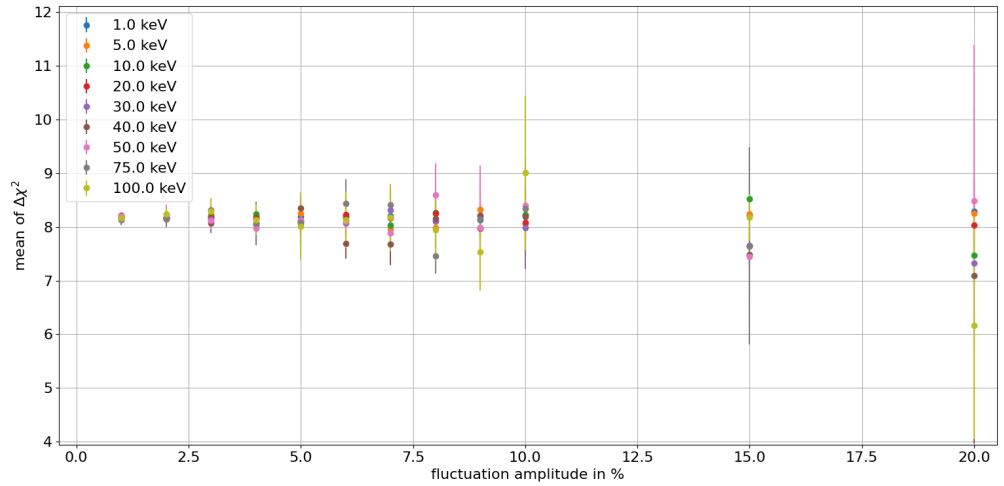

(b)

Figure 44: Mean of the $\Delta\chi^2$ distribution with the respective 95% C.L. uncertainties as a function of the energy width of the fluctuations for all analyzed fluctuation amplitudes (a) and as a function of the fluctuation amplitude for all analyzed energy widths (b) for an assumed true NO.

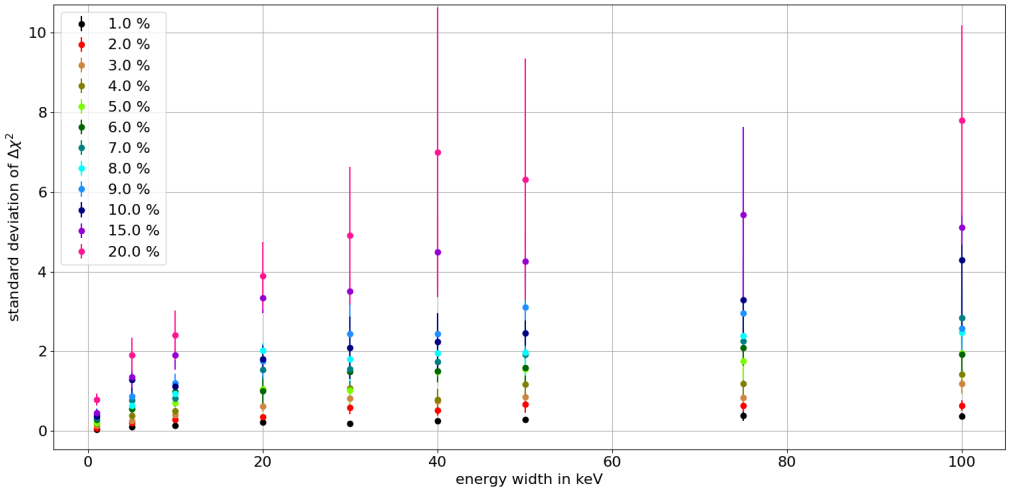

(a)

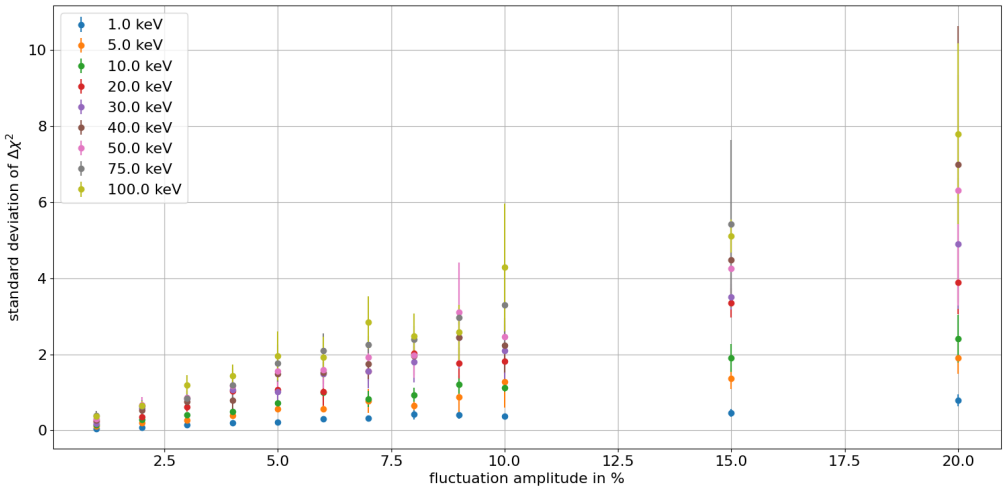

(b)

Figure 45: Standard deviation of the $\Delta\chi^2$ distribution with their respective 95% C.L. uncertainties as a function of the energy width of the fluctuations for all analyzed fluctuation amplitudes (a) and as a function of the fluctuation amplitude for all analyzed energy widths (b) for an assumed true NO.

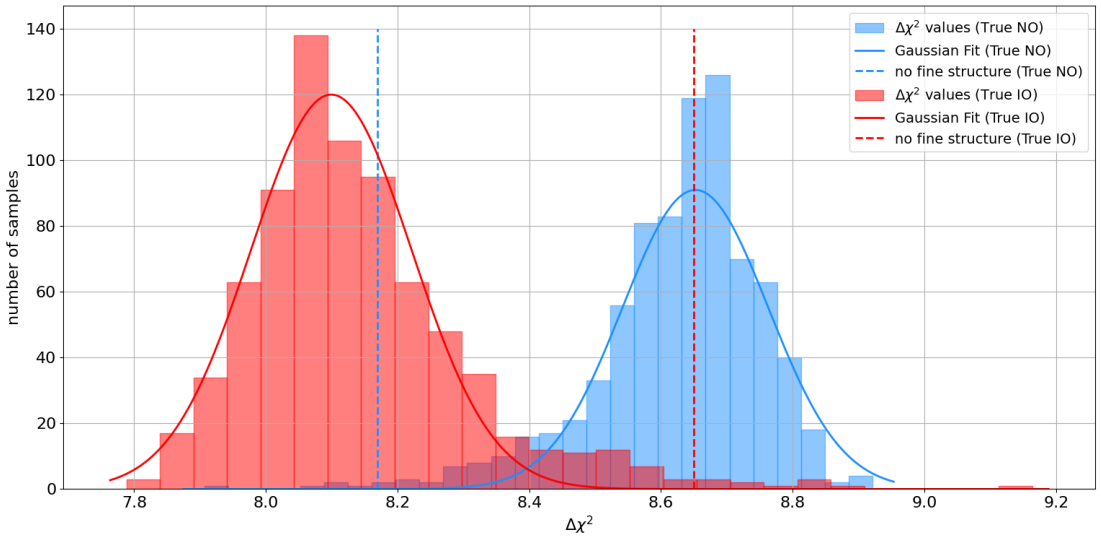

Figure 46: Distribution of the $\Delta\chi^2$ for assumed true NO (blue) and IO (red) for 1000 summation spectra with fine structure used as input spectra for the Asimov data while the fit model was built with the smooth Daya Bay corrected Huber-Mueller model. As reference the $\Delta\chi^2$ for Asimov data without fine structure is shown as vertical lines for true NO and IO.

7.3 NMO sensitivity for summation spectra with fine structure

After the extensive tests with various versions of fine structure-like fluctuations applied to the spectral input data, the following section focuses on the implications on the NMO sensitivity of JUNO using input spectra for the reactor antineutrinos that were generated via the summation method as it is explained in chapter 6.2 and corrected for the rate and bump as described in chapter 6.3.2. This represents the most realistic approach to investigate the possible effect by the fine structure on JUNO's NMO sensitivity. Three major cases are investigated where the effect of different reactor input spectra in the fit model on the NMO sensitivity is analyzed. First, the fit model is simply based on the Daya Bay corrected Huber-Mueller model, second, an average of the summation spectrum is used to include an assumption of the fine structure and last the spectrum model is extended with spectral weights that allow for variations in the model compared to the data.

7.3.1 Huber-Mueller model based fit

For this analysis, the 1000 generated summation spectra with fine structure were used as input spectra to create the Asimov datasets while the smooth Daya Bay corrected Huber-Mueller model was used to build the fitmodel due to the lack of knowledge on the fine structure appearance.
Again, we calculate the standard minimum χ^2 value for the fit of the model with assumed false and true NMO to estimate the sensitivity to distinguish between the mass orderings. The resulting distribution of the Asimov $\Delta\chi^2$ for assumed true NO and IO for the 1000 summation spectra are shown in figure 46. It can be seen that the mean of the distributions significantly changes in presence of the fine structure. For an assumed true NO the average $\Delta\chi^2$ is with a value of $\overline{\Delta\chi^2} = 8.65 \pm 0.02\,(95\%\text{C.L.})$ increased by 0.48 ± 0.02 compared to the case without fine structure while the average $\Delta\chi^2$ for a true IO is reduced by 0.55 ± 0.02 to $\overline{\Delta\chi^2} = 8.10 \pm 0.02\,(95\%\text{C.L.})$. This also leads to the effect of the sensitivities being

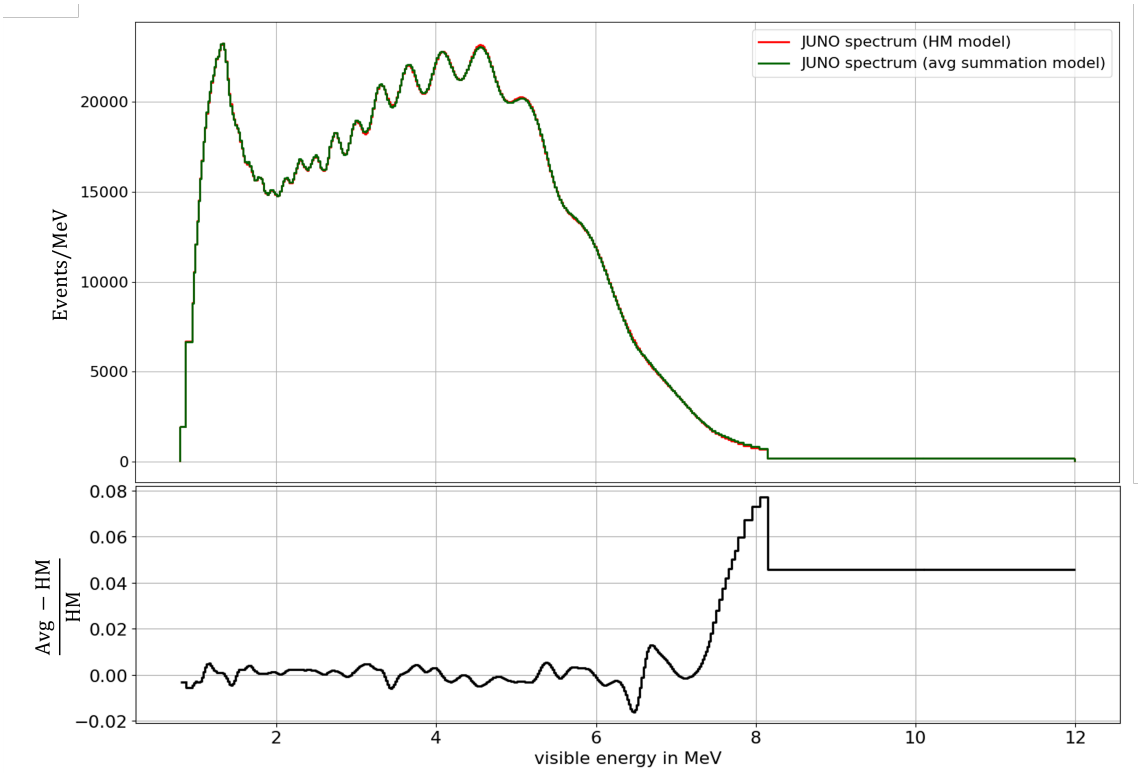

Figure 47: The upper panel shows the expected JUNO spectrum for assumed normal ordering calculated with the Daya Bay corrected Huber-Mueller model (red) compared to the expected JUNO spectrum for the same ordering with the average summation model as input (green). The lower panel displays the relative difference between the two spectra shown in the upper plot. In the region up to 6 MeV a fine structure is visible while for higher energies a small difference due to a technical issue in the rate and bump correction arises (see chapter 8.3) which is however of plausible magnitude considering the usual spectral uncertainty.

swapped between both assumed true orderings. The analysis of random fine structure-like fluctuations (see chapter 7.2) however showed no large impact on the average Asimov sensitivity. The now observed effect can be explained by the fact that the average spectrum of the 1000 generated samples does not reproduce the Huber-Mueller model which is used for the fit model. Therefore, the observed increase and decrease in sensitivity is not a single effect by the fine structure in the spectrum itself, but caused by the insufficient fit model. Figure 47 shows the expected JUNO spectrum calculated with both the Daya Bay corrected Huber-Mueller model and the average summation model as spectrum input as well as their relative difference.
It shows a small fluctuation of less than 1% due to the fine structure for energies up to 6 MeV. In the interval from $6 - 7$ MeV, the fluctuation increases to around 2% while for energies above 7 MeV the relative difference between the spectrum models is $5 - 8\%$. We observe a higher rate for high energies compared to the Daya Bay corrected Huber-Mueller model which is a small technical issue from the difference in fission fractions between the Daya Bay and the JUNO experiment which arises in the rate and bump correction of the spectra (see chapter 6.3). This issue will be discussed in more detail in chapter 8.3. Despite its origin in the construction of these spectra, however, this difference is still plausible as the uncertainty of the reactor antineutrino spectrum models is between $5 - 30\%$ depending

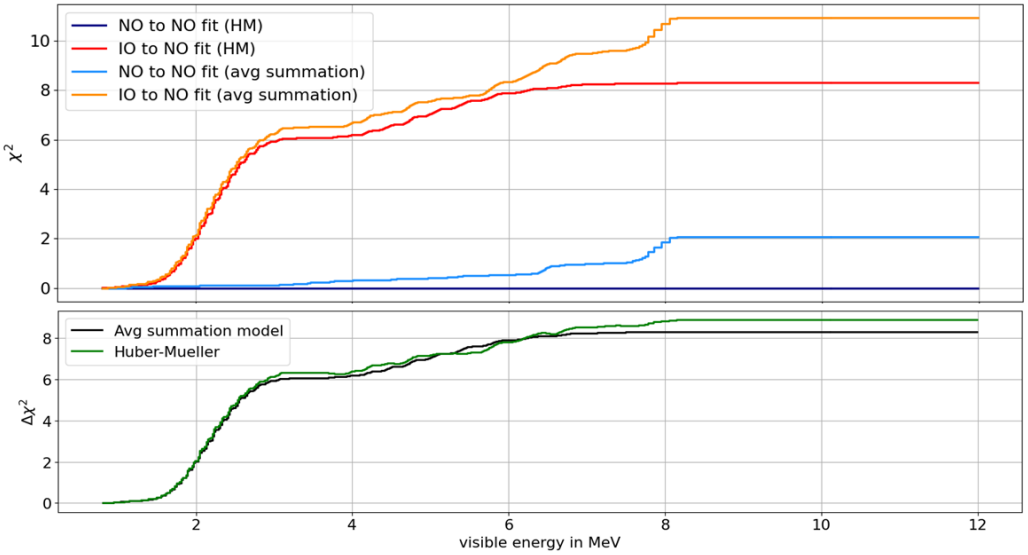

Figure 48: The upper plot shows the total χ^2 as a function of the visible energy up to which the spectrum is included. It compares how the total χ^2 builds up for increasing energy for the fit of the JUNO spectrum model with Huber-Mueller input spectrum to Asimov data created with the Huber-Mueller model and normal ordering for assumed NO (violet) and IO (red). Additionally, this dependence of the χ^2 is plotted for the case when the Asimov dataset is generated with the average summation model while the fitmodel is still based on the Huber-Mueller model for assumed NO (blue) and IO (orange). The additional increase of the χ^2 in the average summation model case is caused by the difference between model and Asimov data as shown in figure 47. The lower panel shows how the $\Delta\chi^2$ behaves according to the displayed χ^2 for the two different Asimov datasets depending on the upper limit of the included visible energy range.

on the specific isotope above 8 MeV [78, 79]. Additionally to the fine structure, one has also to take into account these possible variations in the spectrum. To check how this affects the total value of the $\Delta\chi^2$, the contribution of every energy bin to the total χ^2 is calculated for both assumed mass orderings for the fit of the Huber-Mueller model to the average summation spectrum which is shown in figure 48. Additionally, the contribution to the χ^2 is shown for the case without fine structure, where fit model and Asimov data are calculated with the Huber-Mueller model as input. In case of same model and same mass ordering, the fit perfectly reproduces the data resulting in $\chi^2 = 0$ while a difference between the models and the mass orderings does not. Due to differences between the input spectrum used to generate the Asimov data and for the fitmodel, the χ^2 also increases with every bin for the same assumed mass ordering, however, this does not happen to the same amount for the fit of the false NMO and for the fit of the true one, yielding a residual effect on the $\Delta\chi^2$ which is therefore not representative for a sensitivity estimation to the NMO only.

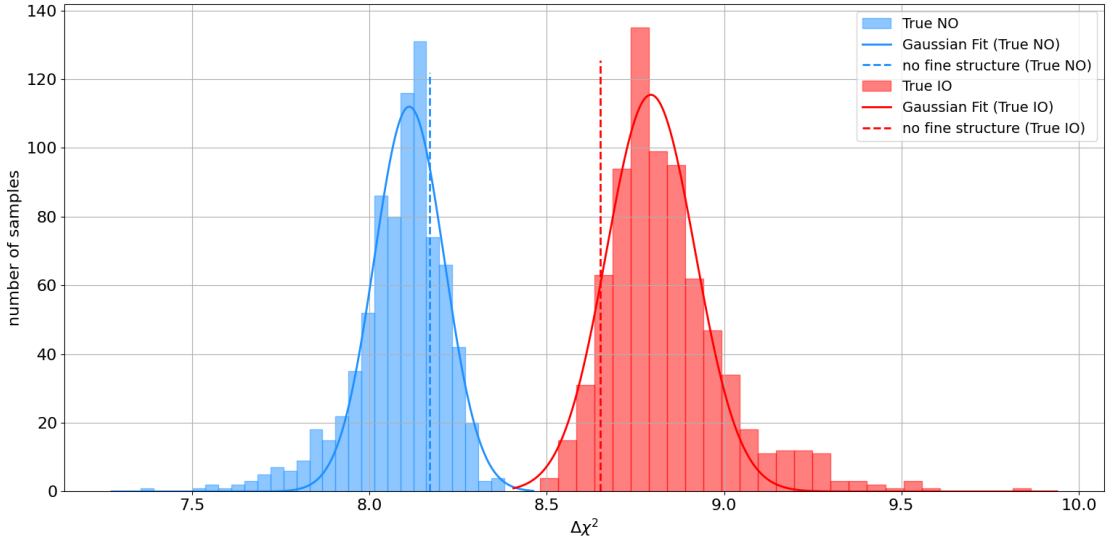

Figure 49: Distribution of the Asimov $\Delta\chi^2$ for assumed true NO (blue) and IO (red) for 1000 summation spectra with fine structure used as input spectra for the Asimov data while the fitmodel was built with the average spectrum of all 1000 spectra. As reference, the $\Delta\chi^2$ for Asimov data without fine structure (Daya Bay corrected Huber-Mueller model) is shown as vertical lines for true NO and IO.

7.3.2 Average summation spectrum based fit model

To estimate JUNO's sensitivity to distinguish between the two mass orderings, the model has to be adapted to remove any bias due to a wrong model. In a first step, the fitmodel can be changed from being based on the Huber-Mueller model to the average summation model. This would represent a similar approach as in the previous analysis on the random fluctuations which gives an estimation on the distribution of the $\Delta\chi^2$ by the individual variations in the generated spectra. The result for the 1000 Asimov datasets generated based on summation spectra with fine structure is shown in figure 49. Compared to the previous analysis, the significant increase in $\Delta\chi^2$ for a true normal ordering and decrease for true inverted ordering is still present, but reduced now. The mean values of the distributions are $\overline{\Delta\chi^2} = 8.11 \pm 0.01$ (95%C.L.) for NO and $\overline{\Delta\chi^2} = 8.79 \pm 0.02$ (95%C.L.) for IO which is in much better agreement with the sensitivity in the case without fine structure. However, there is still a shift of $\sim 0.1 - 0.2$ between the cases which cannot been explained by a difference in the total event statistics. Additionally, the fine structure is not well known and therefore this is just an exemplary analysis. A more reliable analysis will be performed in the following.

7.3.3 NMO sensitivity including spectral weights

As the studies presented in chapters 7.3.1 and 7.3.2 have shown, already small differences between the actual data and the model used to describe the data can introduce significant bias to the NMO sensitivity. Since the reactor spectrum cannot be predicted precisely enough for the NMO determination, a possible variation in the model has to be implemented to avoid bias due to an insufficient reactor spectrum model. Therefore, a parametrization of the antineutrino spectrum is introduced. For each of the four reactor

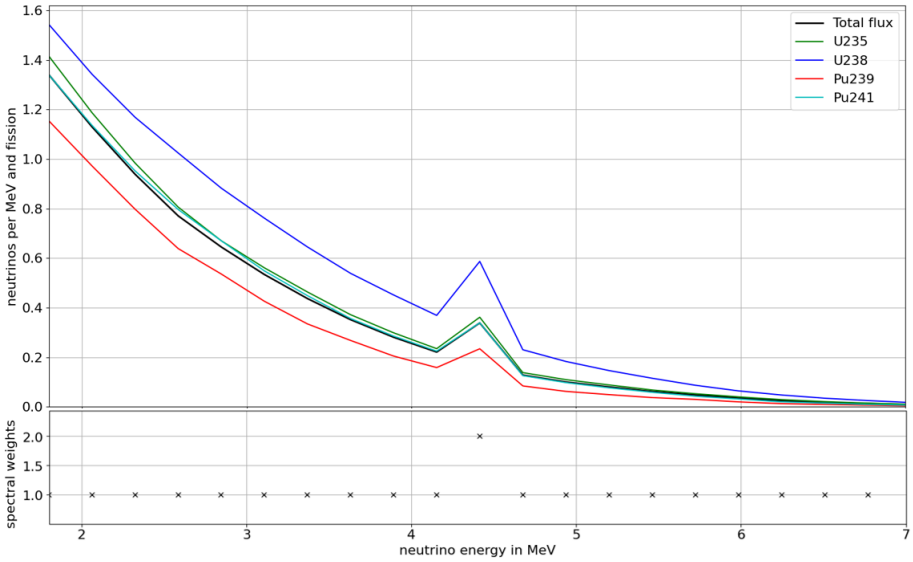

Figure 50: Exemplary illustration how the spectral weights in the parametrization of the antineutrino spectrum affect its shape. The multiplication with the weights changes the shape of the spectrum for every isotope to the same amount which corresponds to a change of the total spectrum by the same amount.

isotopes i, a piecewise exponential is calculated based on the input spectrum model with correction for the Daya Bay rate and shape. For a predefined segmentation of the antineutrino energy with edges E_j, the spectrum parametrization in a segment with $E \in (E_j, E_{j+1})$ is given by [87]

$$S_{ij}(E) \;=\; n_j \, k_{ij} \, \mathrm{e}^{-b_{ij}(E-E_j)} \quad . \tag{52}$$

Here, the parameters k_{ij} are defined by the antineutrino yield for isotope i in segment j as given by the input spectrum model. The parameters b_{ij} are defined to provide a continuous exponential and therefore depend on the k_{ij} and the n_j. The parameters n_j are scale parameters that are estimated by the fit to account for the difference between the input spectrum model and the actual observed data via

$$n_j(E) \;=\; \frac{\langle S(E) \rangle_{j,\mathrm{obs}}}{\langle S(E) \rangle_{j,\mathrm{mod}}} \quad . \tag{53}$$

Figure 50 illustrates how the spectral weights n_j affect the spectrum. The size of the energy segments for the parametrization is chosen considering the energy resolution $\sigma(E)$ and the number of events in every segment. The first and last segment is chosen to contain more than 500 events while the following segments start from 30 keV width and increase by 10 keV if the width would be less than $1.5\sigma(E)$. This definition was proven sufficient for the no fine structure case [87] and is therefore used for the following analysis. A more detailed analysis on the energy segmentation of the spectrum parametrization will be presented in chapter 9.1.
The application of this spectrum parametrization introduces 150 additional parameters to the fitmodel. Depending on the estimated difference between the actual reactor neutrino spectrum with fine structure and the spectrum model used as input to the fitmodel, these parameters can be assigned with constraints. The χ^2 statistics which is minimized is then extended by a nuisance term for every spectral weight n_j.

The scale of the fine structure in the Daya Bay corrected summation spectra compared to the average summation spectrum is in the order of $2-3\%$ for neutrino energies up to 7 MeV but increases to several tens of percent for higher energies. Therefore, for the largest part of the spectrum, a constraint of 5% for the spectral weights should account for the spectral difference. However, an underestimation of the uncertainty can affect the NMO sensitivity estimation and therefore, a less tight constraint would reduce the risk of underestimating the spectral difference. The best option would be a complete model-independent fit meaning to add no artificial constraint on the spectral weights.
To analyze how the application of these spectral weights affect the NMO sensitivity, 100 Asimov datasets generated with the summation spectra were selected from the set of 1000 datasets used in the previous analyses and the spectral weights were introduced to the fitmodel based on the average summation spectrum. These spectral weights were set to a value of 1.0 and assigned with relative uncertainties of 5%, 10%, 25%, 50%, 75%, and 200% as well as without any constraint.
The resulting distributions of the $\Delta\chi^2$ for an assumed true normal ordering is shown in figure 51. It can be seen that the average $\Delta\chi^2$ reduces with less tight constraint on the spectral weights and goes to zero for free spectral weights. Already a small but necessary constraint of 5%[b] reduces the average sensitivity by 1.27 ± 0.03 to $\overline{\Delta\chi^2} = 6.90 \pm 0.03$ compared to the Asimov sensitivity without fine structure. This reduction of the average sensitivity can be explained by the spectral weights taking into account any difference between the fitmodel and the data which also includes the difference in the spectra between an assumed false mass ordering in the fitmodel and the true ordering in the Asimov data. Additionally, the width of the distribution for the 100 analyzed datasets reduces also reaching almost zero for free spectral weights due to the increasing ability to correct for the different fine structures in the spectra causing the initial distribution. The upper panel of figure 52 shows the spectral weights determined by the fit with assumed false mass ordering to the Asimov dataset yielding the sensitivity closest to the average for the different uncertainties assigned to the spectral weights as constraint as well as in the case of free parameters. Additionally, the ratio between the expected JUNO spectra for normal and inverted ordering is displayed for comparison. The lower plot of figure 52 shows the spectral weights for the same datasets when the true ordering is assumed in the fitmodel. For large constraints on the parameters, they stay close to a value of 1.0 only varying on a small scale in case of the fit with assumed true NMO due to the difference between the spectrum models. For the fit with false NMO, it is observed that the spectral weights partially fit the oscillating difference in the spectra between the two mass orderings which therefore reduces the $\Delta\chi^2$ and the ability to distinguish between the two mass orderings. For less tight constraints like relative uncertainties larger than 25%, the spectral weights show an oscillatory behavior independent of the assumed NMO in the fitmodel which significantly reduces the sensitivity to distinguish between the mass orderings. When increasing the freedom of the fitmodel, the fitter does not find a proper value for the spectral weight as it correlates with the other parameters. Therefore, more information on the data are needed to improve the estimation of the spectral weights. This is solved by adding the data measured by JUNO's satellite detector TAO to the analysis which will be discussed in chapter 8.

[b] A constraint of 5% is already quite optimistic as the variation of the estimated summation spectra (see chapter 6.2.3) as well as the uncertainty of the Daya Bay measurement (see chapter 6.3) is at least in the order of $5-10\%$ which has to be taken into account.

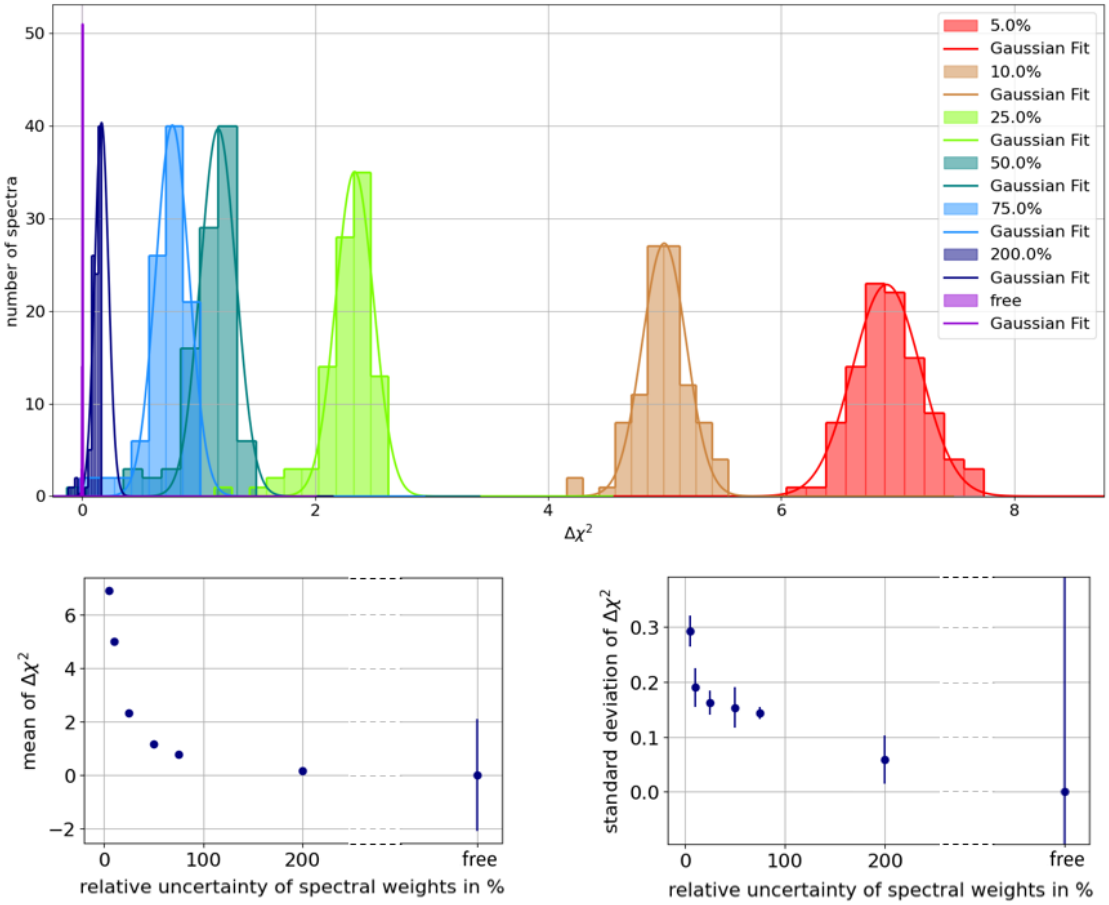

Figure 51: The upper plot shows the distributions of the $\Delta\chi^2$ for the fit of the JUNO spectrum model based on the Daya Bay corrected average summation spectrum model with spectral weights for different relative uncertainties assigned as constraint as well as for the case of free parameters. Additionally, fits of a Gaussian to the individual histograms are displayed. The lower left plot shows the mean of the distributions in the upper plot while the lower right plot displays the standard deviation of the distributions as a function of the assigned uncertainties to the spectral weights.

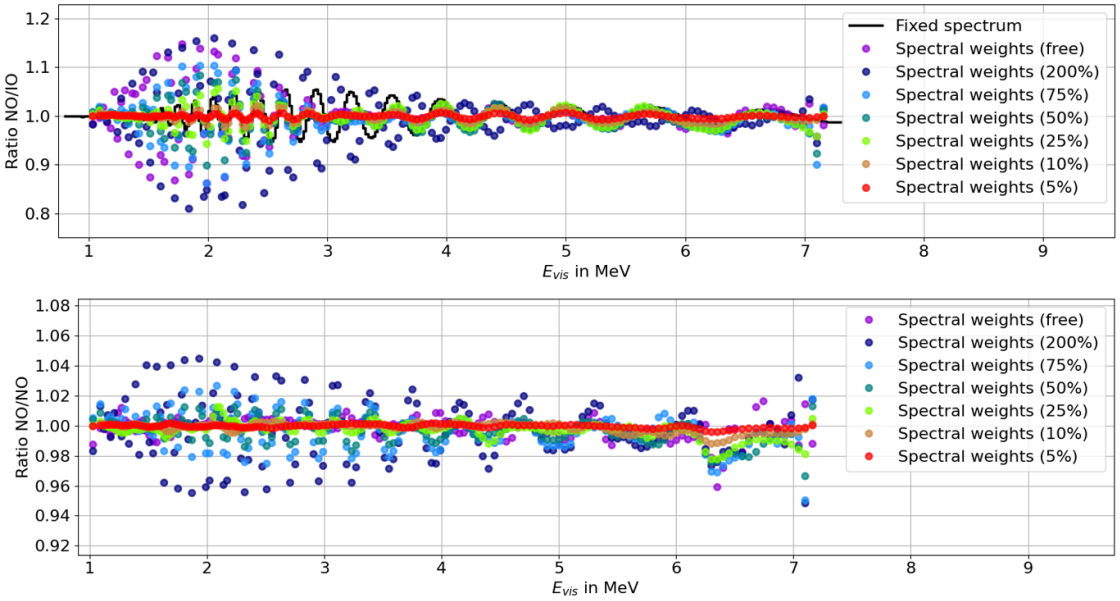

Figure 52: The upper panel shows the spectral weights determined by the fit with assumed false mass ordering to the Asimov dataset yielding the sensitivity closest to the average for the different uncertainties assigned to the spectral weights as constraint: 5% (red), 10% (orange), 25% (green), 50% (darkgreen), 75% (blue), and 200% (darkblue) as well as in the case of free parameters (violet). Additionally, the ratio between the expected JUNO spectra for normal and inverted ordering is displayed (black). The lower plot shows the spectral weights for the same datasets when the true ordering is assumed in the fitmodel. It has to be mentioned that the spectral weights are defined for the neutrino energy which is converted to visible energy for the comparison to the NO/IO ratio of the fixed spectrum.

8 Combined Analysis with the Satellite Detector TAO

"Was steht an erster Stelle deiner Not-To-Do Liste?", rufe ich. Das Känguru blickt hoch. "Aufgeben", sagt es.

– Marc-Uwe Kling - *Das Känguru-Manifest*

In chapter 7 we saw how the presence of a fine structure in the reactor antineutrino spectrum could impact JUNO's sensitivity to the NMO. As described in chapters 3 and 5.2, the experiment will feature the satellite detector TAO which provides an unoscillated reference spectrum from the reactor cores at the Taishan NPP. This measured spectrum can be used to correct the oscillated spectrum measured in JUNO for unknown differences between the model predictions and the actual emitted spectrum of the nuclear reactors.
This can be done via a combined fit of the JUNO and TAO spectra using the spectrum parametrization introduced in equation 52 that accounts for differences between the spectrum model and the actual measurement of the spectrum by TAO. The parametrization of the spectrum is part of the JUNO as well as the TAO model and therefore affects both models in a combined fit.
For this combined fit, the vectors containing the event number in each bin for the JUNO and TAO spectra are concatenated for both the Asimov data $\boldsymbol{x}$ and the fitmodel $\boldsymbol{\mu}$ building a new combined dataset

$$\boldsymbol{\mu} = \left[\mu_1^{JUNO},\ldots,\mu_N^{JUNO},\mu_1^{TAO},\ldots,\mu_N^{TAO}\right] \quad , \tag{54}$$

$$\boldsymbol{x} = \left[x_1^{JUNO},\ldots,x_N^{JUNO},x_1^{TAO},\ldots,x_N^{TAO}\right] \quad , \tag{55}$$

where $\mu_i(\boldsymbol{\theta},\boldsymbol{\eta})$ is the expected number of events in each bin i which depends on free parameters $\boldsymbol{\theta}$ and nuisance parameters $\boldsymbol{\eta}$ and x_i is the observed number of events in bin i. The test statistic is in analogy to the previous analyses for the JUNO-only case also based on Pearson's χ^2 function. It is then given by

$$\chi^2 = \left[\boldsymbol{x}-\boldsymbol{\mu}(\boldsymbol{\theta},\boldsymbol{\eta})\right]^T V^{-1} \left[\boldsymbol{x}-\boldsymbol{\mu}(\boldsymbol{\theta},\boldsymbol{\eta})\right] \tag{56}$$

with the combined covariance matrix

$$V = \begin{pmatrix} V_{\text{JUNO}} & 0 \\ 0 & V_{\text{TAO}} \end{pmatrix} \quad , \tag{57}$$

where V_{JUNO} and V_{TAO} are the covariance matrices for the JUNO and TAO models[c].

[c] As the only parameters correlated between JUNO and TAO in this analysis are the spectral weights which are however not correlated between different bins, the off-diagonal elements are zero. However, since the TAO covariance matrix is non-diagonal, the combined covariance matrix is also non-diagonal.

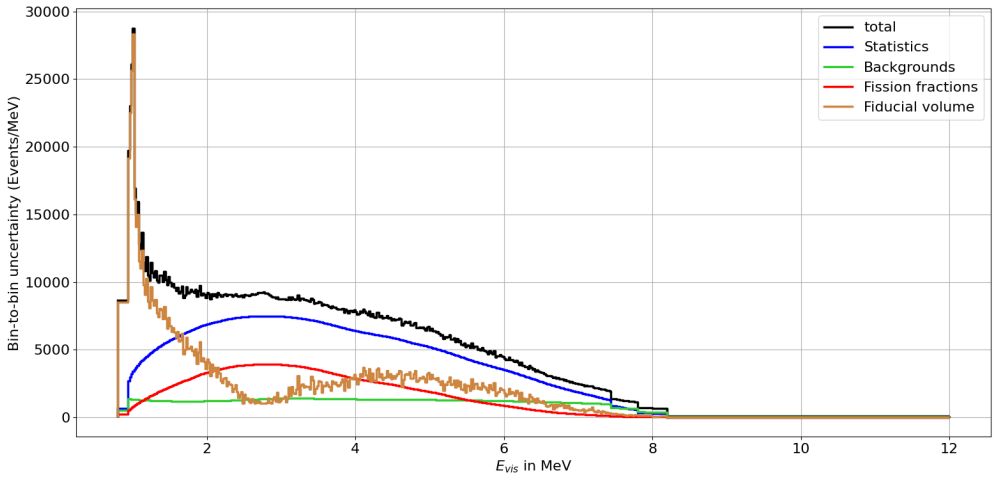

Figure 53: Total contribution to the diagonal of the covariance matrix due to bin-to-bin uncertainties for the TAO spectrum model (black) as well as the individual contributions from statistics only (blue), residual backgrounds (green), the different reactor burn-up compared to JUNO (red), and the fiducial volume cut (brown).

Since the bin-to-bin uncertainties of TAO are now included in the covariance matrix by V_{TAO}, the covariance matrix of JUNO now only includes the bin-to-bin uncertainties from statistics and the residual backgrounds (c.f. figure 39). The bin-to-bin uncertainties included in the diagonal of V_{TAO} are displayed in figure 53. The total bin-to-bin uncertainty consists of the usual statistic uncertainties and the uncertainties of the residual backgrounds as well as the additional systematic uncertainties caused by a slightly different reactor burn-up history between JUNO and TAO which introduces a small offset in the fission fractions and the contribution due to the fiducial volume cut which is a full non-diagonal covariance matrix [87].
Similar to the previous analyses, the final test statistic to estimate the NMO sensitivity is the $\Delta\chi^2 = \min \chi^2_{\text{False NMO}} - \min \chi^2_{\text{True NMO}}$ which is connected to the median sensitivity as given in equation 69.

8.1 NMO sensitivity in case of no fine structure

First, the median Asimov sensitivity in absence of any fine structure in the spectrum is calculated as a reference as it was done for the JUNO-only case in chapter 7.1, however, now the spectral weights are included which are set as free parameters. The Daya Bay corrected Huber-Mueller spectrum is used as input model for the calculation of the Asimov dataset and the construction of the fitmodel. This again leads to the case that the model perfectly describes the data for the assumed true ordering giving $\chi^2_{\text{true NMO}} = 0$ while the fit of the model with wrong assumed NMO does not. This is shown in figure 54 where the Asimov dataset for a true normal ordering for the JUNO and TAO spectra are shown as well as the best fit with assumed true and false mass ordering. While the JUNO spectrum shows the usual oscillation pattern for a different NMO, the relative difference in the TAO spectrum for the fit with assumed wrong mass ordering to the Asimov data is almost two orders of magnitude smaller which is suitable for a reference spectrum that should be able to account for spectral differences between actual data and the assumed reactor spectrum model.

For the combined fit of the JUNO and TAO spectrum with an exposure of 6 years × 26.6 GW_{th}[d], the results are $\Delta\chi^2 = 8.06$ for a true NO and $\Delta\chi^2 = 8.62$ for a true IO which is by 0.11 (true NO) and 0.03 (true IO) lower compared to the JUNO only fit discussed in chapter 7.1 due to the additional spectral fit. However, it has to be emphasized that the JUNO-only fit used the same fixed model for Asimov data and fitmodel without free spectral weights. Compared to the JUNO-only fit with free spectral weights discussed in chapter 7.3.3 which gives no information on the NMO, nearly the full sensitivity is restored by the combined fit.

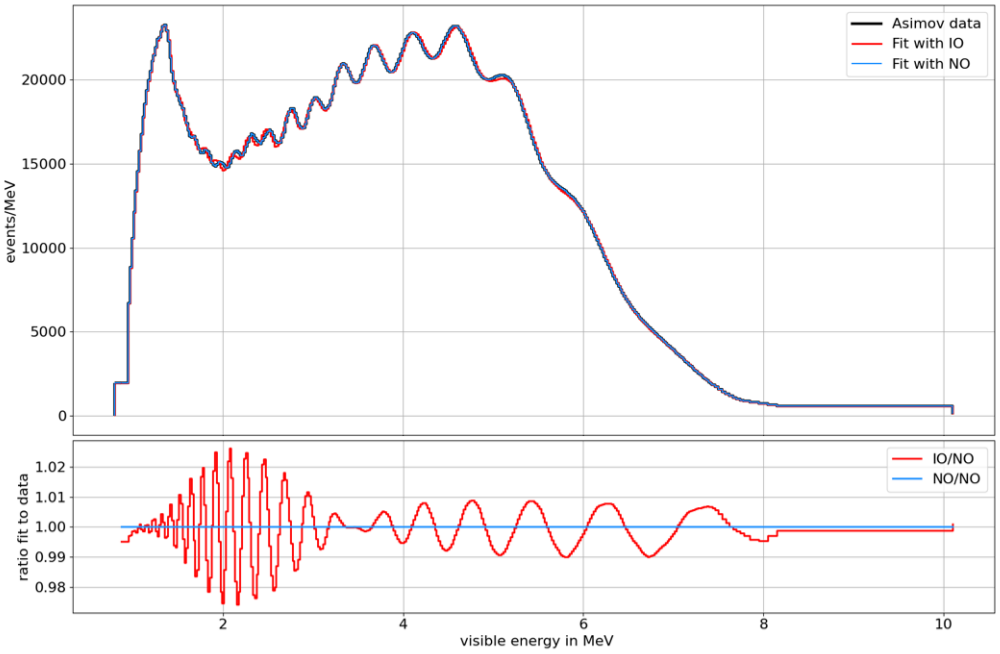

(a) JUNO spectrum

[d]This exposure will be used throughout this chapter unless mentioned otherwise.

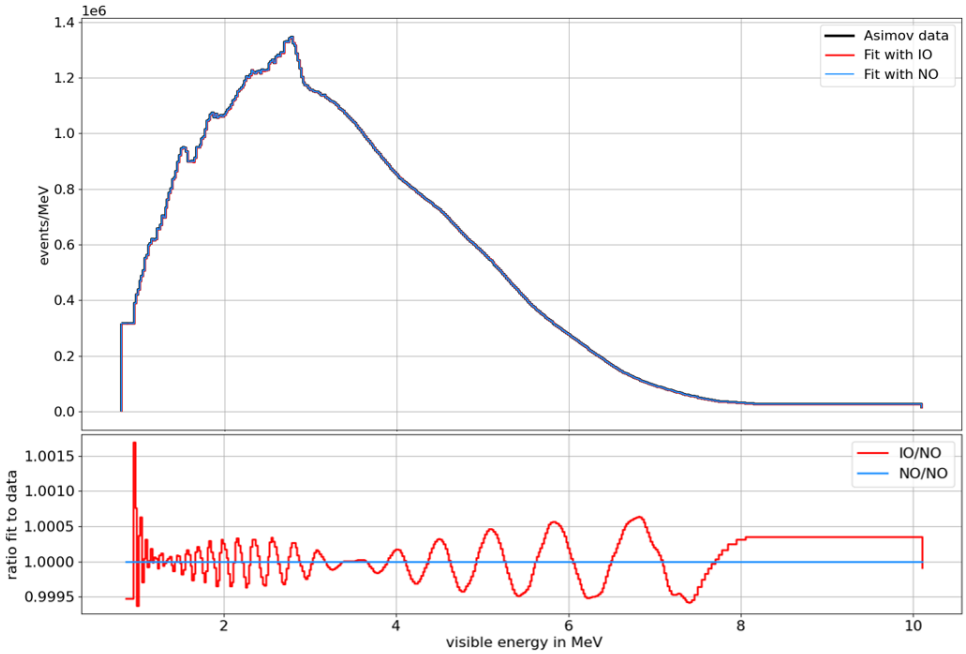

(b) TAO spectrum

Figure 54: The upper panels show the expected Asimov data for assumed true normal ordering (black) in JUNO (a) and TAO (b) and the fit of the model with assumed NO (blue) and IO (red). Since the fit with normal ordering is in perfect agreement with the Asimov data, the black line is covered by the blue line in the plots. The lower panels show the ratio of the model fit to the Asimov data for both assumed orderings which also shows the perfect agreement in case of the true ordering while the oscillatory difference is seen for the wrong ordering.

8.2 NMO sensitivity in presence of fine structure-like fluctuations

In chapter 7.2 it was shown how random fine structure-like fluctuations in the reactor antineutrino spectrum can affect the NMO sensitivity of JUNO for different properties of these fluctuations. A variety of fluctuation amplitudes and energy scales of the individual fluctuations was tested showing that the width of the distribution of possible $\Delta\chi^2$ values increases for more extreme fluctuations. In the following, the potential of TAO will be discussed to reduce these implications for selected cases of these fluctuations. The energy scale and the fluctuation amplitude was chosen to 1 keV, 10 keV, and 100 keV of energy width with 1%, 5%, and 10% of fluctuation amplitude each to test a extremely small and large fine structure case as well as a more realistic medium case. For the estimation of the NMO sensitivity, an Asimov dataset was created for each of the fluctuations applied to the spectrum assuming a true normal mass ordering. For the fitmodel, the spectrum parametrization based on the smooth corrected Huber-Mueller model with free spectral weights is used to perform a de facto model-independent analysis just relying on the TAO measurement. The energy segmentation of the parametrization was chosen to be the same variable definition starting from 30 keV as described in chapter 7.3.3.
Figure 55 shows the distribution of the calculated $\Delta\chi^2$ for the combined JUNO+TAO fit for each dataset containing the fine structure-like fluctuations as well as Gaussian fits to the histograms. A more detailed comparison is shown in figure 92 in appendix D which displays a sample-wise comparison of the $\Delta\chi^2$ values for the 100 spectra with fluctuations of 1%, 5%, and 10% for the combined JUNO+TAO fit as well as the JUNO only fit. The right panel of the same figure additionally displays the distributions of the $\Delta\chi^2$ for both fits and all three fluctuation amplitudes.
To evaluate and compare the improvement by the inclusion of the TAO spectrum in the analysis, the mean and standard deviation of the Gaussians are shown in figure 56 depending on the different fluctuation amplitudes and the varying energy widths for both the JUNO+TAO and JUNO only fits. It is clearly visible that the mean of the $\Delta\chi^2$ distribution is in good agreement with the Asimov value of the combined JUNO+TAO fit without any fine structure fluctuations (see figure 56a). The inclusion of the TAO spectrum in the fit to constrain the spectral parameters yields a significant reduction of the width of the distributions compared to the JUNO only case by more than a order of magnitude (see figure 56b). For larger energy widths and amplitudes of the fluctuations, the standard deviation of the distribution is increasing, but the increase is much less compared to the JUNO only case. As the spectral weights in the spectrum parametrization are now constrained by the TAO measurement, the differences between the observed data with fluctuations and the smooth model are taken into account reducing the width of the distribution. However, it is still observed that the width of the $\Delta\chi^2$ distribution is still dependent on the energy width and fluctuation amplitude of the fluctuations.
It has to be emphasized that these investigations are exemplary tests how fine structure-like fluctuations of various size and shape affect the NMO sensitivity and how well these effects can be reduced by using the TAO spectrum as constraint. While the inclusion of TAO in comparison to the JUNO only case shows this large improvement, the overall $\Delta\chi^2$ distribution in the JUNO+TAO case still shows a standard deviation of $\sim$ 0.2 for fluctuations of up to 10%. However, these large fluctuations are an extreme case which is not expected by the actual fine structure in the reactor antineutrino spectrum. With this in mind, the TAO measurement can even help to restore most of the sensitivity in very unlikely cases of large fluctuations. The case of a more realistic fine structure based on the summation model will be discussed in the following.

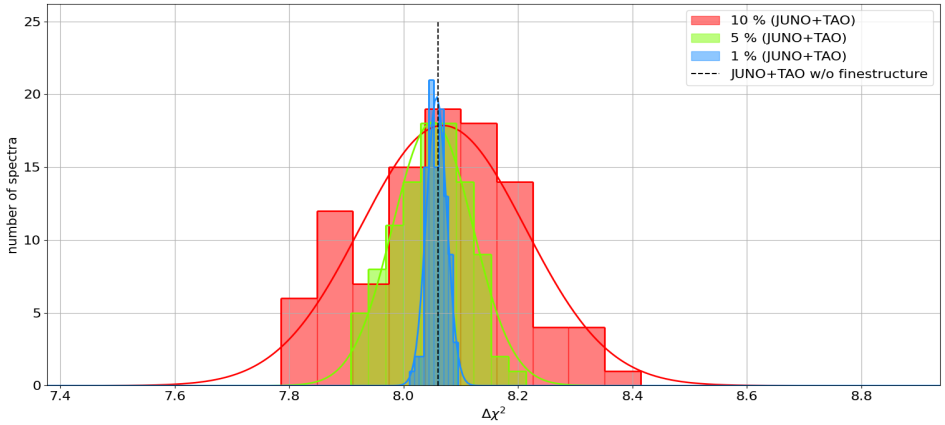

(a) 1 keV

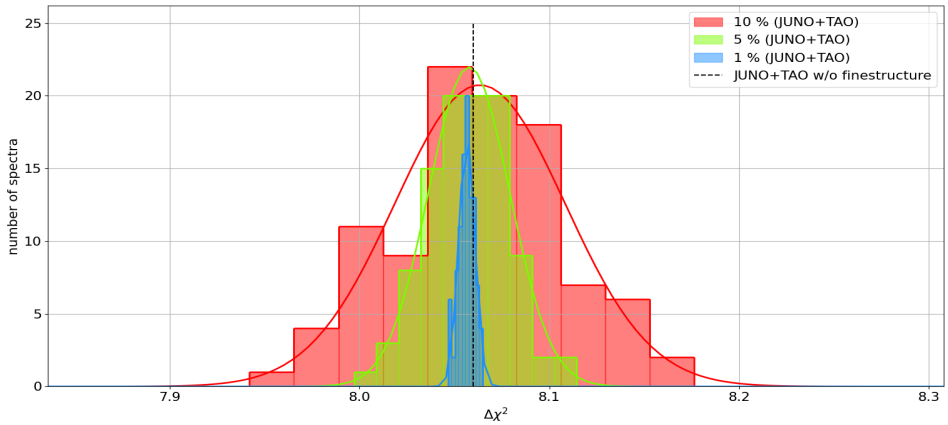

(b) 10 keV

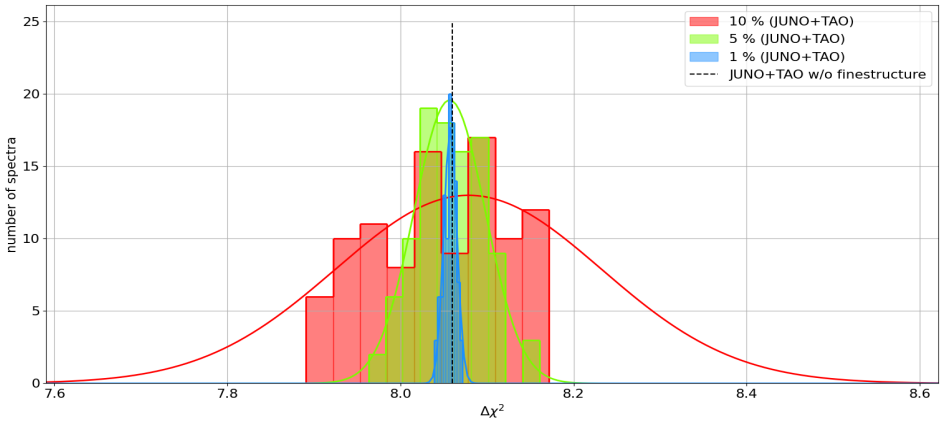

(c) 100 keV

Figure 55: Distribution of $\Delta\chi^2$ values assuming a true NO for sets of 100 spectra with fluctuation of 1% (blue), 5% (green), and 10% (red) for the combined JUNO+TAO fit as well as Gaussian fits to the histograms (solid colored lines). The dashed black line indicates the $\Delta\chi^2$ for the case without fine structure. These results are shown for the fluctuation energy widths (compare chapter 6.1.1) of 1 keV (a), 10 keV (b), and 100 keV (c).

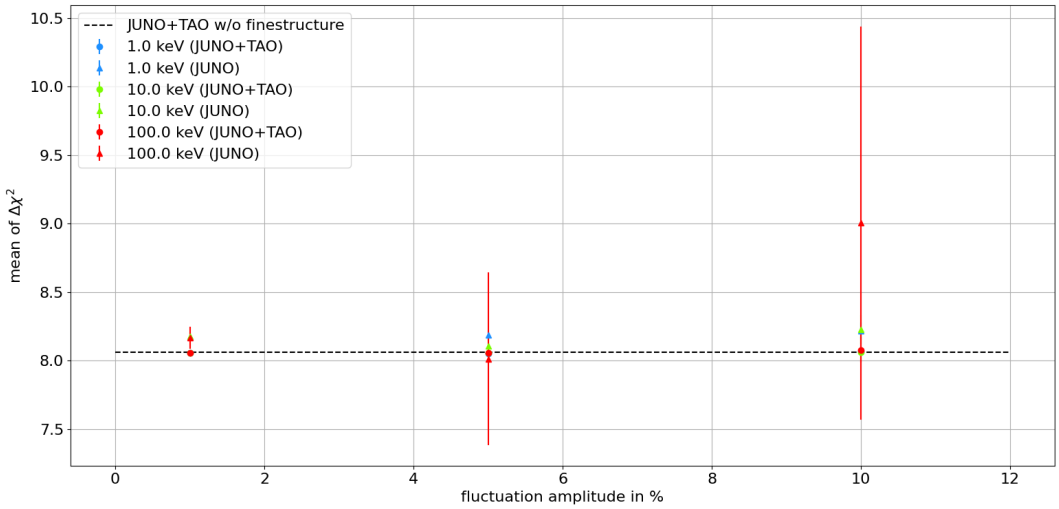

(a) Mean of $\Delta\chi^2$

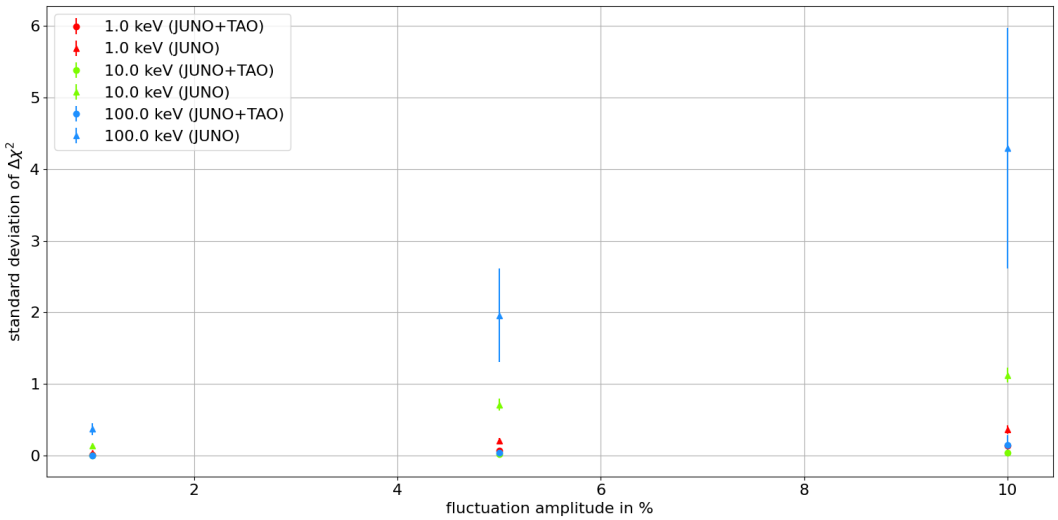

(b) Standard deviation of $\Delta\chi^2$

Figure 56: Mean (a) and standard deviation (b) of the $\Delta\chi^2$ distributions for each set of 100 analyzed spectra with fluctuation energy widths of 1 keV (blue), 10 keV (green), and 100 keV (red) as a function of the fluctuation amplitude for the combined JUNO+TAO fit (circles) as well as the JUNO only fit (triangles). The dashed black line in figure (a) indicates the Asimov $\Delta\chi^2$ for the case without fine structure.

8.3 NMO sensitivity for summation spectra with fine structure

In chapter 7.3 it was discussed how the NMO sensitivity of the JUNO detector alone is affected if there is an unknown fine structure in the reactor antineutrino spectrum that originates from the summation of the individual beta decay spectra. Now, we will also use the measurement of the TAO spectrum to constrain the spectral weights in the fitmodel in a simultaneous combined fit of the JUNO and TAO data. Therefore, the same 1000 generated summation spectra with Daya Bay-based rate and shape correction are used to calculate the estimated JUNO and TAO spectrum to be able to compare the result with the JUNO only case. Since the actual representation of the fine structure is not well-known, the preferred method is again a complete model-independent fit which means that the spectral weights are treated as free parameters as already done in chapters 8.1 and 8.2. Therefore, no information on the fine structure is included in the model. The combined JUNO+TAO fit was performed for all 1000 spectrum samples for assumed true normal and inverted ordering. Figure 57 shows the distribution of the $\Delta\chi^2$ for both assumed true orderings as well as the Asimov $\Delta\chi^2$ value for the case without fine structure and the case where the fitmodel is based on the average spectrum of all 1000 individual summation spectra.
For a true NO the mean of the distribution is $\overline{\Delta\chi^2} = 8.080 \pm 0.001$ (95% C.L.) and the standard deviation is 0.013 ± 0.001 (95% C.L.). Compared to the JUNO only case with a 5% constraint on the spectral parameters (see figure 51 in chapter 7.3.3) this is an increase in the average $\Delta\chi^2$ of 1.18 ± 0.03. Additionally, the standard deviation of the distribution is reduced from 0.30 ± 0.04 by 0.287 ± 0.04 proving the ability of TAO to correct differences for any individual fine structure.

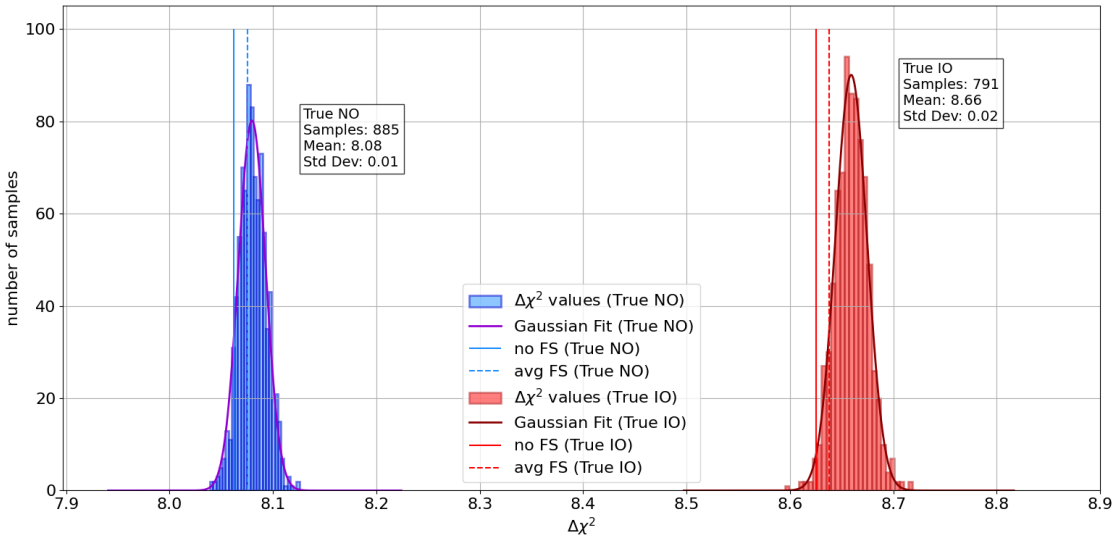

Figure 57: Distribution of the $\Delta\chi^2$ for the same set of 1000 tested summation spectra with assumed true NO (blue) and IO (red) as well as the Asimov $\Delta\chi^2$ value for the case without fine structure (solid vertical lines) and the case where the Asimov data and fitmodel are based on the average spectrum of all 1000 individual summation spectra (dashed vertical line). Additionally, Gaussian fits to the distributions are displayed with the respective mean and standard deviations (Std Dev) shown in the boxes. The number indicated as "Samples" refers to the actual number of fits that converged and results in a valid $\Delta\chi^2$ value which is not the case for all 1000 analyzed spectra.

For an assumed true IO the mean of the distribution is $\overline{\Delta\chi^2} = 8.6592 \pm 0.0007$ (95% C.L.) which is larger compared to the NO case, however also expected as this increase is also observed in the case without fine structure. The standard deviation of the distribution is 0.0154 ± 0.0007 (95% C.L.) which is comparably narrow as in the NO case. In conclusion, the NMO sensitivity is affected in a similar way for both possible mass orderings.
However, there are a few findings that should be discussed in more detail. First, the Asimov value for the average summation spectrum with 8.075 for NO and 8.638 for IO is slightly lower than the corresponding mean values of the distributions. A possible explanation is that the average spectrum is build by calculating the average flux of all spectra for each energy which may cause larger fine structure effects in individual spectra to cancel out leading to the difference in the $\Delta\chi^2$.
Second, the sensitivity is larger in case of fine structure compared to the case without. This can mainly be explained by the difference of the fission fractions between the Daya Bay reactors and the JUNO reactors. To correct the spectrum models for the reactor anomaly and 5-MeV-bump (see chapter 6.3), the total spectrum is calculated using the fission fractions from the Daya Bay experiment and a correction factor is retrieved from the ratio to the Daya Bay data. The spectrum of each single isotope is then corrected according to the total correction factor to fit the data. This leads to a small shape difference between the spectra when the total spectrum is calculated with the different fission fractions for JUNO although they have been corrected to the same data. Figure 58 shows the ratio of the estimated JUNO and TAO spectrum after 6 years of data taking to the same spectrum using the Daya Bay fission fractions for the case without fine structure and the case with average fine structure. It can be seen that the ratios are differing on a sub-percent level showing a different impact of the change of fission fractions for the smooth Huber-Mueller spectrum and the summation spectrum with fine structure. Additionally, this leads also to a difference in event statistics and therefore, a difference on a similar level in the $\Delta\chi^2$ is possible.

Table 16: Expected total number of events measured in the JUNO and TAO detector for input spectra with average fine structure (avg FS) and no fine structure (no FS) calculated with the fission fractions from the Daya Bay experiment (DYB FF) and those from JUNO (JUNO FF).

	JUNO		TAO	
	DYB FF	JUNO FF	DYB FF	JUNO FF
average FS	103761	103764	4577773	4577383
no FS	103763	103674	4577582	4573624

The total expected number of events measured in the JUNO and TAO detectors for both fission fractions are shown in table 16 for the case without fine structure and the average fine structure. The difference in number of events for the average fine structure case between both fission fractions and also between the case with average fine structure and no fine structure for the Daya Bay fission fraction is ≤ 10 (as the spectra are normalized to the Daya Bay spectrum). In contrast, the difference for the number of events between the two fission fractions for the no fine structure case is 89 for JUNO and 3958 for TAO which is a difference of 0.09% in both cases. To analyze the effect of this difference in event statistics, the total flux for the spectrum with average fine structure is reduced by these 0.09% and

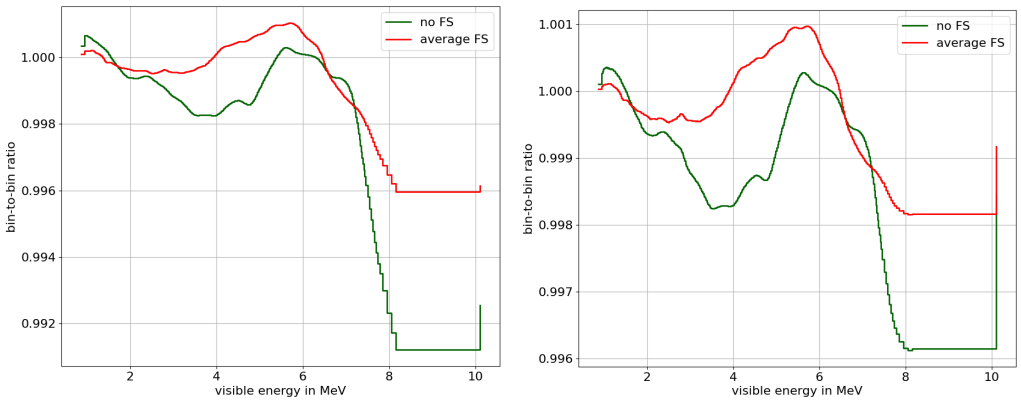

(a) JUNO **(b)** TAO

Figure 58: Ratio of the estimated spectrum after 6 years of data taking with JUNO fission fractions to the same respective spectrum with the fission fractions being changed to the Daya Bay values for the JUNO (a) and TAO (b) detector. The ratio is displayed for the case without fine structure (green) and the case with average fine structure (red).

the fit is repeated to calculate the Asimov $\Delta\chi^2$ for the average fine structure case with same event number as the no fine structure case. With this correction, the difference in the Asimov $\Delta\chi^2$ between the case without fine structure and the average fine structure is reduced from 0.013 to 0.0033 for NO and from 0.013 to 0.0009 for IO. With this result, we can conclude that the largest part of the small difference comes from the small error introduced on the total spectrum rate by the correction of the spectra using different fission fractions while some remaining increase of sensitivity has its origin in the shape difference caused by the fine structure itself. Regarding the approximation of $n\sigma = \sqrt{\Delta\chi^2}$, however, this difference can in general be seen as negligible.
A third finding in the results is that of 1000 summation spectra used as input to the analysis, only 885 in case of NO and 791 for IO produced a valid result while the fit did not converge in the remaining cases. As the fit has 150 free spectral parameters that have to fit the fine structure in the reactor spectrum, it seems that some appearances of the fine structure may lead to the fitter not being able to find the proper minimum due to the complexity of the fit. A possible solution to reduce the complexity of a fit is the application of regularization which will be discussed in the following.

8.4 Application of regularization to the NMO fit

The general idea of regularization is to add a measure of smoothness as an additional constraint to the fit to prevent overfitting of fluctuating adjacent bins. This method was first proposed by Thikhonov [107] and Philips [108]. As the fine structure introduces a lot of fluctuations between adjacent bins, the application of regularization could help to solve the issue of the non-converging fits.

8.4.1 Regularization of the χ^2 function

The regularization is applied by adding an additional regularization term to the statistics function χ^2_{stat} that is minimized [109, 110]. This is adapted to the χ^2 statistics which is minimized resulting in the new form [111]

$$\chi^2_{\text{tot}} = \chi^2_{\text{stat}} + \tau^2 \chi^2_{\text{reg}} \quad , \tag{58}$$

where τ is the regularization strength that defines the amount to which the regularization impacts the statistics function. The regularization strength has to be chosen to achieve a suitable fit. The smaller τ is, the less the regularization impacts the fit while keeping the bias to the χ^2_{tot} small. The larger τ is, the larger the constraint on the fit by the regularization gets, however, also the bias introduced by the additional term increases. For an optimal choice of the regularization strength, the contribution of the regularization term to χ^2_{tot} should be large enough for a good fitresult, but as small as possible to keep the bias as low as possible.
The regularization term has a similar matrix form as the statistics term [109]

$$\chi^2_{\text{reg}} = |Lx|^2 = x^T L^T L x \quad , \tag{59}$$

where x is the vector to be regularized and L the regularization matrix.

8.4.2 Regularization matrix

The choice of the regularization matrix depends on the type of ill-posed problem that should be solved by the regularization. Since the fine structure in the reactor antineutrino spectrum has the form of small fluctuations with sharp edges, two types of regularization based on the first and second derivative were introduced to account for the variations [109, 110].

First Order Derivative Regularization

This regularization method is based on minimizing the square of the first derivative of the vector to be regularized. It penalizes too large differences between consecutive values that could appear in the fit. The regularization matrix is therefore usually given by

$$L_{\text{TV}} = \begin{pmatrix} -1 & 1 & 0 & 0 & \cdots & 0 \\ 0 & -1 & 1 & 0 & \cdots & 0 \\ \vdots & \vdots & \vdots & \vdots & \ddots & \vdots \\ 0 & 0 & 0 & \cdots & -1 & 1 \end{pmatrix} \quad . \tag{60}$$

However, since the energy segments in the analyzed spectrum are not equidistant, the width has also to be taken into account. The variation between consecutive points is then given by

$$\frac{1}{E_{i+1} - E_i} (x_{i+1} - x_i) = \frac{1}{\Delta_{i,i+1}} (x_{i+1} - x_i) \quad . \tag{61}$$

The correct regularization matrix for application on data without equidistant width is

$$L_{\text{TV}} = \begin{pmatrix} \frac{-1}{\Delta_{12}} & \frac{1}{\Delta_{12}} & 0 & 0 & \cdots & 0 \\ 0 & \frac{-1}{\Delta_{23}} & \frac{1}{\Delta_{23}} & 0 & \cdots & 0 \\ \vdots & \vdots & \vdots & \vdots & \ddots & \vdots \\ 0 & 0 & 0 & \cdots & \frac{-1}{\Delta_{N-1,N}} & \frac{1}{\Delta_{N-1,N}} \end{pmatrix} \quad . \tag{62}$$

Squared Second Derivative Regularization

This type of regularization is usually used to penalize non-smooth solutions. Although the fine structure in the reactor antineutrino spectrum actually is non-smooth, a weak regularization could also help to prevent the fitter from fitting too large fluctuations.
For the squared second derivative regularization, the calculation of the matrix is less trivial in case of variable energy segments. To find the proper representation of the second derivative, we use the differential quotient for the second derivative

$$\frac{\mathrm{d}^2x(E)}{\mathrm{d}E^2} = \frac{x'(E_3) - x'(E_1)}{E_3 - E_1} \tag{63}$$

with x' being the first derivative of x.
Inserting also the differential quotient for the first derivative gives

$$\frac{\mathrm{d}^2x(E)}{\mathrm{d}E^2} = \frac{\frac{x(E_3)-x(E_2)}{E_3-E_2} - \frac{x(E_2)-x(E_1)}{E_2-E_1}}{E_3 - E_1} \tag{64}$$

which can be simplified to

$$\frac{\mathrm{d}^2x(E)}{\mathrm{d}E^2} = \frac{x_3}{2\Delta_{23}\overline{\Delta_{13}}} - \frac{x_2}{\Delta_{12}\Delta_{23}} + \frac{x_1}{2\Delta_{12}\overline{\Delta_{13}}} \tag{65}$$

with $x_i = x(E_i)$, $\Delta_{ij} = E_j - E_i$, and $\overline{\Delta_{ij}} = \frac{1}{2}(E_j - E_i)$. The regularization matrix can then be written as

$$L_2 = \begin{pmatrix} \frac{1}{\Delta_{12}\overline{\Delta_{13}}} & \frac{-2}{\Delta_{12}\Delta_{23}} & \frac{1}{\Delta_{23}\overline{\Delta_{13}}} & 0 & 0 & \cdots & 0 & 0 & 0 \\ \frac{1}{\Delta_{12}\overline{\Delta_{13}}} & \frac{-2}{\Delta_{12}\Delta_{23}} & \frac{1}{\Delta_{23}\overline{\Delta_{13}}} & 0 & 0 & \cdots & 0 & 0 & 0 \\ 0 & \frac{1}{\Delta_{23}\overline{\Delta_{24}}} & \frac{-2}{\Delta_{23}\Delta_{34}} & \frac{1}{\Delta_{34}\overline{\Delta_{24}}} & 0 & \cdots & 0 & 0 & 0 \\ \vdots & \vdots & \vdots & \vdots & \vdots & \ddots & \vdots & \vdots & \vdots \\ 0 & 0 & 0 & 0 & 0 & \cdots & \frac{1}{\Delta_{N-2,N-1}\overline{\Delta_{N-2,N}}} & \frac{-2}{\Delta_{N-2,N-1}\Delta_{N-1,N}} & \frac{1}{\Delta_{N-1,N}\overline{\Delta_{N-2,N}}} \end{pmatrix} \tag{66}$$

where the whole matrix was multiplied by a factor of 2 for convenience. Since the contribution from the regularization is multiplied by the regularization strength, a multiplication by a constant value does not change the effect of the regularization. In case of the first energy segment, the derivative was approximated to be the same as in the second one as there is no previous value to approximate the derivative. As this is only one small segment, the effect of an error in the approximation of the second derivative is negligible.

8.4.3 Implementation in GNA

The technique of regularization was introduced to the GNA software as part of this work as an addition to the already available standard χ^2-statistics minimization. The definition of the regularization matrix L and calculation of the regularization contribution $\chi^2_{\mathrm{reg}} = |Lx|^2 = x^T L^T L x$ is done in a transformation *regularization* for each of the two regularization types (defined in *RegTV.cc* for first order derivative and *RegMat.cc* for squared second derivative regularization). The transformation has the inputs *edges* and *values* and the output *reg*, where *edges* defines the bin edges or points of the regularized vector given via *values* input depending on whether the length of the *edges* input array is equal (points) or by one entry larger (edges) than the regularized vector. From the definition of the sample points or edges, the matrix entries are calculated and then the multiplication with the vector is performed. The result for χ^2_{reg} is then provided via the *reg* output.

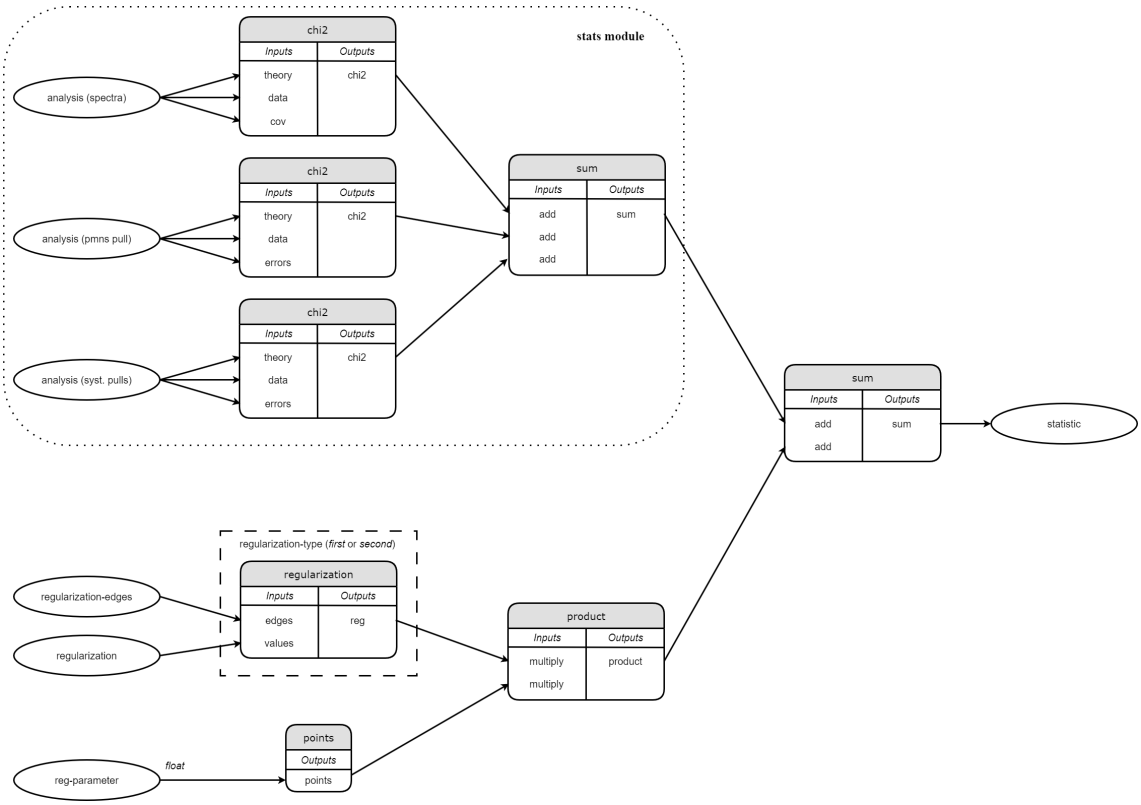

Figure 59: Schematic overview of the *reg_ stats_ v01* module to calculate the statistics to be minimized including regularization. It takes the theory, data and uncertainties/covariance matrix from the defined analysis for the spectrum definition as well as the pull terms and calculates the χ^2 contribution as sum according to equation 50. This part is taken from the already existing *stats* module in GNA. For the regularization part, it calculates the contribution by the regularization via *regularization* transformation from the *regularization-edges* and *regularization* inputs and multiplies the result with the square of the regularization strength given as float via the *reg-parameter* option. The type of regularization can be defined via *regularization-type* option. The product of regularization result and square of the strength is then added to the χ^2 contribution and the sum finally stored as statistics output in the *env* to be used by the minimizer.

The transformation is used to add the contribution from the regularization to the standard calculation of the χ^2 via *reg_ stats_ v01* module. It is based on the existing *stats* module from GNA [85, 86] which calculates the contribution from the statistics definition and is extended by the regularization option which calculates the contribution of the regularization for the given type (*first* or *second*), multiplies it with the square of the regularization parameter and adds it to the statistics contribution. The output of the module can then be passed to the minimizer. A schematic overview of the module is shown in figure 59.

8.4.4 Regularized fitresults

The two previously introduced regularization methods were used to address the issue of the non-converging fits in $\sim 10 - 20\%$ of the spectra with fine structure. Therefore, the spectra that did not yield a valid fitresult were identified and the analysis was repeated with the application of regularization. As the fluctuating fine structure is fitted by the spectral parameters of the spectrum parametrization, the regularization is only applied to

the vector containing the spectral parameters. The most difficult part in the analysis is to find a suitable value for the regularization strength τ. In principle, there is an optimal value for each individual minimization of the χ^2-function which can be determined with the *L-curve* method [112]. Here, the norm of the solution vector is plotted against the norm of the residual difference between model and data which corresponds to the minimum of the χ^2_{stat}. This plot should show a curve shaped like the letter "L". The best regularization parameter produces the (X, Y)-pair in the graph at the point of largest curvature (the kink of the "L"). At this point, the contribution by the regularization is the lowest while still providing a as low as possible residual between model and data. However, since the minimized χ^2_{stat} is calculated from the JUNO and TAO spectrum models and the regularization vector is given by the spectral weights that are only parameters of the spectrum models, this approach is not fully adaptable to this case. For an example spectrum with fine structure, the analysis was performed for various regularization strengths to investigate the appearance of the L-curve. Figure 60 shows the plot of the regularization part against the standard χ^2_{stat} part for different regularization strengths. It can be seen that no typical L-curve is observed, but with an increasing value for τ also χ^2_{reg} and χ^2_{stat} are increasing. Therefore, the regularization strength introducing the smallest bias while still yielding a converging fit is used for further analysis.

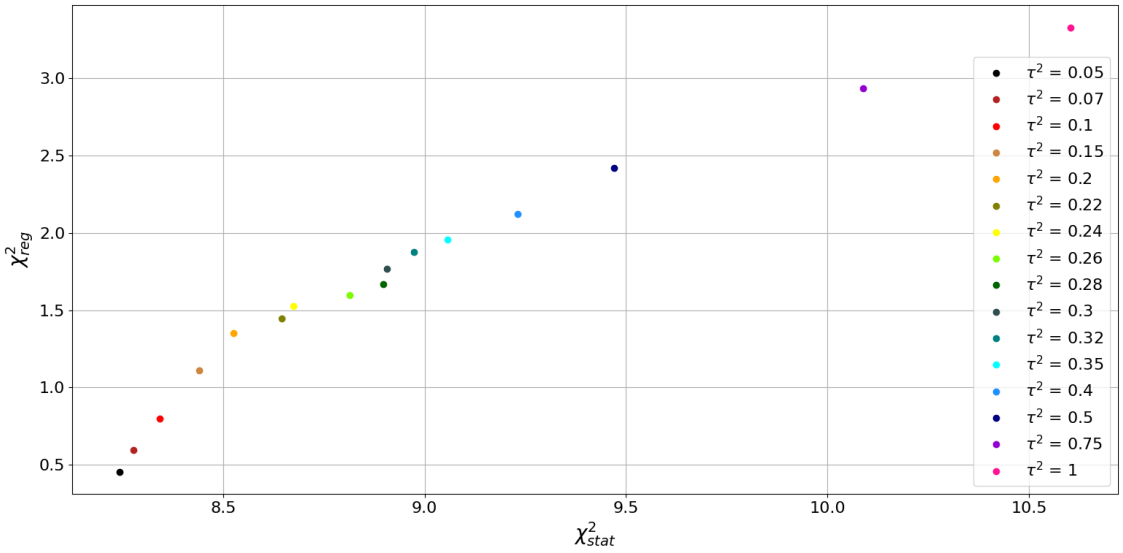

Figure 60: Contribution of the regularization χ^2_{reg} vs. the standard χ^2_{stat} for different regularization strengths τ for an exemplary spectrum with fine structure and assumed true normal ordering for a fit of a model without fine structure and inverted ordering using first order derivative regularization on the spectral weights. For $\tau^2 < 0.05$ the fits did not converge.

Despite the regularization strength, also the type of regularization has to be investigated. The two types based on first and second order derivative that were introduced, were applied to the NMO sensitivity estimation for the spectra that did not converge in the first approach without regularization. For both cases, the same regularization strength of $\tau^2 = 0.05$ was used in first place for comparison. Figure 61 displays the distributions for the $\Delta\chi^2$ for true normal and inverted ordering for no regularization and for the application of first and second order derivative regularization on the spectral weights for the spectra that did not yield a result in the case without regularization.

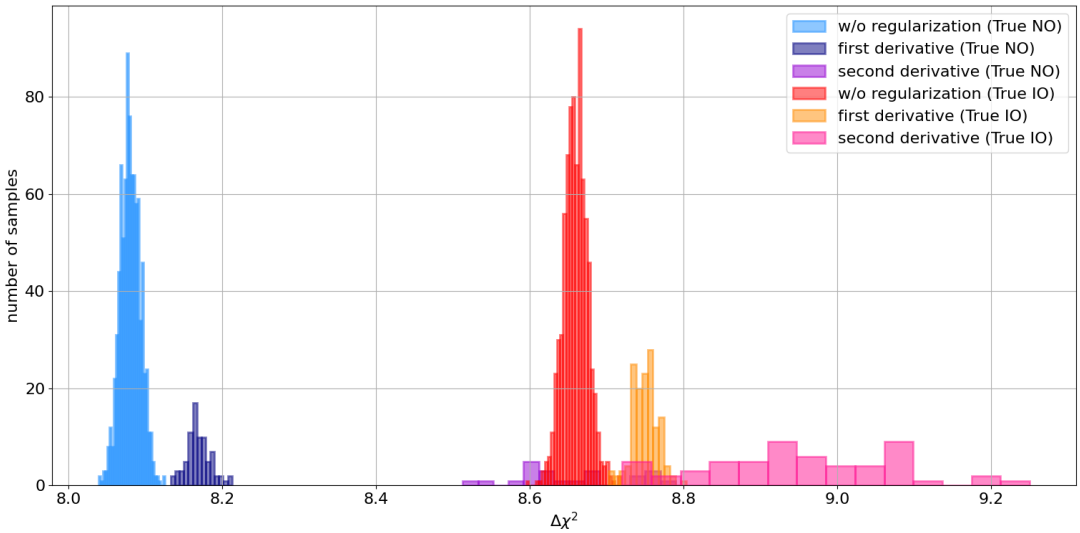

Figure 61: Distributions for the $\Delta\chi^2$ for true normal and inverted ordering for no regularization (lightblue/red) and for the application of first (darkblue/orange) and squared second (violet/pink) order derivative regularization on the spectral weights using a regularization strength of $\tau^2 = 0.05$ for the spectra that did not yield a result in the case without regularization.

In both cases, the regularization adds some average bias to the $\Delta\chi^2$ distribution which is larger in case of the squared second derivative regularization. However, this could possibly be controlled by a different regularization strength. While the resulting distribution for first order derivative regularization maintains a Gaussian shape with comparable width, the application of squared second derivative regularization gives a very broad distribution. In addition, for the chosen regularization parameter, the first order derivative regularization produces a converging fit in 80 of 115 (true NO) and 144 of 209 (true IO) cases while the squared second derivative regularization only gives a valid result in 22 of 115 and 56 of 209 cases respectively. This can also possibly be solved by tuning the regularization strength which, however, takes large computation time as all fits have to be performed individually for a variety of regularization parameters.
In addition, the squared second derivative regularization is designed to introduce a constraint on the smoothness of the data [113]. Since the fine structure in the reactor spectrum is by definition not smooth and cannot be considered as noise in the data, this type of regularization may not be suitable at all causing the worse performance compared to the first order derivative regularization. Therefore, further application of regularization in this work is only done using the first order derivative regularization.

As observed in the previous comparison of the regularization types, not all spectra yield a valid result raising the necessity to tune the regularization parameter. This has been done by increasing the regularization strength for the spectra that did not produce a converging fit with lower regularization strength until it yields a valid result. The distributions of the $\Delta\chi^2$ for true NO and IO in dependence of the regularization parameter is shown in figure 62. In both cases, a regularization strength was found to produce a converging fit for each spectrum sample, however, it introduces the expected bias to the $\Delta\chi^2$ which increases for larger values of the regularization parameter. Since the aim is to estimate

an unbiased sensitivity value, the resulting model parameters from the regularized fit are used in a second step as start values to an unregularized fit. Although the minima for the unregularized and the regularized fit are not the same, they may be closer to each other than to the initial input model. With this assumption, the regularization as intermediate step could help the fitter to find the global minimum of the unbiased $\Delta\chi^2$.

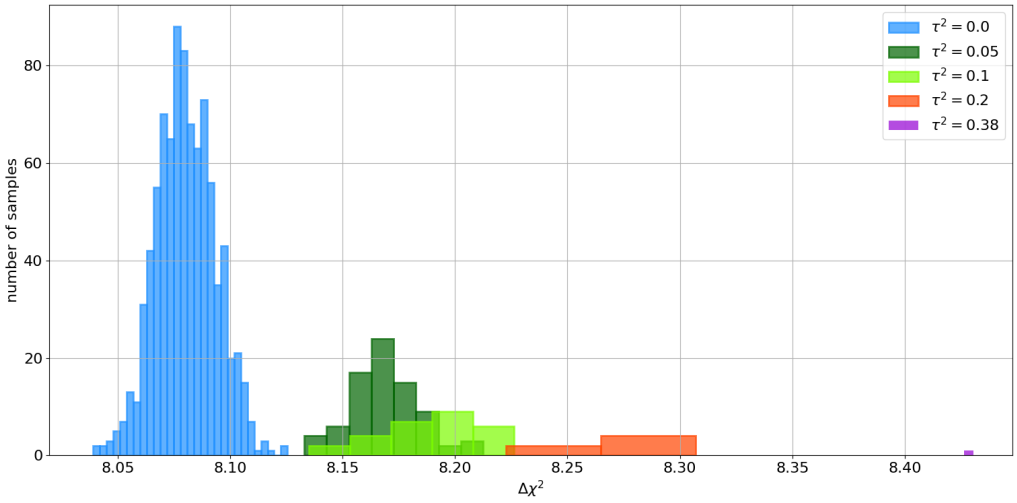

(a) True NO

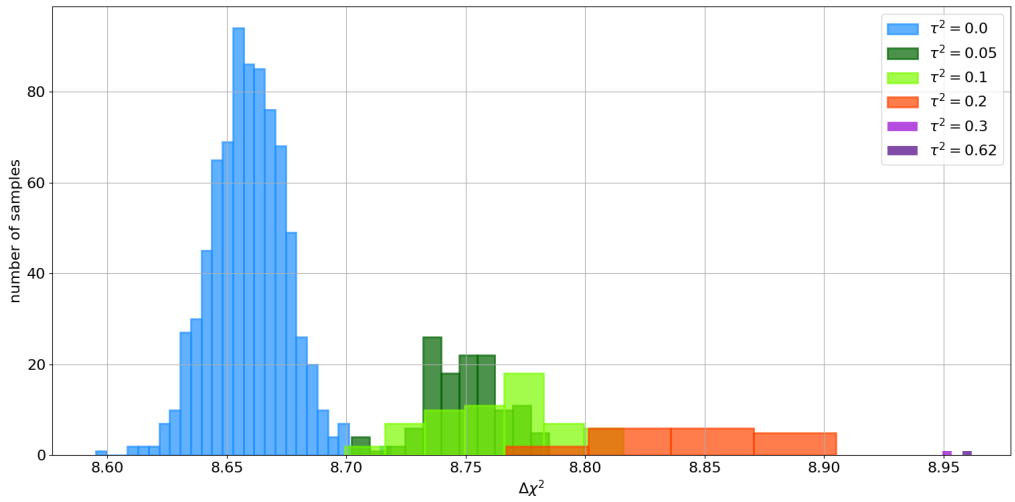

(b) True IO

Figure 62: Distributions of the Asimov $\Delta\chi^2$ for 1000 different spectra with fine structure in case of assumed true normal (a) and inverted (b) mass ordering for the respective lowest tested values of the square of the regularization strength for first order derivative regularization on the spectral weights that lead to converging fits.

8.4.5 Refitting the regularized model

To get an estimation of the NMO sensitivity without any bias introduced by the regularization, the resulting model from the fit with first order derivative regularization with its corresponding best fit values is used as input fitmodel to a second analysis which uses

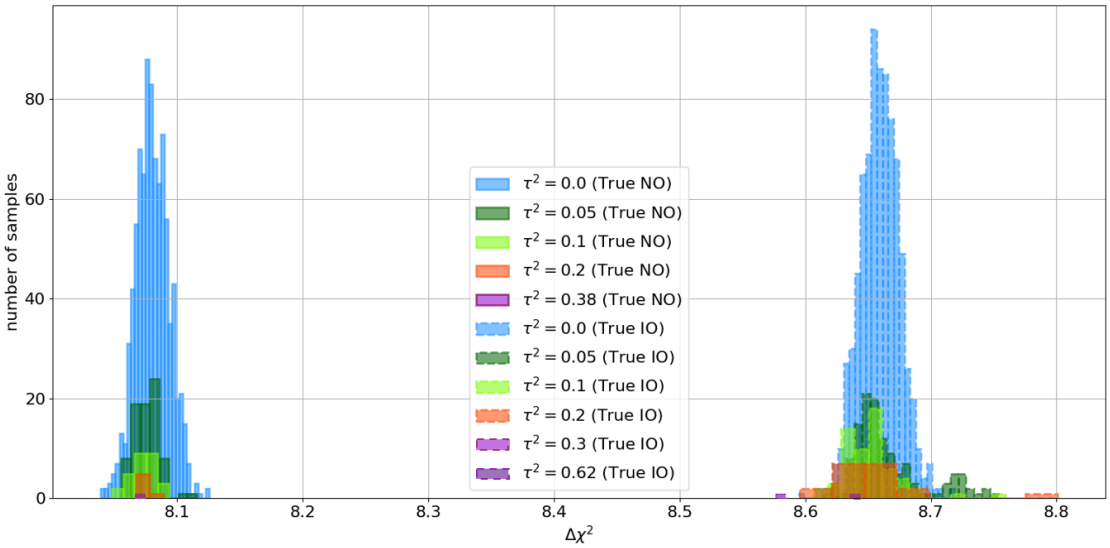

Figure 63: Distributions of the Asimov $\Delta\chi^2$ for the 1000 analyzed summation spectra with fine structure after using the resulting fitmodel of the regularized fit as input model to a standard χ^2 fit without regularization for true normal (solid) and inverted (dashed) ordering. The colors indicate the square of the regularization strength used to compute the input model via regularized fit as shown in figure 62.

the minimization of the standard χ^2-statistics without any form of regularization. This is done for all summation spectra with fine structure that did not yield a valid result without regularization in first place and were analyzed using regularization. Figure 63 shows the distributions of the Asimov $\Delta\chi^2$ for all 1000 spectra with fine structure after using the resulting fitmodel of the regularized fit as input model to a standard χ^2 fit without regularization for true NO and IO. It can be seen that most of the spectra that were reanalyzed after regularization are now showing a similar distribution for the $\Delta\chi^2$ as in the original case without regularization. This shows that the application of regularization can be used as a technical tool to make the fit converge. However, for true inverted ordering, the resulting distribution still shows 22 spectra that yield a $\Delta\chi^2 > 8.7$ which do not fit the Gaussian distribution. This could again be caused by a fitting problem. If the χ^2-statistics has local minima near its global minimum, the fitter can converge into one of the local minima if the input model is too close to one of these. To investigate this possibility, the corresponding spectra were analyzed again increasing the regularization parameter to produce a different input model for the unregularized analysis.
For the spectra not converging to the global minimum with $\tau^2 = 0.05$ the regularization parameter was increased to $\tau^2 = 0.075$, $\tau^2 = 0.1$, and $\tau^2 = 0.15$ depending on whether it produced a valid fitresult. For the case with the original $\tau^2 = 0.1$ and $\tau^2 = 0.2$ it was increased to $\tau^2 = 0.15$ and $\tau^2 = 0.25$ respectively. The distribution of the $\Delta\chi^2$ for these 22 reevaluated spectra for a fit without regularization using the new regularized input models is shown in figure 64. It can be seen that the $\Delta\chi^2$ for the 22 spectra now follows a Gaussian distribution that is in better agreement with the original unregularized distribution. Although the regularization proves to be a useful tool to enable the fitter to converge to a minimum, the regularization parameter still has to be chosen carefully in each case to reach the actual global minimum of the $\Delta\chi^2$.

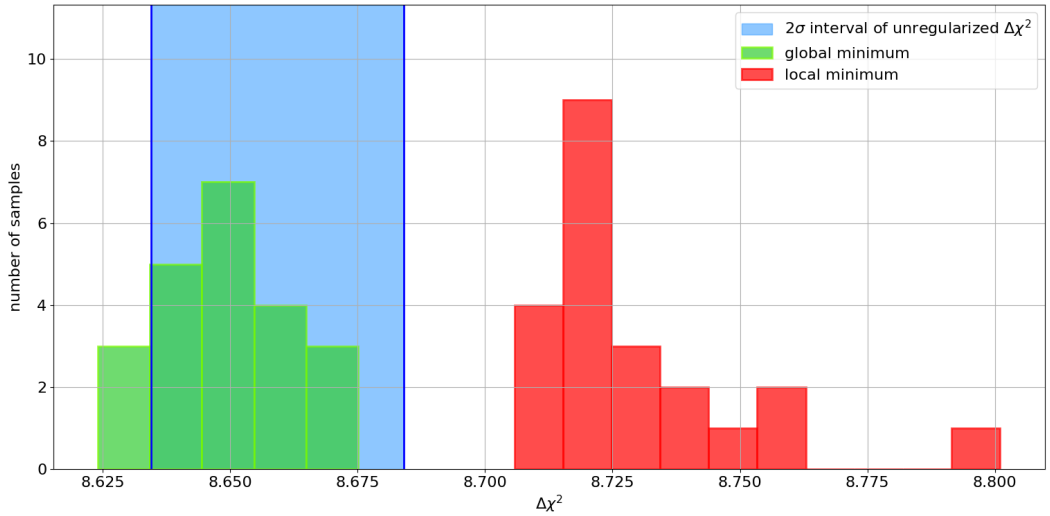

Figure 64: Distribution of the Asimov $\Delta\chi^2$ for the 22 spectra not converging to the global minimum with the input model from the original regularization approach (red) which correspond to the outliers of the distribution for a true IO shown in figure 63 and the respective results with optimized input model (green). Therefore, the original regularization parameter of $\tau^2 = 0.05$ was increased to $\tau^2 = 0.075$, $\tau^2 = 0.1$, and $\tau^2 = 0.15$ depending on whether it produced a valid fitresult. For the case with the original $\tau^2 = 0.1$ and $\tau^2 = 0.2$ it was increased to $\tau^2 = 0.15$ and $\tau^2 = 0.25$ respectively. The blue shaded area displays the region of two standard deviations of the unregularized result for true IO as shown in figure 57.

The final result for the Asimov $\Delta\chi^2$ for true NO and IO including the results from the spectra analyzed using the regularization technique to make the fit converge to its global minimum is shown in figure 65. For an assumed true normal ordering, the mean of the $\Delta\chi^2$ is $\overline{\Delta\chi^2} = 8.079 \pm 0.001$ (95% C.L.) with a standard deviation of the distribution of 0.013 ± 0.001 (95% C.L.) which is still comparable to the original result discussed in chapter 8.3 and still shows the same difference to the case without fine structure due to the different rate caused by the difference in fission fractions between Daya Bay and JUNO. The same is observed for a true inverted ordering with $\overline{\Delta\chi^2} = 8.657 \pm 0.001$ (95% C.L.) and a standard deviation of the distribution of 0.016 ± 0.001 (95% C.L.). Due to the regularization technique, all analyzed spectrum samples yield a valid result that fits the overall distribution which shows that the fine structure in the reactor antineutrino spectrum does not have any negative effects on the NMO sensitivity for the combined JUNO+TAO analysis for the given energy resolution and 6 years of data taking.

8.5 Comparison to the official JUNO sensitivity

The official median sensitivity to reject the wrong NMO hypothesis with JUNO was published in [45] to be 3σ (3.1σ) for a true NO (IO) with an exposure of $6.5\,\text{years} \times 26.6\,\text{GW}_{\text{th}}$. The published analysis was performed by three independent groups using the same inputs but individual software to compute the IBD spectrum prediction and evaluate the sensitivity. One of the three groups used the GNA software that was also used throughout this work (see chapter 5.1), however, this work was performed independently from the analysis published in [45] as there no fine structure was considered.

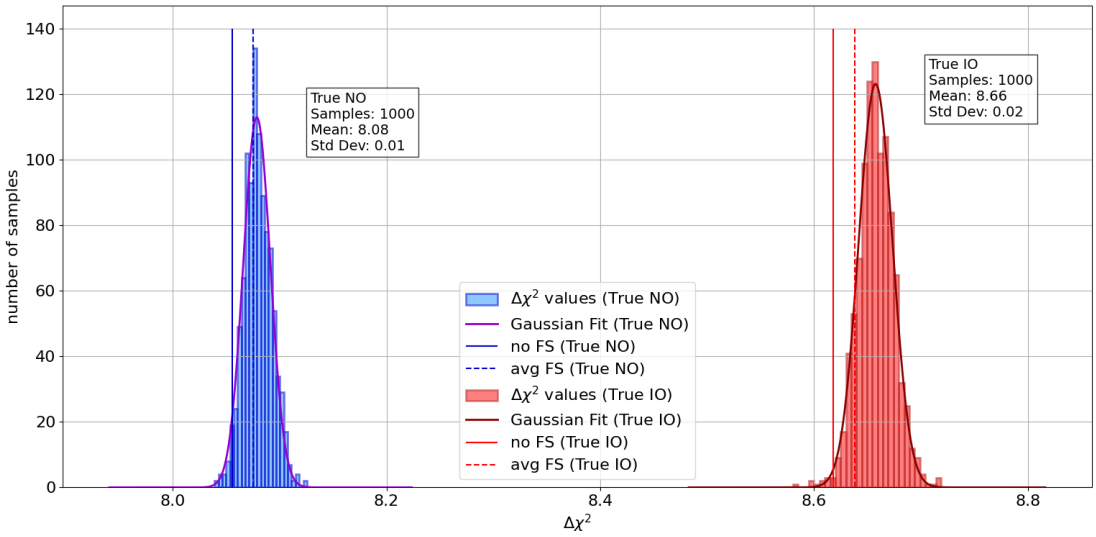

Figure 65: Distribution for the Asimov $\Delta\chi^2$ for assumed true NO (blue) and IO (red) of all 1000 analyzed spectra including the results from the spectra analyzed using the regularization technique to make the fit converge to its global minimum with the corresponding Gaussian fits. Additionally, the Asimov $\Delta\chi^2$ value for the case without fine structure (solid vertical lines) and the case where the Asimov data and fitmodel are based on the average spectrum of all 1000 individual summation spectra (dashed vertical line) are displayed. The boxes show the respective mean and standard deviations (Std Dev) for the Gaussian fits to the distributions.

The analysis in this work presented in chapters 7 and 8 therefore differs concerning the input reactor antineutrino spectrum models (see chapter 6). Additionally, further differences between the presented results and the published sensitivity are the different reactor baselines for the TAO detector (see chapter 3.4) and the shorter DAQ time of 6 years compared to the 7.1 years stated in [45]. Moreover, the analysis in [45] used updated rates for the accidental and fast neutron backgrounds in TAO as well as an updated geoneutrino spectrum.
Using equation 69 to convert the $\Delta\chi^2$ presented in this work, this leads to the sensitivity of 2.8σ (2.9σ) for a true NO (IO) with an exposure of $5.5\,\text{years} \times 26.6\,\text{GW}_{\text{th}}$ which is different in exposure and sensitivity due to the discussed differences.
The updated reactor baseline of the TAO detector, backgrounds and geoneutrino spectrum were included in the analysis in this work at a later point. Updated results on the NMO sensitivity including the fine structure will be presented in chapter 9.2 [e]. Additionally, the dependence of the sensitivity on the DAQ time of the experiment is addressed in chapter 9.4 to make the results of this work comparable to the official median sensitivity without fine structure presented in [45].

[e]The results presented in chapters 9.3 and 9.4 also include the updated baselines and backgrounds as in chapter 9.2

9 Systematic impacts on the NMO sensitivity

I have to say that I've always believed perfectionism is more of a disease than a quality. I do try to go with the flow but I can't let go.

– Rowan Atkinson - *British Actor and Comedian*

In this chapter, studies on the impact of the binning of the spectrum parametrization, the updated TAO baseline, the energy resolution of the TAO detector, and the data taking time of the detectors on the NMO sensitivity of JUNO+TAO in presence of the fine structure in the spectrum are discussed. The general analysis remains unchanged from the spectrum prediction presented in chapters 5.2 and 7.3.3 as well as the combined sensitivity estimation described in chapter 8 except for the specific changes introduced for the analysis which is described in the individual section.

9.1 Influence of spectrum parametrization binning on NMO sensitivity

As described in chapter 7.3.3, the reactor antineutrino spectrum in the fitmodel is given as a parametrization (see equation 52). In previous analyses, the standard energy segmentation *var-30* was used which starts with a segment width of $w = 30\,\text{keV}$ and increases to meet the criterion of $w > 1.5\sigma(E)$ as well as to fulfill the requirement of more than 500 events in a segment to have suitable statistics [87]. A representation of the definition of the energy segments is shown in figure 66.
Since the spectral weights defined by the spectrum parametrization have to compensate for the small spectral differences caused by an unknown fine structure in the reactor antineutrino spectrum, it is important to check the proper definition of these energy segment definitions. In addition to the *var-30* option, some more energy segment definitions have been tested [87].
Due to the smearing caused by the energy resolution, a fraction of events ends up in neighboring bins depending on the chosen width of the segments. Figure 67 shows that for a width similar to the energy resolution, only less than 40% of the original events are left in the same segment while already around 50% are shifted into the first neighboring segments. Therefore, definitions with a width less than the energy resolution are not considered. Additionally, too large segments would reduce the ability to resolve the spectral effects and the sensitivity obtained from the combined fit could be biased as the model does not fully correspond to the data. With these constraints, segment definitions with $w > \sigma(E)$ (*var-20*) and $w > 2\sigma(E)$ (*var-40*) are used. A visualization of these definitions is shown in figure 68.

For cross-check, a definition with mostly constant segment width for the three constraints was additionally tested. A detailed summary with the definitions of the energy segments is given in table 17.

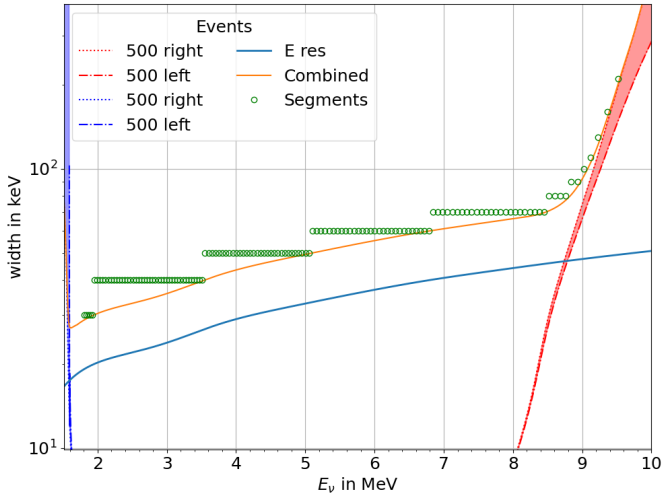

Figure 66: Width of the energy segments of the spectrum parametrization for the *var-30* option as a function of the energy at the left edge of the segment (green). The blue curve displays the energy resolution of the TAO detector. The blue and red curves show the low and high energy limits for the left and right edges above which the requirement of 500 events per segment is fulfilled. As the criterion for the *var-30* option is $w > 1.5\sigma(E)$, the orange curve (combination of energy resolution and statistics requirements) is shifted upwards compared to the blue curve. The width of the segments is increased by 10 keV when the criterion is not met anymore yielding the steps in the definition. A detailed definition is given in table 17.

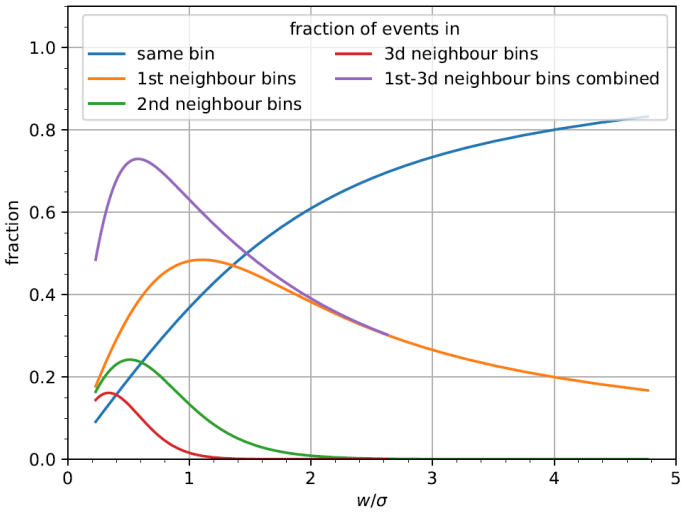

Figure 67: Fraction of events staying in the same segment (blue) or shifted to another segment due to the energy smearing as a function of the ratio of segment width to energy resolution. Figure taken from [87].

Table 17: Definition of the different options for the energy segments of the spectrum parametrization with their corresponding number of resulting segments. The definition gives the edges in MeV (large font) and the step size in keV (small font) up to the next given edge in MeV. For usage in the analysis, the first two segments for the 20 keV and 30 keV options as well as all segments for $E > 8$ MeV are combined to one segment respectively.

Option	Segments	Definition
var-20	172	1.8023, 1.8423, $_{+20...}$, 1.9623, $_{+30...}$, 4.2423, $_{+40...}$, 6.8423, $_{+50...}$, 7.9923, 12.7823
var-30	149	1.8123, 1.8723, $_{+30...}$, 3.2523, $_{+40...}$, 5.1323, $_{+50...}$, 7.2823, $_{+60...}$, 7.9423, 12.7823
var-40	110	1.8023, $_{+40...}$, 2.9623, $_{+50...}$, 4.1123, $_{+60...}$, 5.6123, $_{+70...}$, 7.1523, $_{+80...}$, 7.9523 ,12.7823
const-20	293	1.8023, 1.8423, $_{+20...}$, 7.4423, $_{+50...}$, 7.9923, 12.7823
const-30	196	1.8123, 1.8723, $_{+30...}$, 7.4223, 7.4623, $_{+60...}$, 7.9423, 12.7823
const-40	148	1.8023, $_{+40...}$, 7.4023, 7.4723, $_{+80...}$, 7.9523, 12.7823

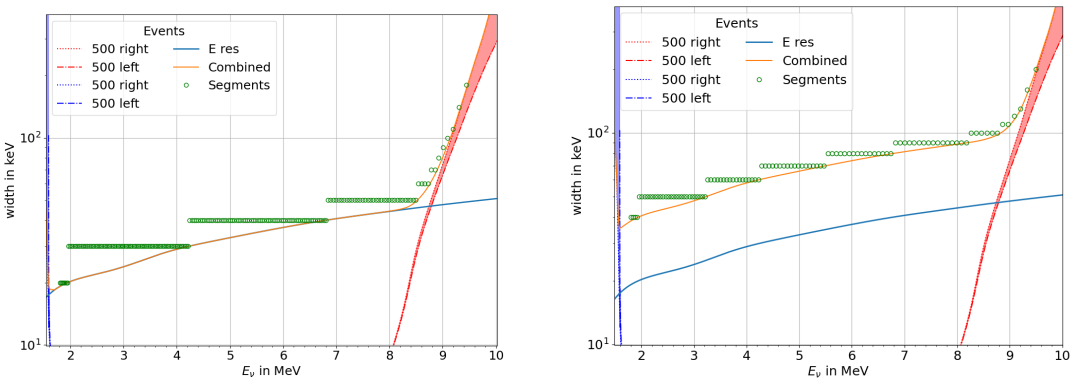

(a) *var-20* **(b)** *var-40*

Figure 68: Definition of the segment options *var-20* (a) with $w > \sigma(E)$ and *var-40* (b) with $w > 2\sigma(E)$. For a more detailed description how to interpret the plot, see caption of figure 66.

Table 18: Number of converged fits for the different energy segmentation options for assumed true NO and IO using a total of 120 spectra with fine structure to generate the Asimov data.

Option	True NO	True IO
var-20	99	106
var-30	108	95
var-40	107	107
const-20	43	21
const-30	107	87
const-40	107	107

9.1.1 NMO sensitivity results

For all six previously defined parametrization options, the NMO sensitivity was estimated for true normal and inverted ordering using 120 spectra with fine structure to generate Asimov data. The distribution of the $\Delta\chi^2$ values for both mass orderings for the energy segmentation options *var-20*, *var-30*, *var-40*, *const-30*, and *const-40* are shown in figure 69. As the *const-20* option causes the fit to be unstable due to the large number of segments, only a small fraction of the spectra gives a valid result and also in case of a smooth spectrum the fit failed, showing that the *const-20* option is not suitable for the analysis at all. The $\Delta\chi^2$ is significantly reduced compared to the other segmentation options for the fraction that produces a result and the width of the distribution is also much larger[f].
The other options in contrast are much more stable which can be also seen in table 18 which displays the number of converged fits from the total of 120 analyzed spectra. While for the *const-20* option only less than one third of the fits converge, the numbers for the other options are more comparable. For options with 40 keV, most spectra give a valid result, which shows that a smaller number of energy segments stabilizes the fit.
Comparing the results for the different options as shown in figure 69 shows the best performance for the *var-30* option for both assumed mass orderings. Figure 70 shows the mean and standard deviations of the $\Delta\chi^2$ distributions for the five options that produce an acceptable fraction of valid results. The standard deviation is in agreement within the 95% C.L. for all options except for the *const-30* option which is in case of an assumed true IO with 0.032 ± 0.004 around twice as large as for the remaining options. Concerning the mean of $\Delta\chi^2$, it is observed that the same starting segment widths give similar results, showing that using constant segments for the entire energy range does not improve the sensitivity but needs more computation time and leads to a broader distribution in the case of the *const-30* option for true IO. In the case of true NO also the mean of $\Delta\chi^2$ is reduced to the level of the 40 keV segment options. Excluding this exception, the same behavior is also observed for the case without fine structure, which again shows the previously discussed lower sensitivity due to the rate and shape correction (see chapter 8.3).
Therefore, the choice of the *var-30* segmentation option for the spectrum parametrization proves to be the most suitable to perform the analyses. An additional justification that the *var-30* option does not give a biased sensitivity can be seen in figure 51 in chapter 7.3.3. For free spectral weights without the constraints by the TAO spectrum, the sensitivity to the NMO is reduced to zero, proving that the spectrum parametrization does not favor any specific mass ordering.

[f]The $\Delta\chi^2$ distributions for both true mass orderings are shown in figure 93 in appendix E for completeness.

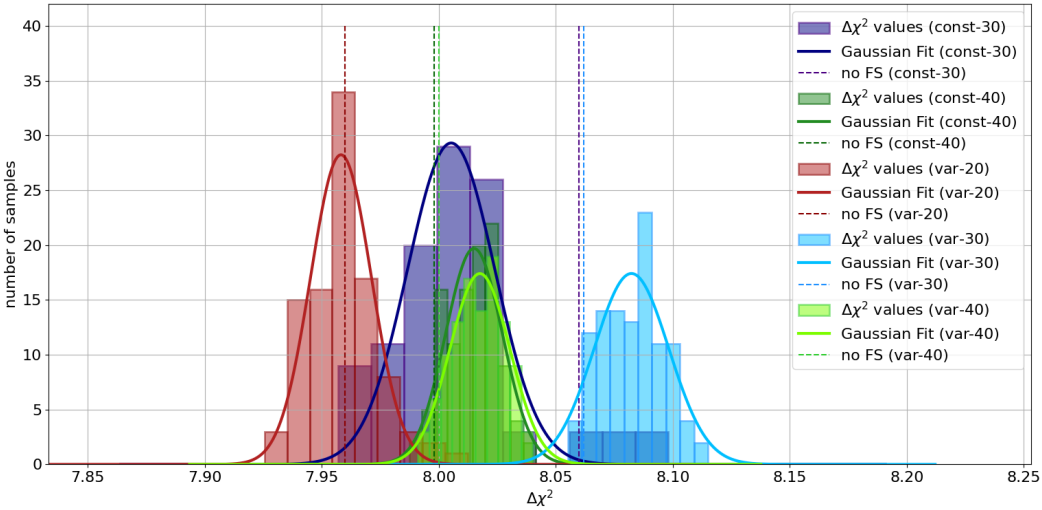

(a) True NO

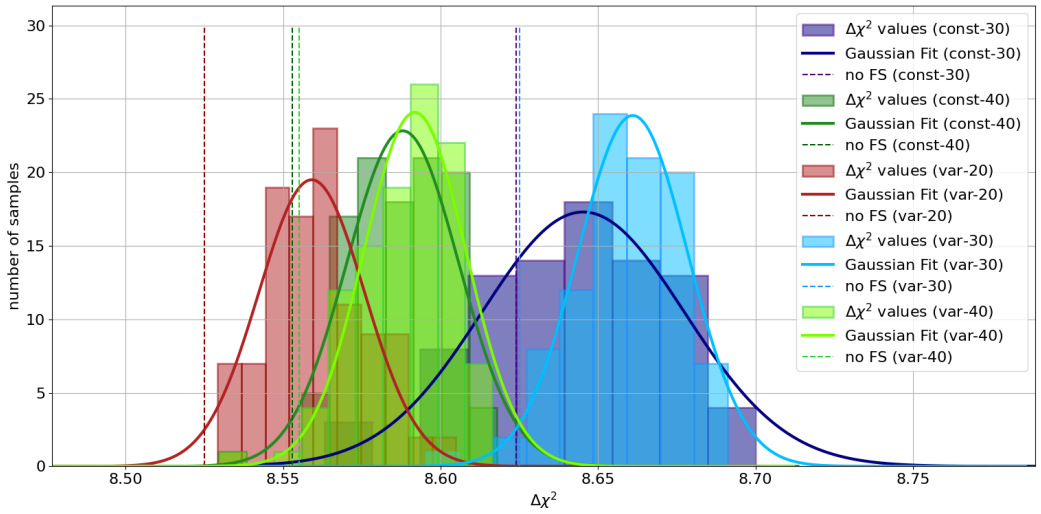

(b) True IO

Figure 69: Distribution of the Asimov $\Delta\chi^2$ for assumed true NO (a) and IO (b) for the energy segmentation options *const-30* (violet), *const-40* (darkgreen), *var-20* (darkred), *var-30* (lightblue), and *var-40* (lightgreen) for a set of 120 analyzed summation spectra with fine structure as Asimov data. The number of bins is chosen as square root of the total number yielding different binwidths for the different histograms as the number of converged fits differs (see table 18). As reference, the $\Delta\chi^2$ for Asimov data without fine structure is shown as dashed vertical lines. Additionally, Gaussian fits to the histograms are shown.

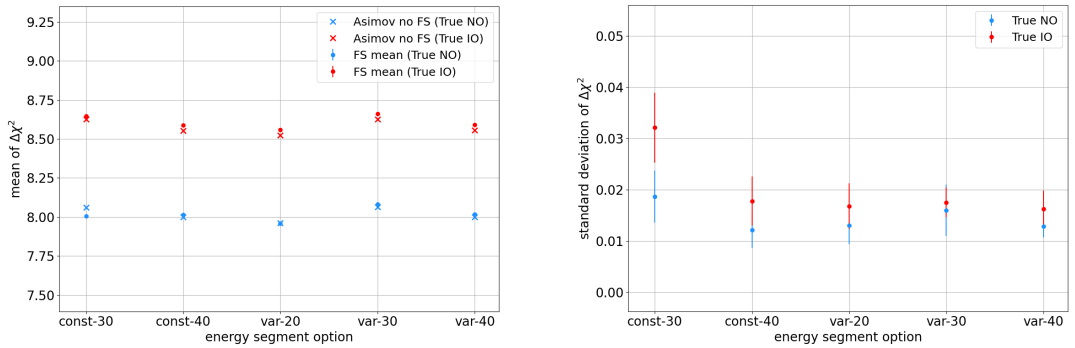

(a) Mean of $\Delta\chi^2$ **(b)** Standard deviation of $\Delta\chi^2$

Figure 70: Mean (a) and standard deviation (b) of the $\Delta\chi^2$ distributions for the energy segment options *const-30*, *const-40*, *var-20*, *var-30*, and *var-40* for assumed true NO (blue) and IO (red). In (a), additionally, the Asimov $\Delta\chi^2$ for the case without fine structure is displayed for each option for comparison.

9.2 Impact by new TAO baselines

As it was described in chapter 3.4, the distance of the TAO detector to the two reactor cores of the Taishan NPP had to be changed from the originally planned value. As the baseline to the closest reactor core is changed from 30 m to 44 m, the flux at the TAO detector location is geometrically reduced by a factor of ~ 2 which has a direct impact on the NMO sensitivity. To investigate this effect, the analysis is repeated in the same way as described in chapter 8 using the updated baseline values for the TAO detector to calculate the expected spectrum measured by TAO. The analysis was performed for 1000 summation spectra with fine structure for both assumed true mass orderings. The resulting $\Delta\chi^2$ distributions are shown in figure 71. Comparing this result to the one with the originally planned baselines shown in figure 65 in chapter 8.4.5, a shift of the average Asimov $\Delta\chi^2$ from 8.08 to 7.81 for true NO and from 8.66 to 8.35 for true IO is observed while the standard deviations of the distributions stay with 0.01 equally small for both mass orderings. This shows that the reduction is caused by the reduced statistics but the ability of TAO to correct for the fine structure is not significantly impacted. The reduction of the average $\Delta\chi^2$ is also observed for the case without fine structure which also shows a smaller value due to the different fission fractions used for the rate and shape correction (see chapter 8.3). Therefore, the change in baseline does reduce the median Asimov sensitivity, however, an additional reduction due to the fine structure is not observed.

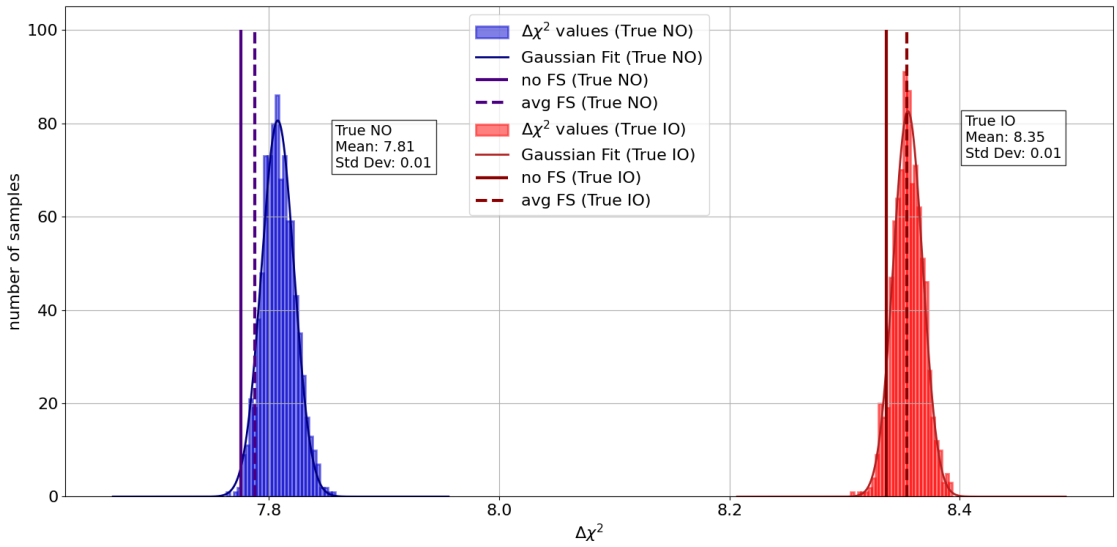

Figure 71: Distribution of the $\Delta\chi^2$ for assumed true NO (blue) and IO (red) as well as the Asimov $\Delta\chi^2$ value for the case without fine structure (solid vertical lines) and the case where the Asimov data and fitmodel are based on the average spectrum of all 1000 individual summation spectra (dashed vertical line) using the updated baseline values for the TAO detector. Additionally, Gaussian fits to the distributions are displayed with the respective mean and standard deviations (Std Dev) shown in the boxes.

9.3 Influence of TAO's energy resolution

The TAO detector is designed to have an energy resolution of better than 2% at 1 MeV to provide a high resolution reference spectrum for the JUNO measurement. As this is an unprecedented value and challenging task, it is worth to check how a different energy resolution of the TAO detector would impact the NMO sensitivity of the combined JUNO and TAO measurement. Therefore, the analysis is performed using a set of summation spectra with fine structure and assumed true normal mass ordering applying the new TAO baseline (see section 9.2) to generate the Asimov dataset for different energy resolutions of the TAO detector. For the calculation of the energy resolution, the parametrization described in equation 16 was used changing the photon statistics parameter a. Additionally, the actual energy resolutions of the JUNO detector and of the Daya Bay experiment ($a = 0.081$, $b = 0.016$, $c = 0.026$) [114] were applied. Figure 72 displays the energy resolution curves that were used for the TAO detector in the analysis to investigate the impact on the NMO sensitivity.

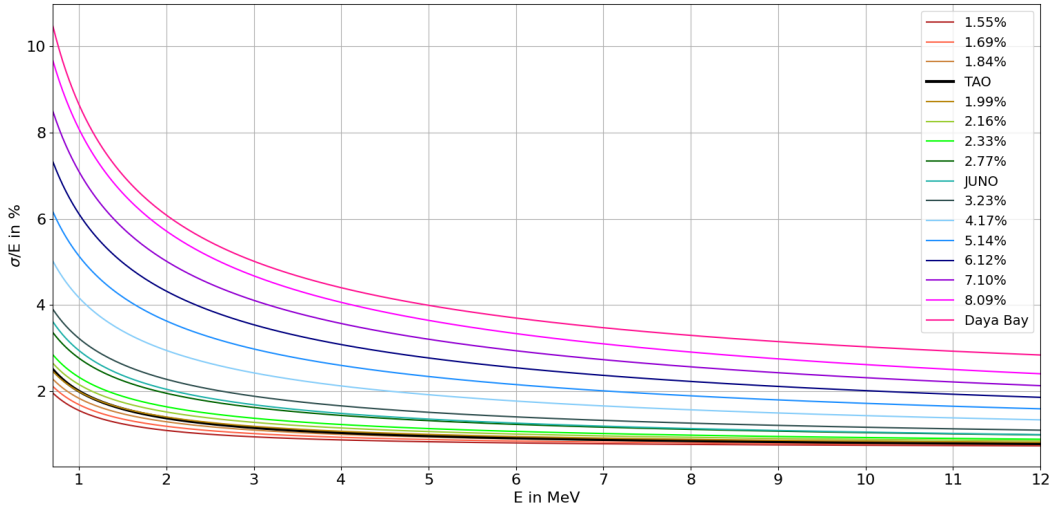

Figure 72: Energy resolution curves of the TAO detector used in the analysis to investigate the impact on the NMO sensitivity. The curves are calculated via the abc-parametrization (see equation 16) varying only the photon statistics parameter a. The given percentage values are the specific values at $E = 1$ MeV. For JUNO and Daya Bay, the actual energy resolution curves are used. The bold black line shows the nominal TAO energy resolution curve for reference.

The distributions of the $\Delta\chi^2$ for the analyzed energy resolutions of the TAO detector for assumed true NO are shown in figure 73. It is observed that the energy resolution of TAO significantly impacts the NMO sensitivity. The mean of the $\Delta\chi^2$ rapidly decreases for resolutions worse than 2.5% at 1 MeV. For an energy resolution comparable to the Daya Bay experiment, the possibility to distinguish between the two mass orderings has nearly vanished with a mean value of $\overline{\Delta\chi^2} = 0.075$. This proves the importance of TAO with its high energy resolution. Using the Daya Bay measurement as reference spectrum does not constrain the spectrum well enough due to the insufficient energy resolution yielding a NMO sensitivity of almost zero. In contrast, a further improvement of the TAO energy resolution beyond 2% would only increase the $\Delta\chi^2$ by around 0.1.

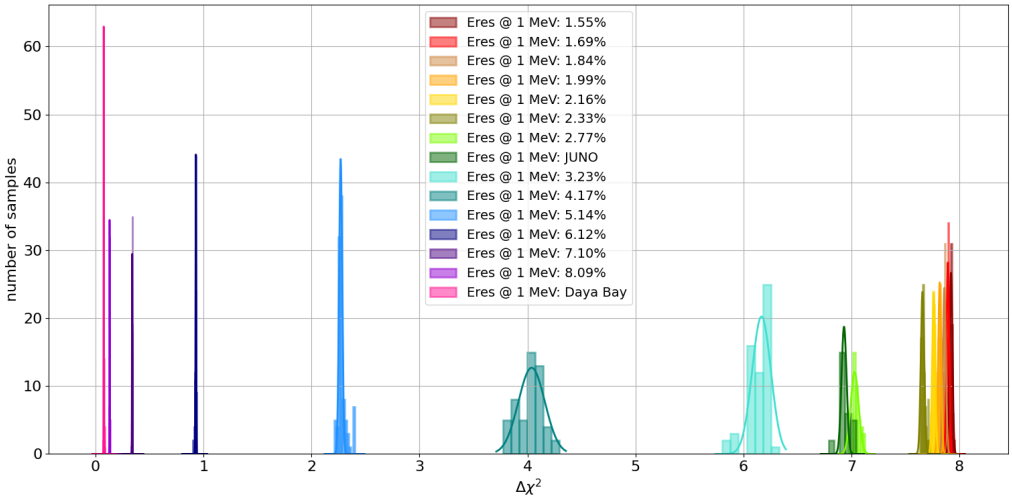

Figure 73: Distribution of the $\Delta\chi^2$ for summation spectra with fine structure and assumed true NO for different energy resolutions at 1 MeV. Additionally, the actual energy resolutions of the JUNO detector (darkgreen) and the Daya Bay experiment (pink) were used. The solid curves show the Gaussian fits to the distributions. As already observed in chapter 8.3, not all fits produced a valid result. While in case of most energy resolutions with 13 of 120 tested spectra only the usual fraction of fits did not converge, some exceptions were observed. Therefore, for some energy resolutions also a larger number of spectra was analyzed to increase statistics. For 2.77% (lightgreen) only 49 of 120, for 3.23% (cyan) 59 of 240, for 4.17% (grayblue) 51 of 240, and for JUNO (darkgreen) 26 of 120 fits did converge.

Figure 74 shows the mean and standard deviation of the $\Delta\chi^2$ distributions for the different analyzed energy resolutions. Additionally, the Asimov $\Delta\chi^2$ for the case without fine structure is displayed. It shows a similar dependence on the energy resolution as the mean in presence of fine structure. Also, the usual lower value due to the statistics difference caused by the different fission fractions when applying the rate and shape correction is observed (see chapter 8.3). However, in the region between 3% and 6% a larger difference is observed. This different behavior can also be seen at the standard deviations of the Gaussian distributions. Below 2.5% and above 6% it is not much affected by the energy resolution of TAO, but within this region, a large increase is observed which resembles some kind of resonance pattern. Since this is the region around the energy resolution of the JUNO detector, there could be a problem of the fitter when the spectral resolution is similar in both detectors and therefore the spectral weights are constraint to the same amount by both detectors. An additional finding is that in this region the number of converging fits is with 30% to 50% significantly lower than for the other energy resolutions ($\sim$ 10%) and also the fit for the case without fine structure for the JUNO energy resolution did not converge, which also indicates the fitting problem. An application of regularization (c.f. chapter 8.4) was not successful in these cases.
One possibility to address this effect is to change the energy segmentation which defines the spectral weights. In the analysis the standard *var-30* option is used which was found to perform best for the actual TAO energy resolution as discussed in section 9.1. An optimization of the energy segments for the different energy resolutions improves the stability of the fit, however, a larger width of the segments does not correctly account for the fine structure and therefore does not reflect a valid sensitivity.

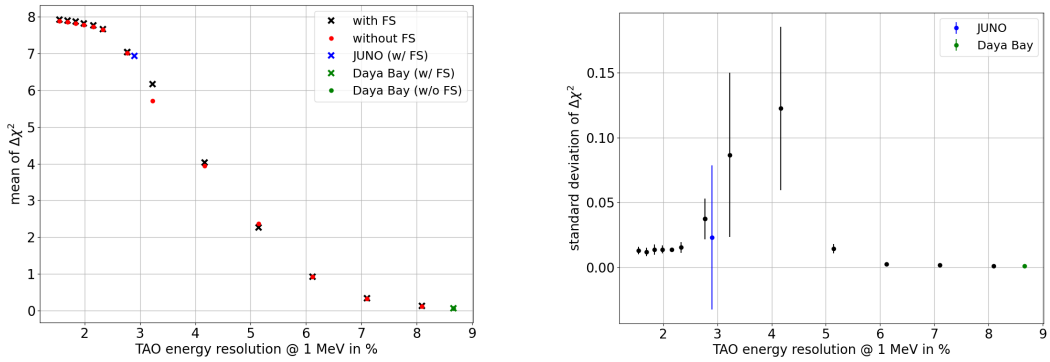

(a) Mean of $\Delta\chi^2$ **(b)** Standard deviation of $\Delta\chi^2$

Figure 74: Figure (a) shows the mean of the $\Delta\chi^2$ for the set of analyzed summation spectra with fine structure (black) and the Asimov $\Delta\chi^2$ for the case without fine structure (red) as a function of the assumed TAO energy resolution. The mean of the distributions using the specific JUNO (blue) and Daya Bay (green) energy resolutions in the presence of fine structure are also shown. For the JUNO energy resolution, the fit in case of no fine structure did not converge and therefore no result is displayed. Figure (b) displays the standard deviation of the $\Delta\chi^2$ distributions obtained from the Gaussian fits for the assumed energy resolutions (black) and for the specific JUNO (blue) and Daya Bay (green) energy resolutions.

9.4 Time evolution of the NMO sensitivity

Another interesting systematic effect is the evolution of the NMO sensitivity with increasing DAQ time. Since the TAO spectrum serves as a high resolution reference spectrum, it is important to investigate how the corrective power to the fine structure evolves with increasing measurement time. Therefore, the standard NMO analysis procedure is repeated using the new TAO baseline values for different periods of DAQ time but same reactor duty cycle according to equations 30 and 31 in chapter 5.2.3.
The analysis was performed using 100 summation spectra with fine structure with assumed true normal and inverted ordering. The resulting $\Delta\chi^2$ distributions are shown in figure 75 for an assumed true NO and IO. The mean of the distributions is increasing with larger DAQ time in both cases as shown in figure 76a which is also in good agreement with the Asimov sensitivity in the case without fine structure. With an exposure of 6.5 years $\times$ 26.6 $\mathrm{GW_{th}}$ reactor power, JUNO will reach a median sensitivity of 3σ (3.1σ) on the normal (inverted) neutrino mass ordering. This is also in agreement with the results from other analysis groups within the JUNO collaboration published in [45]. Additionally, the standard deviation of the distribution for the analyzed summation spectra with fine structure is smaller than 0.05 for a runtime up to 20 years as displayed in figure 76b showing only a small variation in the sensitivity depending on the fine structure. Increasing DAQ time and therefore increasing statistics also causes an approximately linear increase in the standard deviation which is however smaller in case of true IO to which JUNO has an overall higher sensitivity compared to a true NO.

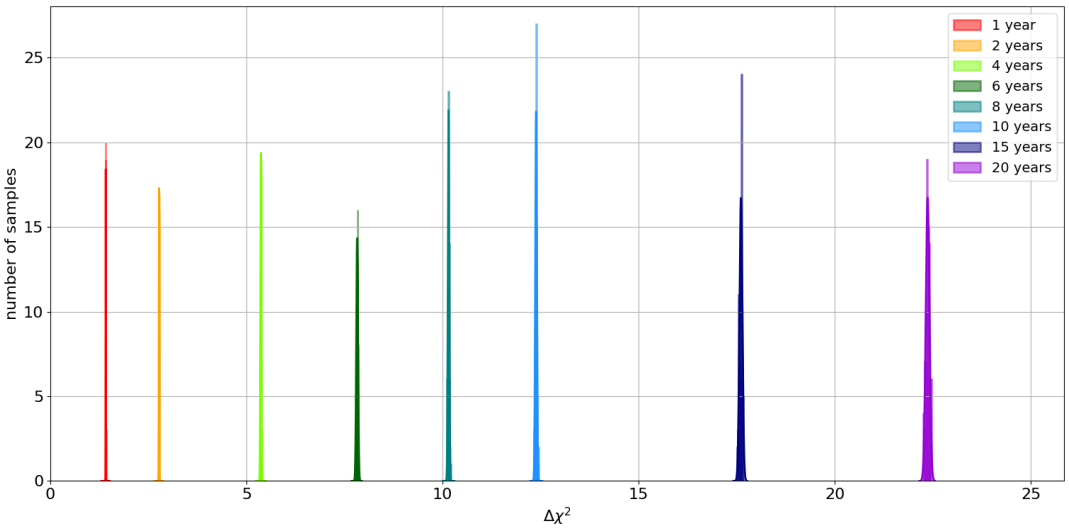

(a) True NO

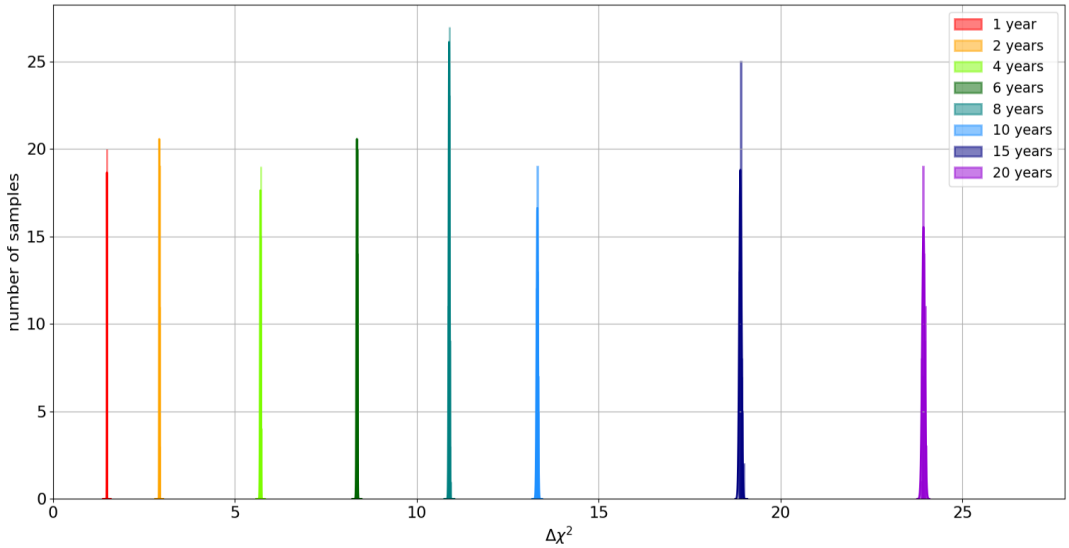

(b) True IO

Figure 75: Distributions of the $\Delta\chi^2$ for different assumed runtimes of the JUNO and TAO detector. Gaussian fits to the histograms are additionally displayed. The upper plot shows the results for an assumed true NO while the lower plot displays the same results for an assumed true IO.

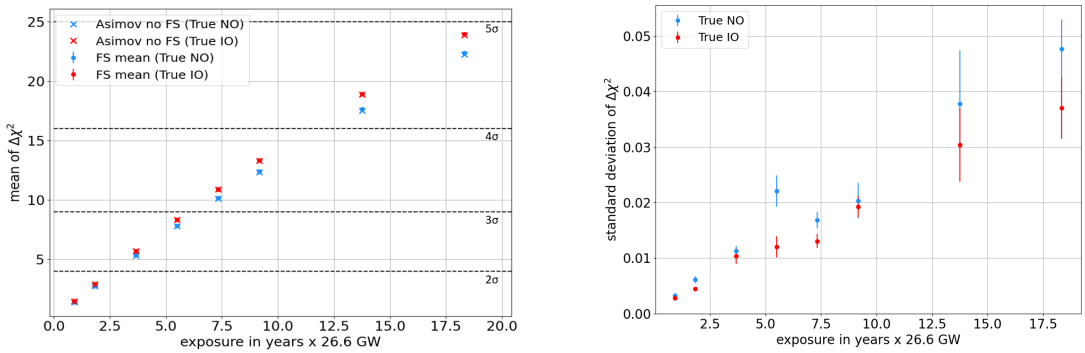

(a) Mean of $\Delta\chi^2$ **(b)** Standard deviation of $\Delta\chi^2$

Figure 76: Figure (a) shows the mean of the $\Delta\chi^2$ for the 100 analyzed summation spectra with fine structure (dots) and the Asimov $\Delta\chi^2$ for the case without fine structure (crosses) as a function of the exposure (runtime multiplied with duty cycle of 11/12 with 26.6 GW thermal power) of JUNO and TAO for assumed true NO (blue) and IO (red). Figure (b) displays the standard deviation of the $\Delta\chi^2$ distributions obtained from the Gaussian fits for assumed true NO (blue) and IO (red).

Previously, it was assumed that the JUNO and TAO detectors have the same DAQ time. Since the information on the fine structure comes from the reference spectrum measured by TAO, a scenario when TAO would have less exposure than JUNO should also be investigated. Therefore, the DAQ time of JUNO was fixed to six years while the TAO DAQ time was increased from one year up to the six years using the same 100 summation spectra with fine structure as in the previous analysis. Figure 77 shows the $\Delta\chi^2$ for the different DAQ times of TAO with assumed true NO and IO. It can be seen that the sensitivity to the NMO rapidly increases in the first 2-3 years and then asymptotically converges to the value for the same exposure for JUNO and TAO. The mean of the distributions is shown in figure 78a in comparison to the median Asimov $\Delta\chi^2$ in the case without fine structure which has a similar behavior. This shows that a certain event statistics has to be achieved for the TAO measurement to be able to constrain the reactor antineutrino spectrum well enough to obtain a high median sensitivity. Regarding the impact of different individual spectra with fine structure, figure 78b shows the standard deviation of the $\Delta\chi^2$ distributions which are on the sub-percent level of the mean value and within their uncertainties independent of the TAO exposure. Already one year of data taking with TAO can constrain the spectrum well enough that different fine structure shapes do not affect the sensitivity to a negative extent. However, it is observed that in case of a true inverted ordering, the mean of the $\Delta\chi^2$ for the analyzed summation spectra is slightly lower than the Asimov value in the case without fine structure for a TAO DAQ time of less than 2 years which is shown in figure 78c. This shows a potential minimal additional effect of the fine structure in the reactor neutrino spectrum in case of an insufficient spectral constraint from the TAO measurement. This difference is, however, less than 0.02 which is also in the order of the standard deviation. For larger TAO exposures, this small effect of the fine structure is vanishing.
In conclusion, using the spectrum measured with the satellite detector TAO provides enough corrective power to the fine structure that the median Asimov sensitivity proves to be a valid estimate of JUNO's sensitivity to the NMO.

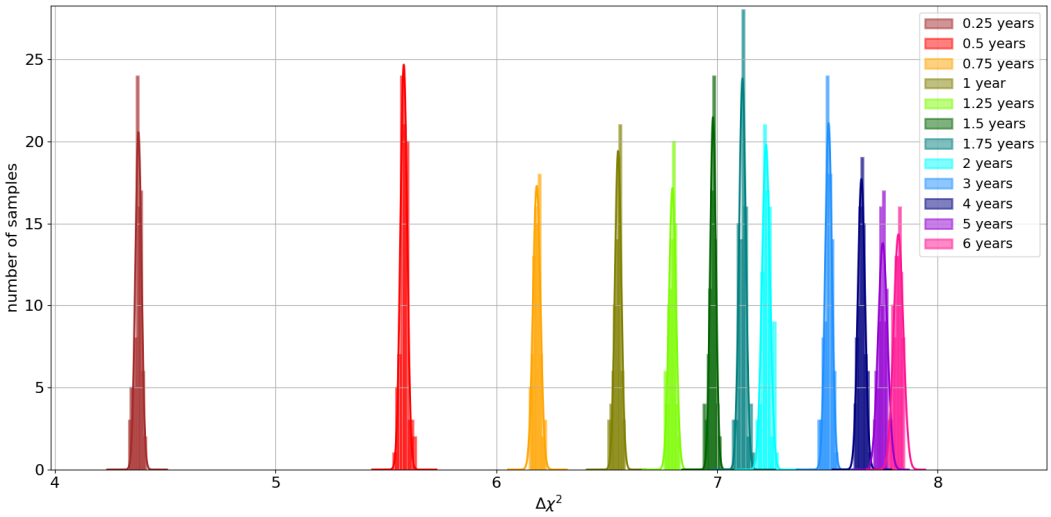

(a) True NO

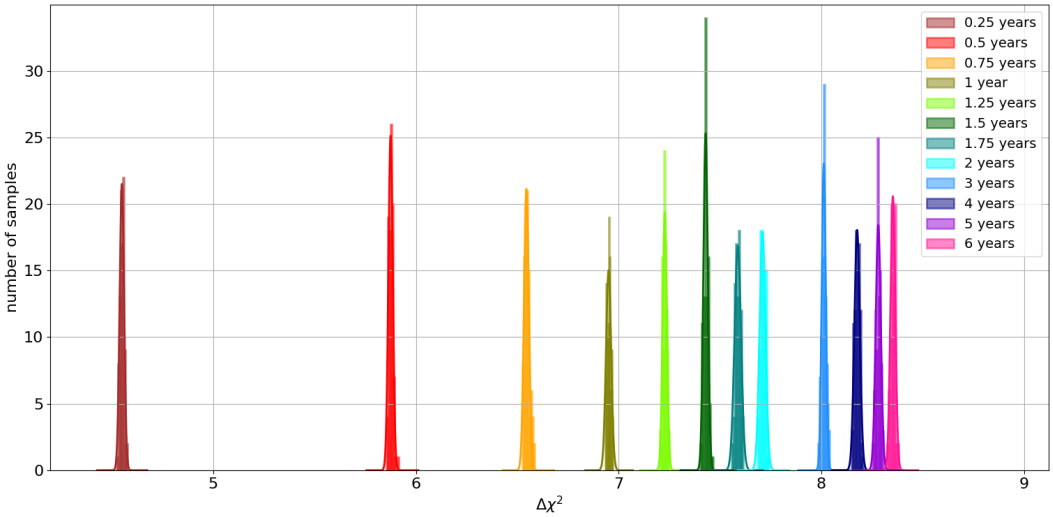

(b) True IO

Figure 77: Distributions of the $\Delta\chi^2$ for different assumed runtimes of the TAO detector while the DAQ time of JUNO is fixed to 6 years. Gaussian fits to the histograms are additionally displayed. The upper plot (a) shows the results for an assumed true NO while the lower plot (b) displays the same results for an assumed true IO.

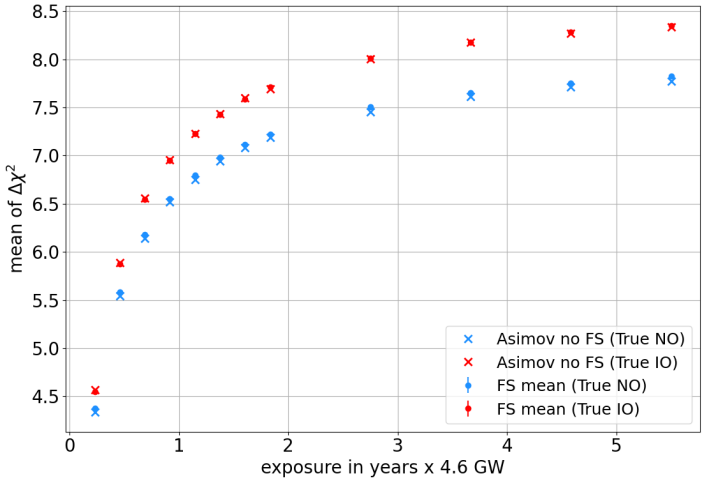

(a) Mean of $\Delta\chi^2$

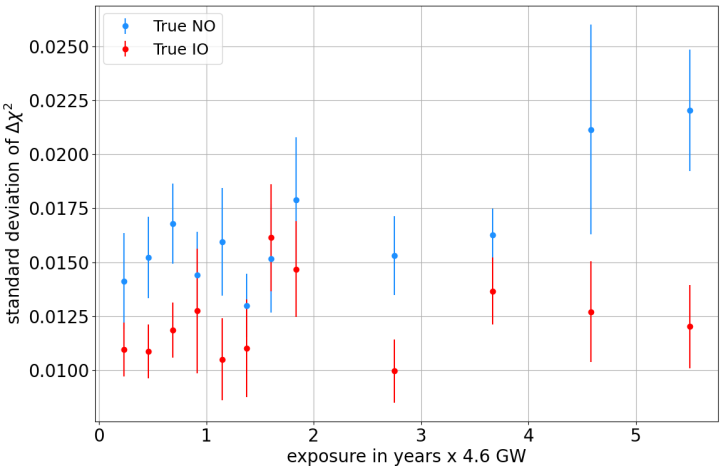

(b) Standard deviation of $\Delta\chi^2$

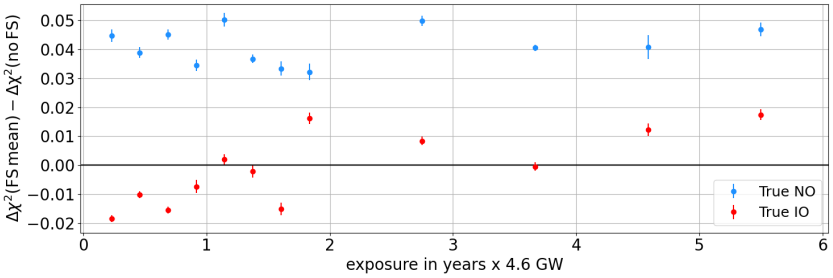

(c) Difference of $\Delta\chi^2$

Figure 78: Figure (a) shows the mean of the $\Delta\chi^2$ for the 100 analyzed summation spectra with fine structure (dots) and the Asimov $\Delta\chi^2$ for the case without fine structure (crosses) as a function of the exposure (runtime multiplied with duty cycle of 11/12 with 4.6 GW thermal power) of TAO for assumed true NO (blue) and IO (red) while the DAQ time of JUNO is fixed to 6 years. Figure (b) displays the standard deviation of the $\Delta\chi^2$ distributions obtained from the Gaussian fits for assumed true NO (blue) and IO (red). Figure (c) shows the difference of the mean of the $\Delta\chi^2$ for the 100 analyzed spectra to the Asimov $\Delta\chi^2$ for the case without fine structure for true NO (blue) and IO (red).

10 | Conclusion

Your destiny is what you make. It's the choices that you make. And for every choice, there's a consequence.

– Paul "Triple H" Levesque - *Chief Content Officer of WWE*

The Jiangmen Underground Neutrino Observatory aims to determine the neutrino mass ordering to 3σ in around 6 years of data taking by measuring the oscillated electron antineutrino spectrum from two nuclear power plants at a distance of 53 km. To achieve this goal, a precise knowledge of the reactor antineutrino spectrum is crucial. New predictions of the reactor antineutrino spectrum from nuclear data suggest the existence of small scale fluctuations in the spectrum that have not yet been experimentally observed but could have implications on the NMO sensitivity. Therefore, the JUNO experiment features the Taishan Antineutrino Observatory, a satellite detector located a few meters from one of the reactor cores to provide an unoscillated reference spectrum. Both detectors are currently under construction and will start taking data in the near future.

In this work, the implications of such a possible fine structure in the reactor antineutrino spectrum on JUNO's sensitivity to the NMO are investigated. In a first approach, an extension of the existing Global Neutrino Analysis software, which was also used to estimate the official sensitivity published in [45], was implemented to apply the fine structure as random fluctuations of variable energy scale and amplitude to the smooth and widely used Huber-Mueller spectrum model. In a second approach, the reactor antineutrino spectra with fine structure have been calculated via the summation method based on data from nuclear databases, varying each nuclear parameter of the contributing isotopes within its given uncertainties to generate a sample of 1000 possible spectra.
To investigate the implications on the NMO sensitivity of JUNO, random fluctuations with amplitudes of $1 - 10\%$ in steps of 1% as well as 15%, and 20% have been used as input spectra to generate 100 Asimov datasets to calculate the $\Delta\chi^2$ to discriminate between the mass orderings. Additionally, different energy scales of 1 keV, 5 keV, 10 keV, 20 keV, 30 keV, 40 keV, 50 keV, 75 keV, 100 keV of the fluctuations have been analyzed by a fit with a spectrum model based on the smooth Huber-Mueller spectrum. It showed that the mean of the sensitivity for the 100 sample spectra was not affected by the amplitudes or energy scale of the fluctuations but the standard deviation of the $\Delta\chi^2$ distribution increases significantly with increasing amplitude or energy scale. This showed the importance of taking the variations in the spectrum into account in the fitmodel. The same conclusion was obtained when the summation spectra were used as input to the analysis. The 1000 spectra with fine structure had been fitted with a smooth Huber-Mueller based fitmodel

showing a biased result as the fine structure fluctuations are not taken into account in the model. Therefore, a spectrum parametrization was introduced with spectral weights that allow to take into account spectral variations caused by the fine structure. An analysis was performed using the spectrum parametrization in the fitmodel with different constraints on the spectral weights. It was shown that the less tight the constraint on the spectral weights is, the less the average median sensitivity gets. For a completely free fitmodel, the NMO sensitivity reduces to zero as the spectral difference between the two mass orderings is completely compensated by the spectral weights without constraints.
In the next part of the thesis, the spectrum measured by the satellite detector TAO was used to constrain the spectral weights in a combined fit of the JUNO and TAO spectrum. Exemplary fluctuations with energy scales of 1keV, 10keV, and 100keV and amplitudes of 1%, 15%, and 10% have been added to the smooth spectrum and it was found that the standard deviations of the $\Delta\chi^2$ distributions are by an order of magnitude smaller than without the TAO constraint. Again, a similar observation was made for the 1000 summation spectra with fine structure. Here, an additional finding was made that depending on the true mass ordering around $10 - 20\%$ of the performed fits did not converge. To solve this issue, an option for the application of regularization was implemented in the analysis tool GNA and applied on the spectral weights. It was found that regularization based on first order derivative performs better than regularization based on the second order derivative. Additionally, it was found that the result does not show a characteristic L-curve to find the best regularization strength due to the application of the regularization to the spectral weights only and that some bias is introduced by the regularization as expected. Therefore, it was studied if the regularized fitmodel does serve as a better input model for an unregularized fit which was found to be true. With this technique to refit the result from the regularized fit in a second unregularized fit, all 1000 spectra provided a valid and unbiased result after some additional adjustment of the regularization strength. The overall results of $\overline{\Delta\chi^2} = 8.08$ (True NO) and $\overline{\Delta\chi^2} = 8.66$ (True IO) with a standard deviation of 0.01 and 0.02 respectively show a good agreement with the median Asimov sensitivity for the case without fine structure proving that the spectral constraint from the TAO detector allows to compensate any potential effects from the fine structure on the NMO sensitivity.
In the last part of this work, systematic effects on the NMO sensitivity in presence of a fine structure in the reactor antineutrino spectrum were investigated. In a first analysis, the spectrum parametrization used in the combined fit was studied regarding the width of the chosen energy segments. A total of six different options with 20 keV, 30 keV, and 40 keV using constant and variable segment widths that follow the energy resolution curve of TAO have been tested. The difficulty is to guarantee that the segments are fine enough to account for the fine structure measured in JUNO and still maintaining a stable fit. It was found that the variable option starting from 30 keV which is comparable to the resolution of the JUNO detector, performs the best for both assumed true mass orderings.
Due to changes in the construction plans, the location of the TAO detector shifted changing the distance to the reactor core from 30 m to 44 m. This reduces the flux in the TAO detector to almost the half of the originally planned flux. The analysis using 1000 summation spectra with fine structure was repeated with the new detector location and it was found that the average sensitivity is reduced to $\overline{\Delta\chi^2} = 7.81$ (True NO) and $\overline{\Delta\chi^2} = 8.35$ (True IO) which is again comparable to the case without fine structure. The standard deviation remains with 0.01 in both cases equally small. Despite the decrease of sensitivity due to the lower statistics, the ability to correct for the fine structure is not affected.

Further, it was analyzed how the energy resolution of the TAO detector impacts the NMO sensitivity and the possibility to correct for the fine structure in the spectrum. Various energy resolutions from 1.55% to 8% at 1 MeV and for the specific energy resolutions of the JUNO and Daya Bay detectors have been tested. It showed a similar decrease of the average $\Delta\chi^2$ as in the case of no fine structure. However, for energy resolutions from $3-5\%$, the standard deviation significantly increased and the fit was unstable. For a TAO resolution similar to the one of the JUNO detector, the estimation of the spectral weights proves to be difficult. The requirement of the TAO energy resolution being better than the one of JUNO is therefore also shown.
Lastly, the evolution of the NMO sensitivity with increasing DAQ time was analyzed to test if the impact by the fine structure has a temporal dependency. It was found that on average the sensitivity follows the temporal evolution like in the case without fine structure and the standard deviation of the distribution was found to be smaller than 0.05 up to 20 years of data taking showing no significant additional implications by the fine structure. A potential minimal effect by the fine structure in the reactor spectrum was found for TAO DAQ times of less than 2 years for 6 years of data taking with JUNO which is vanishing for larger exposures.

In this work, the implications of a spectral fine structure in the reactor antineutrino spectrum on the NMO sensitivity of the JUNO experiment have been thoroughly investigated and with the constraint by the reference spectrum of the satellite detector TAO, a negative impact could not be observed and with an exposure of 6.5 years $\times$ 26.6 $\mathrm{GW_{th}}$ a median sensitivity of 3σ (3.1σ) for a true normal (inverted) mass ordering can be achieved with JUNO regardless of the presence of a fine structure in the reactor antineutrino spectrum. Therefore, the Asimov sensitivity of the case without fine structure gives a valid estimate of JUNO's median sensitivity to the NMO which is in agreement with the official sensitivity published in [45].

Future analysis could include data from atmospheric neutrinos measured in JUNO as well as data from other experiments for a combined sensitivity analysis which could possibly increase the sensitivity to the NMO. Another focus could be set on the precision measurement of the neutrino oscillation parameters in presence of the fine structure which was beyond the scope of this thesis but would be of high interest for the JUNO experiment. Additionally, the ability of the TAO detector to test the nuclear databases could be investigated. With its high energy resolution it can provide the most precise measurement of rate and shape of the reactor antineutrino spectrum which could be sensitive to small changes of the parameters in the nuclear databases and therefore help to benchmark their current values.

With the results from JUNO and TAO expected to be taken in the next decade, new insights into the field of neutrino physics will be offered. By providing unprecedented precision in measuring the reactor antineutrino spectrum, it will not only increase our understanding of neutrino oscillations and mass ordering, but will also potentially provide the first measurement of the fine structure in the spectrum and can therefore help improving the modeling of the reactor antineutrino spectrum which will also have an important impact on future reactor neutrino experiments.

Appendices

A Further inputs to the IBD spectrum prediction

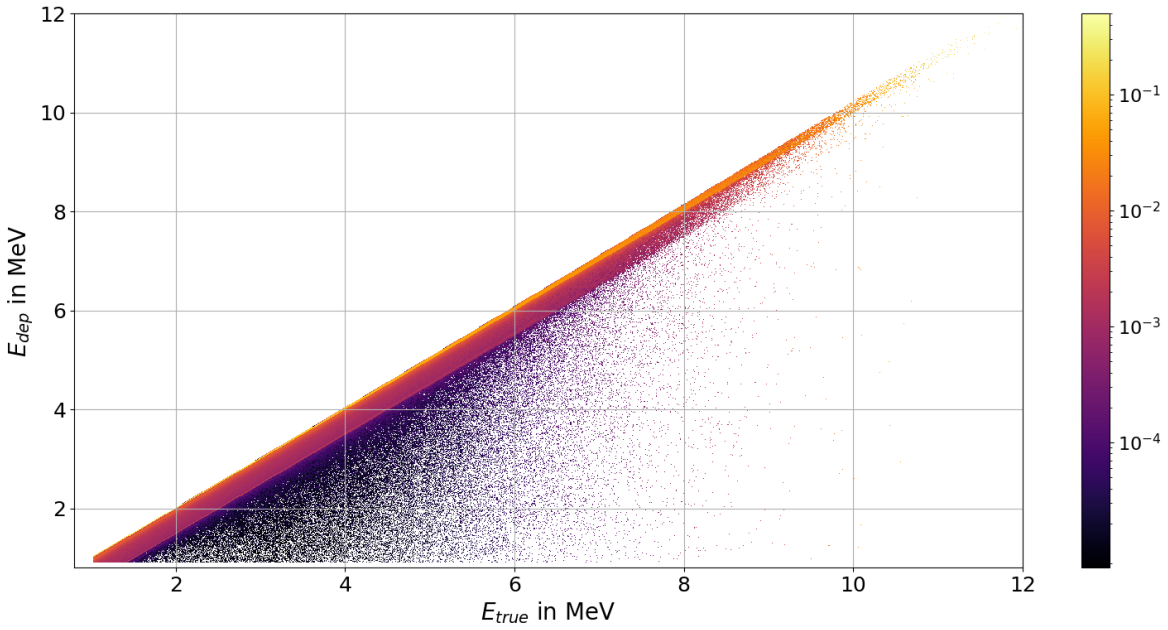

Figure 79: Plot of the energy leakage matrix C_{leak} obtained from the TAO detector simulation. It represents how the true positron energy $E_{\text{true}} = T_e + 2m_e$ is smeared to get the actual energy deposited in the fiducial volume E_{dep}.

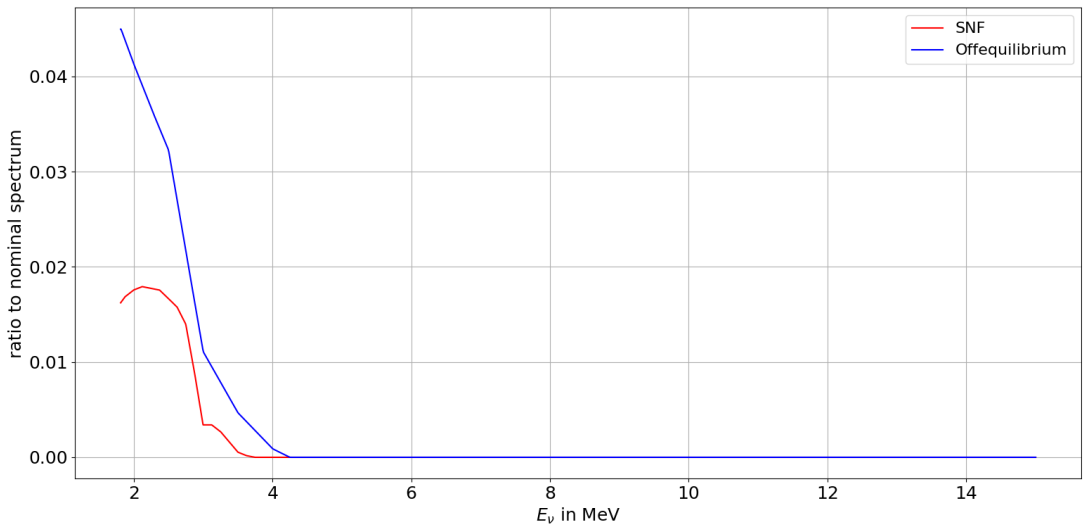

Figure 80: Spent nuclear fuel $C_{\text{SNF}}(E_\nu)$ (red) and offequilibrium correction $C_{\text{offeq}}(E_\nu)$ (blue) given as ratio to the nominal reactor antineutrino spectrum.

B Gaussian case of the $\Delta\chi^2$ statistics

To quantify the sensitivity, usually the number of Gaussian standard deviations is used. Using some approximations, this can also be calculated for the NMO sensitivity in case of JUNO according to [106]. As a valid approximation, it can be assumed that the $\Delta\chi^2$ test statistics given in equation 43 is Gaussian distributed. The median sensitivity itself is defined as the probability to accept the correct hypothesis H_0 while the probability to accept the wrong hypothesis H_1 is $P(H_1) = 0.5$. Figure 81 shows the Gaussian probability density with mean $\Delta\chi^2_{H_{0,1}}$ and standard deviation $2\sqrt{\Delta\chi^2_{H_{0,1}}}$ for the true and false hypothesis [106]. The median sensitivity is given by the integral of the probability density for the true hypothesis H_0 with the lower limit defined by the mean of the wrong hypothesis $\Delta\chi^2_{H_1}$ as

$$P(H_0) = \int_{\Delta\chi^2_{H_1}}^{\infty} \mathcal{P}(\Delta\chi^2 \,|\, \Delta\chi^2_{H_0}, 2\sqrt{\Delta\chi^2_{H_0}})\ \mathrm{d}\Delta\chi^2 \quad . \tag{67}$$

For a simpler calculation, the approximation of $\Delta\chi^2_{H_1} \approx -\Delta\chi^2_{H_0}$ can be made [106]. The probability is then given by

$$\begin{aligned} P(H_0) &= \int_{-\Delta\chi^2_{H_0}}^{\infty} \frac{1}{2\sqrt{\Delta\chi^2_{H_0}}\sqrt{2\pi}} \exp\left(-\frac{1}{2}\frac{(\Delta\chi^2 - \Delta\chi^2_{H_0})^2}{4\Delta\chi^2_{H_0}}\right)\ \mathrm{d}\Delta\chi^2 \\ &= -\frac{1}{2}\left[\mathrm{erf}\left(\frac{\Delta\chi^2_{H_0} - \Delta\chi^2}{2\sqrt{2}\sqrt{\Delta\chi^2_{H_0}}}\right)\right]_{-\Delta\chi^2_{H_0}}^{\infty} \\ &= \frac{1}{2}\left[1 - \mathrm{erf}\left(\sqrt{\frac{\Delta\chi^2_{H_0}}{2}}\right)\right] \quad , \end{aligned} \tag{68}$$

where $\mathrm{erf}(x)$ is the Gaussian error function. Since this is the probability to identify the true hypothesis H_0, it can be written as $P(H_0) = 1 - \alpha$ with the p-value α that is connected to the sensitivity given in multiples n of σ by $n = \sqrt{2}\mathrm{erfc}^{-1}(2\alpha)$ [106]. Using these relations, the definition of the inverse complementary error function $\mathrm{erfc}^{-1}(2\alpha) = \mathrm{erf}^{-1}(1-2\alpha)$, and the probability given in equation 68, the median sensitivity in terms of $n\sigma$ is given by

$$n = \sqrt{\Delta\chi^2_{H_0}} \quad . \tag{69}$$

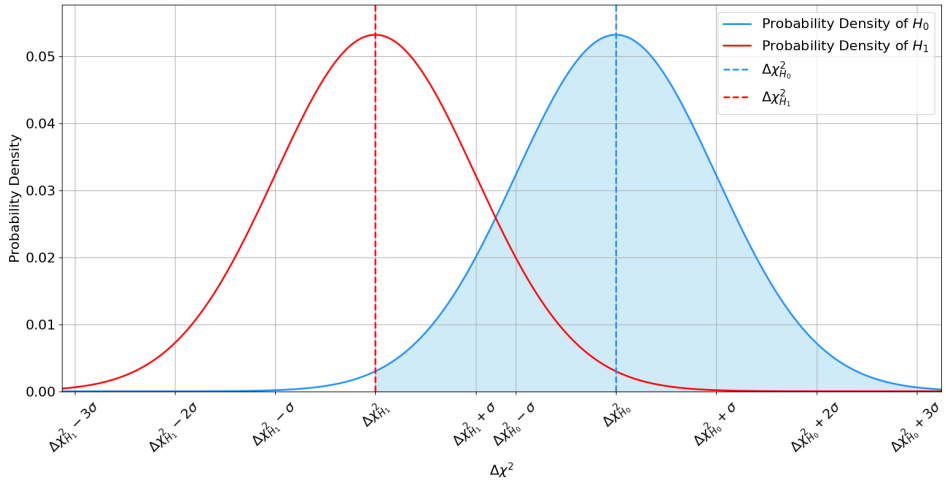

Figure 81: Gaussian probability distribution for the true hypothesis H_0 with mean $\Delta\chi^2_{H_0}$ (blue) and for the wrong hypothesis H_1 with mean $\Delta\chi^2_{H_1}$ (red). The blue shaded area shows the integral that defines the median sensitivity to identify the true hypothesis H_0 while the probability to identify the wrong hypothesis H_1 is 50%.

C Histograms for NMO sensitivity in presence of fluctuations

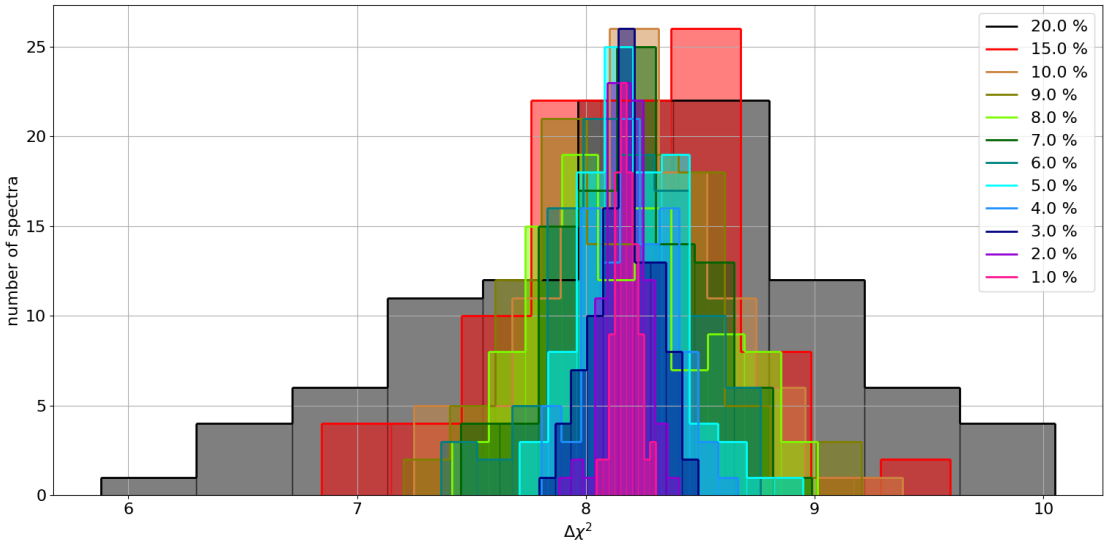

Figure 82: Distribution of the $\Delta\chi^2$ values for the Asimov datasets with true NO and a fluctuation energy width of 1 keV for all fluctuation amplitudes. The histograms are binned to 10 bins.

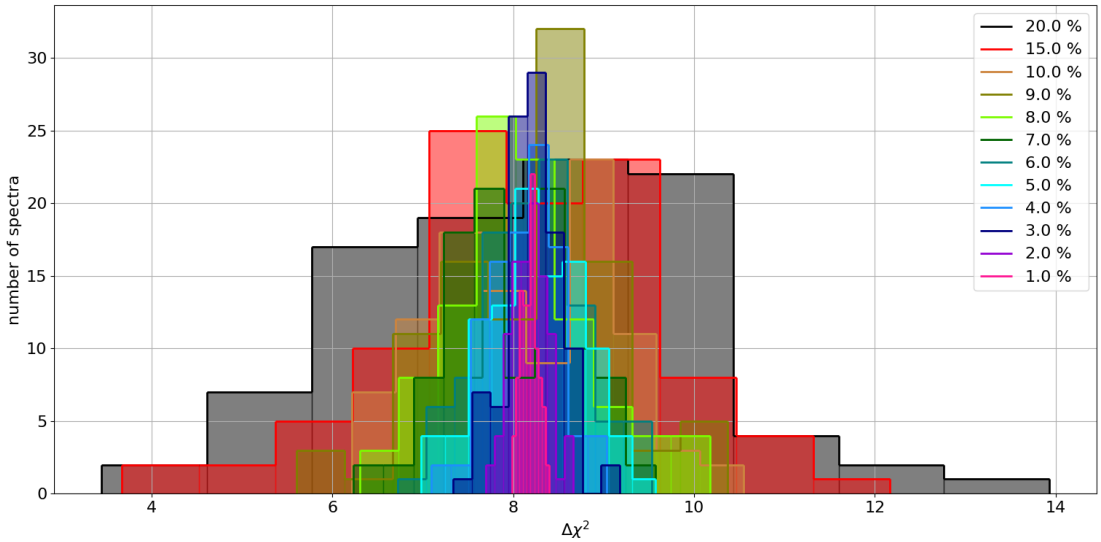

Figure 83: Distribution of the $\Delta\chi^2$ values for the Asimov datasets with true NO and a fluctuation energy width of 5 keV for all fluctuation amplitudes. The histograms are binned to 10 bins.

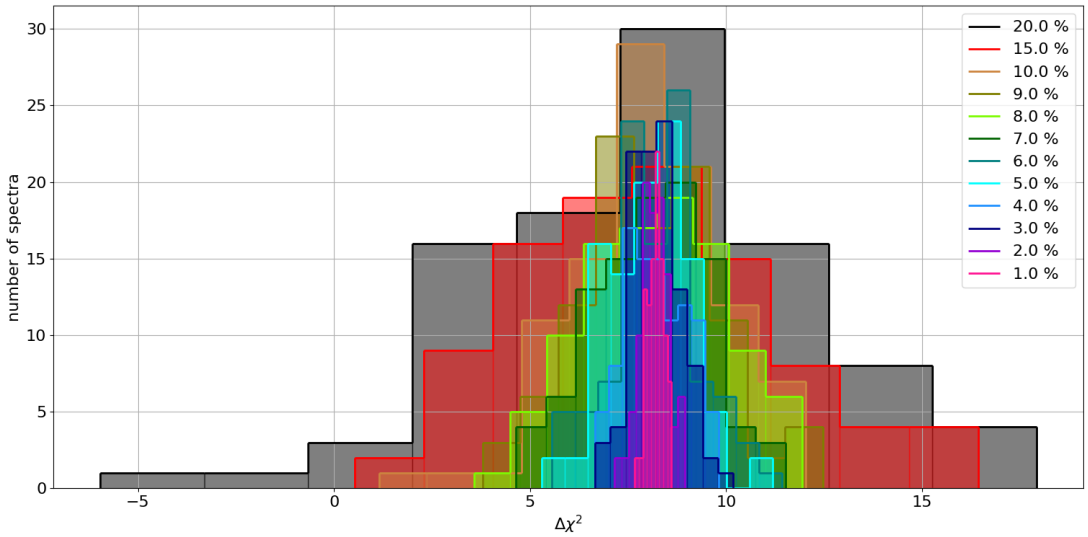

Figure 84: Distribution of the $\Delta\chi^2$ values for the Asimov datasets with true NO and a fluctuation energy width of 20 keV for all fluctuation amplitudes. The histograms are binned to 10 bins.

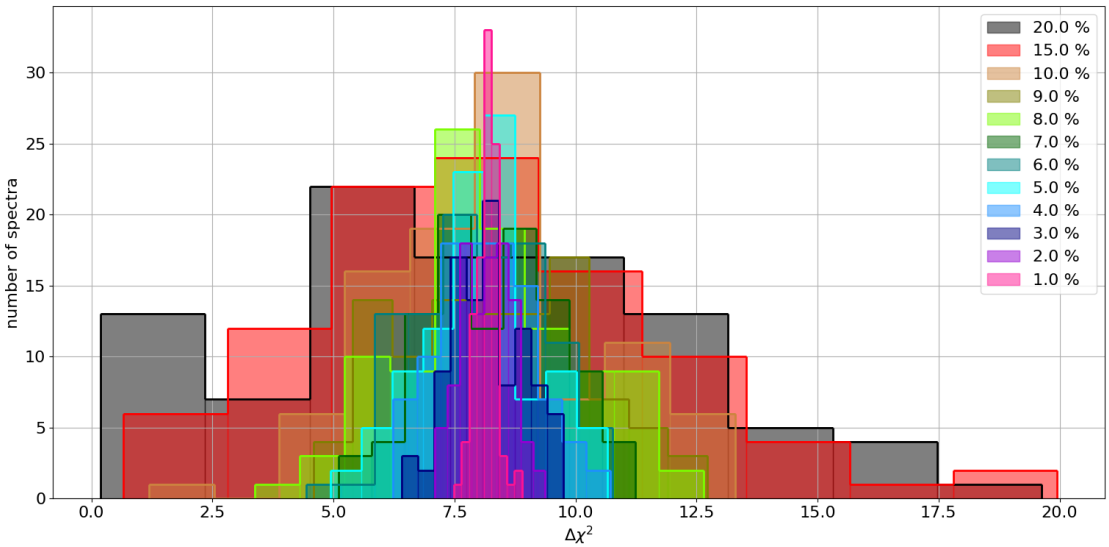

Figure 85: Distribution of the $\Delta\chi^2$ values for the Asimov datasets with true NO and a fluctuation energy width of 30 keV for all fluctuation amplitudes. The histograms are binned to 10 bins.

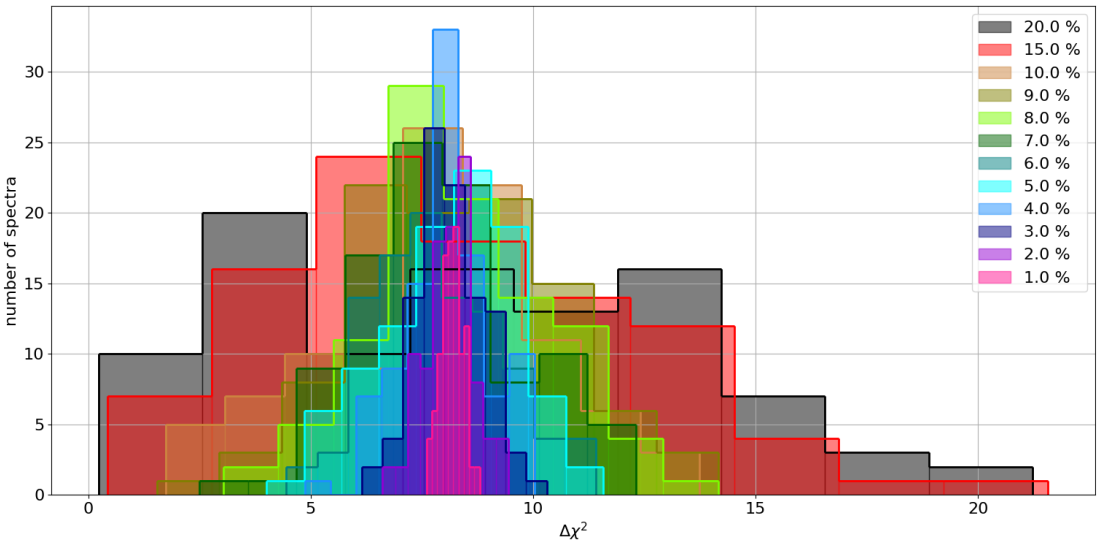

Figure 86: Distribution of the $\Delta\chi^2$ values for the Asimov datasets with true NO and a fluctuation energy width of 40 keV for all fluctuation amplitudes. The histograms are binned to 10 bins.

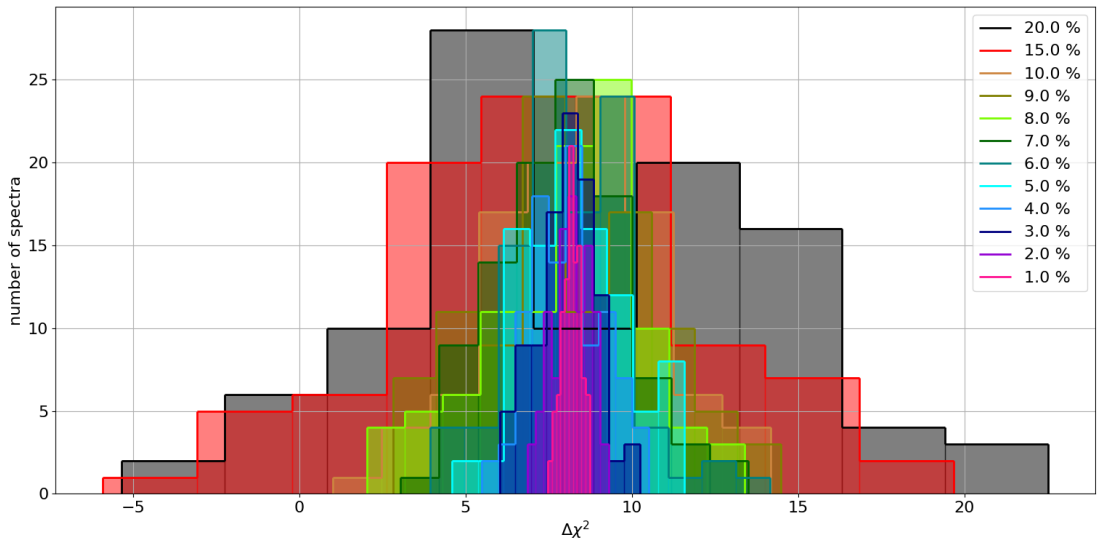

Figure 87: Distribution of the $\Delta\chi^2$ values for the Asimov datasets with true NO and a fluctuation energy width of 50 keV for all fluctuation amplitudes. The histograms are binned to 10 bins.

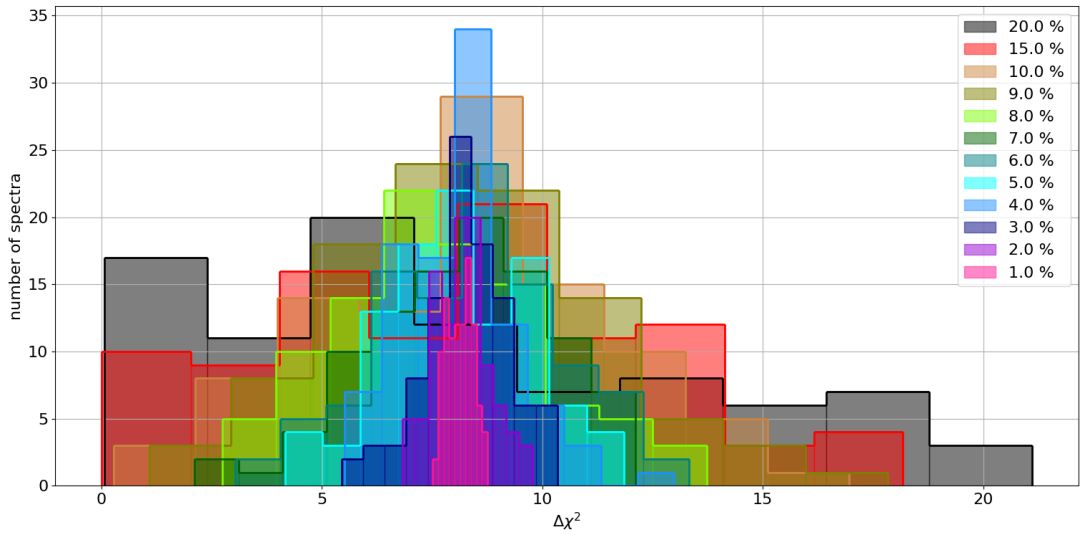

Figure 88: Distribution of the $\Delta\chi^2$ values for the Asimov datasets with true NO and a fluctuation energy width of 75 keV for all fluctuation amplitudes. The histograms are binned to 10 bins.

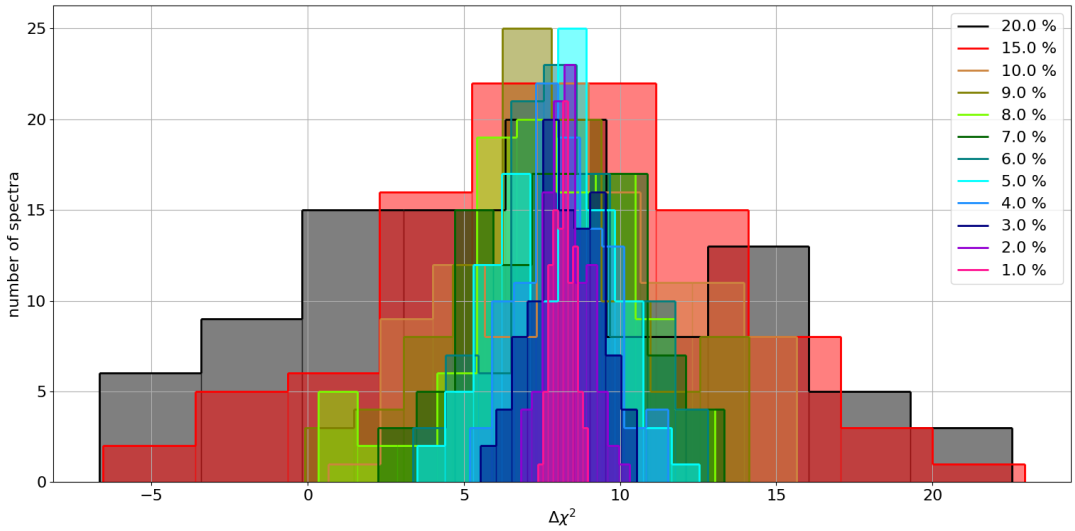

Figure 89: Distribution of the $\Delta\chi^2$ values for the Asimov datasets with true NO and a fluctuation energy width of 100 keV for all fluctuation amplitudes. The histograms are binned to 10 bins.

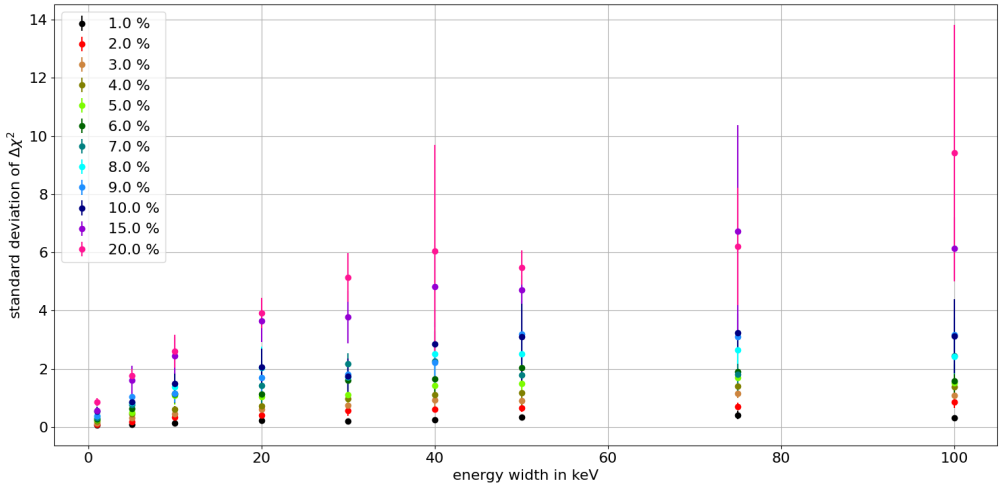

(a)

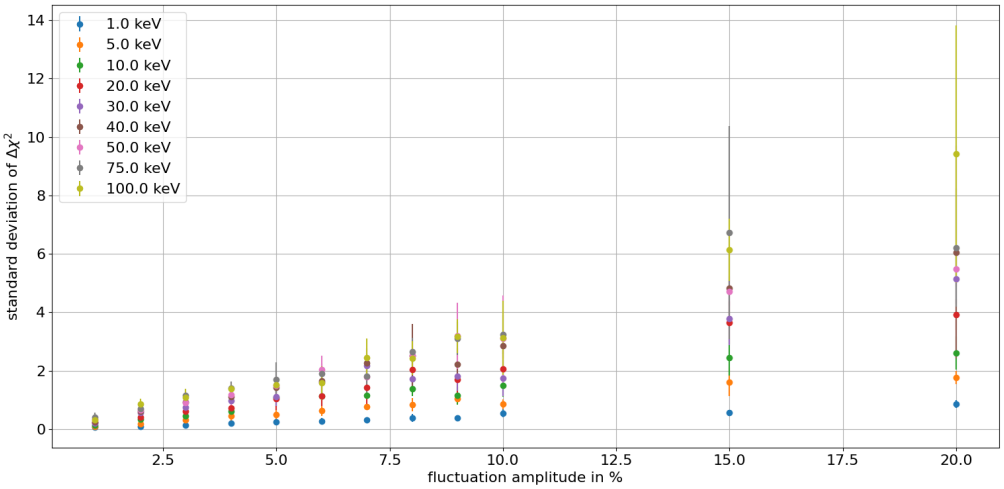

(b)

Figure 90: Standard deviation of the $\Delta\chi^2$ distribution with their respective 95% C.L. uncertainties as a function of the energy width of the fluctuations for all analyzed fluctuation amplitudes (a) and as a function of the fluctuation amplitude for all analyzed energy widths (b) for an assumed true IO.

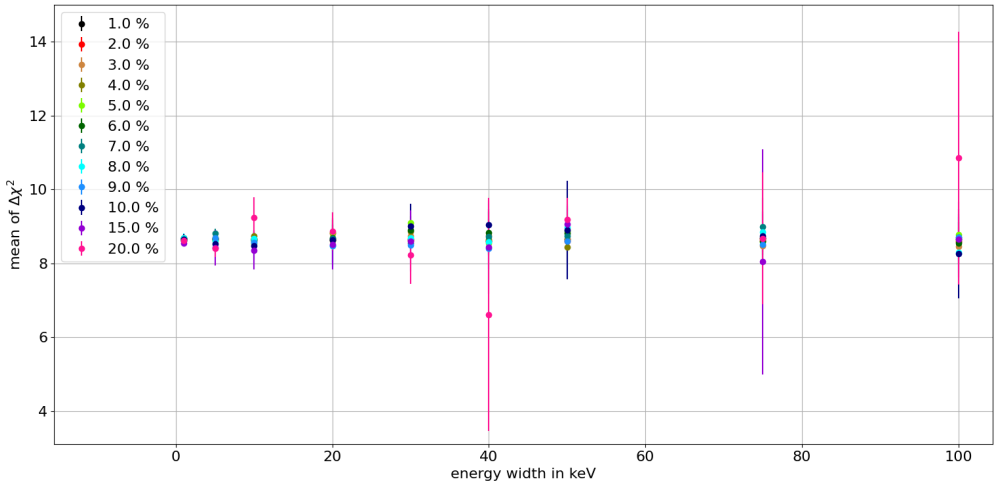

(a)

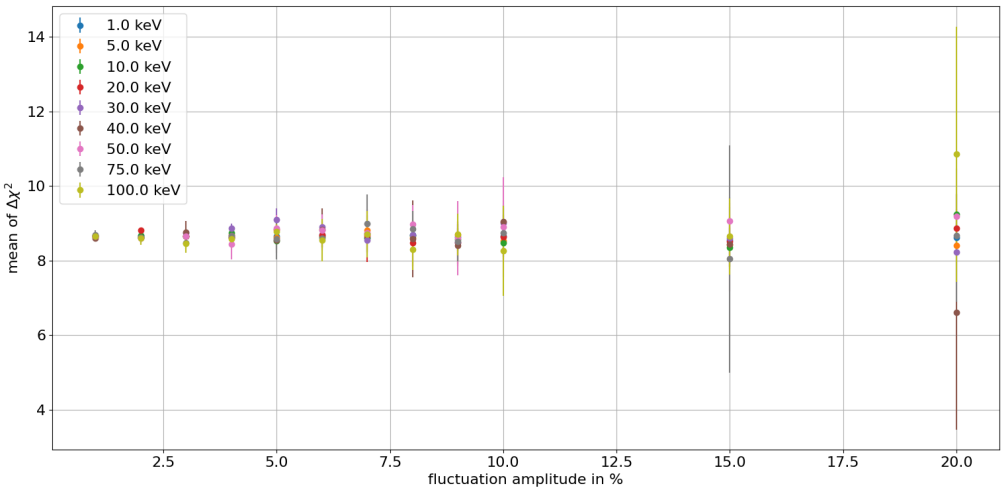

(b)

Figure 91: Mean of the $\Delta\chi^2$ distribution with the respective 95% C.L. uncertainties as a function of the energy width of the fluctuations for all analyzed fluctuation amplitudes (a) and as a function of the fluctuation amplitude for all analyzed energy widths (b) for an assumed true IO.

D NMO sensitivity comparison in presence of fluctuations

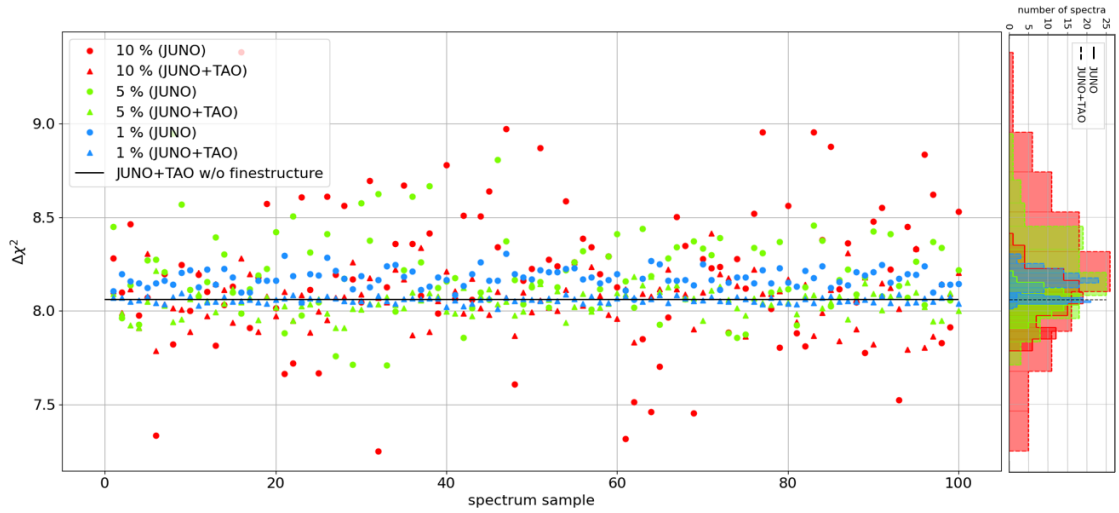

(a) 1 keV

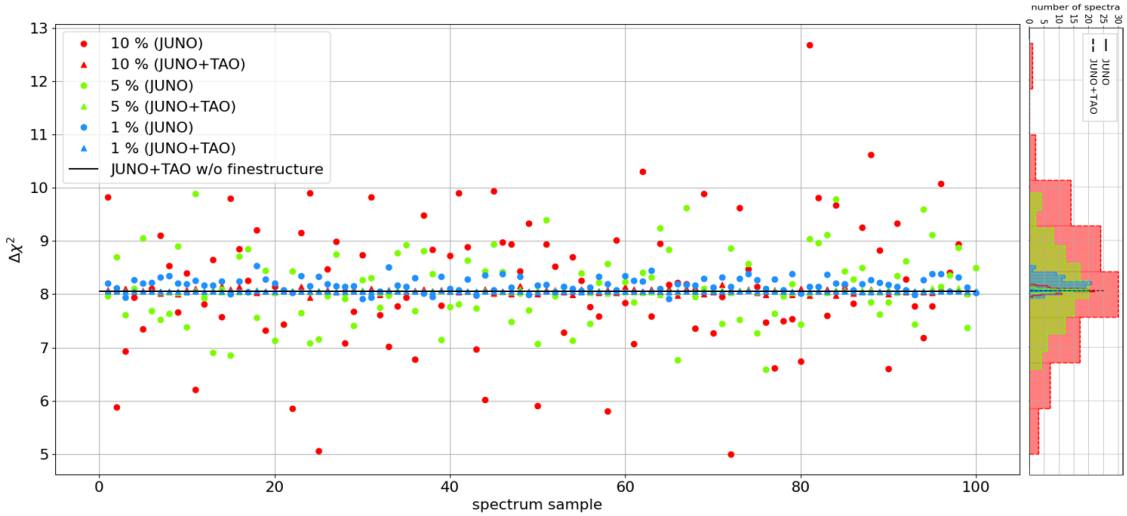

(b) 10 keV

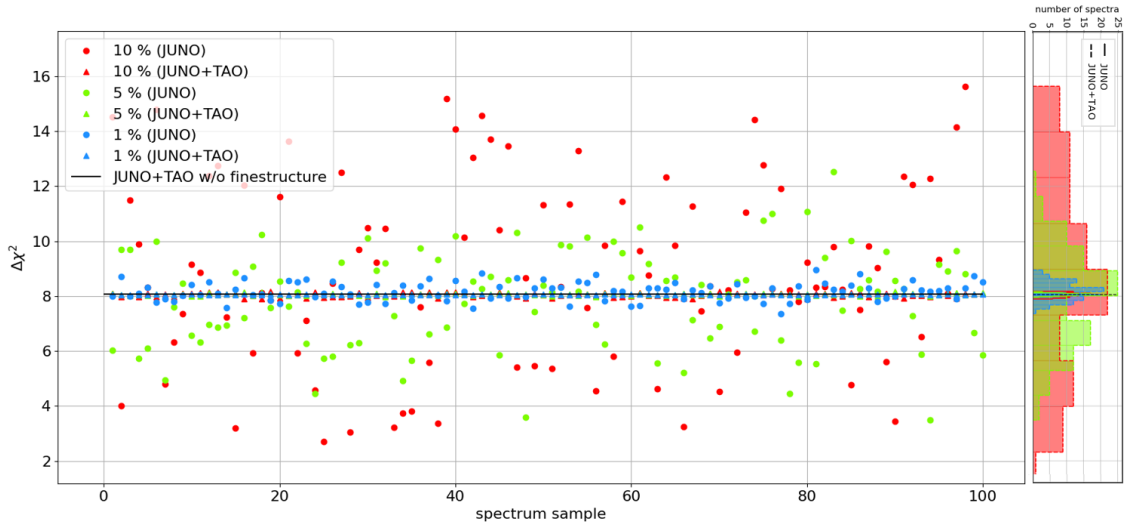

(c) 100 keV

Figure 92: $\Delta\chi^2$ values for 100 spectra with fluctuation amplitudes of 1% (blue), 5% (green), and 10% (red) for the combined JUNO+TAO fit (triangles) as well as the JUNO only fit (circles) as comparison. The right panel displays the distributions of the $\Delta\chi^2$ for both fits and all three fluctuation amplitudes. The black line indicates the $\Delta\chi^2$ for the case without fine structure. These results are shown for the fluctuation energy widths of 1 keV (a), 10 keV (b), and 100 keV (c).

E Unstable fitresult for const-20 spectrum parametrization

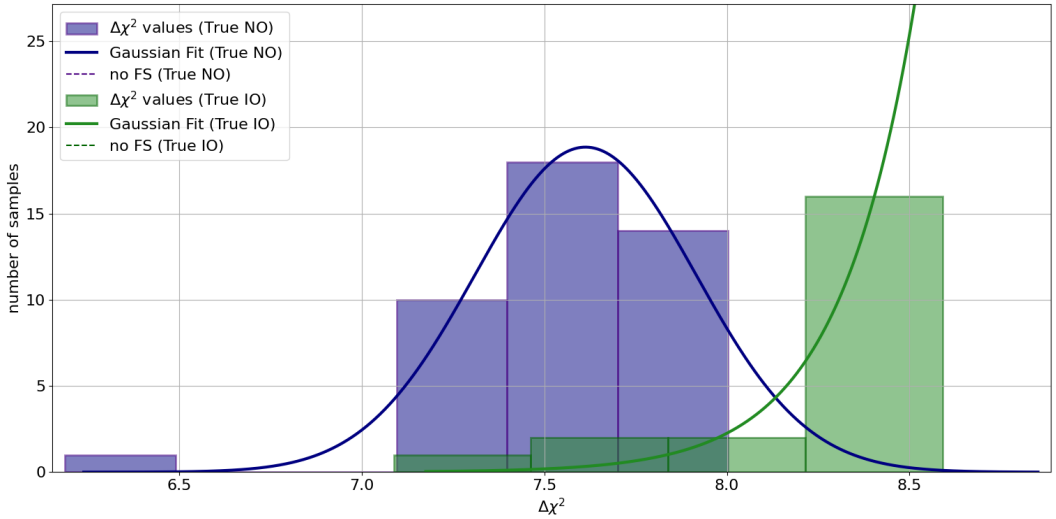

Figure 93: Distribution of the Asimov $\Delta\chi^2$ for assumed true NO (violet) and IO (green) for the energy segmentation option *const-20* for 120 analyzed summation spectra with fine structure as Asimov data. As the large number of segments makes the fit unstable, only 43 and 21 in case of true NO and IO (see table 18) converged. For the Asimov data without fine structure also no result was obtained. Additionally, Gaussian fits to the histograms are shown which does not provide a useful result for the IO case.

References

[1] W. Pauli. Offener Brief an die Gruppe der Radioaktiven bei der Gauvereins-Tagung zu Tübingen. In *Open letter to the group of radioactive people at the Gauverein meeting in Tübingen*, 1930.

[2] F. Reines, C.L. Cowan Jr, F.B. Harrison, A.D. McGuire, and H.W. Kruse. Detection of the free antineutrino. *Physical Review*, 117(1):159, 1960.

[3] K. Eguchi et al. First results from KamLAND: evidence for reactor antineutrino disappearance. *Physical Review Letters*, 90(2):021802, 2003.

[4] C. Giunti, Y.F. Li, C.A. Ternes, and Z. Xin. Reactor antineutrino anomaly in light of recent flux model refinements. *Phys. Lett. B*, 829:137054, 2022. URL `https://doi.org/10.1016/j.physletb.2022.137054`.

[5] A.A. Sonzogni, M. Nino, and E.A. McCutchan. Revealing fine structure in the antineutrino spectra from a nuclear reactor. *Physical Review C*, 98(1):014323, 2018. URL `https://doi.org/10.1103/PhysRevC.98.014323`. Reprinted figure with permission from Sonzogni, A.A. et al., Physical Review C, 98, 014323, 2018. Copyright 2018 by the American Physical Society.

[6] C. Spiering. Towards high-energy neutrino astronomy: a historical review. *The European Physical Journal H*, 37(3):515–565, 2012. URL `https://doi.org/10.1140/epjh/e2012-30014-2`. Reproduced with permission from Springer Nature.

[7] V.S. Berezinsky and A.Y. Smirnov. Cosmic neutrinos of ultra-high energies and detection possibility. *Astrophysics and Space Science*, 32:461–482, 1975.

[8] A. Faessler, R. Hodak, S. Kovalenko, and F. Simkovic. Search for the cosmic neutrino background. In *Journal of Physics: Conference Series*, volume 580, page 012040. IOP Publishing, 2015.

[9] G. Eder. Terrestrial neutrinos. *Nuclear Physics*, 78(3):657–662, 1966.

[10] W.C. Haxton, R.G. Hamish Robertson, and A.M. Serenelli. Solar neutrinos: status and prospects. *Annual Review of Astronomy and Astrophysics*, 51:21–61, 2013.

[11] P. Antonioli et al. SNEWS: The SuperNova early warning system. *New Journal of Physics*, 6(1):114, 2004.

[12] J.F. Beacom. The diffuse supernova neutrino background. *Annual Review of Nuclear and Particle Science*, 60:439–462, 2010.

[13] B. T. Cleveland et al. Measurement of the solar electron neutrino flux with the Homestake chlorine detector. *The Astrophysical Journal*, 496(1):505, 1998.

[14] W. Hampel et al. GALLEX solar neutrino observations: Results for GALLEX IV. *Physics Letters B*, 447(1-2):127–133, 1999.

[15] K.S. Hirata et al. Real-time, directional measurement of B-8 solar neutrinos in the Kamiokande II detector. *Physical Review D*, 44(8):2241, 1991.

[16] Y. Fukuda et al. Evidence for Oscillation of Atmospheric Neutrinos. *Phys. Rev. Lett.*, 81:1562–1567, Aug 1998. doi: 10.1103/PhysRevLett.81.1562. URL `https://link.aps.org/doi/10.1103/PhysRevLett.81.1562`.

[17] Q.R. Ahmad et al. Measurement of the Rate of $\nu_e + d \rightarrow p + p + e^-$ Interactions Produced by ^{8}B Solar Neutrinos at the Sudbury Neutrino Observatory. *Physical Review Letters*, 87(7):071301, 2001.

[18] R. L. Workman et al. Review of Particle Physics. *PTEP*, 2022:083C01, 2022. doi: 10.1093/ptep/ptac097.

[19] M. Thomson. *Modern particle physics*. Cambridge University Press, 2013.

[20] I. Tanseri, S. Hagstotz, S. Vagnozzi, E. Giusarma, and K. Freese. Updated neutrino mass constraints from galaxy clustering and CMB lensing-galaxy cross-correlation measurements. *Journal of High Energy Astrophysics*, 36:1–26, 2022.

[21] M. Aker et al. Direct neutrino-mass measurement with sub-electronvolt sensitivity. *Nature Physics*, 18(2):160–166, 2022.

[22] J.H. Christenson, J.W. Cronin, V.L. Fitch, and R. Turlay. Evidence for the 2π Decay of the $K_2{}^0$ Meson. *Physical Review Letters*, 13(4):138, 1964.

[23] L.L. Chau and W.Y. Keung. Comments on the parametrization of the Kobayashi-Maskawa matrix. *Physical Review Letters*, 53(19):1802, 1984.

[24] S. Cao. Long Baseline Neutrino Oscillation Results (T2K and NOνA). *arXiv preprint arXiv:2310.09855*, 2023.

[25] H. Fritzsch and Z. Xing. How to describe neutrino mixing and CP violation. *Physics Letters B*, 517(3-4):363–368, 2001.

[26] V. D'Andrea. Neutrinoless Double Beta Decay Search with ^{76}Ge: Status and Prospect with LEGEND. *arXiv preprint arXiv:1905.06572*, 2019.

[27] D.Q. Adams et al. New Direct Limit on Neutrinoless Double Beta Decay Half-Life of Te 128 with CUORE. *Physical review letters*, 129(22):222501, 2022.

[28] S. Abe et al. Search for the Majorana nature of neutrinos in the inverted mass ordering region with KamLAND-Zen. *Physical review letters*, 130(5):051801, 2023.

[29] M. Tanabashi et al. Review of Particle Physics: particle data groups. *Physical Review D*, 98(3), 2018.

[30] M. Danilov. Review of sterile neutrino searches at very short-baseline reactor experiments. *Physica Scripta*, 97(9):094001, 2022.

[31] T. Adam et al. JUNO Conceptual Design Report. *arXiv preprint arXiv:1508.07166*, 2015.

[32] A. Abusleme et al. TAO Conceptual Design Report: a precision measurement of the reactor antineutrino spectrum with sub-percent energy resolution. *arXiv preprint arXiv:2005.08745*, 2020.

[33] F.P. An et al. Neutrino physics with JUNO. *arXiv preprint arXiv:1507.05613*, 2015.

[34] A. Abusleme et al. Sub-percent precision measurement of neutrino oscillation parameters with JUNO. *Chinese Physics C*, 46(12):123001, 2022. URL `https://doi.org/10.1088/1674-1137/ac8bc9`.

[35] A. Abusleme et al. JUNO physics and detector. *Progress in Particle and Nuclear Physics*, 123:103927, 2022. URL `https://doi.org/10.1016/j.ppnp.2021.103927`.

[36] T. Heinz. JUNO's Sensitivity to the Neutrino Mass Ordering, 2023. URL `https://indico.cern.ch/event/1199289/contributions/5447360/attachments/2703025/4691891/TAUP-poster_final.pdf`. Poster at the XVIII International Conference on Topics in Astroparticle and Underground Physics (TAUP 2023), Vienna, August 28 - September 1, 2023. Slides online available, last accessed: December 9th, 2023.

[37] Y. Boxiang. Status of JUNO liquid scintillator. Talk at Technology & Instrumentation in Particle Physics (TIPP 2023), Cape Town, South Africa, September 4-8, 2023. Slides online available, last accessed: November 27, 2023, 2023. URL `https://indico.tlabs.ac.za/event/112/contributions/2804/attachments/1132/1528/Status%20of%20JUNO%20Liquids%20scintillator.pdf`.

[38] A. Abusleme et al. The design and sensitivity of JUNO's scintillator radiopurity pre-detector OSIRIS. *The European Physical Journal C*, 81(11):973, 2021.

[39] A. Abusleme et al. Prediction of Energy Resolution in the JUNO Experiment. 2024.

[40] J.B. Birks. Scintillations from organic crystals: specific fluorescence and relative response to different radiations. *Proceedings of the Physical Society. Section A*, 64 (10):874, 1951.

[41] B. Wonsak et al. A container-based facility for testing 20000 20-inch PMTs for JUNO. *Journal of Instrumentation*, 16(08):T08001, 2021.

[42] L.J. Wen et al. A quantitative approach to select PMTs for large detectors. *Nuclear Instruments and Methods in Physics Research Section A: Accelerators, Spectrometers, Detectors and Associated Equipment*, 947:162766, 2019.

[43] A.F. Tietzsch. *Development, installation and operation of a container-based mass testing system for 20-inch photomultiplier tubes for JUNO.* PhD thesis, Universität Tübingen, 2020.

[44] N. Anfimov. Large photocathode 20-inch PMT testing methods for the JUNO experiment. *Journal of Instrumentation*, 12(06):C06017, 2017.

[45] A. Abusleme et al. Potential to Identify the Neutrino Mass Ordering with Reactor Antineutrinos in JUNO. 2024.

[46] A. Abusleme et al. Calibration strategy of the JUNO experiment. *Journal of high energy physics*, 2021(3):1–33, 2021.

[47] J. Liu et al. Automated calibration system for a high-precision measurement of neutrino mixing angle θ_{13} with the Daya Bay antineutrino detectors. *Nuclear Instruments and Methods in Physics Research Section A: Accelerators, Spectrometers, Detectors and Associated Equipment*, 750:19–37, 2014. ISSN 0168-9002. doi: https://doi.org/10.1016/j.nima.2014.02.049. URL https://www.sciencedirect.com/science/article/pii/S0168900214002332.

[48] Y. Zhang et al. Cable loop calibration system for Jiangmen Underground Neutrino Observatory. *Nuclear Instruments and Methods in Physics Research Section A: Accelerators, Spectrometers, Detectors and Associated Equipment*, 988:164867, 2021. ISSN 0168-9002. doi: https://doi.org/10.1016/j.nima.2020.164867. URL https://www.sciencedirect.com/science/article/pii/S016890022031264X.

[49] H. Lu et al. The JUNO water Cherenkov detector system. *Nuclear Instruments and Methods in Physics Research Section A: Accelerators, Spectrometers, Detectors and Associated Equipment*, 1056:168623, 2023.

[50] T. Adam et al. The OPERA experiment target tracker. *Nuclear Instruments and Methods in Physics Research Section A: Accelerators, Spectrometers, Detectors and Associated Equipment*, 577(3):523–539, 2007.

[51] A. Abusleme et al. The JUNO experiment Top Tracker. *Nuclear Instruments and Methods in Physics Research Section A: Accelerators, Spectrometers, Detectors and Associated Equipment*, 1057:168680, 2023.

[52] J. Cao. Status of JUNO, 2024. URL https://agenda.infn.it/event/37867/contributions/234015/attachments/121923/178326/CJ_JUNO_Neutrino2024.pdf. Poster at the Neutrino 2024 Conference, Milano, June 16-22, 2024. Slides online available, last accessed: July 10th, 2024.

[53] C. Lombardo. JUNO-TAO design, prototype and its impact for JUNO physics, 2023. URL https://indico.desy.de/event/34916/contributions/147027/attachments/83844/110949/JUNO-TAO_poster_Lombardo.pdf. Poster at the European Physical Society Conference for High Energy Physics (EPS-HEP 2023), Hamburg, August 21-25, 2023. Slides online available, last accessed: December 1st, 2023.

[54] H. Xu et al. Calibration strategy of the JUNO-TAO experiment. *The European Physical Journal C*, 82(12):1112, 2022.

[55] K. Hirata et al. Observation of a neutrino burst from the supernova SN1987A. *Physical Review Letters*, 58(14):1490, 1987.

[56] R.M. Bionta et al. Observation of a neutrino burst in coincidence with supernova 1987A in the Large Magellanic Cloud. *Physical Review Letters*, 58(14):1494, 1987.

[57] E.N. Alexeyev, L.N. Alexeyeva, I.V. Krivosheina, and V.I. Volchenko. Detection of the neutrino signal from SN 1987A in the LMC using the INR Baksan underground scintillation telescope. *Physics Letters B*, 205(2-3):209–214, 1988.

[58] A. Abusleme et al. Real-time Monitoring for the Next Core-Collapse Supernova in JUNO. *arXiv preprint arXiv:2309.07109*, 2023.

[59] A. Abusleme et al. Prospects for detecting the diffuse supernova neutrino background with JUNO. *Journal of Cosmology and Astroparticle Physics*, 2022(10):033, 2022.

[60] M. Agostini et al. Comprehensive measurement of pp-chain solar neutrinos. *Nature*, 562(7728):505–510, 2018.

[61] A. Abusleme et al. JUNO sensitivity to ^{7}Be, *pep*, and CNO solar neutrinos. *Journal of Cosmology and Astroparticle Physics*, 2023(10), 2023.

[62] J. Zhao et al. Model Independent Approach of the JUNO ^{8}B Solar Neutrino Program. *arXiv preprint arXiv:2210.08437*, 2022.

[63] A. Abusleme et al. JUNO sensitivity to low energy atmospheric neutrino spectra. *The European Physical Journal C*, 81:1–16, 2021.

[64] T. Araki et al. Experimental investigation of geologically produced antineutrinos with KamLAND. *Nature*, 436(7050):499–503, 2005.

[65] M. Agostini et al. Comprehensive geoneutrino analysis with Borexino. *Physical Review D*, 101(1):012009, 2020.

[66] R. Han, Y.F. Li, L. Zhan, W.F. McDonough, J. Cao, and L. Ludhova. Potential of geo-neutrino measurements at JUNO. *Chinese Physics C*, 40(3):033003, 2016.

[67] A.D. Sakharov. Violation of CP-invariance, C-asymmetry, and baryon asymmetry of the Universe. In *In The Intermissions... Collected Works on Research into the Essentials of Theoretical Physics in Russian Federal Nuclear Center, Arzamas-16*, pages 84–87. World Scientific, 1998.

[68] K. Abe et al. Search for proton decay via p$\rightarrow \nu$ K^{+} using 260 kiloton $\cdot$ year data of Super-Kamiokande. *Physical Review D*, 90(7):072005, 2014.

[69] A. Abusleme et al. JUNO sensitivity on proton decay p$\rightarrow \nu$ K^{+} searches. *Chinese Physics C*, 47(11):113002, 2023.

[70] A. Abusleme et al. JUNO sensitivity to the annihilation of MeV dark matter in the galactic halo. *Journal of Cosmology and Astroparticle Physics*, 2023(09):001, 2023.

[71] A.C. Hayes and P. Vogel. Reactor neutrino spectra. *Annual Review of Nuclear and Particle Science*, 66:219–244, 2016.

[72] X.B. Ma, W.L. Zhong, L.Z. Wang, Y.X. Chen, and J. Cao. Improved calculation of the energy release in neutron-induced fission. *Physical Review C*, 88(1):014605, 2013.

[73] M. Estienne et al. Updated summation model: an improved agreement with the Daya Bay antineutrino fluxes. *Physical review letters*, 123(2):022502, 2019.

[74] F. von Feilitzsch, A.A. Hahn, and K. Schreckenbach. Experimental beta-spectra from ^{239}Pu and ^{235}U thermal neutron fission products and their correlated antineutrino spectra. *Phys. Lett B*, 118:365, 1982.

[75] K. Schreckenbach, G. Colvin, W. Gelletly, and F. von Feilitzsch. Determination of the antineutrino spectrum from ^{235}U thermal neutron fission products up to 9.5 MeV. *Physics Letters B*, 160(4-5):325–330, 1985. URL https://doi.org/10.1016/0370-2693(85)91337-1. Reprinted from Physics Letters B, Vol. 160, Schreckenbach, K. and Colvin, G. and Gelletly, W. and von Feilitzsch, F., Determination of the antineutrino spectrum from ^{235}U thermal neutron fission products up to 9.5 MeV, 325-330, Copyright 1985, with permission from Elsevier.

[76] V. Kopeikin, M. Skorokhvatov, and O. Titov. Reevaluating reactor antineutrino spectra with new measurements of the ratio between ^{235}U and ^{239}Pu β spectra. *Physical Review D*, 104(7):L071301, 2021.

[77] N. Haag, A. Guetlein, M. Hofmann, L. Oberauer, W. Potzel, K. Schreckenbach, and F.M. Wagner. Experimental determination of the antineutrino spectrum of the fission Products of ^{238}U. *Physical review letters*, 112(12):122501, 2014.

[78] P. Huber. Determination of antineutrino spectra from nuclear reactors. *Physical Review C*, 84(2):024617, 2011.

[79] T.A. Mueller et al. Improved predictions of reactor antineutrino spectra. *Physical Review C*, 83(5):054615, 2011.

[80] F.P. An et al. Improved measurement of the reactor antineutrino flux and spectrum at Daya Bay. *Chinese Physics C*, 41(1):013002, 2017. URL https://doi.org/10.1088/1674-1137/41/1/013002.

[81] Y. Abe et al. Improved measurements of the neutrino mixing angle θ_{13} with the Double Chooz detector. *Journal of High Energy Physics*, 2014(10):1–44, 2014. URL https://doi.org/10.1007/JHEP10%282014%29086.

[82] J.H. Choi et al. Observation of energy and baseline dependent reactor antineutrino disappearance in the RENO experiment. *Physical review letters*, 116(21):211801, 2016. URL https://doi.org/10.1103/PhysRevLett.116.211801. Reprinted figure with permission from Kim, S.B., Physical review letters, 116, 221801, 2016. Copyright 2016 by the American Physical Society.

[83] G. Mention, M. Fechner, Th. Lasserre, T.A. Mueller, D. Lhuillier, M. Cribier, and A. Letourneau. Reactor antineutrino anomaly. *Physical Review D*, 83(7):073006, 2011.

[84] M. Gonchar et al. GNA — high performance fitting for neutrino experiments. https://indico.cern.ch/event/773049/contributions/3473271/attachments/1931767/3212693/gonchar_chep2019_gna.pdf, 2019. 24th International Conference on Computing in High Energy & Nuclear Physics.

[85] M. Gonchar et al. Global Neutrino Analysis. https://github.com/gnafit/gna.

[86] Global Neutrino Analysis. http://gna.pages.jinr.ru/gna/. Accessed: 2021-11-20.

[87] D. Dolzhikov, M. Gonchar, and V. Zavadskyi. Neutrino Mass Ordering sensitivity TechNote, 2023. Password protected internal collaboration document.

[88] A.N. Khan, H. Nunokawa, and S.J. Parke. Why matter effects matter for JUNO. *Physics Letters B*, 803:135354, 2020.

[89] P. A. Zyla et al. Review of Particle Physics. *PTEP*, 2020(8):083C01, 2020. doi: 10.1093/ptep/ptaa104.

[90] P. Vogel and J.F. Beacom. Angular distribution of neutron inverse beta decay. *Physical Review D*, 60:053003, 1999.

[91] D. Adey et al. A high precision calibration of the nonlinear energy response at Daya Bay. *Nuclear Instruments and Methods in Physics Research Section A: Accelerators, Spectrometers, Detectors and Associated Equipment*, 940:230–242, 2019. ISSN 0168-9002. doi: https://doi.org/10.1016/j.nima.2019.06.031. URL `https://www.sciencedirect.com/science/article/pii/S016890021930871X`.

[92] R. Li. Veto Simulation Summary, 2021. Password protected internal collaboration document.

[93] A. Abusleme et al. Radioactivity control strategy for the JUNO detector. *Journal of High Energy Physics*, 2021(11):1–39, 2021.

[94] F.P. An et al. Measurement of electron antineutrino oscillation based on 1230 days of operation of the Daya Bay experiment. *Physical Review D*, 95(7):072006, 2017.

[95] S. Abe et al. Production of radioactive isotopes through cosmic muon spallation in KamLAND. *Physical Review C*, 81(2):025807, 2010.

[96] G. Bellini et al. Measurement of the solar B 8 neutrino rate with a liquid scintillator target and 3 MeV energy threshold in the Borexino detector. *Physical Review D*, 82 (3):033006, 2010.

[97] G. Bellini et al. Cosmogenic Backgrounds in Borexino at 3800 m water-equivalent depth. *Journal of Cosmology and Astroparticle Physics*, 2013(08):049, 2013.

[98] J. Cheng, Y.F. Li, L.J. Wen, and S. Zhou. Neutral-current background induced by atmospheric neutrinos at large liquid-scintillator detectors: I. Model predictions. *Physical Review D*, 103(5):053001, 2021.

[99] D. Dwyer. OKLO: A toolkit for modeling nuclides and nuclear reactions. `https://github.com/dadwyer/oklo`. Accessed: 2022-06-14.

[100] Brookhaven National Laboratory National Nuclear Data Center. ENDF/B-VIII.0 Library. `https://www.nndc.bnl.gov/endf-b7.1/download.html`, . Accessed: 2022-06-14.

[101] Brookhaven National Laboratory National Nuclear Data Center. ENDF/B-VII.1 Library. `https://www.nndc.bnl.gov/endf-b8.0/download.html`, . Accessed: 2022-06-15.

[102] D.H. Wilkinson. Analysis of neutron β-decay. *Nuclear Physics A*, 377(2):474–504, 1982. ISSN 0375-9474. doi: https://doi.org/10.1016/0375-9474(82)90051-3. URL `https://www.sciencedirect.com/science/article/pii/0375947482900513`.

[103] A.C. Hayes, J.L. Friar, G.T. Garvey, G. Jungman, and G. Jonkmans. Systematic uncertainties in the analysis of the reactor neutrino anomaly. *Physical Review Letters*, 112(20):202501, 2014.

[104] A. Sirlin. Radiative correction to the $\overline{\nu}_e$ (ν_e) spectrum in β decay. *Physical Review D*, 84(1):014021, 2011.

[105] G. Cowan, K. Cranmer, E. Gross, and O. Vitells. Asymptotic formulae for likelihood-based tests of new physics. *The European Physical Journal C*, 71:1–19, 2011.

[106] M. Blennow, P. Coloma, P. Huber, and T. Schwetz. Quantifying the sensitivity of oscillation experiments to the neutrino mass ordering. *Journal of High Energy Physics*, 2014(3):1–41, 2014.

[107] A.N. Thikhonov. On the solution of improperly posed problems and the method of regularization. *Sov. Math.*, 4:1035, 1963.

[108] D.L. Phillips. A technique for the numerical solution of certain integral equations of the first kind. *J. Assoc. Comput. Mach.*, 9:84–97, 1962.

[109] V. Blobel. Methods for Non-parametric Density Estimation and Unfolding, 2015. URL `https://www.desy.de/~sschmitt/blobel/dresden.pdf`. Presentation at Institutsseminar, Institut für Kern- und Teilchenphysik, TU Dresden, Accessed: 2023-04-17.

[110] H. Voss. Regularization of Least Squares Problems, 2010. URL `https://www.mat.tuhh.de/lehre/material/RegLS.pdf`. Talk in Valencia, Accessed: 2023-04-17.

[111] S. Schmitt. Data unfolding methods in high energy physics. In *EPJ web of conferences*, volume 137, page 11008. EDP Sciences, 2017.

[112] P.C. Hansen. The L-curve and its use in the numerical treatment of inverse problems. In P. Johnston, editor, *Computational Inverse Problems in Electrocardiology*, pages 119—-142. WIT Press, 2001.

[113] V. Blobel. Data unfolding. `https://indico.desy.de/event/2786/contributions/63735/attachments/41017/50786/blobel_100325.pdf`, 2010. Talk at the Terascale Statistics Tools School Spring 2010, DESY Hamburg.

[114] N. Viaux et al. Energy response model of the Daya Bay experiment. *Journal of Physics: Conference Series*, 888(1):012129, sep 2017. doi: 10.1088/1742-6596/888/1/012129. URL `https://dx.doi.org/10.1088/1742-6596/888/1/012129`.

List of Figures

List of Tables

Acronyms

ACU automatic calibration unit

AGN active galactic nuclei

bis-MSB 1,4-Bis(2-methylstyryl)benzene

CC charged current

CCSN core-collapse supernova

CKM Cabibbo-Kobayashi-Maskawa

CLS cable loop system

CMB cosmic microwave background

CUORE Cryogenic Underground Observatory for Rare Events

DAQ data acquisition

DSNB diffuse supernova neutrino background

ENDF Evaluated Nuclear Data File

ENSDF Evaluated Nuclear Structure Data File

GALLEX Gallium-Experiment

GNA Global Neutrino Analysis

HDPE high density polyethylene

IBD inverse beta decay

ILL Institut Laue–Langevin

IO inverted ordering

JINR Joint Institute for Nuclear Research

JUNO Jiangmen Underground Neutrino Observatory

KamLAND Kamioka Liquid Scintillator Antineutrino Detector

KATRIN Karlsruhe Tritium Neutrino Experiment

LAB linear alkyl benzene

LEGEND Large Enriched Germanium Experiment for Neutrinoless $\beta\beta$ Decay

LS liquid scintillator

LSNL liquid scintillator non-linearity

MSW Mikheyev–Smirnov–Wolfenstein

NC neutral current

NMO neutrino mass ordering

NNVT North Night Vision Technology

NO normal ordering

NOνA NuMI Off-Axis ν_e Appearance

NPP nuclear power plant

OPERA Oscillation Project with Emulsion tRacking Apparatus

OSIRIS Online Scintillator Internal Radioactivity Investigation System

PDG Particle Data Group

PMNS Pontecorvo-Maki-Nakagawa-Sakata

PMT photomultiplier tube

PPO 2,5-diphenyloxazole

QED quantum electrodynamics

RENO Reactor Experiment for Neutrino Oscillation

SiPM silicon photomultiplier

SNF spent nuclear fuel

SNO Sudbury Neutrino Observatory

T2K Tokai to Kamioka

TAO Taishan Antineutrino Observatory

Danksagung/Acknowledgements

Abschließend möchte ich mich bei allen bedanken, die auf ihre Weise dazu beigetragen haben, dass ich diese Arbeit anfertigen konnte.

Zunächst möchte ich mich bei Prof. Dr. Tobias Lachenmaier für die Möglichkeit und das entgegengebrachte Vertrauen bedanken, diese Arbeit in einem einzigartigen und spannenden Themenfeld in seiner Gruppe anfertigen zu können. Durch die Arbeit und die vielen fruchtbaren Diskussionen habe ich sehr viel in verschiedenen Bereichen lernen können.

A big thanks also goes to Maxim Gonchar for his support on working with the GNA software, all the helpful discussions about the NMO sensitivity analysis which had an important impact on realizing the studies in this work and also for showing understanding and the cooperation when the time of collaboration got difficult.

Ein weiterer Dank geht an alle aus der Arbeitsgruppe für die immer wieder hilfreichen und auch oft unterhaltsamen Gespräche zwischendurch oder bei den gemeinsamen Mittagessen im Glaskasten. Ebenfalls möchte ich mich bei meinem Zweitbetreuer Prof. Dr. Josef Jochum bedanken sowie bei Dr. Günter Lang, Gaby Behring und Gabriele Enßlin-Richter für die ganze Unterstützung bei organisatorischen und bürokratischen Angelegenheiten.

Ein besonderer Dank gilt meinen Bürokollegen Tobias Sterr und Marc Breisch, sowie den anderen "Gentlemen" Gina Grünauer, Jessica Eck, Katja Wurster, Katharina Kilgus, Lukas Wolz, Colin Heckmeyer sowie Dr. Ann-Kathrin Schütz und Dr. Lukas Rauscher für die schöne Zeit innerhalb und außerhalb der Uni, die vielen mehr und manchmal auch weniger niveauvollen Gespräche über alle möglichen Themen und die vielen gemeinsamen Unternehmungen von gelegentlichen Feierabend-Bieren oder Grillen bis zu einem fast schon traditionellen jährlichen Europapark-Ausflug.

Ebenfalls möchte ich mich bei allen aus der deutschen JUNO-Forschergruppe für die gute Zusammenarbeit und die tolle Atmosphäre bei den gemeinsamen Meetings bedanken, die auch immer bis weit nach Feierabend anhielt. Unter anderem die verschiedenen Reisen nach China, das Meeting in Moskau und ein legendärer Abend in einem Pub in Bordeaux werden mir sicher noch lange in Erinnerung bleiben (zumindest was davon noch übrig ist).

Ohne einen Ausgleich zur Arbeit geht es natürlich auch nicht, weshalb ein großer Dank auch meiner Tanzpartnerin Jenny und allen meinen Freunden vom TTC Rot-Gold Tübingen gilt, die mitunter dafür gesorgt haben, dass ich immer beim Betreten der Halle auf andere Gedanken kommen und vom Alltag abschalten konnte. Und natürlich auch nochmal Danke an Jessi, ohne die ich gar nicht erst mit dem Turniertanz angefangen hätte, wenn sie mich nicht an der Uni so lange bearbeitet hätte, wodurch mir in den letzten Jahren sicher einiges gefehlt hätte.

Ein großer Dank geht auch an die "Fäuste" Luk, Chris und Jack, die seit der Schulzeit nicht mehr aus meinem Leben weg zu denken sind und auf die ich mich immer verlassen kann sowie an alle anderen aus meinem Freundeskreis, die mich immer wieder unterstützt haben.

Nicht zuletzt danke ich meiner Familie und besonders meinen Eltern, die immer an meiner Seite standen und mich in allen Lebenslagen unterstützt haben, für ihren Glauben an mich, ihre Geduld, ihre vielen Ratschläge, ihre Ermutigung während der gesamten Promotion und das Gefühl, jederzeit einen sicheren Rückzugsort zu haben.

Da ich niemanden vergessen möchte und auch gar nicht alle aufzählen kann, gilt mein Dank abschließend auch allen anderen, die irgendwie zum Gelingen dieser Dissertation beigetragen haben, auch wenn sie hier nicht namentlich erwähnt wurden.